

Projet de Recherche INTERREG-V océan Indien 2014-2020
A1/OT1/OS-01a - Action II-2 TN

ReNovRisk-Cyclones et Précipitations



L15: Compilation des articles scientifiques

Olivier BOUSQUET

Laboratoire de l'Atmosphère et des Cyclones
(UMR 8105 CNRS/Météo-France/Université de La Réunion)



Livrable 15 : Compilation des articles scientifiques

Le projet ReNovRisk-CP a fait l'objet de six publications dans des revues scientifiques internationales de rang A

⇒ Quatre dans la revue Atmosphere (MDPI, Impact factor 3.11*)

- Bousquet et al, 2021 (<https://doi.org/10.3390/atmos12050544>, 11 citations à ce jour)
- Durand et al. 2021 (<https://doi.org/10.3390/atmos12070868>, 2 citations à ce jour)
- Manhique et al. 2021 (<https://doi.org/10.3390/atmos12060739>, 2 citations à ce jour)
- Mavume et al. 2021 (<https://doi.org/10.3390/atmos12050588>, 11 citations à ce jour)

⇒ Un dans la revue Natural Hazards (Springer, Impact factor : 3.1*)

- Tulet et al. 2021 (<https://doi.org/10.1007/s11069-021-04624-w>, 5 citations à ce jour)

⇒ Un dans la revue Journal of Climate (AMS, Impact factor : 5.48*)

- Cattiaux et al. 2020 (<https://doi.org/10.1175/JCLI-D-19-0591.1>, 14 citations à ce jour)

* Le facteur d'impact est une variable statistique indiquant le nombre moyen de citations par article publié depuis la date de création du journal. Plus ce nombre est élevé, plus la revue est considérée comme prestigieuse. Les journaux ayant un facteur d'impact > 1 sont considérés comme des revues de référence dans le domaine des sciences de la terre (Rang A).

⇒ Deux articles sont dédiés à l'exploitation des mesures expérimentales collectées dans le cadre de l'action 1

Bousquet O, Barruol G, Cordier E, Barthe C, Bielli S, Calmer R, Rindraharisaona E, Roberts G, Tulet P, Amelie V, Fleischer-Dogley F, Mavume A, Zucule J, Zakariasy L, Razafindradingina B, Bonnardot F, Singh M, Lees E, Durand J, Mekies D, Claeys M, Pianezze J, Thompson C, Tsai C-L, Husson R, Mouche A, Ciccione S, Cattiaux J, Chauvin F, Marquestaut N. Impact of Tropical Cyclones on Inhabited Areas of the SWIO Basin at Present and Future Horizons. Part 1: Overview and Observing Component of the Research Project RENOVRIISK-CYCLONE. *Atmosphere*. 2021; 12(5):544.
<https://doi.org/10.3390/atmos12050544>

Durand J, Lees E, Bousquet O, Delanoë J, Bonnardot F. Cloud Radar Observations of Diurnal and Seasonal Cloudiness over Reunion Island. *Atmosphere*. 2021; 12(7):868.
<https://doi.org/10.3390/atmos12070868>

⇒ Trois articles traitent des problématiques de climat (climatologie des cyclones, impact du changement climatique), abordées dans le cadre de l'action 2

Manhique AJ, Guirruogo IA, Nhantumbo BJ, Mavume AF. Seasonal to Interannual Variability of Vertical Wind Shear and Its Relationship with Tropical Cyclogenesis in the Mozambique Channel. *Atmosphere*. 2021; 12(6):739.
<https://doi.org/10.3390/atmos12060739>

Mavume AF, Banze BE, Macie OA, Queface AJ. Analysis of Climate Change Projections for Mozambique under the Representative Concentration Pathways. *Atmosphere*. 2021; 12(5):588.
<https://doi.org/10.3390/atmos12050588>

Cattiaux, J., Chauvin, F., Bousquet, O., Malardel, S., & Tsai, C. (2020). Projected Changes in the Southern Indian Ocean Cyclone Activity Assessed from High-Resolution Experiments and CMIP5 Models, *Journal of Climate*, 33(12), 4975-4991. Retrieved Feb 7, 2023, <https://journals.ametsoc.org/view/journals/clim/33/12/jcli-d-19-0591.1.xml>

⇒ Le dernier article traite du programme ReNovRisk dans son ensemble (communication en lien avec l'action 3 du projet).

Tulet, P., Aunay, B., Barruol, G. *et al.* ReNovRisk: a multidisciplinary programme to study the cyclonic risks in the South-West Indian Ocean. *Nat Hazards* **107**, 1191–1223 (2021). <https://doi.org/10.1007/s11069-021-04624-w>

Ces articles sont reproduits ci-après tels que publiés dans les revues.



Article

Impact of Tropical Cyclones on Inhabited Areas of the SWIO Basin at Present and Future Horizons. Part 1: Overview and Observing Component of the Research Project RENOVRIISK-CYCLONE

Olivier Bousquet, Guilhem Barruol, Emmanuel Cordier, Christelle Barthe, Soline Bielli, Radiance Calmer, Elisa Rindraharisaona, Gregory Roberts, Pierre Tulet, Vincent Amelie et al.

Special Issue







Tropical Cyclones in the Indian Ocean

Edited by
Prof. Dr. Olivier Bousquet



Article

Impact of Tropical Cyclones on Inhabited Areas of the SWIO Basin at Present and Future Horizons. Part 1: Overview and Observing Component of the Research Project RENOVRISK-CYCLONE

Olivier Bousquet ^{1,2,*}, Guilhem Barruol ³, Emmanuel Cordier ⁴, Christelle Barthe ^{1,5} , Soline Bielli ¹, Radiance Calmer ^{1,6}, Elisa Rindraharisaona ^{3,7} , Gregory Roberts ^{8,9}, Pierre Tulet ^{1,5}, Vincent Amelie ¹⁰, Frauke Fleischer-Dogley ¹¹, Alberto Mavume ¹² , Jonas Zucule ¹³, Lova Zakariasy ¹⁴, Bruno Razafindradina ¹⁴, François Bonnardot ¹⁵, Manvendra Singh ¹⁶, Edouard Lees ¹, Jonathan Durand ¹, Dominique Mekies ¹, Marine Claeys ^{1,9}, Joris Pianezze ¹, Callum Thompson ¹, Chia-Lun Tsai ^{1,17} , Romain Husson ¹⁸, Alexis Mouche ¹⁹ , Stephane Ciccione ²⁰, Julien Cattiaux ⁹, Fabrice Chauvin ⁹ , and Nicolas Marquestaut ^{1,4}



Citation: Bousquet, O.; Barruol, G.; Cordier, E.; Barthe, C.; Bielli, S.; Calmer, R.; Rindraharisaona, E.; Roberts, G.; Tulet, P.; Amelie, V.; et al. Impact of Tropical Cyclones on Inhabited Areas of the SWIO Basin at Present and Future Horizons. Part 1: Overview and Observing Component of the Research Project RENOVRISK-CYCLONE. *Atmosphere* **2021**, *12*, 544. <https://doi.org/10.3390/atmos12050544>

Academic Editor: Corene Matyas

Received: 31 March 2021

Accepted: 20 April 2021

Published: 23 April 2021

Publisher's Note: MDPI stays neutral with regard to jurisdictional claims in published maps and institutional affiliations.



Copyright: © 2021 by the authors. Licensee MDPI, Basel, Switzerland. This article is an open access article distributed under the terms and conditions of the Creative Commons Attribution (CC BY) license (<https://creativecommons.org/licenses/by/4.0/>).

- ¹ Laboratoire de l'Atmosphère et des Cyclones (UMR8105 LACy), Université de La Réunion, CNRS, Météo-France, 97400 Saint-Denis, France; christelle.barthe@aero.obs-mip.fr (C.B.); soline.bielli-bousquet@univ-reunion.fr (S.B.); radiance.calmer@colorado.edu (R.C.); pierre.tulet@aero.obs-mip.fr (P.T.); edouard.lees@meteo.fr (E.L.); jonathan.durand@live.com (J.D.); dominique.mekies@meteo.fr (D.M.); marine.claeys@meteo.fr (M.C.); joris.pianezze@univ-reunion.fr (J.P.); callum-thompson@ucsb.edu (C.T.); chialun@knu.ac.kr (C.-L.T.); nicolas.marquestaut@univ-reunion.fr (N.M.)
 - ² Institute for Coastal Marine Research (CMR), Nelson Mandela University, Port-Elizabeth 6031, South Africa
 - ³ Institut de Physique du Globe de Paris, Université de Paris, CNRS, 75238 Paris, France; barruol@ipgg.fr (G.B.); elisa.rindraharisaona@univ-reunion.fr (E.R.)
 - ⁴ Observatoire de Sciences, Univers de La Réunion (UMS 3365 OSU-R), 97400 Saint-Denis, France; emmanuel.cordier@univ-reunion.fr
 - ⁵ Laboratoire d'Aérodynamique, Université de Toulouse, UT3, CNRS, IRD, 31400 Toulouse, France
 - ⁶ Cooperative Institute for Research in Environmental Sciences, National Snow and Ice Data Center (NSIDC), University of Colorado Boulder, Boulder, CO 80304, USA
 - ⁷ Laboratoire GéoSciences Réunion (LGSR), Université de La Réunion, 97400 Saint-Denis, France
 - ⁸ Scripps Institution of Oceanography, University of California, San Diego, CA 92093, USA; greg.roberts@meteo.fr
 - ⁹ Centre National de Recherche Météorologique (UMR3589 CNRM), Université de Toulouse, CNRS, Météo-France, 31057 Toulouse, France; julien.cattiaux@meteo.fr (J.C.); fabrice.chauvin@meteo.fr (F.C.)
 - ¹⁰ Seychelles Meteorological Authority, International Airport, Mahe 670311, Seychelles; v.amelie@meteo.gov.sc
 - ¹¹ Seychelles Islands Foundation, Mont-Fleuri, POB 853, Victoria, Mahe 670311, Seychelles; ceo@sif.sc
 - ¹² Department of Physics-Faculty of Sciences, Eduardo Mondlane University, Maputo CP 257, Mozambique; amavume@yahoo.co.uk
 - ¹³ Instituto Nacional de Meteorologia (INAM), Maputo CP 256, Mozambique; jonas_z@inam.gov.mz
 - ¹⁴ Institut Supérieur de Technologie d'Antsiranana, Antsiranana BP 509, Madagascar; lova.zakariasy@ist-antsiranana.mg (L.Z.); hbrazafindradina@ist-antsiranana.mg (B.R.)
 - ¹⁵ Direction Interrégionale de Météo-France pour l'Océan Indien, 97400 Saint-Denis, France; francois.bonnardot@meteo.fr
 - ¹⁶ Mauritius Oceanography Institute, Morcellement de Chazal, Albion 95410, Mauritius; msingh@moi.intnet.mu
 - ¹⁷ Department of Astronomy and Atmospheric Sciences, Center for Atmospheric REmote Sensing (CARE), Kyungpook National University, Daegu 41566, Korea
 - ¹⁸ Collecte Localisation Satellites (CLS), 29280 Brest, France; rhusson@cls.fr
 - ¹⁹ Laboratoire d'Océanographie Physique et Spatiale, Ifremer, CNRS, IRD, UBO, 29280 Plouzané, France; Alexis.Mouche@ifremer.fr
 - ²⁰ Kelonia, Observatoire des Tortues Marines de La Réunion, 97436 Saint-Leu, France; stephane.ciccione@museesreunion.re
- * Correspondence: olivier.bousquet@meteo.fr

Abstract: The international research program “ReNovRisk-CYCLONE” (RNR-CYC, 2017–2021) directly involves 20 partners from 5 countries of the south-west Indian-Ocean. It aims at improving the observation and modelling of tropical cyclones in the south-west Indian Ocean, as well as to foster regional cooperation and improve public policies adapted to present and future tropical cyclones risk in this cyclonic basin. This paper describes the structure and main objectives of this ambitious

research project, with emphasis on its observing components, which allowed integrating numbers of innovative atmospheric and oceanic observations (sea-turtle borne and seismic data, unmanned airborne system, ocean gliders), as well as combining standard and original methods (radiosoundings and global navigation satellite system (GNSS) atmospheric soundings, seismic and in-situ swell sampling, drone and satellite imaging) to support research on tropical cyclones from the local to the basin-scale.

Keywords: tropical cyclone; south-west Indian Ocean; gliders; unmanned airborne system; bi-logging; sea turtles; global satellite navigation system; ReNovRisk; numerical modelling; climate modelling; austral and cyclonic swells; seismic data

1. Introduction

Due to their highly destructive potential, tropical cyclones (TCs) have long been considered a major risk for populations, territorial economies, and biodiversity. In this regard, predicting their outcome and impacts at present and future times is one of the major concerns of both the Intergovernmental Panel on Climate Change (IPCC) and the World Meteorological Organization (WMO).

As highlighted in the latest reports of WMO's International Workshop on Tropical Cyclones (IWTC), research carried out over the last four years has considerably improved our understanding of TC intensification processes [1,2], as well as TC tracking and intensity forecasting [3,4]. The operational implementation of coupled ocean-atmosphere (OA) numerical weather prediction (NWP) systems by many national weather services has, in particular, played a key role in reducing forecasting errors at all space and time scales [5–8]. Despite these important advances, additional efforts are still needed to accurately predict and characterize the potential impacts of tropical cyclones on a given territory, especially during landfall. Such efforts include, for instance, the collection of novel atmospheric and oceanic observations, to better constrain (and verify) the performance of coupled NWP systems [9,10], as well as the implementation of wave models and specific microphysical parameterizations to improve roughness, swell, wind speed, and momentum flux representation in TC forecasting systems [11–13].

Accurate modelling of OA interactions is particularly crucial in areas such as the tropical south-west Indian Ocean (SWIO) basin (30–90° E, 0–40° S), where the atmospheric variability is associated with a particularly strong oceanic response (and vice versa). The SWIO (Figure 1), which contributes to approximately 10–12% of the worldwide cyclonic activity [14–16], is indeed widely considered as the cyclonic basin with the highest prevalence of OA interactions [17] due to the unique structure of the thermocline in the Seychelles-Chagos Thermocline Ridge area (55–70° E, 5–15° S) [18,19]. Like most TC basins, the SWIO includes many fragile countries, whose economic development and infrastructure, as well as food, medicine and water supply chains, are regularly impacted by tropical cyclones.

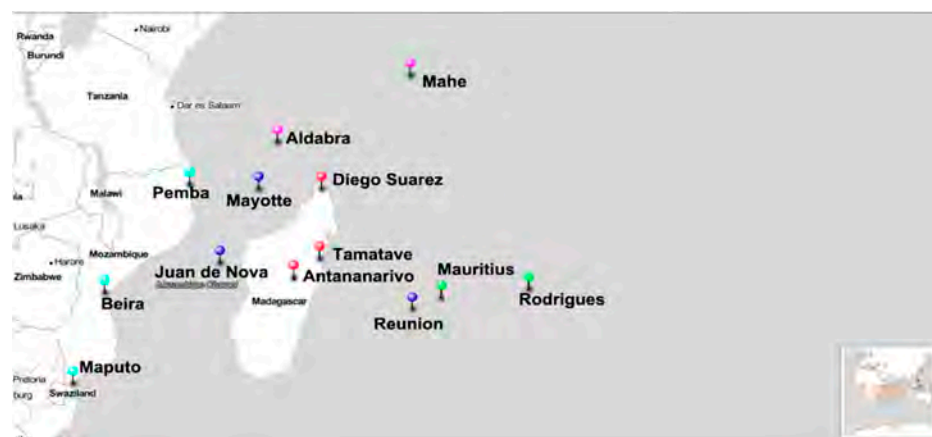


Figure 1. Map of the south-west Indian Ocean (SWIO) tropical cyclone basin (30–90° E, 0–40° S). The principal locations discussed in the paper are indicated by dark blue (France), light blue (Mozambique), green (Mauritius), red (Madagascar), and pink (Seychelles) circles.

In very recent years, countries bordering the Mozambique Channel (MC) have indeed been struck by a series of extremely intense and devastating events, whose economic impact will be felt for many years to come. Heavy rains associated with TC DINEO (2017) have caused 700,000 refugees and tens of millions of USD of damage in Mozambique, while the overall cost of TCs ENAWO (2017) and AVA (2018), which affected nearly one million people in Madagascar, was estimated to be more than USD 600 million (about 7% of Madagascar's average annual gross domestic product). These heavy tolls are, however, out of all proportion to those of TCs IDAÏ (considered by the United Nations as the worst natural disaster ever in the MC) and KENNETH (the most intense TC ever reported in the MC [20]), which both made landfall in Mozambique in 2019 [21]. According to the latest economic reports, these two storms have affected a total of nearly 1.7 million people and caused damage and losses estimated at ~USD three billion—plus a further recovery cost estimated at USD 3.4 billion—by the World Bank and Mozambican officials [22].

Given the colossal impact of TCs on the local populations, infrastructure, and economic development of many countries in the SWIO basin, the European Union (EU), together with the Regional Council of Réunion Island and the French State, have designed the transdisciplinary research program "Réunion NOVative research on cyclonic RISks" (ReNovRisk), to improve the resilience of SWIO countries to TC hazards and mitigate associated economic vulnerability, damages, and risks (e.g., winds, rainfall, landslides, submersion) in inhabited areas. To achieve these objectives, ReNovRisk has been divided into four interlinked research projects, referred to as ReNovRisk-Cyclone, -Erosion, -Impacts and -Transfer, whose overall objectives are described in [23]. The present paper focuses on the Cyclone component of this program, which involves a large international consortium of research institutes, universities, and weather services originating from France (e.g., universities of Réunion Island and Toulouse, Centre National de Recherche Scientifique (CNRS), Météo-France, Institut de Physique de Globe de Paris (IPGP), Institut National de l'Information Géographique et Forestière (IGN), Institut Français de Recherche pour l'Exploitation de la MER (IFREMER)), Mozambique (Eduardo Mondlane and Pemba Unilurio universities, Mozambique Weather Service (INAM)), Madagascar (Institut Supérieur de Technologie de Diego Suarez, Université d'Antananarivo), the Seychelles (Seychelles Meteorological Authority, Seychelles Islands Foundation), Mauritius (Mauritius Oceanography Institute), as well as international institutions such as the European Space Agency (ESA) and WMO, among others.

Through its observing, modelling, climate and outreach components, ReNovRisk-Cyclone (hereafter referred to as RNR-CYC) aims to improve the observation and modelling of TCs, as well as to provide inputs for other components of the global ReNovRisk program focusing on hydrological (RNR-Erosion and RNR-Transfer) and economical (RNR-Impact)

consequences of tropical cyclones [23]. Another key objective of RNR-CYC is to foster regional cooperation and improve public policies adapted to present and future TC risks faced by territories bordering the SWIO. The latter is all the more essential because predicted changes in the coupled OA system due to global warming are likely to generate significant modifications of the cyclonic activity in the coming decades. Consequently, regions that are currently spared or moderately affected by TCs, and that often lack experience-based adaptation strategies, may soon have to face potentially increasing TC-related hazards [24,25]. Such changes include, for instance, the widening of the tropical belt resulting from ocean warming [26,27], which has already been shown to induce a poleward migration of TC's lifetime maximum intensity (LMI) in both hemispheres [28–31], or significant modifications in TC frequency and/or length of the TC season [32].

This paper aims to describing the structure and main objectives of the project RNR-CYC, as well as to present an overview of the main applications and results of its observation component—modelling aspects are presented in more details in the companion paper [33]. This article is organized as follows: Section 2 provides an overview of the four components of RNR-CYC (observation, mesoscale modelling, climate modelling, cooperation, and outreach). Section 3 presents the major achievements of RNR-CYC regarding oceanic and atmospheric observations, while Section 4 concludes and discusses new research topics to be investigated beyond the end of this program.

2. Structure and Objectives of RNR-CYC

The project RNR-CYC focuses on the meteorological and oceanographic impacts of TCs in the SWIO (Figure 1) at both present and future horizons. It aims, in particular, to better apprehend the impacts of these extreme storms on the main inhabited islands of this oceanic basin by providing innovative modelling and observing products that will also feed the cascade risk analysis tools deployed in the other research components of the global ReNovRisk program [23]. In order to achieve these objectives, RNR-CYC has been divided into four components (Figure 2): (i) an observation component, to improve both long-term and temporary observations of TCs and their atmospheric and oceanic environments; (ii) a mesoscale modelling component, to improve modelling and short-term forecasting of TCs; (iii) a climate component, to evaluate the consequences of climate change on the variability and structure of TCs at both local and basin scales; and (iv) an outreach component, aimed at improving capacity building in the three aforementioned research areas through strengthening cooperation between SWIO countries. An overview of the structure and objectives of these four components is described hereafter.



Figure 2. Structure and main objectives of ReNovRisk-CYCLONE.

2.1. Observing Component

The observing component of RNR-CYC is aimed at providing additional observations of TCs and their environment by improving regional and local observing capabilities in the SWIO. It has been built around three complementary approaches:

(i) A “conventional” approach, based on the reinforcement of regional ground-based meteorological observation facilities and, in particular, of the water vapor Global Navigation Satellite System (GNSS) observation network operated by the International GNSS Service (IGS). Starting in November 2017, 10 new public observation sites (composed of ground-based GNSS receivers and collocated surface weather stations) have been deployed in Madagascar, Eparses Islands, and the Seychelles in the frame of RNR-CYC’s sub-program “Indian Ocean GNSS Applications for Meteorology” (IOGA⁴MET [34]) to increase the number of tropospheric GNSS measurements (e.g., zenithal delay, integrated water vapor amounts) and positioning data throughout the western part of the basin (see Section 3.2.2.). The first analysis of GNSS-derived observations collected during RNR-CYC have already demonstrated the benefit of these new permanent stations to investigate the water vapor cycle at diurnal to inter-annual time scales [34,35], but also to provide new and continuous observations to investigate the dynamics of the Earth’s crust in this particularly active part of the world [34,36].

(ii) An “experimental” approach, based on the temporary collection of atmospheric and oceanic observations at various locations in the basin. For this purpose, several atmospheric and oceanographic field campaigns have been organized throughout the 3.5-year duration of RNR-CYC, with the goal to provide novel datasets to evaluate numerical model developments and simulations performed in the frame of the project [33]. The main achievements include:

- A three-year satellite acquisition campaign (2017–2020), set up in collaboration with ESA and IFREMER, to collect high-resolution (1 km) observations of surface winds and sea roughness from spaceborne synthetic aperture radars (SARs) deployed onboard the satellites Sentinel 1A/1B of the European Earth Observation Program Copernicus (<https://www.copernicus.eu/fr>, see Section 3.3., accessed on 20 March 2021);
- A regional field campaign, organized from late January to early April 2019, to investigate atmospheric and oceanic environmental conditions prevailing in the vicinity of TCs during the 2018–2019 TC season. During this 2.5 month period, a regional radiosounding network, allowing for the collection of nearly 500 soundings, was deployed in Mayotte (France), Toamasina (Madagascar) and Maputo (Mozambique) to both sample the atmospheric environment of TC and train students and academics in experimental meteorology (see Section 2.4.);
- The deployment of two ocean gliders from Réunion Island to sample the vertical properties of the upper ocean layers in the Mascarene Archipelago (see Section 3.1.4.);
- The deployment of an unmanned airborne system (UAS), equipped with aerosol, turbulence, sea state, and meteorological sensors to measure OA fluxes and aerosol concentrations off the shore of Réunion Island (see Section 3.2.1.);
- The organization of several local observation campaigns to sample sea swell properties during austral winters and summers using acoustic Doppler current profilers (ADCP) and wave gauges deployed near the shore of Réunion Island (see Section 3.1.1.).

(iii) An “exploratory” approach, based on the deployment and evaluation of innovative methods to collect oceanographic observations. A particularly original approach, based on biologging technology, has been evaluated for two years to collect data from sea turtles (ST) equipped with dedicated ARGOS environmental tags in the frame of RNR-CYC’s subprogram “Sea Turtle for Ocean Research and Monitoring” (STORM, see Section 3.1.3.). Another original approach, based on the previous work of [37–39], was also further investigated to quantify extreme swell phenomena from microseismic noise measurements recorded by ground seismometers (see Section 3.1.2.). The preliminary assessment of terrestrial seismic observations collected in Réunion Island against oceanographic records and offshore wave model data have demonstrated that land-based seismic stations could be particularly useful to observe both austral [40] and cyclonic swell [41] (this Special Issue).

2.2. Modelling Component

Protecting life and property requires a precise estimate of the environmental changes associated with the passage of TCs in the vicinity of inhabited areas. The challenge in the face of the cyclonic threat is to simultaneously predict the track and intensity of the storms, but also the consequences resulting from their landfall, or transit near inhabited areas. Hence, damages caused to a given territory, which are essentially related to rainfall intensity, wind strength and sea state (e.g., swell), could significantly differ depending on whether it is affected by a tropical storm (TS), a monsoon depression, or a more or less intense TC. To this end, many operational meteorological services and research centers concerned with TC hazards have made considerable efforts to develop deterministic and ensemble coupled NWP systems providing high spatial resolution forecasts in all TC basins [42–46]). Another fundamental element to improve TC impact predictions, which is partly addressed in the hydrological component (RNR-Erosion) of the global ReNovRisk program, is to also take into account the role of land surface and hydrological processes even after the dissipation of the storm. The recent case of TC IDAÏ, whose catastrophic damage in Beira was mainly caused by flooding occurring days after the storm had passed over the city, is a perfect example of the urgent need to also improve hydrological forecasting.

Improving TC forecasting first and foremost implies a proper representation of the interactions between the storm and the ocean, and vice versa [47]. During the propagation of a TC over an oceanic area, mixing caused by surface winds usually induces a significant drop in surface temperature [48,49] that strongly reduces surface enthalpy and heat fluxes [50,51]. These air–sea fluxes can also be significantly impacted by waves, which redistribute momentum in the near-surface layer and modify the enthalpy fluxes through the emission of sea spray [52–57]. In this regard, new parameterizations reproducing the impact of marine aerosols on turbulent heat exchanges have been proposed and validated in recent years [58,59], but are yet to be implemented in atmospheric models to thoroughly evaluate their impact on TC behavior.

Radiative cooling [60,61], evaporation [62,63] and latent heat release [64] have long been recognized to play a key role in the development and intensification of tropical cyclones; therefore, particular attention must also be paid to microphysical schemes implemented in NWP systems. These schemes must, in particular, allow for an efficient representation of the radiative cooling at the top of the storms (which is a constraining criterion of TC intensity) and of the vertical distribution of latent heat (which represents the main source of energy of TCs). They should thus also be able to realistically take into account the role of atmospheric aerosols, that (indirectly) affect the radiation balance by impacting on the radiative and precipitating properties of the clouds. Improving TC forecasting therefore also implies the development of coupled aerosol–microphysical–radiation schemes to be integrated in fully coupled ocean–wave–atmosphere (OWA) models.

An important objective of RNR-CYC was to develop high-resolution OWA and OA modelling systems capable of representing, as exhaustively as possible, the multitude of physical interactions that control the variations of intensity of TCs, as well as their impacts (wind, rain, swell) at the scale of SWIO territories. The main modelling developments made in the frame of this project can be found in [11,65], (this Special Issue, [66]) and in the companion paper [33].

2.3. Climate Component

Evaluating the impact of climate change on the frequency and intensity of tropical cyclones is considered as one of the top five issues of concern by the IPCC. Currently, regional and global climate models make it possible to identify the preferred areas of cyclogenesis and occurrence of tropical low-pressure systems at the basin scale, but cannot yet be effectively relied upon to investigate potential changes in their structure and intensification mechanisms. Although it is now widely accepted that the global increase in sea surface temperatures in tropical areas will be a favorable element for TC development, it is not clear how other ingredients involved in their formation and intensification will evolve in

the future. In this regard, another important objective of RNR-CYC was to evaluate the global evolution of cyclonic activity in the SWIO, but also to investigate potential structural and intensity changes of TCs resulting from the ongoing modification of their oceanic and atmospheric environments.

The modelling strategy was based on two complementary approaches, allowing to both estimate the evolution of cyclonic activity at the basin scale (i.e., changes in trajectory, intensity, and frequency of TCs at different time scales), and to assess potential structural changes and impacts of TCs at the local scale. This strategy relies on the exploitation of unprecedented high-resolution global climate simulations [32], as well as of mesoscale coupled simulations to estimate the impact of climate change on the intensity, behavior, and consequences of TCs at the scale of a given territory. Examples of results obtained from such high-resolution model runs are discussed in [33,67] (both in this Special Issue).

2.4. Regional Cooperation

Another important objective of RNR-CYC is to provide enhanced tools and knowledge to SWIO countries facing cyclonic hazards. Responding to this strong societal issue requires a better structuring of the regional scientific community, as well as significant reinforcement of the cooperation between countries bordering the SWIO basin. While regional collaboration already exists through WMO's regional structures (e.g., Tropical Cyclone Programme (<https://public.wmo.int/en/our-mandate/focus-areas/natural-hazards-and-disaster-risk-reduction/tropical-cyclones>, accessed on 20 March 2021) and Réunion Island's Regional Specialized Meteorological Center (RSMC La Réunion, http://www.meteo.fr/temps/domtom/La_Reunion/webcmrs9.0/anglais/index.html, accessed on 20 March 2021)) and the Indian Ocean Committee (<https://www.commissionoceanindien.org/>, accessed on 20 March 2021), interactions remain essentially focused on operational and technical applications, and only modestly promote research development in this area.

One of the strengths of RNR-CYC consists of the implementation of a partnership involving many regional research institutes, universities, and meteorological services that agreed to pool their resources and expertise to strengthen the resilience to TC hazards, and develop public policies better adapted to the risks faced by SWIO territories. RNR-CYC is thus a fundamentally collaborative project that is not only based on the large sharing of data and experiences, but also on training programs and capacity-building initiatives in the fields of observation and forecasting. These actions include, for instance, the organization of forecasting training sessions at RSMC La Réunion, of training courses in climatology and climate change, as well as numerous co-supervised MSc internships based on the analysis of experimental measurements collected in the project.

For instance, the project's field phase, which involved nearly one hundred participants from late January to mid-April 2019, was an opportunity for many students and researchers to initiate themselves to the technique of atmospheric radiosounding (RS). During this 2.5-month campaign, ~500 radiosoundings were performed from three experimental sites specifically deployed for this occasion in Maputo (INAM's headquarters, Mozambique), Mayotte (Météo-France weather center, France), and Toamasina (Toamasina international airport, Madagascar). On this occasion, nearly 60 students and academics from Antananarivo (Madagascar), Eduardo Mondlane (Mozambique) and Réunion universities came to Toamasina and Maputo to conduct RS measurements, while many senior forecasters of INAM and Météo-France Mayotte had, for the first time, the opportunity to operate and familiarize themselves with an RS station (Figure 3).

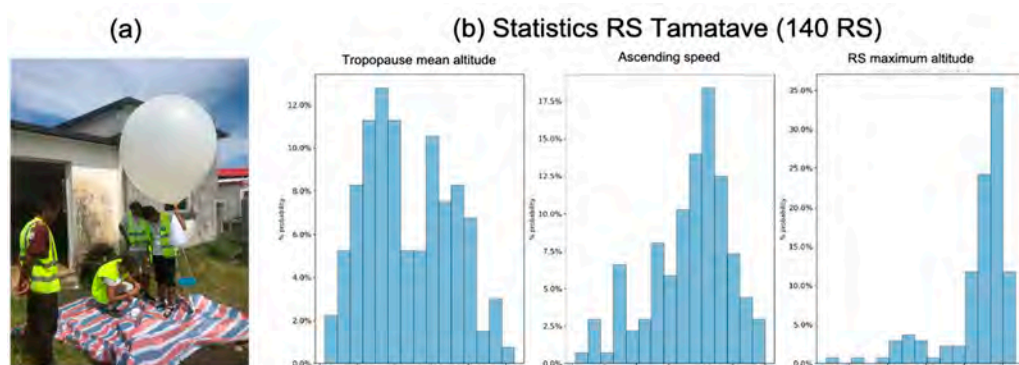


Figure 3. The Toamasina (Madagascar) radiosounding campaign. (a) Training of students from Antananarivo University at Toamasina airport. (b) Statistical analysis of the 140 RS measurements performed in Toamasina: mean altitude of the tropopause, ascending speed, and maximum RS altitude. Picture: Olivier Bousquet

The involvement of the French consular services in the project also made it possible to communicate widely to the general public, the scientific community, and the media in Mozambique, Madagascar and the Seychelles on the issues of adaptation to climate change and natural hazards. As will be seen in Section 4, these regional collaborations will continue for many years to come through several new research projects initiated by RNR-CYC.

3. Results

3.1. Oceanic Observations

3.1.1. In Situ Swell Observations

One of the main objectives of RNR-CYC is to assess the impact of tropical cyclones on land, including possible submersion resulting from cyclonic swell surge along coastlines. In many tropical islands, the latter are bordered by coral reefs that can serve as a defense against flooding. These reef systems, particularly fringing reefs, protect the coastline by acting as low-pass filters that can reduce the energy of wave flows reaching the coast by up to 98% in the gravitational part of the wave spectrum [68]. The physical processes underlying coral reef coastal protection consist of a complex combination of incident waves, tides, and wind-induced surges [69–71].

Ocean wave energy is concentrated in the gravitational frequency band of the wave spectrum, generally between 0.04 Hz and 0.25 Hz. These gravitational waves (GWs) are the main drivers of the hydrodynamics of reef systems, as well as of beaching, runup, and submersion. During and after breaking at the edge of reef systems, GWs are dissipated while low frequency waves (infragravity waves ($0.004 < IG \text{ (Hz)} < 0.04$) and very low-frequency waves ($0.001 < VLF \text{ (Hz)} < 0.004$) propagate to the shore. Previous analyses of these propagation and transformation processes across various coral reefs have shown that wave dynamics could vary considerably depending on the characteristics and location of reef systems [71,72].

In order to both quantify the physical processes linked to severe sea states and assess the protective role of reef systems, a cross-shore transect, composed of bottom-fixed wave gauges and ADCPs, was deployed in Réunion Island from February to April in 2019 and 2020. Instruments were installed at the fringing reef of “Trou d’Eau”, located along the west coast of the island (Figure 4a). At the near-shore site, reef-base (RS) and reef-flat (RF) stations were deployed through the fringing reef along a cross-shore transect. The RS station was installed at the base of the reef slope at an average depth of 12 m, while three RF stations (RF1, RF2 and RF3 in Figure 4a) were aligned on the flat reef inside the lagoon at a depth of 1 m (Figure 4b,c). RS and RF stations were all equipped with synchronized ocean sensor system instrument (OSSSI) wave gauges, enabling continuous recording pressure at a sampling frequency of 10 Hz. The RS station also featured an upward-looking Nortek AQuadopp (AQP) profiler configured to measure current profiles every 20 min, with a 2 Hz hourly burst mode to record wave parameters. In 2020, an ADCP (RDI Sentinel V100)

was also deployed at an ocean offshore (OC) site at a depth of 45 m. This instrument was configured to record incident wave parameters from hourly bursts of 2100 samples at 2 Hz, and current profiles from the bottom to the surface.

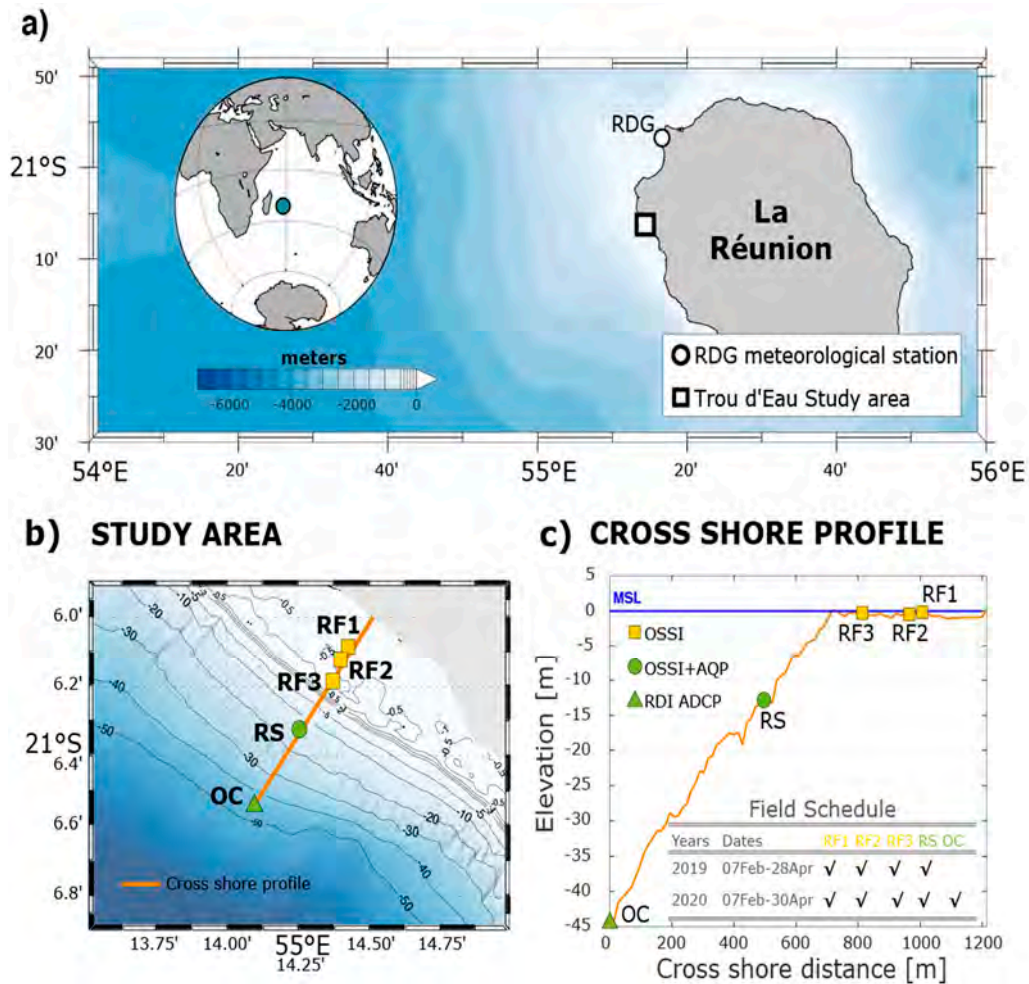


Figure 4. Overview of the experimental setup deployed in “Trou d’Eau” (Réunion Island) in February–April 2019 and 2020. (a) Coastal study area, (b,c) details of the cross-shore transect instrumented during the experiments. The stations are labeled OC for ocean offshore, RS for reef-slope, and RF for reef-flat. In (c), labels OSSI, AQP and RDI ADCP correspond to wave gauges, Nortek AQuadopp current Profiler, and RDI ADCP current profiler, respectively. Instrument deployment dates are indicated in (c).

Observations collected at the offshore stations OC and RS were relied upon to describe and quantify the main properties (height, period, and direction) of the waves impinging on the reef in the GW frequency band (wave periods ranging from 4 to 25 s), while data gathered at RF stations were used to investigate wave transformation (across the fringing reef) and propagation (from outside the lagoon to the shore). Observations collected at OC and RS stations were processed with the RDI software “Velocity” and the PUV method [73], respectively. All OSSI pressure data were corrected from atmospheric mean sea level pressure data recorded at the surface weather station of “La Rivière Des Galets” (located 20 km northward of the experimental site, RDG on Figure 4a) and non-hydrostatic pressure following the linear wave theory [74].

The mean surface elevation was computed from a 20 min moving average of the signal, while the wave spectrum and average wave parameters were obtained through the application of a fast Fourier-transform (FFT). The latter was applied over 4096 data points for incident gravity wave band or swells ($0.04 < SW < 0.25$ Hz), and 32,768 data values for infragravity ($0.004 < IG < 0.04$ Hz) and very low frequency ($0.001 < VLF < 0.004$ Hz) bands.

The recorded signal was not perfectly periodic; therefore, a Hamming window, leading to zero value at the edges, was also applied to mitigate artifacts resulting from leakage issues. To avoid resulting loss of information at the edges, a 30-min (resp. 3 h) time average was then performed for the incident (resp. IG and VLF) bands. Time series of power spectral density deduced from data collected in 2019 along the cross-shore transect are shown in Figure 5, together with the associated mean power spectra at each station.

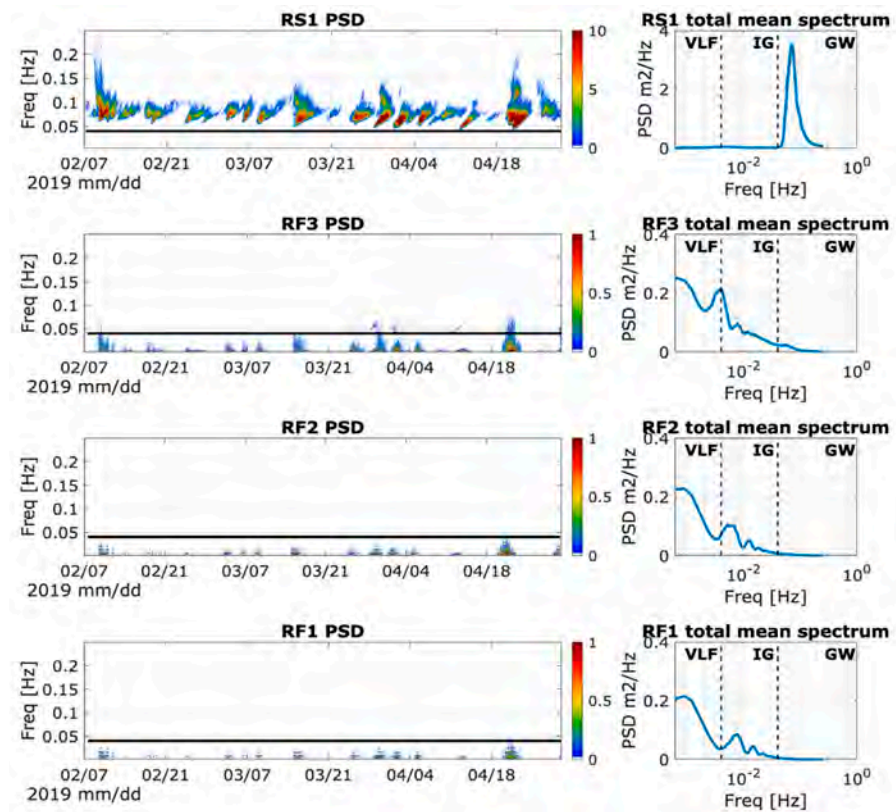


Figure 5. Spectral wave characteristics observed along the instrumental transect presented Figure 4b. The plots are organized in the shoreward direction from the top to the bottom (reef slope RS1 station on the top, and reef flat station RF1 closest to the shore on the bottom). The left panels show the temporal variation of the wave spectrum recorded at each station from February to April 2019. The black solid line indicates the frequency cut at 0.04 Hz between the gravity frequency band (GW) and the infragravity (IG) frequency band. The right panels show the mean power spectral density for each station averaged over the whole period, with the frequencies band GW, IG and VLF (for very low frequency) indicated.

Measurements collected at the reef slope station RS clearly show that the wave energy spectrum is concentrated in the gravity band, with an averaged peak period of 13.5 s over the whole period. After breaking at the reef crest, most of this energy is dissipated (by breaking and/or by friction on the reef bottom), while the remaining part (in IG and VLF bands) is transferred inside the reef system. For the two strong wave events observed in February (likely associated with TC GELENA to the north of Réunion Island) and April 2019 (austral swell event), the total wave energy reduction between the reef slope station RS and the adjacent reef flat station RF3 reaches 98%, a value in good agreement with previous meta-analyses [68]. Within the reef, the transfer of the remaining energy between the three stations was nevertheless slightly different for these two events. In February (TC event), the wave energy reduction reached 64% from RF3 to RF2 and 2% from RF2 to RF1, but only 47% from RF3 to RF2 and 15% from RF2 to RF1 in April (austral swell event). The main difference between these two events is related to the period of the incident waves (11.8 s for the TC-related event and 16 s for the austral swell event); this result suggests that the

generation and propagation of IG waves inside the reef might be less important for short waves, induced by the wind, than for longer-period swells. This shoreward propagation with less energy reduction is also noticeable in the average spectra, which show a small translation of the peak frequency toward higher frequencies in the IG band, between the RF2 and RF1 station, and a reduction in the peak amplitude.

These preliminary analyses show that Réunion Island's fringing reef plays a strong role in protecting the shore against incident waves. Further investigations will be conducted in order to thoroughly investigate the physical processes and the role of both reef topography and roughness on the dynamics of IG waves. This includes, for instance, the impact of shoreward-propagating IG waves on onshore suspended-sediment transport [75], and the relationship between long wave propagation (and transformation) across the reef and sea water level above the reef—the remaining long waves propagating through the reef have been shown to increase the back-reef set-up and beach runup, which could lead to increased coastal erosion during extreme events such as tropical cyclones or strong storms [76,77].

3.1.2. Ground-Based Swell Observations

The global monitoring of swell activity induced by tropical storms (TS) and TCs is of major interest to quantify the risk associated with extreme swells, but also to validate numerical models used to predict ocean activity. Direct swell observations such as those presented in the previous section are, however, strongly limited by the low number of oceanographic sensors available in this area, as well as by their deployment (and servicing) costs and their vulnerability during tropical cyclones. These limitations motivated the use of indirect observations as alternative and complementary observables to quantify the swell parameters. In this regard, the analysis of wave-induced seismic noise is known to be an interesting substitute for monitoring ocean activity and has been proven to be particularly relevant for assessing the impact of waves on coastal environments [38]. The possibility to derive swell measurements from the seismic noise generated by ocean swell and transmitted to the solid earth as seismic waves recorded by terrestrial seismological instruments [78], is discussed hereafter from data collected in RNR-CYC.

Microseisms recorded by seismic stations worldwide are known to be generated by ocean gravity waves [79]. Seismic energy spectra at terrestrial seismic stations showed two clear peaks in separate frequency bands, known as primary and secondary microseisms (hereafter named PM and SM, respectively), originating from different physical processes involving local or distant sources of ocean wave activity [80]. Primary microseisms (PM) are mostly visible at coastal and island stations and are assumed to be generated by direct interactions of swell-induced pressure variation with the coastal seafloor [81–83]. PM noise has the same periods as the ocean swell (i.e., between 8 and 20 s), providing a powerful way to characterize the local impact of swell approaching the shore. On the other hand, SM noise is generally generated in the deep oceans and at larger distances from coastal areas [37,84–86]. It dominates seismic noise at both continental and oceanic stations and exhibits a large peak at half the period of ocean waves (i.e., between 3 and 10 s), generated by the interference of swells of similar periods travelling in opposite directions [79] and generating seismic surface waves travelling horizontally within the solid crust.

In the Indian Ocean, most remote sources of seismic noise are located in the southernmost part of the Austral Ocean basin and are associated with storm systems moving around Antarctica [84,87,88]. Some noise sources may also develop at tropical latitudes in association with tropical cyclones [41] (this Special Issue). Recent seismic deployments on the ocean floor enabled the making of in situ observations of SM underneath TCs in the neighborhood of Réunion Island [37] and confirmed the possibility to track TC and TS from the ocean bottom. Although SM are generally created by distant storms, they can also be generated by the coastal reflection of waves if incident and reflected waves propagate in opposite directions [89,90]. In this latter case, the incoming swell may interfere with its reflected swell, resulting in the generation of standing waves close to coastal areas that

oscillate at twice the frequency of the propagating wave [91]. Some studies suggest that local and distant sources of noise in the SM frequency peak may coexist [39,92,93].

Previous seismic analyses conducted in the Pacific and Indian Oceans have already demonstrated that several swell parameters can be derived from the seismic data. This includes: (i) the swell peak period T_p , derived from the dominant frequency of the PM and SM using the power spectral density analysis of the seismic records; (ii) the local or distant wave significant height H_s (in the case of the PM or SM band, respectively), obtained by measuring the microseism amplitudes through hourly Root Mean Square (RMS); and (iii) the wave peak direction D_p for the case of the PM band, or the source direction in the case of the SM band, which can both be deduced from the polarization analysis of the three seismic data components, to determine the dominant direction and strength of the recorded microseismic noise.

To illustrate this innovative approach, we analyse hereafter seismic observations collected during the tropical storm (TS) ELIAKIM that developed in March 2018. This storm has clear signatures, despite not reaching tropical cyclone intensity, and developed at a large distance from Réunion Island, demonstrating the potential of the method in quantifying remote systems. As mapped on Figure 6a, TS ELIAKIM started as a depression located north-east of Madagascar on 13 March 2018. It then intensified to a tropical storm on 14 March and to a strong tropical storm on 15 and 16 March while approaching the eastern coast of Madagascar, where it made landfall on 17 March. TS ELIAKIM continued its southward motion and returned over the ocean on 18 March. After a final burst on 19 March, the storm collapsed on 20 March, while entering its extratropical transition phase.

Our analysis was performed from data recorded by seismic stations of the permanent seismic network of the Piton de la Fournaise Volcano Observatory (OVPE, seismic code PF, red triangles on Figure 6b) and from a temporary seismic network deployed in the frame of the RNR program (code ZF, blue triangles on Figure 6b). Seismic data were compared with swell parameters issued from the WaveWatch3 (WW3) model [94,95] at nodes surrounding the island from the global wave model hindcast [96], indicated by stars on Figure 6b.

The seismological energy content of the vertical ground displacement of station MAT (Figure 6b) is shown in the spectrogram of Figure 7a. It displays the temporal variation of the Power Spectral Density (PSD) during the period 10 to 25 March 2018 over the frequency band of the ocean activity (0.05–0.5 Hz, i.e., 20–2 s periods). Superimposed to the spectrogram is the distance curve of the storm center to Réunion Island (dashed line), together with the storm intensity curve (black line indicating the mean wind speed and the colored dots the storm classification, as in Figure 6a). The seismic energy at this station shows good correlation with the storm intensity, despite its large distance, varying from 500 to 1500 km with two pulses of energy with the maximum at a frequency range of 0.1–0.3 Hz, i.e., in the SM band, culminating on 16 and 19 March during maximum storm intensity. Below 0.1 Hz, i.e., in the PM band, the PSD still displays clear energy increasing during the two storm peaks.

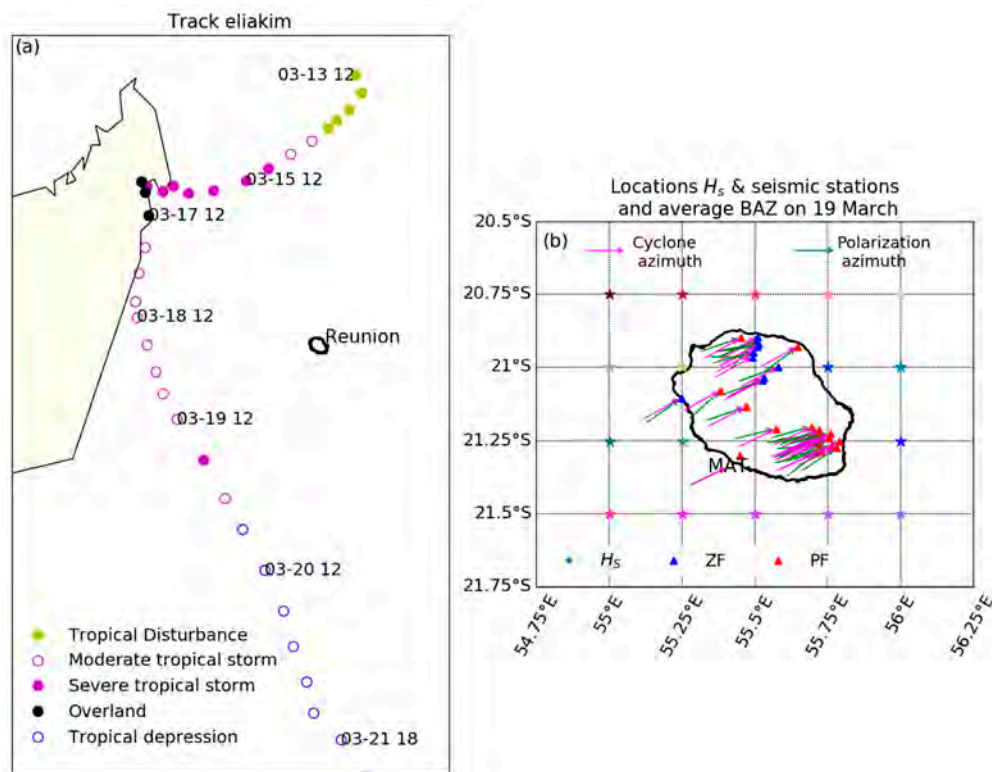


Figure 6. (a) Track of TS ELIAKIM as derived from RSMC La Réunion best-track data. The colored circles indicate the position and intensity of the storm every 6 h. (b) Locations of the seismic stations (blue triangle, temporary ZF network, and red triangle, permanent PF stations) and WaveWatch3 nodes [96] surrounding the island, where wave height H_s (colored stars) is extracted. Vectors indicate the average azimuth on March 19, 2018, obtained from the polarization analysis in the SM frequency band (green) and computed from the storm track and the RER seismic station (pink).

The hourly RMS amplitudes of the seismic noise recorded at the various seismic stations on the island are shown in Figure 7b,c, for both the SM and the PM bands, respectively. Note that the vertical axes are different, and that the SM amplitude is almost one order of magnitude larger than the PM. The 21 seismic stations analyzed over Réunion island display similar variation patterns. This indicates that this noise is not a purely local source; the storm acting as a distant SM source, or that the source—if local—is larger than the size of the island, which is the case for the swell generating the PM. The observed station-to-station variability in RMS amplitudes suggests the influence of local site effects such as the installation, the coupling of the seismic sensor with the ground, the nature of the bedrock, and the attenuation around the station.

The RMS peaks at seismic station MAT (Figure 7b) are observed on 16 and 19 March. This period corresponds to the maximum intensity of TS ELIAKIM and to the local variation of the swell height, as visible on H_s data issued from the WW3 model at various points around Réunion island (Figure 8). The maximum H_s observed on 19 March (corresponding to the nodes at the longitude of 55° E) interacted with the local bathymetry slightly later, which explains the small delay with the PM. A small peak was also observed on 21 March in both SM and PM data with dominating energy at period ~10s, likely originating from a distant source and not related to any local swell activity increase.

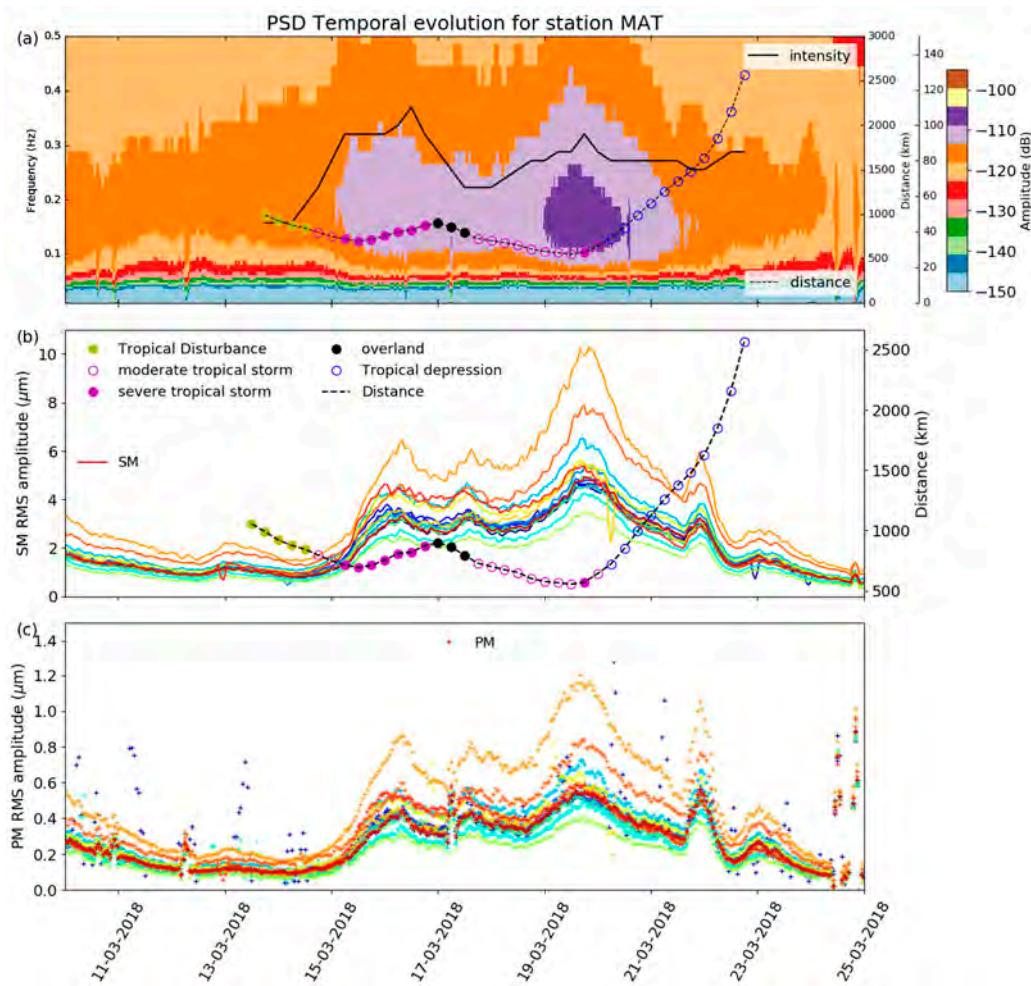


Figure 7. Temporal variation of the microseismic noise recorded during TS ELIAKIM. (a) Spectrogram at seismic station MAT (see location in Figure 6b) between 10 and 25 March and up to 0.5 Hz, together with the storm intensity (continuous black line) and distance between the storm center and the seismic station (dashed black line). The colored circles indicate the intensity of the storm every 6 h, as on Figure 6a). (b) Secondary microseisms RMS amplitude variations measured at the island seismic stations (left axis, in micrometers), together with the distance between the storm and seismic station (right axis, in km). (c) PM RMS amplitude variations (left axis) at Réunion Island seismic stations.

If one accepts that the SM is generated in the vicinity of the storm center and that the PM is generated in coastal areas closer to the seismic stations, one should observe a delay between the two curves. Such a delay was previously observed for austral swells generated by distant storms [40] and proposed as a precursor for predicting coastal submersion in Réunion island. In the present case, considering the involved distances (TS ELIAKIM was located ~ 800 km of the coast of Réunion Island on 16 March, and 500 km on 19 March) and the involved velocities (3 km s^{-1} for the surface waves carrying the SM signal, and $\sim 50 \text{ km h}^{-1}$ for the long period waves at the surface of the ocean), one should expect a delay of >10 h for each peak. However, Figure 8 shows a delay of only ~ 4 h between the SM and PM. This may indicate that the SM is not generated at the storm center, but likely closer to the island. Alternatively, it may also indicate a slow wind–wave growth that may take from a few hours to few days [97]. The swell–noise amplitude correlation can be used to build a transfer function to translate the amplitude of the seismic noise in terms of swell height. Although such a relation is station-related, and therefore not universal, it was nevertheless shown to provide particularly good results for strong swell events [40,41,81].

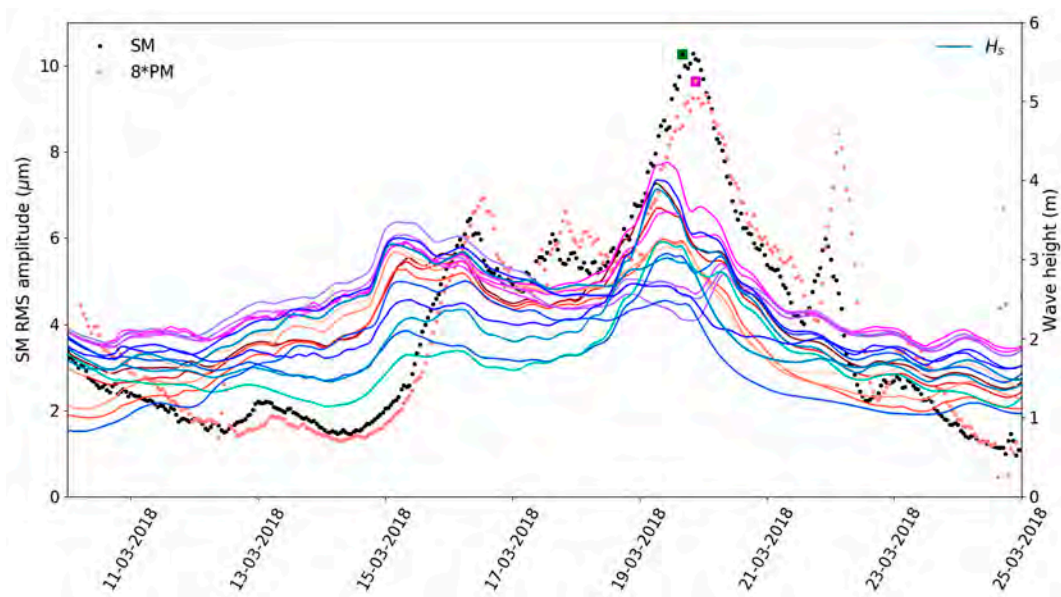


Figure 8. Seismic and swell amplitudes recorded during TS ELIAKIM in March 2018. SM (black dots) and PM (pink dots) RMS amplitude at seismic station MAT (see location Figure 6b) versus the significant wave heights (H_s) at different nodes around La Réunion (colored lines). Note that the amplitude of the PM is multiplied by 8 to reach about the same scale as the SM. The green and magenta dots indicate the maximum SM and PM, respectively, showing a delay of 4 h between the two. The significant waves heights H_s extracted at the various model nodes around the island (Figure 6b) are plotted in continuous colored lines with the same color codes as the stars in Figure 6b.

The recordings of the three components of the ground motion also make the seismic noise a vectorial observation for measuring the direction and strength of the signal polarization. In the case of the SM band, the polarization is expected to point towards the noise source, i.e., the storm center, whereas it should indicate the very local swell propagation direction in the case of the PM. In this PM case, some angle may exist between the swell propagation direction at a large distance offshore and the swell at the coast, due to refraction of the swell and the coastal bathymetry. In the case of TS ELIAKIM, the polarization was measured on an hourly basis in the SM frequency band. Figure 6b displays the average polarization recorded on 19 March at the various land seismic stations in the 0.1–0.33 Hz frequency band (pink) that can be compared to the azimuth computed from the storm center position. This map illustrates a very homogeneous orientation of the noise polarization across the island, pointing to the SW (toward the storm center location on that date) and confirming that the SM originated in the vicinity of the storm center.

These results confirm that seismic noise may provide a useful proxy to quantify the swell parameters. In the PM band (10–20 s period), the seismic noise amplitude allows for a robust quantification of the swell height H_s through a transfer function, the spectrogram allows deciphering the swell dominant period T_p , and the polarization analysis allows retrieving the local swell direction D_p . In the SM band (3–10 s period), the amplitude revealed the storm strength and the polarization indicated the storm azimuth. Terrestrial seismic stations therefore provide alternative and complementary observations of both TC and ocean activities. In some cases, the availability of several decades of seismic archives may also provide new opportunities to derive cyclone climatologies [41].

3.1.3. Biologging Observations

Observing the vertical structure of the ocean is essential to improve knowledge of both the coupled OA system and marine ecosystems. In this regard, an increasingly common alternative to gather high-resolution hydrographic profiles in the world's oceans is to rely on animal-borne sensors (a.k.a. biologging) to collect in situ observations in remote and under-instrumented areas. Compared to conventional oceanographic in situ observation

approaches (e.g., gliders, ARGO drifters, buoys, research cruises), animal-borne electronic ARGOS tags are relatively inexpensive to operate and can be deployed in remote areas with limited human resources. This approach offers all countries the possibility to actively contribute to the collection of ocean observations; therefore, biologging is expected to grow considerably in the future. The recent decision, in August 2020, of the Global Ocean Observing System (GOOS)'s Executive Committee to create a new observing network exclusively dedicated to animal-borne ocean sensors ("ANIBOS") is definitely in line with this perspective and clearly attests of the immense potential of this approach.

The potential of biologging for sampling the thermal structure of the tropical Indian Ocean was evaluated in the frame of RNR-CYC's sub-program "Sea Turtle for Ocean Research and Monitoring" (STORM). STORM was initiated in January 2019 by Réunion's University and Réunion Island's Sea-Turtle Observatory (Kelonia), with the goal of monitoring the state of the tropical Indian Ocean down to several hundred meters below the surface in near-real-time and at high spatial (<100 m) and temporal (5') resolutions. As of March 2021, 22 animals have been equipped with Temperature–Depth (TD) ARGOS tags before being released from Réunion Island (Figure 9). Note that all animal manipulations were made by accredited ST biologists and that all STs were accidentally captured in fisherman's nets in the vicinity of Réunion Island and brought back to Kelonia's care center to be healed and rehabilitated.

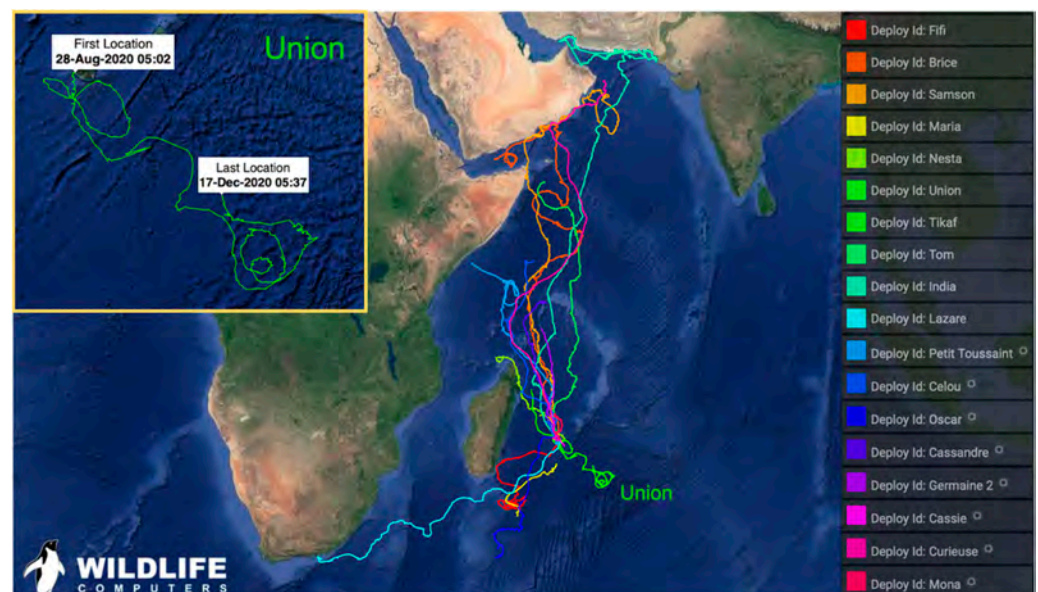


Figure 9. Trajectories and names of the 18 loggerheads and Olive Ridley STs equipped with Wildlife Computers SPLASH10 tags released from Réunion's Island as of 10 March 2021. Circles next to the ST names on the right-hand side indicate active tags as of 20 March 2021. The insert on the left-hand side shows a zoomed view of ST Union trajectory between 28 August and 17 December 2020. Four additional animals, equipped with LOTEK Kiwisat tags, were also released from Réunion island in 2019 (not shown). Plots are extracted from Wildlife Computers' real-time ARGOS tracking platform.

During this experiment, two species of late juvenile sea turtles (loggerhead and Olive Ridley) were equipped with Argos TD tags. While some animals stayed in their pelagic habitats, some loggerheads also began their first homing migration to the Oman Gulf, thus enabling the collection of data both in tropical areas, from loggerheads, and subtropical areas, from Olive Ridelys (Figure 9). STs released from Réunion Island principally swam at (or slightly below) the surface (~50% of the time) and near the bottom of the ocean mixed layer (OML, ~25% of the time). They were found to dive up to 100 times a day, sometimes up to 350 m, allowing the collection of numerous hydrographic profiles within and far below the OML [9]. The analysis of data collected during the first year of this experiment has confirmed the great potential of this approach for sampling the vertical structure of

the ocean, validating ocean models and spaceborne sensors, as well as to investigate the intra-seasonal variability of the tropical Indian Ocean [9].

Sea turtles are known to generally swim in rings and frontal areas in between, and often travel by moving from one ring to another [98]. These rings and eddies are numerous in the Mozambique Channel [99,100], but less common north of Réunion Island, which may explain that loggerhead STs released from there generally tend to follow a straight trajectory (Figure 9)—another explanation (currently under investigation) is that STs rarely feed during their reproductive migration, so as to reach their breeding areas as fast as possible. Nevertheless, according to its circular trajectories, ST Union (Olive Ridley), which moved south-east of Réunion Island in late 2020, apparently travelled in oceanic gyres and eddies (Figure 9).

The surface current analysis of Mercator Ocean’s operational model NEMO-PSY4 (a.k.a Glo12, [101]), averaged from 15 October to 15 December, confirmed that ST Union indeed swam in cyclonic and anticyclonic eddies of variable sizes during this period (Figure 10a). Vertical cross-sections of the ocean temperature field across the center of the main eddy (Figure 10b,c) show strong upwellings at the edges of the vortex (while downwelling can be observed at the center), resulting in significant temperature gradients at the surface (Figure 10a). This vertical transport, which brings nutrient-rich waters from the thermocline up to the surface, makes these eddies prime feeding areas for many marine species and are particularly appreciated by sea turtles. Equipping STs with environmental tags is thus an easy and relatively affordable way to sample the properties of these important transient mesoscale features, which will be further investigated in the continuation of the STORM program (see Section 4).

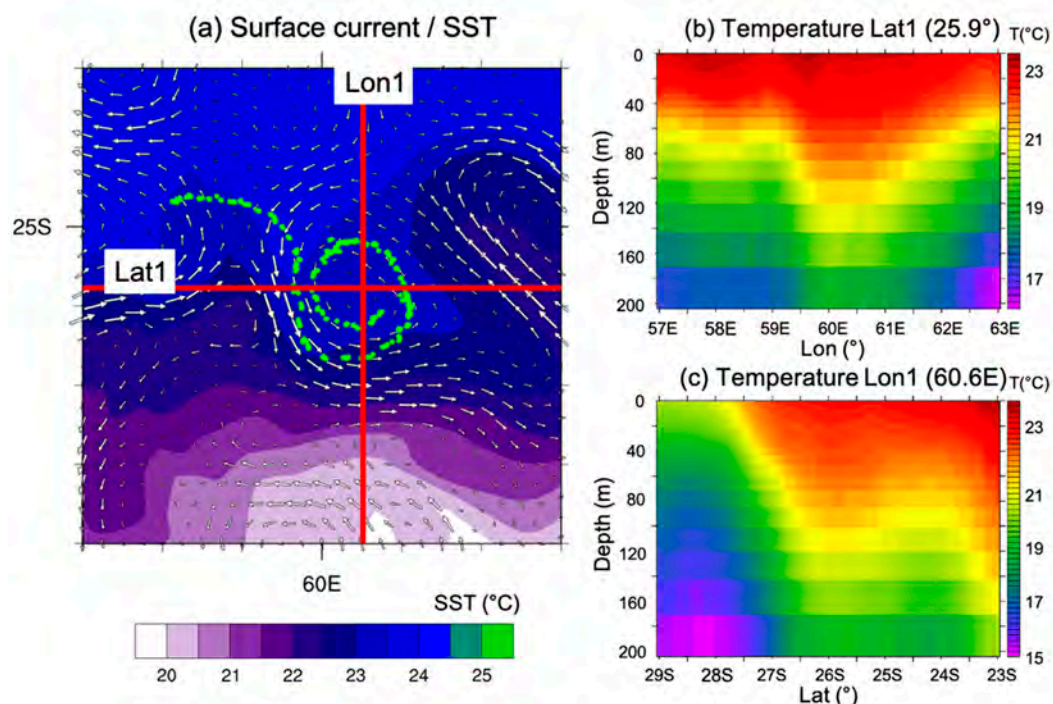


Figure 10. GLO12 model analyses in the area of evolution of ST Union averaged from 15 October to 15 December 2020. (a) surface currents and sea surface temperature superimposed on ST Union track over the 2 month period (green dots), (b,c) vertical cross-sections of ocean temperature through the center of the main vortex travelled by ST Union.

During this experiment, three sea turtles were also caught in the immediate vicinity of tropical cyclones during TC seasons 2018–2019 and 2019–2020: ST Brice, which moved in the vicinity of TC KENNETH (April 2019) during its cyclogenesis (Figure 11a), and STs India and Tom that were trapped in TC HEROLD (March 2020) during its intensification phase (Figure 11b). Spaceborne oceanic observations are generally unavailable under

cloudy conditions; therefore, data collected by these animals also represent a fantastic opportunity to investigate the impact of TCs on the surface and subsurface structure of the ocean.

Sea surface temperature data collected by ST India in TC HEROLD from 14 to 20 March 2020 are shown in Figure 11c. During these six days, the animal remained trapped in the immediate vicinity of the storm center (~ 30 km from the TC eye) and only moved ~ 50 km in the north/north-west direction. In situ surface temperature observations collected from 14 to 17 March showed SST cooling of $\sim 3.5^\circ\text{C}$ (29°C to 25.5°C) in 72 h—during these three days, the animal remained quasi-stationary. As the storm progressively moved south-eastwards, ST India began to slowly move to the north-west, over the area previously affected by the tropical cyclone. Observations collected from 17 to 20 March showed that the temperature surface layer in this area quickly returned to pre-storm conditions, to regain its initial temperature of 29°C on 19 March. As shown in [33], surface and subsurface observations collected by STs in tropical cyclones can also provide key data to evaluate coupled model forecasts in cyclonic conditions.

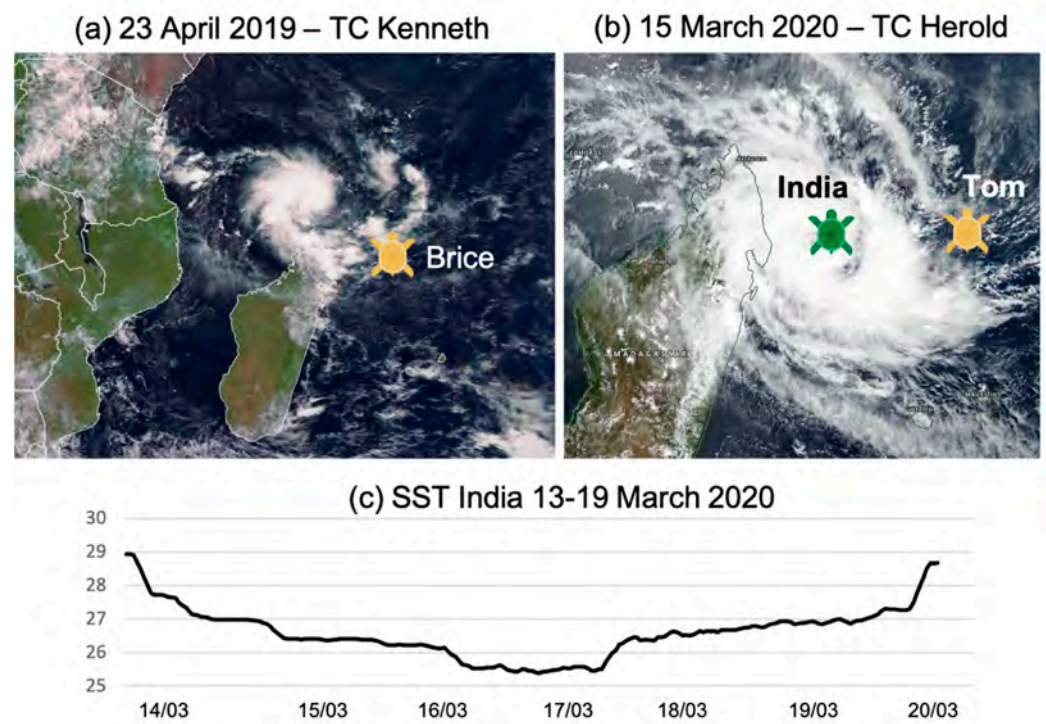


Figure 11. Satellite images of (a) TC KENNETH on 15 April 2019 and (b) TC HEROLD on 15 March 2020. Sea turtle symbols show the location of ST Brice during the cyclogenesis of TC KENNETH (left panel) and of STs India and Tom during the intensification phase of TC HEROLD (right panel). (c) Evolution of sea surface temperature ($^\circ\text{C}$) in the vicinity of TC HEROLD, as measured by ST India between 14 and 20 March 2020 within the area ($51.93\text{--}52.62^\circ\text{E}$; $13.9\text{--}14.67^\circ\text{S}$).

3.1.4. Glider Observations

On 22 January 2019, two SlocumG1 gliders operated by CNRS were deployed from Réunion Island for a period of two months. The two instruments were programmed to follow a north-east (glider GLNE) and a north-west (glider GLNW) trajectory to reach the northernmost region of the Mascarene Archipelago, where a high probability of TC formation was suggested about 400–600 km north of Réunion Island (Figure 12). The data acquisition strategy was set in order to complete a saw-tooth navigation pattern, allowing the gliders to dive with an angle of 26° between 5 m and 980 m depth (resulting in an along-track resolution of about 4 km once the profile was normalized on the vertical).

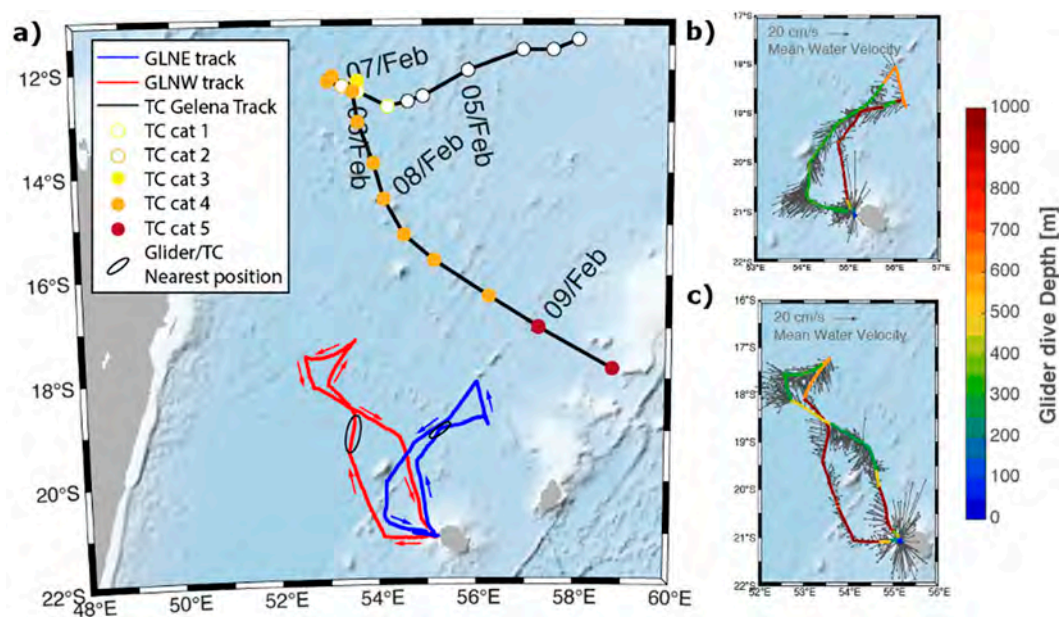


Figure 12. Trajectories of the two gliders deployed from Réunion Island between 22 January 2019 and 22 March 2019. (a) Trajectories of glider GLNE (blue) and GLNW (red), together with the trajectory and intensity (colored dots) of TC GELENA between 5 and 9 February. The positions of the gliders during the TC period are indicated by black ellipses. Right panels show cast depth range and mean current velocities along the glider tracks estimated from glider drift for (b) GLNE and (c) GLNW. Table 1: Glider instrumentation, sampling rate (Hz), vertical resolution (m) and depth range (m) of collected data.

The two gliders were programmed to sample the ocean during descending (downcast) and ascending (upcast) profiles. Observations were transmitted in real time by satellite telemetry after each upcast, when directives for modifying the sampling strategy and glider navigation (based on operational ocean model forecasts) were also received. Each glider was equipped with various physical and optical biogeochemical instruments for sampling the ocean temperature, salinity, oxygen, turbidity, and chlorophyll-a concentration at different rates according to depth, as shown in Table 1. All sensors were operational for glider GLNW, but the oxygen and optical sensors were turned off on glider GLNE.

The primary objective of this experiment was to investigate OA kinetic energy exchanges in cyclonic conditions, with emphasis on the fraction of kinetic energy transmitted to the ocean. As shown by [102], who analyzed the vertical structure of the ocean in a tropical cyclone sampled during the CIRENE field phase [103], this kinetic energy is generated on the left side of the TC track in the southern hemisphere, and later consumed by strong vertical mixing resulting from surface water cooling [104]. Due to the presence of strong currents ($>0.25 \text{ m s}^{-1}$) along the glider trajectories, an important surface drift prevented the full application of the initially planned northward navigation strategy. The navigation parameters were then modified early in the mission to mitigate the battery consumption by reducing the depth range of the glider (because the oil pump that controls the glider buoyancy is the device that consumes the most energy). The gliders profiles were thus reduced to 500 m and 300 m depths (as shown by the colored tracks on Figure 12b,c). Real-time data transmission was also turned-off at some points to reduce the time spent at the surface, when drifting was maximized. The slower-than-expected displacement speed of the gliders prevented them from intercepting the core of TC GELENA, which developed in the area between 5 and 9 February 2019 (Figure 12a). Thanks to real-time trajectory optimization, both systems were nevertheless able to approach relatively close to the storm, as shown by black ellipses displayed in Figure 12a. For instance, glider GLNE was able to move to a distance of about 290 km from the TC center and to collect ocean data in the direct vicinity of this storm.

Table 1. Glider instrumentation, sampling rate (Hz), vertical resolution (m) and depth range (m) of collected data.

Parameter	Instrument	Sampling	Resolution	Depth
GLNE				
Temperature Salinity and Depth	CTD Seabird SBE-41cp	1/8	1.5	−5 to −980
Oxygen	Aanderaa Optode 5013	-	-	-
Fluorescence Turbidity	Wetlabs flbbcd	-	-	-
GLNW				
Temperature Salinity and Depth	CTD Seabird SBE-41cp	1/8	1.5	−5 to −980
Oxygen	Aanderaa Optode 4831	1/8	1.5	−5 to −980
Fluorescence Turbidity	Wetlabs flbbcd	1/8	1.5	−5 to −980

Vertical profiles of temperature, salinity and density collected by the two gliders between 0 and 150 m and 23 January and 17 February 2019 (along the two northward segments of the tracks) are shown in Figure 13, together with corresponding mean profiles for each parameter. The mixed layer depth (MLD), indicated by a black solid line, is estimated as the depth where the temperature differs by 0.2 °C from a surface reference value of 10 dbar [105,106]. Due to the significant distance separating the two gliders from the TC core, and because the maximum kinetic energy generated in the upper ocean occurred on the left side of the TC track, no significant change in the surface temperature could be noticed during the pre-cyclonic, cyclonic, and post-cyclonic phases (Figure 13a,d,g). A relatively constant temperature of 29 °C was observed between the surface and 30 to 40 m depth, but quickly decreased to reach 22 °C at a depth of 150 m. Salinity measurements (Figure 13b,e,h) indicated a freshening of the water within the top 100 m layer, starting around 6 February (−19.22° N) for the GLNW track, and from 28 January (−20.15° N) for the GLNE track. While part of this freshening can be explained by the rainfall generated by TC GELENA between 15° S and 5° N, another possible explanation is related to the advection of fresher water originating from the southern branch of the South Equatorial Current, which flows westward with a 20 Sv transport to feed the East Madagascar Current [107]. The velocity field computed from Mercator-Ocean’s global reanalysis model PHY-001-030, which indicated the presence of strong westward currents between 28 January and 9 February (not shown), and the vertical extent of this freshwater lens, both seem to support this hypothesis. Density measurements (Figure 13c,f,i) did not seem to be impacted by this freshening and showed a well-mixed layer within the top 40 m of the ocean and a well-stratified layer underneath.

The mixed layer depth shows significant frequency variations in relation to the diurnal cycle, and also appears deeper along the GLNW track until 8 February. GLNW was always located southward of GLNE before this date; therefore, these observations suggest a sloping up of the MLD in the northward direction. As GLNW moved northward of GLNE after 8 February, the MLD measured by GLNE became deeper, thus reinforcing the hypothesis of a northward sloping-up of MLD. A significant rise of the MLD of up to 20 m (on 5 and 6 February for GLNE and GLNW, respectively) could also be observed almost immediately after the TC formation (4 February). The MLD then returned to its initial value between 9 February (for GLNW) and 12 February (for GLNE).

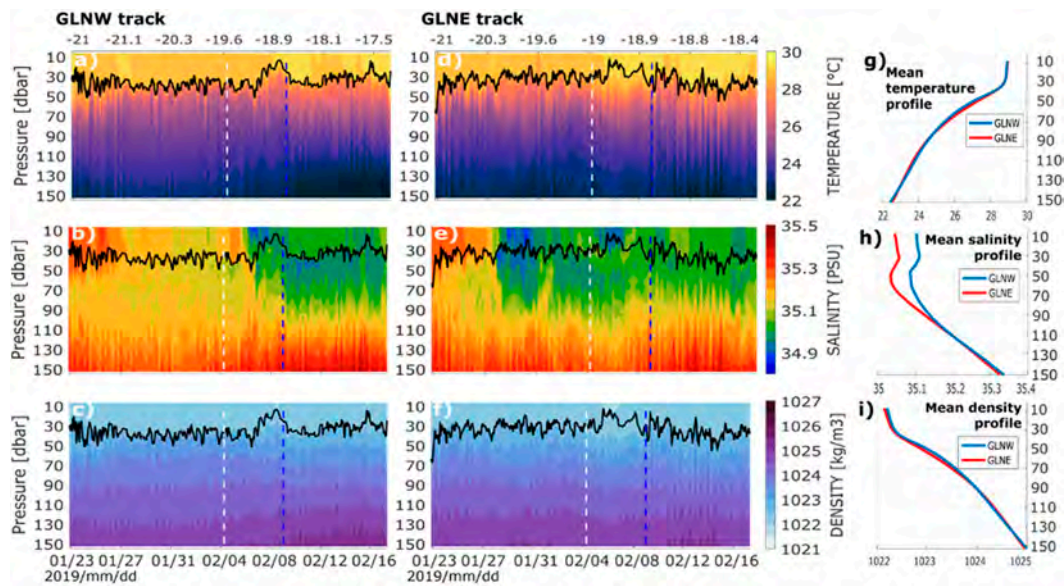


Figure 13. Time series of vertical temperature (top), salinity (middle), and density (bottom) profiles within the top 150 m ocean layer from 23 January 2019 to 17 February 2019 for (a–c) GLNW and (d–f) GLNE tracks. Panels (g–i) show the associated mean vertical profiles over the same period. The vertical white dashed line in (a–f) indicates the date of formation of the Tropical Cyclone GELENA (4 February). The vertical blue dashed line shows the closest position of each glider to the TC core (around 9 February). The top axis indicates the latitudinal location of the profiles.

The temperature–salinity (TS) diagrams collected along the full glider tracks (23 January to 23 March 2019) are shown in Figure 14. The water masses sampled by the two instruments, known as the Indian Central Water, were formed and subducted in the Subtropical Convergence area of the southern gyre of the Indian Ocean [107,108]. The OML in this water mass was generally between 50 and 150 m in depth, with temperature between 25 and 30 °C and salinity in the range of 34.9–35.4 psu. Observations collected from the bottom of the OML to 1000 m showed salinity values between 34.5 and 36 psu and temperatures decreasing from 25 °C to 5 °C.

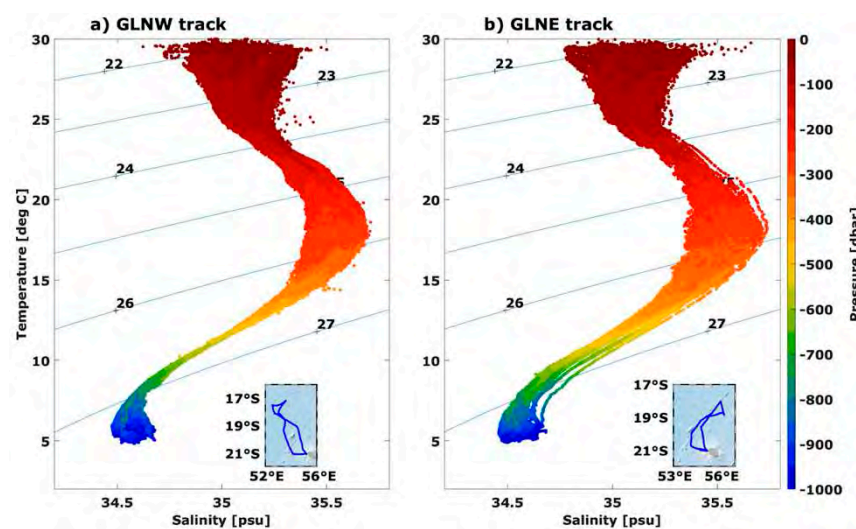


Figure 14. Temperature–salinity (TS) diagram along (a) GLNW and (b) GLNE tracks from 23 January to 23 March 2019. Inserts show corresponding glider tracks.

3.2. Atmospheric Observations

3.2.1. UAS Observations

During RNC-CYC field phase, a UAS system called “BOREAL” was operated from Réunion Island to sample the lower part of the atmosphere (Figure 15). The main objective of this experiment was to provide in situ measurements of air–sea interactions in cyclonic and pre-cyclonic conditions to evaluate numerical models and microphysical parameterizations developed in the frame of the program.

The BOREAL UAS (Boréal SAS, Toulouse, France) is a fixed-wing aircraft with a 4.2 m wingspan propelled by a thermal engine (Figure 15b) that has a maximum take-off weight of 25 kg and can fly in winds up to 25 m s^{-1} . For this experiment, a 5 kg scientific payload was developed to study air–sea interactions using an optical particle counter for measuring the aerosol number and size distribution ($0.3 < \text{diameter} < 3.0 \mu\text{m}$; MetOne), a custom-designed multi-hole probe for measurements of turbulence and three-dimensional winds, a radar altimeter for wave height and sea state measurements, a broadband shortwave pyranometer for downwelling solar radiation (Licor), an infra-red temperature sensor to measure sea-surface temperature, as well as standard meteorological measurements (atmospheric pressure, temperature and relative humidity). With this payload, the endurance and range of the BOREAL UAS was $\sim 7 \text{ h}$, 700 km, and 2000 m above sea level (asl). A live video was also streamed up to 40 km from the ground-station to provide additional safety during low-altitude segments when the UAS flew $\sim 40 \text{ m}$ asl. The BOREAL UAS is autonomous, although its flight plan could be adapted at any time to accommodate weather conditions or air traffic via a radio or a satellite link. A transponder mounted on its wing also allowed it to integrate into international airspace.

The BOREAL UAS flew over the Indian Ocean in two exclusive zones allocated by the French aviation authority to the southeast and northwest sides of Réunion Island (Figure 15a). These two areas were dedicated for scientific flights over the international waters up to 250 km from the ground station and with a ceiling at 1067 m above sea level. BOREAL UAS operations were conducted from the airfields of Cambaie (when flying towards the north of the island) and Bras Panon (when flying towards the south). In total, 12 scientific flights were carried out between February and March 2019, for a total of 53.7 h of research flights and 5012 km of observations over the ocean. Three flights of more than 200 km from the ground station were carried out, the longest of which lasted 6 h and 18 min and covered 610 km. Examples of observations collected by the BOREAL UAS during this two-month operating period are presented below.

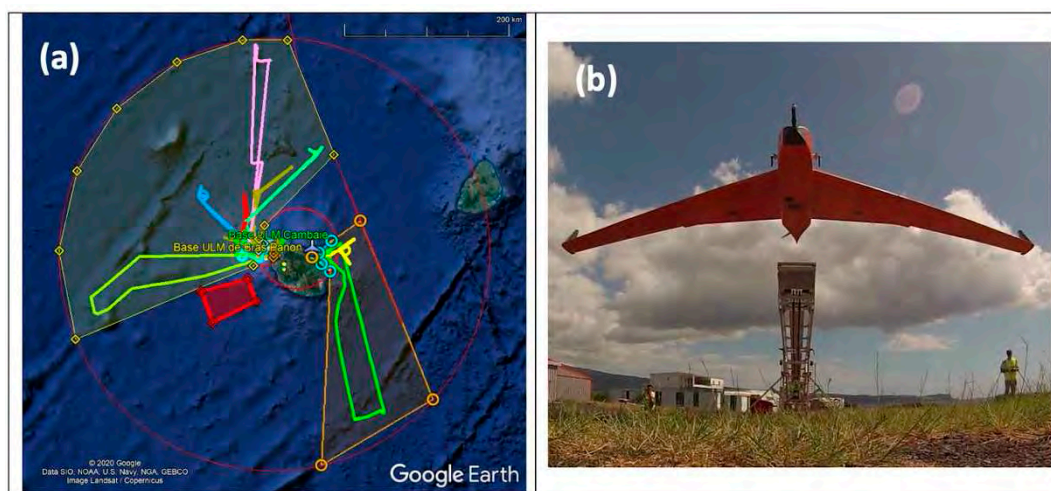


Figure 15. (a) The 12 BOREAL flights operated from Réunion Island during the RNR-CYC campaign in February and March 2019. The yellow and orange polygons represent the authorized flight zones to the northwest and southeast of Réunion Island. The outer red circle denotes an operating radius of 250 km around Réunion Island. (b) The BOREAL UAS leaving the catapult for a scientific mission from Cambaie, Réunion Island. Sources: (a) Google Earth; (b) Greg Roberts.

Figure 16 summarizes the BOREAL UAS measurements of aerosol concentrations for particle diameters $>0.3 \mu\text{m}$ and $>1.0 \mu\text{m}$ within 200 m above the ocean surface, compared to horizontal wind speed (Figure 16a) and wave height (Figure 16b) for conditions encountered during the two-month campaign. As expected, there was an increase in particle concentrations (diameter $>0.3 \mu\text{m}$), which is often associated with primary marine aerosol (PMA) emissions, over the observed range of wind speed (2.2 to 13.5 m s^{-1}) and wave heights (2 to 3.7 m). However, the range of wind speeds and wave heights encountered in the vicinity of Réunion Island during the RNR-CYC field campaign remained relatively small, partly because the paths of the TCs were never closer than a few hundred kilometers to the ground station during the observed period.

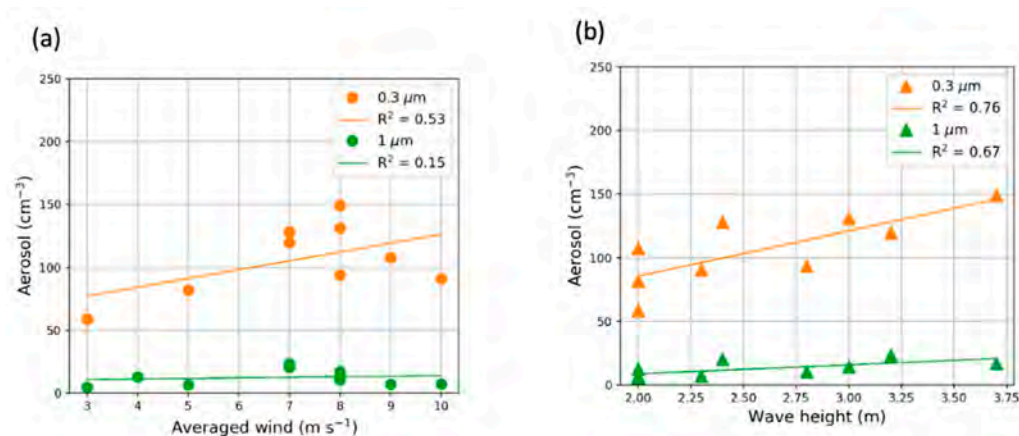


Figure 16. Aerosol concentrations (diameter $>0.3 \mu\text{m}$ and $>1.0 \mu\text{m}$) measured during the BOREAL flights as a function of (a) the averaged horizontal wind in the marine boundary layer and (b) the measured wave height.

Although strong cyclonic conditions were not encountered in the vicinity of Réunion Island during the 2019–2020 TC season, several BOREAL UAS flights were nevertheless impacted by the presence of TC JOANINHA, which developed in the eastern part of the Mascarene Archipelago in March 2019 (Figure 17a). The signature of this storm could be seen up to several hundred kilometers away in observations of ocean waves, atmospheric turbulence structures, and enhanced PMA emissions. These emissions, which occur over a much larger domain than the cyclonic system, have been shown to modify the TC's track and intensity [11].

As TC JOANINHA moved to the east of Mauritius, the BOREAL UAS flew to the west of Réunion Island to sample the TC's perimeter (see flight track in Figure 17a and wave crests, swells and clouds generated by the cyclone recorded by the on-board camera in Figure 17b). In situ measurements were used, in particular, to assess parameterizations of air–sea interactions simulated with the OWA coupled system developed in RNR-CYC (see [33] for details about this system). Results presented hereafter are derived from a coupled OWA simulation based on the ocean model Coastal and Regional Ocean Community (CROCO, <http://www.croco-ocean.org>, accessed on 20 March 2021), the wave model Wave Watch 3 (WW3) [94,95], and the atmospheric model Meso-NH (<http://mesonh.aero.obs-mip.fr/>, accessed on 20 March 2021), which was developed specifically for comparisons with the BOREAL UAS.

Figure 18 presents a vertical profile of aerosol particles conducted during the 25 March flight from near the ocean surface ($<50 \text{ m asl}$) to above the marine boundary layer ($\sim 1000 \text{ m asl}$). Observed aerosol concentrations (diameter $>0.3 \mu\text{m}$) were found to be relatively constant throughout the marine boundary layer (up to $\sim 800 \text{ m asl}$) and decreased above the inversion. A surface layer with enhanced emissions, similar to the profiles observed at the surf zone in the frame of project Miriad [109], was also observed at the lowest part of the vertical profile ($\sim 50 \text{ m asl}$).

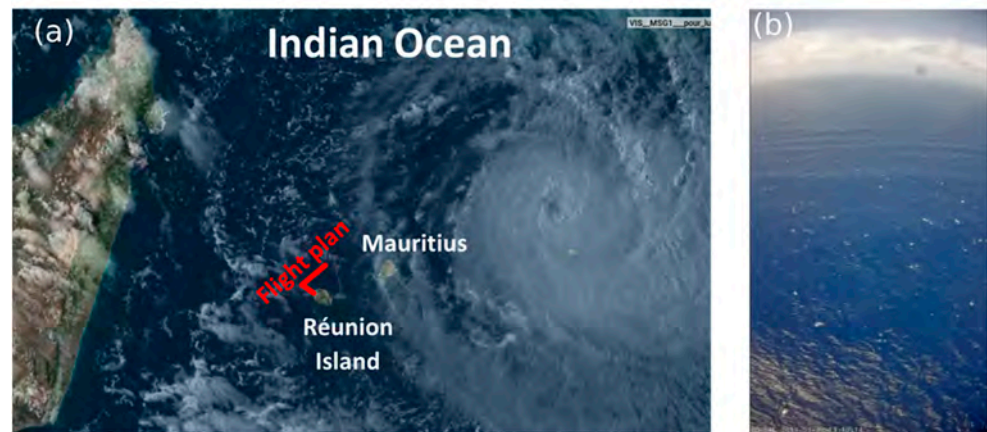


Figure 17. (a) Satellite image of TC JOANINHA on 25 March 2019 in the vicinity of Mauritius and Réunion Island. (b) picture from the BOREAL on-board camera showing the ocean sea-state and the TC on the horizon. Sources: (a) MSG satellite; (b) Christophe Mazel

This surface layer, which was not captured in the model simulation (Figure 18), has not been well-documented so far and has important implications for the transport of aerosols into the well-mixed boundary layer. In addition, the simulations tend to overestimate the aerosol emissions near the ocean surface (i.e., an approximate factor of two enhancement in aerosol concentrations) and show a pronounced vertical gradient throughout the marine boundary layer with an underestimate of aerosol concentrations in the free troposphere. These large differences between observed and simulated vertical profiles of aerosol concentrations suggest that mixing timescales in the marine boundary layer may perhaps be too slow in the model—resulting in an excessive gradient in the aerosol concentration—but could also be related to a possible bias in the CAMS/COPERNICUS analyses used to initialize sea salts in Meso-NH. Although a mass distribution calculation was made to adjust the consistency of aerosol distributions in CAMS and Meso-NH, a small remaining mass difference in the finest modes can also lead to large differences in the number of aerosols, especially in areas with low primary aerosol production, i.e., where aerosol number concentrations mostly arise from initial conditions.

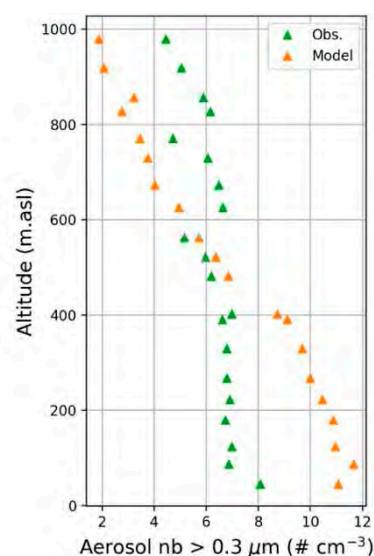


Figure 18. BOREAL profile of aerosol numbers for particles larger than 0.3 μm obtained with the onboard Optical Particle Counter (green) and simulated with the OWA model (orange).

A few days later, a southern swell event occurred when winds shifted to the north-east direction as TC JOANINHA continued its eastward progression through the Indian Ocean. Flight operations were moved to Bras Panon and the BOREAL UAS flew along a southern curtain for more than 200 km to the east of Réunion Island on 29 March 2019 from 6:33 to 12:04 UTC (Figure 19a). The platform followed a flight plan with ascents from 100 to 1000 m asl followed by straight-level legs at 400 and 100 m asl for at least 10 km each. Mean and significant wave height observations collected during this flight by the onboard radar altimeter showed that wave height increased by about one meter (from ~2.5 to 3.5 m) between locations A and D (Figure 19b).

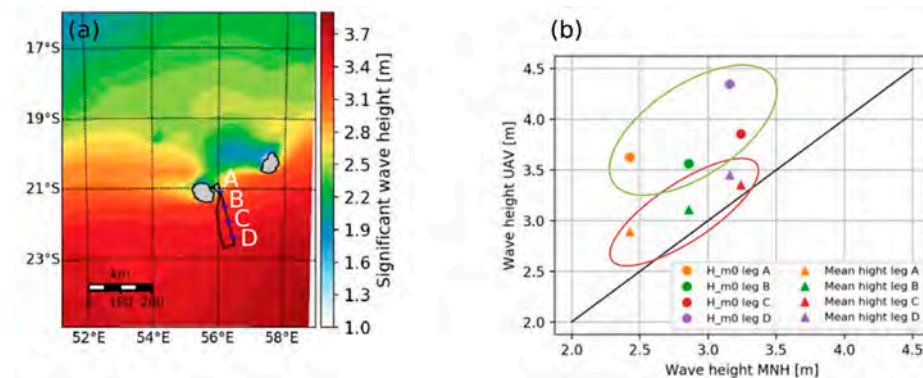


Figure 19. (a) WW3 simulation of significant wave height on 29 March 2019 with the BOREAL UAS flight overlaid on the image (black line). The blue crosses correspond to A, B, C and D legs of the flight at 100 m asl. (b) Significant wave height (H_{m0}) and mean wave height from the BOREAL UAS observations compared to wave height simulated by WW3.

A similar increase in wave height was also obtained from the simulations of this case study (Figure 19a). The associated modelled (Figure 20a) and observed (Figure 20b) spectral density functions provide insight on the composition of the southern swell and show two peaks for both observations and simulations. Azimuth plots from WW3 based on the wave elevation spectrum (Figure 20c) indicate that these peaks corresponded to distinct components of the southern swell; the first component was generated by the northerly winds (red arrow in Figure 20c), and the second component was generated by TC JOANINHA to the east (black arrow in Figure 20c). In spite of the observed increase in wave height (and relatively constant wind field), a horizontal gradient in the aerosol concentration and size distribution at 100 m asl was not observed during this swell event. These results were predictable because the 1 m increase in wave height is relatively small and not expected to generate a significant difference in PMA emissions.

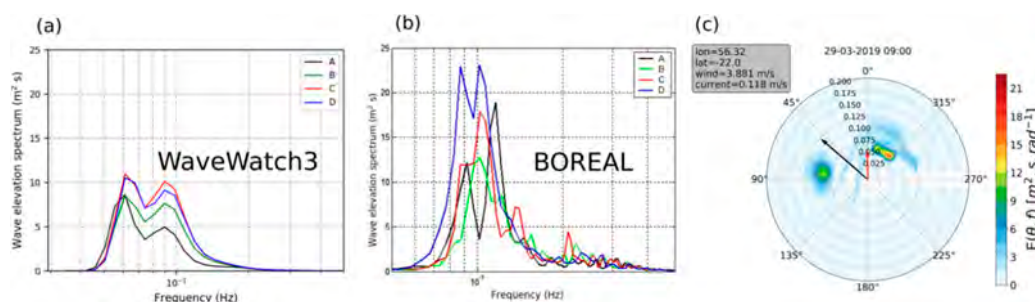


Figure 20. (a) Spectral density function of wave height simulated with WW3 for legs A, B, C, and D. (b) Spectral density function of wave height from BOREAL UAS observations for legs A, B, C, and D. (c) Corresponding azimuth plot to wave elevation spectrum for leg A. The black (resp. red) arrow represents the wind direction (resp. current direction), and the scatter color are the wave crests. The length of the arrows has been scaled by 2.

Due to the low number of TCs passing in the immediate vicinity of Réunion Island during the TC season 2018–2019, the range of wind speeds and ocean wave conditions were not as large as expected to fully assess parameterizations for PMA emissions. Nevertheless, the datasets collected during this campaign have clearly demonstrated the scientific potential of the BOREAL UAS, and of its associated payload, to collect key observations in remote oceanic areas and in the vicinity to tropical cyclones.

3.2.2. GNSS Observations

A well-known (indirect) atmospheric application of GNSS measurement consists of measuring the atmospheric integrated water vapor (IWV) content from the delay induced by water vapor during the crossing of the earth's atmosphere by the GNSS signal [110]. Due to the fundamental role of water vapor in climate and weather dynamics, tropospheric GNSS measurements have rapidly become one of the main tools used by climatologists to monitor the evolution of the water vapor field at all spatio-temporal scales, but also to improve NWP model forecasts (see [111] for a recent review of current GNSS weather applications). The creation of the International GNSS Service (IGS) network in 1994 [112], which now includes more than 500 stations worldwide, has also enabled GNSS-derived measurements collected in all parts of the world to be widely disseminated to the scientific community. However, with only eight operational stations available prior to RNR-CYC (Figure 21), the density of public GNSS stations in the SWIO was the lowest of all TC basins.

During RNR-CYC, 10 new permanent stations were deployed, including one in the Seychelles (Aldabra), four in the Eparses Islands (three RNR-CYC stations at Juan de Nova, Tromelin and Europa and one shared station installed by OPGP in Glorieuses), and five in Madagascar (Diego-Suarez, Toamasina, Sainte-Marie, Nosy Be and Fort-Dauphin), with the goals of increasing the density of the GNSS network in the SWIO and to provide additional near-real-time IWV measurements at various locations in the basin (Figure 21). Although these stations have not yet been included into the IGS network (pending), most collected GNSS observations are transmitted at hourly time steps to IGN's data center, which already allows for routine real-time GNSS calculations and the wide dissemination of derived meteorological and geophysical products through IGN's permanent GNSS network (RGP, <ftp://rgpdata.ign.fr/pub/gnssmayotte>, accessed on 20 March 2021).

These new stations have already been shown to represent a fantastic asset for monitoring the spatio-temporal evolution of the water vapor field at local and regional scales [34,35], as well as to evaluate NWP forecasts [34]. A further modelling application is shown in Figure 22, which presents differences between GNSS-derived IWV observations and daily 6 h analyses of AROME-IO operational NWP systems [42] at 00:00, 06:00, 12:00, and 18:00 UTC at Aldabra (ALBR, The Seychelles), Antananarivo (ABPO, Madagascar), Réunion Island (RUN, France) and Sainte-Marie (MASM, Madagascar) during the year 2019. In order to evaluate the performance of the model at various time scales, 30-day (red), 10-day (yellow) and 3-day (black) moving averages were applied to both the model and GNSS data. GNSS observations were processed following the approach proposed by [35].



Figure 21. Map of public GNSS stations available in the SWIO as of March 2021 (top). Red squares show current IGS stations, green dots show GNSS stations installed during RNR-CYC, and blue triangles show stations to be installed in 2021 in the frame of the new project ESPOIRS (see Section 4). Pictures show GNSS stations installed in Fort-Dauphin (MAFD, upper-left), Tromelin (TRML, lower-left) and Aldabra (ALBR, lower-right). Sources: Google Earth (top); Olivier Bousquet (pictures)

Whatever the time scale, the bias error remained relatively constant at Sainte Marie (MASM, approximately -0.3 kg m^{-2}), Réunion (REUN, approximately 0.5 kg m^{-2}) and Antananarivo (ABPO, approximately -2 kg m^{-2}), but showed more variations in Aldabra (ALBR, between 0.6 and 1.14 kg m^{-2}). Model–observation differences did not show a clear seasonal dependency, except at Aldabra where maximum errors were observed in the middle of the winter, spring, and fall seasons. In the case of this atoll, consisting of land strips of 1–3 km width encircling a lagoon of nearly $30 \text{ km} \times 15 \text{ km}$, the land is considered as submerged by the model, which does not allow taking into account the effect of vegetation and of the diurnal cycle on the atmospheric moisture content. At Aldabra, atmospheric moisture changes in the model thus mostly depend on the variation of ocean temperatures. Interestingly, the sign of the bias error is location-dependent, suggesting that the model is not affected by systematic errors. The associated standard deviation errors also tends to decrease with the length of the smoothing period, because the latter minimized the impact of short-term variations. At short time scales (three days), one can

notice that the strongest discrepancies mostly occur during the TC (wet) season (days 1–120 and 330–365), in relation with the passage of tropical cyclones in the vicinity of the GNSS ground-based stations.

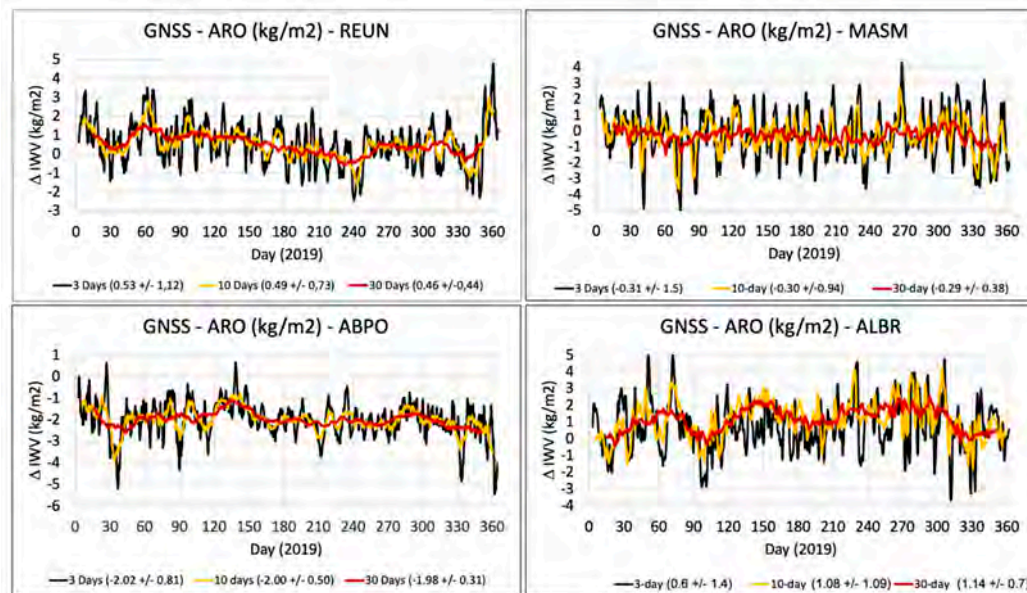


Figure 22. Time series of the differences between IWV contents observed by GNSS and AROME-IO analyses at Réunion Island (REUN, upper left), Sainte-Marie (MASM, upper right), Antananarivo (ABPO, lower left) and Aldabra (ALBR, lower right) throughout the year 2019. 30-day (red), 10-day (orange), and 3-day (black) moving averages were applied to IWV data to evaluate the impact of short and mid-term moisture variations on the model performance.

As already pointed out by [34], who investigated the seasonal variations of AROME-analyzed IWV errors at Diego-Suarez (DSUA), model–observation differences seem exacerbated for stations located in the vicinity of complex orography. Except for the particular case of Aldabra, the same behavior can be noticed here for the high-altitude stations of Réunion (600 m asl, REUN) and Antananarivo (2000 m asl, ABPO), which showed higher errors than for the flat island of Sainte-Marie (MASM). These errors might be related to the difficulties of the model to properly capture the modifications of air masses caused by the orography (lifting and subsiding motions) at the local scale due to an insufficient resolution of its topography. A possible way to correct for such errors could be to assimilate GNSS observations (zenithal delays) into the model. While the operational version of the AROME-IO NWP system does not allow for data assimilation, its research configuration includes a 3D-Var scheme that can be used to perform assimilation experiments [34]. Some studies are currently ongoing to determine whether the assimilation of observations collected from these new GNSS stations can help to reduce this moisture bias.

3.3. Spaceborne Observations

Visible and infrared satellite observations have long been the main source of knowledge for estimating some of the parameters (e.g., radius of maximum wind, various wind radii) characterizing the structure of tropical cyclones—these parameters are, in particular, inputs of the Dvorak method [113], used by TC forecast centers to produce best-track data and issue TC advisory and forecasts. Since the launch of the first Earth observation satellite in the early 1970s, the quality of ocean surface wind estimates in the vicinity of TCs has constantly been improved. This includes, for instance, the deployment of wind scatterometers [114,115] as well as of multifrequency radiometers [116,117] that both allow for a direct, and more precise, estimate of surface winds under TCs. More recently, a new generation of microwave radiometers has also been put into operation by ESA and the National Aeronautics and Space Administration (NASA) in the frame of the Soil Moisture

and Ocean Salinity (SMOS) and Soil Moisture Active Passive (SMAP) space missions, respectively. Thanks to their large coverage and revisit times, these new sensors, which allow for high-resolution (~40 km) surface wind speed sampling in all weather conditions, provide a unique description of TC structure during its whole lifetime [118], and have thus become a key source of information for TC forecasting centers.

In addition to these more or less conventional sensors, a new approach, based on the use of spaceborne synthetic aperture radars (SARs), is also being increasingly used to probe and quantify sea surface properties under extreme wind conditions. Designed in the mid-1990s, SAR systems were initially used for land applications [119], especially for monitoring earth deformation rates ranging from a few millimeters per year (e.g., for glaciers) up to 1 m per h (e.g., earthquakes and landslides). SAR potential for marine applications was already known since the launch of the first SAR satellite [120], but has significantly emerged with the launch of the Canadian Space Agency (CSA)'s RADARSAT-1 (1995) and ESA's Envisat (2002) satellites. Thanks to their unique capability to gather very high-resolution (up to a few meters) surface wind and roughness data in swaths of several hundred kilometers, spaceborne SARs have become key observing systems for monitoring, forecasting, and investigating the properties and evolution of TCs [120,121].

The deployment of a new generation of SAR systems equipped with polarization diversity on-board CSA's RADARSAT-2 (RS2, 2007) and ESA's Sentinel-1 (S1, 2014) satellites has allowed further improvements in the capabilities of these instruments to accurately map the variations of ocean surface winds in TC eyes and eyewalls [122,123]. Acquisitions made by ESA's satellites had, however, never been used to probe tropical cyclones until the implementation of the Satellite Hurricane Observations Campaign (SHOC, 2016–2017), in the Pacific and Atlantic basins. The intercomparison of aircraft reconnaissance wind data against S1 SAR measurements collected in CAT-5 hurricane IRMA (2017) during this experiment definitely demonstrated the capability of these instruments to thoroughly describe TC ocean boundary layer structures at high spatial resolution [124].

The extension of the SHOC program to the SWIO basin (referred to as SHOC-V2) was initiated in 2017, under the frame of RNR-CYC. SAR missions cannot continuously acquire wide swaths of data in high-resolution modes; therefore, a dedicated acquisition procedure was set up to collect data without impacting the operational duty cycle of the satellites. Acquisition requests were passed along to both MDA (MacDonald Dettwiler and Associates, the private company that owns the satellite RS2) and ESA S1 mission planner portals on a 24-to-48 h notice, based on satellite orbit and five-day track forecasts provided by RSMC La Réunion. In order to reduce the workload of participating space agencies, which contributed to this experimental program on a voluntary basis, acquisition requests were also generally limited to storms presenting a threat to SWIO populations.

Between 2017 and 2021, about 150 SAR images were acquired by S1A, S1B and RS2 satellites, allowing the sampling of 20 tropical storms and cyclones over four TC seasons (raw S1 data are available at <https://scihub.copernicus.eu>, accessed on 20 March 2021). Among these acquisitions, nearly 40% were directly obtained within the eye or the eyewall of the systems (Table 2, "hits"). SAR images were collected throughout the SWIO basin (Figure 23) at various storm evolution stages (cyclogenesis, intensification, dissipation). Collected wind data were used for nowcasting and best-track data reanalysis purposes at RSMC La Réunion, model verification [33] and assimilation in NWP systems [125] (this Special Issue).

Table 2. Number of Radarsat-2 and Sentinel-1 SAR acquisitions within the eyewall/eye (hits) of tropical storms (TSs) and tropical cyclones (TCs, ITC) that developed in the SWIO between February 2017 and 2021. * Acquisitions performed from 2021 onwards were made in the frame of the CYMS program (see Section 4).

Storm Name	Date	Hits	Storm Name	Date	Hits
Dineo (TC)	02/2017	2	Idai (ITC)	03/2019	3
Enawo (ITC)	03/2017	1	Joaninha (ITC)	03/2019	7
Ava (TC)	01/2018	3	Kenneth (ITC)	04/2019	1
Berguitta (ITC)	01/2018	4	Lorna (TC)	04/2019	4
Cebile (ITC)	01/2018	8	Belna (TC)	12/2019	5
Dumazile (ITC)	03/2018	5	Calvinia (TC)	12/2019	1
Eliakim (TS)	03/2018	1	Diane (TS)	01/2020	1
Alcide (ITC)	11/2018	1	Francisco (TS)	02/2020	1
Kenanga (ITC)	12/2018	2	Herold (ITC)	03/2020	1
Gelena (ITC)	02/2019	4	* Chalane (TS)	12/2021	3
Haleh (ITC)	03/2019	6	* Eloise (TC)	01/2021	2

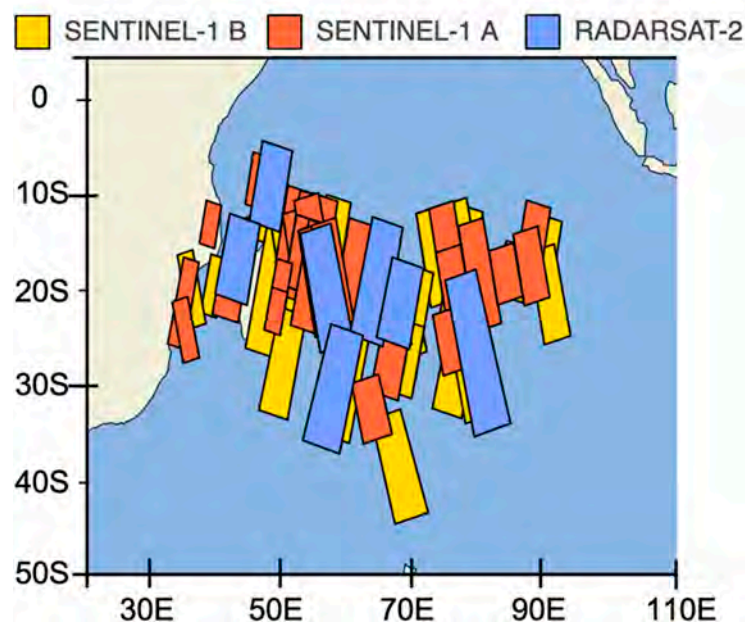


Figure 23. Location of Sentinel-1 (A and B) and RADARSAT-2 swaths listed in Table 2.

Examples of SAR-derived surface wind fields obtained through the application of the retrieval algorithm proposed by [126] are presented hereafter. The first example was taken within TC JOANINHA, which developed in the northeastern part of the Mascarene Archipelago (Figure 17a) and reached its LMI in the vicinity of Rodrigues Island on 26 March 2019, with 10 min of maximum sustained winds of nearly 60 m s^{-1} (Figure 24a). The core structure of this system was observed seven times by the SAR systems deployed onboard satellites S1A/S1B and RS2 (Table 2) at various stages of its life cycle. Of particular interest is the image taken by RS2 on 28 March 2019 at 00:52 UTC (Figure 24b), when the system started to experience an eyewall replacement cycle (ERC). The latter, which often occurs when a TC reaches an intensity of 50 m s^{-1} , has long been recognized as one of the main mechanisms for intense TCs to intensify further [127,128]. During an ERC, outer rainbands strengthen and organize themselves into a ring of thunderstorms that progressively encircle the TC eyewall. The formation of this outer ring, usually referred to as the outer eyewall, eventually cuts off the supply of moisture and angular momentum that maintain convection around the eye, causing a weakening of the system and the eventual dissipation of the inner eyewall. The former ring is then replaced by the outer

ring, which gradually contracts and intensifies, often resulting in a more intense TC than prior to the ERC.

The analysis of the SAR-derived surface wind field shown in Figure 24b clearly indicates the presence of two concentric areas of maximum wind located both around the eye and in the east-to-southeastern quadrant of the system core. The inner structure (maximum wind speed of $\sim 50.2 \text{ m s}^{-1}$) corresponds to the eyewall of the storm, and the outer one (maximum wind speed of $\sim 45 \text{ m s}^{-1}$) to the cyclonic rainbands progressively wrapping around the eyewall that will eventually replace the inner wall. As mentioned previously, the completion of an ERC is often followed by a re-intensification of the system. However, in the present case, such re-intensification did not occur because TC JOANINHA rapidly encountered a strongly sheared environment that caused its dissipation a couple of days later.

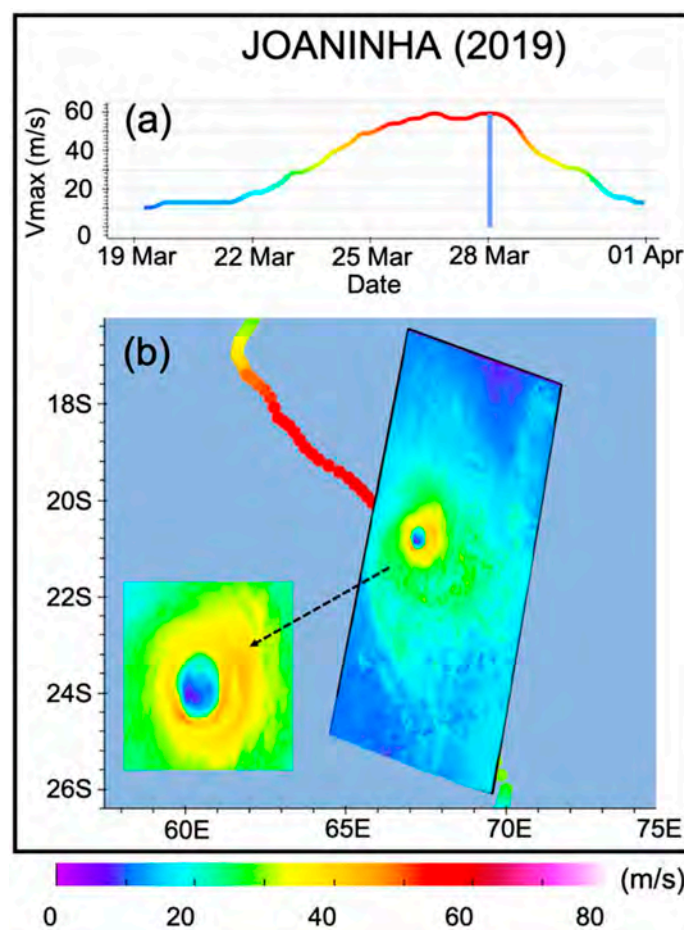


Figure 24. Intensity of TC JOANINHA (color scale at bottom). (a) Wind speed evolution with respect to time as given by ATCF and (b) SAR wind retrieval (RS2) on 28 March 2020 at 00:52 UTC.

The second example is taken from TC IDAÏ (Figure 25), which is considered as the worst natural disaster that has ever affected Mozambique (as well as the surrounding countries of Zimbabwe and Malawi), and the deadliest storm ever recorded in the SWIO. This exceptional TC initiated as a tropical depression along the northern coast of Mozambique on 3 March 2019 (Figure 25a) that initially moved inland in the northwestern part of the country for a few days, with peak winds in the order of $10\text{--}15 \text{ m s}^{-1}$. On 7 March, it made a half-turn near the Mozambique–Malawi border and moved back towards the ocean. After entering the Mozambique Channel, on 9 March, the storm experienced a rapid intensification to reach intense TC intensity (10 min maximum sustained wind $>46 \text{ m s}^{-1}$), with winds gusts estimated at up to 70 m s^{-1} on 11 March. IDAÏ then reversed its track back for the second time in the immediate vicinity of the Eparses island of Juan de Nova

(located approximately 150 km off the west coast of Madagascar) and began its southwestward progression towards Mozambique. Shortly after this half-turn, it entered into a slight weakening trend following the beginning of its ERC. Right after its completion, IDAĭ immediately re-intensified and reached its LMI on 14 March, with a minimum central pressure of 940 hPa and (estimated) 10 min maximum sustained winds of $\sim 55 \text{ m s}^{-1}$. The storm then gradually weakened while progressing towards Beira, where it made landfall on 15 March at the TC stage.

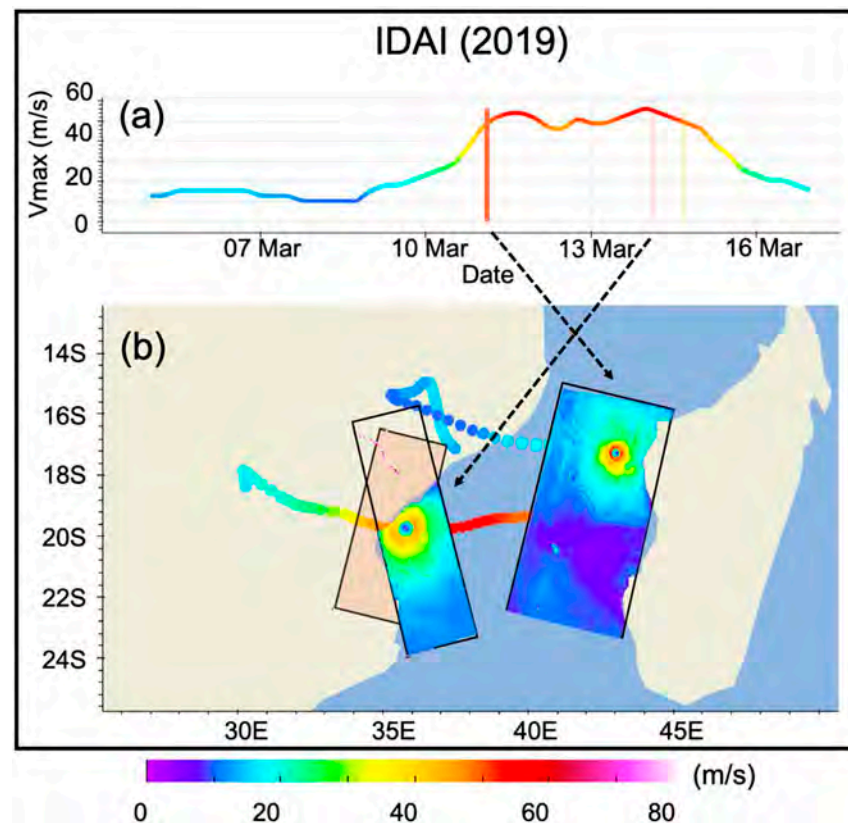


Figure 25. As in Figure 24, but for (a) TC IDAĭ and (b) SAR images collected by S1A on 11 (02:43 UTC) and 14 (03:08 UTC) March 2019.

Numerous acquisitions were made in this system by S1 satellites, including three images collected directly in the core of the storm (Figure 25b). Two of these hits were made over the ocean by S1A, at the stage of intense TC (11 March at 02:43 UTC and 14 March at 03:08 UTC), while a third one was made at landfall by S1B on 14 March at 16:00 UTC (because 90% of this swath occurred over land, this third acquisition is not exploitable). SAR wind data shown in Figure 25 are the only high-resolution wind observations collected during the oceanic phase of this system—WMO’s JDN weather station broke down a week before the passage of the storm over the island and the weather station deployed at Beira in the frame of RNR-CYC was lost during landfall—therefore, these observations represent an invaluable asset for accurately assessing numerical model simulations of this storm [33].

SAR data collected in IDAĭ and other tropical cyclones can also meaningfully complement best-track (BT) data produced by RSMC La Réunion. According to RSMC La Réunion best-track, TC IDAĭ reached its LMI on 14 March 2019 at 00:00 UTC with maximum winds of nearly 55 m s^{-1} . This value is in good agreement with the maximum intensity measured by S1B a few hours later ($\sim 52 \text{ m s}^{-1}$). SAR data, however, show that these strong wind values were only observed in the eastern quadrant of the storm’s core, but that the average wind speed throughout the eyewall was significantly less intense and mostly comprised between 42 and 45 m s^{-1} . On 11 March, the agreement between best-track and SAR-derived

wind data was less good, with maximum wind speed in the order of 50 m s^{-1} for the BT and 60 m s^{-1} for SAR observations. According to SAR observations, the strongest wind speed values were also more or less uniformly distributed throughout the eyewall. Hence, the comparison of the two SAR images suggests that the destructive potential, and overall global intensity of the system, was probably much greater on 11 March, despite a 10% lower maximum wind speed (50 m s^{-1} vs. 55 m s^{-1}) in BT data.

4. Conclusions and Perspectives

ReNovRisk-Cyclone (RNR-CYC) is an ambitious international research program aimed at developing regional cooperation in the SWIO with emphasis on the observation and modeling of tropical cyclones at both current and future time horizons. The observation component of RNR-CYC, presented in detail in this paper, has enabled the collection of numerous innovative oceanic (gliders, sea-turtle borne and seismometer-derived data) and atmospheric (UAS and SAR-derived wind data) measurements, together with more conventional observations (GNSS-derived IWV, atmospheric radiosoundings, ADCP, and wave gauge swell measurements) to investigate tropical cyclones and their environment from the local to the basin scale. Its mesoscale modelling and climate components, presented in more detail in the companion paper [33], also allowed for the development of innovative modelling systems, while its outreach component significantly increased regional collaboration between SWIO countries affected by TC hazards. The innovative data collected in the SWIO during RNR-CYC have also proven particularly useful to evaluate the performance of both research and operational TC forecasting models in this under-sampled region of the world. SAR measurements, which allow for accurate evaluations of TC forecasts, can also be assimilated into NWP systems [126]; in situ and remote swell measurements can be relied upon to evaluate wave model performance; while biologging measurements are priceless to assess ocean model representation of the ocean mixed layer in cyclonic conditions.

The promising results obtained during the 3.5-year observation component of RNR-CYC have already led to the development of numerous new research projects aimed at maintaining some of these novel measurements and further reinforcing overall observation capabilities in the SWIO beyond the end of this program (July 2021). Among the principal new research projects directly arising from RNR-CYC, one can mention STORM-IO (Sea Turtle for Ocean Research and Monitoring in the Indian Ocean), ESPOIRS (Etude des systèmes précipitants de l'océan Indien par radar et satellites—Studies of Indian Ocean precipitation systems by radars and satellites), and MAP-IO (Marion Dufresne Atmospheric Program—Indian Ocean).

STORM-IO (starting May 2021) will enable the extension ST-borne measurements conducted from Réunion Island to the whole Indian Ocean (Figure 26), in collaboration with the Terres Australes et Antarctiques Françaises (TAAF) administration (in Eparses Islands of Juan de Nova and Tromelin), Kelonia (Réunion Island), and five marine reservations in Comoros (Moheli), Madagascar (Nosy Tanikely), Seychelles (Aldabra), Mozambique (Ponto di Ouro), and South Africa (iSimanliso). This transdisciplinary project, constructed in close cooperation with ST specialists and oceanographers, will extend the research initiated during RNR-CYC to: (i) investigate Indian Ocean properties and spatio-temporal variability; and (ii) improve knowledge of the ecology of the five species of sea turtles living in the Indian Ocean. A particular emphasis will be put on the observation of mesoscale eddies and coastal currents that develop in the Mozambique Channel (to assess their impact on water mass distribution, transport, and mixing, as well as their role in the dynamics of the Greater Agulhas current system), and on the assimilation of collected ST-borne data in global and limited-area configurations of the ocean model NEMO [129]. This new component of the global STORM program, which is now strongly supported by the EU, UNESCO (through the GOOS/ AniBOS), CNES and CNRS, among others, will be conducted for the many years to come, and is likely to be extended to other ocean basins in the mid-term.

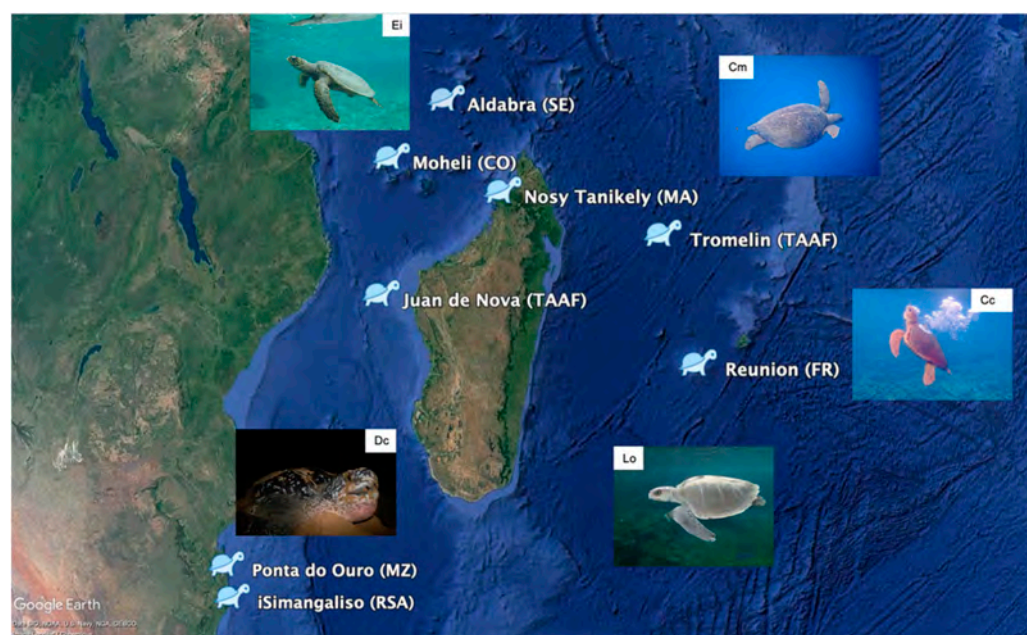


Figure 26. Release locations and sea turtle species to be equipped in the frame of the STORM-IO project: Ei: *Eretmochelys imbricata* (Hawksbill); Cm: *Chelonia mydas* (Green); Cc: *Caretta caretta* (Loggerhead); Lo: *Lepidochelys olivacea* (Olive Ridley); Dc: *Dermochelys coriacea* (Leatherback). Sources: background, Google Earth; Pictures, Kelonia

ESPOIRS (started in December 2020) will carry on with the densification of the GNSS water vapor observation network initiated in the framework of RNR-CYC's sub-program IOGA⁴MET through the deployment of five additional stations in Madagascar and Mozambique (Figure 21). Some existing, or soon to be deployed, GNSS stations will also be upgraded with co-located oceanographic sensors to monitor sea level on a regional scale. In the mid-term, these instruments will be integrated into the Global Sea Level Observing System (GLOSS, <https://www.gloss-sealevel.org/>, accessed on 20 March 2021) network, which monitors sea level rise on a global scale, and into the IGS network, which disseminates GNSS data to the worldwide scientific community. ESPOIRS also includes an ambitious local component aimed at collecting wind and precipitation measurements in tropical cyclones with a transportable polarimetric weather radar to be deployed in Réunion Island (2021), the Seychelles (Mahe, 2022), and Madagascar (Tamatave or Diego Suarez, 2023). This weather radar component will notably focus on the impact of orography on tropical cyclones (or outer cyclonic rainbands in the Seychelles) [130], and will help to develop regional cooperation in the field of atmospheric remote sensing.

The goal of the MAP-IO program (started in January 2021) is to deploy an atmospheric and marine biology observatory in the Indian and Southern Oceans onboard the French vessel Marion Dufresne (Figure 27), operated by the TAAF administration (for its logistical needs in the Eparses Island and French Austral Territories) and IFREMER (for scientific campaigns in the IO). With the deployment of nearly 20 new sensors on-board this RV (e.g., cytometer, titrator, thermosalinograph, cytometer, titrator, NO_x, CO, CO₂, O₃ and CH₄ analyzers, GNSS, UV radiometer, CCN, photometer, weather station), observations at the OA interface and within the atmospheric column will be collected over the long term in this region particularly sensitive to the impact of climate change (note that all observations will be transmitted in near-real-time through the RV onboard satellite communication system). The data collected in the Southern Ocean for sea and wind conditions close to those encountered in tropical cyclones will also be used to carry on with the evaluation of OA exchange parameterizations (turbulent fluxes, aerosol, and sea-spray emissions) in extreme conditions [33]. This exploratory research project, which benefits from strong

support from the EU, IFREMER, CNRS, TAAF and Réunion University, among others, is likely to be maintained in the long term.



Figure 27. Picture of the RV Marion Dufresne anchored at Mayotte during TAAF's Eparses Island rotation in April 2019. Source: Olivier Bousquet

Finally, one can also mention ESA's pre-operational program CYclone Monitoring Service based on Sentinel-1 (CYMS, <https://www.esa-cyms.org>, accessed on 20 March 2021), which is aiming to extend SAR acquisitions to all TC basins and provide real-time ocean surface wind measurements to further demonstrate SAR potential for operational TC forecasting. This new program, motivated in large part by the results obtained in RNR-CYC, will further develop understanding of the impact of TCs on the earth system, and likely open new scientific applications of SAR measurements.

Author Contributions: Conceptualization O.B. and G.B.; software, C.B., S.B., P.T., J.P., J.C. and F.C.; data acquisition and processing, O.B., G.B., E.C., E.R., R.C., G.R., J.D., A.M. (Alexis Mouche), R.H., S.C., E.L., D.M. and N.M.; writing—original draft preparation, O.B., G.B., E.C., R.C., E.R., G.R. and C.B.; writing—review and editing, all co-authors; supervision, O.B.; project administration, O.B.; funding acquisition, O.B., P.T. All authors have read and agreed to the published version of the manuscript.

Funding: This research was principally funded by the European Union, the Regional Council of Réunion Island, and the French State through INTERREG-V Océan Indien 2014–2020 projects “ReNovRisk-Cyclones and Climate Change” (TF) and “ReNovRisk Cyclones and Precipitation” (TF), as well as by Université de La Réunion and Centre National de la Recherche Scientifique (CNRS) in the frame of the “Contrat Plan Etat Région” (CPER) “ReNovRisk”. The gliders were provided, operated, and co-funded by CNRS DT-INSU (Direction Technique—Institut National des Sciences de l'Univers). The seismic stations deployed in the “Rivière des Pluies” network (code ZF) were provided by the INSU-RESIF/SISMOB instrumental pool. The provision and operating of the BOREAL UAS were co-funded by Météo-France. The installation of GNSS stations on Eparses islands was funded by the Eparses consortium of the Terres Australes et Antarctiques Françaises (TAAF) administration under the frame of project “IOGA4MET-EI”. Part of the STORM operations were also co-funded by CNRS-INSU under the frame of the LEFE project “PreSTORM”. Access to RADARSAT-2 data was supported by Institut Mines Télécom and by public funds (Ministère de l'Education Nationale, de l'Enseignement Supérieur et de la Recherche, FEDER, Région Bretagne, Conseil Général du Finistère, Brest Métropole) received in the framework of the VIGISAT project managed by Groupement Bretagne Télédétection (GIS BreTel – Brittany Remote Sensing).

Institutional Review Board Statement: All sea turtles equipped in this programme were handled by qualified and officially accredited personnel from Kelonia's care center. The used tags meet all

the requirements of the international conventions for the protection of sea turtles and were directly purchased from manufacturers specializing in marine biology and biologging.

Informed Consent Statement: Informed consent was obtained from all subjects involved in the study.

Data Availability Statement: Some of the data used in this study are available in public repositories: <https://scihub.copernicus.eu/> and <https://cycloblogs.ifremer.fr/> (S1 and RS2 SAR data); http://www.meteo.fr/temps/domtom/La_Reunion/webcmrs9.0/anglais/index.htm (best-track data); <ftp://rgpdata.ign.fr/pub/gnssmayotte> (GNSS data); <http://seismology.resif.fr/> (seismic data—FDSN network codes PF and ZF), accessed on 20 March 2021. Other data used in this study are not yet publicly available due to temporary use restrictions by data owners (these data, available on request from the corresponding author, will be soon deposited in the project’s data repository).

Acknowledgments: The authors are grateful to the numerous students, researchers, and engineers who participated in the field phase of the project, as well as to the staff of IGN, for processing GNSS data, Kelonia and Centre d’Etude et de Découverte des Tortues Marines (CEDTM), for equipping sea turtles, CNRS (DT-INSU), for operating the gliders, and Centre National de Recherches Météorologiques (CNRM, Météo-France), for operating the BOREAL UAS. The BOREAL UAS had been developed in the MIRIAD project (Système de Mesures scientifiques de flux de surface en milieu maritime embarqué sur Drone), financed by the European Union and the Occitanie Region. The SHOC initiative has been possible thanks to SAR data access supported by the ESA Sentinel-1 mission ground segment team and GIS BreTel. Sentinel-1 is part of the European space component of Copernicus European program. RADARSAT-2 is a commercial mission and data were provided by MDA’s Geospatial Services (<https://mdacorporation.com/geospatial/international> (accessed on 18 April 2021)). We are grateful to the OVPF (Observatoire Volcanologique du Piton de la Fournaise) and to IGP colleagues who maintain the PF seismic stations and to F.R. Fontaine, E. Delcher, and A. Gonzalez for the Riviere des Pluies seismic data acquisition (<http://dx.doi.org/10.15778/RESIF.ZF2015>, accessed on 20 March 2021). We would also like to warmly thank Mayeul Dalleau (CEDM) for his important contribution in the design of the STORM sub-programme, and Navalona Ravoson (Université d’Antananarivo), for contributing to seismic data analysis. Finally, we would also like to express our warmest thanks to Mrs Sandrine Prunier and Nina Breznik, who successfully ensured the administrative management of this project.

Conflicts of Interest: The authors declare no conflict of interest.

References

- Jiang, H.; Oyama, R.; Bousquet, O.; Vigh, J.; Huang, Y.-H.; Smith, R.; Corbosiero, K.L.; Hendricks, E.; Kepert, J.D.; Miyamoto, Y.; et al. A Review of Tropical Cyclone Intensity Change (2014–2018). Part II: Rapid Intensification via Internal Influences. *Atmosphere* **2021**. Submitted.
- Vigh, J.L.; Huang, Y.-H.; Miyamoto, Y.; Li, Q. A Review of Intensity Change (2014–2018). Part III: Internal Influences. *J. Meteorol. Soc. Jan.* **2021**. Submitted.
- Courtney, J.B.; Langlade, S.; Barlow, S.; Birchard, T.; Knaff, J.A.; Kotal, S.; Kriat, T.; Lee, W.; Pasch, R.; Sampson, C.R.; et al. Operational perspectives on tropical cyclone intensity change Part 2: Forecasts by operational agencies. *Trop. Cyclone Res. Rev.* **2019**, *8*, 226–239. [[CrossRef](#)]
- Heming, J.; Prates, F.; Bender, M.A.; Bowyer, R.; Cangialosi, J.; Caroff, P.; Coleman, T.; Doyle, D.J.; Dube, A.; Faure, G.; et al. Review of recent progress in tropical cyclone track forecasting and expression of uncertainties. *Trop. Cyclone Res. Rev.* **2019**, *8*, 181–218. [[CrossRef](#)]
- Yablonsky, R.M. Ocean Component of the HWRF Coupled Model and Model Evaluation. In *Advanced Numerical Modeling and Data Assimilation Techniques for Tropical Cyclone Prediction*; Mohanty, U.C., Gopalakrishnan, S.G., Eds.; Springer: Dordrecht, The Netherlands, 2016. [[CrossRef](#)]
- Mogensen, K.S.; Magnusson, L.; Bidlot, J.-R. Tropical cyclone sensitivity to ocean coupling in the ECMWF coupled model. *J. Geophys. Res. Oceans* **2017**, *122*, 4392–4412. [[CrossRef](#)]
- Feng, X.; Klingaman, N.P.; Hodges, K.I. The effect of atmosphere–ocean coupling on the prediction of 2016 western North Pacific tropical cyclones. *Q. J. R. Meteorol. Soc.* **2019**, *145*, 2425–2444. [[CrossRef](#)]
- Vellinga, M.; Copsey, D.; Graham, T.; Milton, S.; Johns, T. Evaluating Benefits of Two-Way Ocean–Atmosphere Coupling for Global NWP Forecasts. *Weather Forecast.* **2020**, *35*, 2127–2144. [[CrossRef](#)]
- Bousquet, O.; Dalleau, M.; Bocquet, M.; Gaspar, P.; Bielli, S.; Ciccione, S.; Remy, E.; Vidard, A. Sea Turtles for Ocean Research and Monitoring: Overview and Initial Results of the STORM Project in the Southwest Indian Ocean. *Front. Mar. Sci.* **2020**, *7*, 859. [[CrossRef](#)]

10. Leroux, M.-D.; Wood, K.; Elsberry, R.L.; Cayan, E.O.; Hendricks, E.; Kucas, M.; Otto, P.; Rogers, R.; Sampson, B.; Yu, Z. Recent Advances in Research and Forecasting of Tropical Cyclone Track, Intensity, and Structure at Landfall. *Trop. Cyclone Res. Rev.* **2019**, *7*, 85–105. [[CrossRef](#)]
11. Pianezze, J.; Barthe, C.; Bielli, S.; Tulet, P.; Jullien, S.; Cambon, G.; Bousquet, O.; Claeys, M.; Cordier, E. A New Coupled Ocean-Waves-Atmosphere Model Designed for Tropical Storm Studies: Example of Tropical Cyclone Bejisa (2013–2014) in the South-West Indian Ocean. *J. Adv. Model. Earth Syst.* **2018**, *10*, 801–825. [[CrossRef](#)]
12. Pant, V.; Prakash, K.R. Response of Air–Sea Fluxes and Oceanic Features to the Coupling of Ocean–Atmosphere–Wave during the Passage of a Tropical Cyclone. *Pure Appl. Geophys. Pageoph.* **2020**, *177*, 3999–4023. [[CrossRef](#)]
13. Prakash, K.R.; Pant, V.; Nigam, T. Effects of the sea surface roughness and sea spray-induced flux parameterization on the simulations of a tropical cyclone. *J. Geophys. Res. Atmos.* **2019**, *124*, 14037–14058. [[CrossRef](#)]
14. Mavume, A.F.; Rydberg, L.; Lutjeharms, J.R.E. Climatology of tropical cyclones in the South-West Indian Ocean; landfall in Mozambique and Madagascar. *West. Indian Ocean J. Mar. Sci.* **2008**, *8*, 15–36.
15. Matyas, C.J. Formation and movement of tropical cyclones in the Mozambique channel. *Int. J. Clim.* **2014**, *35*, 375–390. [[CrossRef](#)]
16. Leroux, M.-D.; Meister, J.; Mekies, D.; Dorla, A.-L.; Caroff, P. A Climatology of Southwest Indian Ocean Tropical Systems: Their Number, Tracks, Impacts, Sizes, Empirical Maximum Potential Intensity, and Intensity Changes. *J. Appl. Meteorol. Clim.* **2018**, *57*, 1021–1041. [[CrossRef](#)]
17. Vialard, J.; Foltz, G.R.; McPhaden, M.J.; Duvel, J.-P.; Montégut, C.D.B. Strong Indian Ocean sea surface temperature signals associated with the Madden-Julian Oscillation in late 2007 and early 2008. *Geophys. Res. Lett.* **2008**, *35*, L19608. [[CrossRef](#)]
18. Hermes, J.C.; Reason, C.J.C. The sensitivity of the Seychelles–Chagos thermocline ridge to large-scale wind anomalies. *ICES J. Mar. Sci.* **2009**, *66*, 1455–1466. [[CrossRef](#)]
19. Yokoi, T.; Tozuka, T.; Yamagata, T. Seasonal Variation of the Seychelles Dome. *J. Clim.* **2008**, *21*, 3740–3754. [[CrossRef](#)]
20. Mawren, D.; Hermes, J.; Reason, C.J.C. Exceptional Tropical Cyclone Kenneth in the Far Northern Mozambique Channel and Ocean Eddy Influences. *Geophys. Res. Lett.* **2020**, *47*, e2020GL088715. [[CrossRef](#)]
21. Emerton, R.; Cloke, H.; Ficchi, A.; Hawker, L.; de Wit, S.; Speight, L.; Prudhomme, C.; Rundell, P.; West, R.; Neal, J.; et al. Emergency flood bulletins for Cyclones Idai and Kenneth: A critical evaluation of the use of global flood forecasts for international humanitarian preparedness and response. *Int. J. Disaster Risk Reduct.* **2020**, *50*, 101811. [[CrossRef](#)]
22. Matera, M. World Bank’s Cyclone IDAI & Kenneth Emergency Recovery and Resilience Project 171040. 2019. Available online: <http://documents1.worldbank.org/curated/en/727131568020768626/pdf/Project-Information-Documents-Mozambique-Cyclone-Idai-Kenneth-Emergency-Recovery-and-Resilience-Project-P171040.pdf> (accessed on 21 April 2021).
23. Tulet, P.; Aunay, B.; Barruol, G.; Barthe, C.; Belon, R.; Bielli, S.; Bonnardot, F.; Bousquet, O.; Cammas, J.-P.; Cattiaux, J.; et al. ReNovRisk: A multidisciplinary programme to study the cyclonic risks in the South-West Indian Ocean. *Nat. Hazards* **2021**, 1–33. [[CrossRef](#)]
24. Sharmila, S.; Walsh, K.J.E. Recent poleward shift of tropical cyclone formation linked to Hadley cell expansion. *Nat. Clim. Chang.* **2018**, *8*, 730–736. [[CrossRef](#)]
25. Camargo, S.J.; Wing, A.A. Increased tropical cyclone risk to coasts. *Science* **2021**, *371*, 458–459. [[CrossRef](#)]
26. Seidel, D.J.; Fu, Q.; Randel, W.J.; Reichler, T.J. Widening of the tropical belt in a changing climate. *Nat. Geosci.* **2008**, *1*, 21–24. [[CrossRef](#)]
27. Yang, H.; Lohmann, G.; Lu, J.; Gowan, E.J.; Shi, X.; Liu, J.; Wang, Q. Tropical Expansion Driven by Poleward Advancing Midlatitude Meridional Temperature Gradients. *J. Geophys. Res. Atmos.* **2020**, *125*, 033158. [[CrossRef](#)]
28. Kossin, J.P.; Emanuel, K.A.; Vecchi, G.A. The poleward migration of the location of tropical cyclone maximum intensity. *Nat. Cell Biol.* **2014**, *509*, 349–352. [[CrossRef](#)]
29. Kossin, J.P.; Emanuel, K.A.; Camargo, S.J. Past and Projected Changes in Western North Pacific Tropical Cyclone Exposure. *J. Clim.* **2016**, *29*, 5725–5739. [[CrossRef](#)]
30. Sun, J.; Wang, D.; Hu, X.; Ling, Z.; Wang, L. Ongoing Poleward Migration of Tropical Cyclone Occurrence Over the Western North Pacific Ocean. *Geophys. Res. Lett.* **2019**, *46*, 9110–9117. [[CrossRef](#)]
31. Krupar, R.J.; Smith, D.J. Poleward Migration of Tropical Cyclone Activity in the Southern Hemisphere: Perspectives and Challenges for the Built Environment in Australia. In *Hurricane Risk*; Collins, J., Walsh, K., Eds.; Springer: Cham, Switzerland, 2019; Volume 1. [[CrossRef](#)]
32. Cattiaux, J.; Chauvin, F.; Bousquet, O.; Malardel, S.; Tsai, C.-L. Projected Changes in the Southern Indian Ocean Cyclone Activity Assessed from High-Resolution Experiments and CMIP5 Models. *J. Clim.* **2020**, *33*, 4975–4991. [[CrossRef](#)]
33. Barthe, C.; Bousquet, O.; Bielli, S.; Tulet, P.; Pianezze, J.; Claeys, M.; Tsai, C.-L.; Thompson, C.; Bonnardot, F.; Chauvin, F.; et al. Impact of tropical cyclones on inhabited areas of the SWIO basin at present and future horizons. Part 2: Modelling component of the research program RENOVIRISK-CYCLONE. *Atmosphere* **2021**. submitted to this Special Issue.
34. Bousquet, O.; Lees, E.; Durand, J.; Peltier, A.; Duret, A.; Mekies, D.; Boissier, P.; Donal, T.; Fleischer-Dogley, F.; Zakariasy, L. Densification of the Ground-Based GNSS Observation Network in the South-west Indian Ocean: Current Status, Perspectives, and Examples of Applications in Meteorology and Geodesy. *Front. Earth Sci.* **2020**, *8*, 609757. [[CrossRef](#)]
35. Lees, E.; Bousquet, O.; Roy, D.; De Bellevue, J.L. Analysis of diurnal to seasonal variability of Integrated Water Vapour in the South Indian Ocean basin using ground-based GNSS and fifth-generation ECMWF reanalysis (ERA5) data. *Q. J. R. Meteorol. Soc.* **2021**, *147*, 229–248. [[CrossRef](#)]

36. Cesca, S.; Letort, J.; Razafindrakoto, H.N.T.; Heimann, S.; Rivalta, E.; Isken, M.P.; Nikkhoo, M.; Passarelli, L.; Petersen, G.M.; Cotton, F.; et al. Drainage of a deep magma reservoir near Mayotte inferred from seismicity and deformation. *Nat. Geosci.* **2020**, *13*, 87–93. [[CrossRef](#)]
37. Davy, C.; Barruol, G.; Fontaine, F.R.; Sigloch, K.; Stutzmann, E. Tracking major storms from microseismic and hydroacoustic observations on the seafloor. *Geophys. Res. Lett.* **2014**, *41*, 8825–8831. [[CrossRef](#)]
38. Davy, C.; Barruol, G.; Fontaine, F.; Cordier, E. Analyses of extreme swell events on La Réunion Island from microseismic noise. *Geophys. J. Int.* **2016**, *207*, 1767–1782. [[CrossRef](#)]
39. Barruol, G.; Davy, C.; Fontaine, F.R.; Schlindwein, V.; Sigloch, K. Monitoring austral and cyclonic swells in the “Iles Eparses” (Mozambique channel) from microseismic noise. *Acta Oecologica* **2016**, *72*, 120–128. [[CrossRef](#)]
40. Rindraharisaona, E.J.; Cordier, E.; Barruol, G.; Fontaine, F.R.; Singh, M. Assessing swells in La Réunion Island from terrestrial seismic observations, oceanographic records and offshore wave models. *Geophys. J. Int.* **2020**, *221*, 1883–1895. [[CrossRef](#)]
41. Rindraharisaona, E.J.; Barruol, G.; Cordier, E.; Fontaine, F. and Gonzales, A.. Inferring cyclone signatures in the South-West of Indian Ocean from microseismic noise recorded on Réunion island. *Atmosphere* **2021**, *12*, 488. [[CrossRef](#)]
42. Bousquet, O.; Barbary, D.; Bielli, S.; Kebir, S.; Raynaud, L.; Malardel, S.; Faure, G. An evaluation of tropical cyclone forecast in the Southwest Indian Ocean basin with AROME-Indian Ocean convection-permitting numerical weather predicting system. *Atmos. Sci. Lett.* **2020**, *21*, e950. [[CrossRef](#)]
43. Hsiao, L.-F.; Chen, D.-S.; Hong, J.-S.; Yeh, T.-C.; Fong, C.-T. Improvement of the Numerical Tropical Cyclone Prediction System at the Central Weather Bureau of Taiwan: TWRF (Typhoon WRF). *Atmosphere* **2020**, *11*, 657. [[CrossRef](#)]
44. Takeuchi, Y. An Introduction of Advanced Technology for Tropical Cyclone Observation, Analysis and Forecast in JMA. *Trop. Cyclone Res. Rev.* **2019**, *7*, 153–163. [[CrossRef](#)]
45. Mehra, A.; Tallapragada, V.; Zhang, Z.; Liu, B.; Zhu, L.; Wang, W.; Kim, H.S. Advancing the State of the Art in Operational Tropical Cyclone Fore-casting at NCEP. *Trop. Cyclone Res. Rev.* **2018**, *7*, 51–56. [[CrossRef](#)]
46. Davidson, N.E.; Xiao, Y.; Ma, Y.; Weber, H.C.; Sun, X.; Rikus, L.J.; Kepert, J.D.; Steinle, P.X.; Dietachmayer, G.S.; Lok, C.C.F.; et al. ACCESS-TC: Vortex Specification, 4DVAR Initialization, Verification, and Structure Diagnostics. *Mon. Weather Rev.* **2014**, *142*, 1265–1289. [[CrossRef](#)]
47. Bender, M.A.; Ginis, I. Real-case simulations of hurricane-ocean interaction using a high-resolution coupled model: Effects on hurricane intensity. *Mon. Weather Rev.* **2000**, *128*, 917–946. [[CrossRef](#)]
48. Black, W.J.; Dickey, T.D. Observations and analyses of upper ocean responses to tropical storms and hurricanes in the vicinity of Bermuda. *J. Geophys. Res. Space Phys.* **2008**, *113*, 08009. [[CrossRef](#)]
49. Price, J.F. Upper ocean response to a hurricane. *J. Phys. Ocean.* **1981**, *11*, 153–175. [[CrossRef](#)]
50. Jullien, S.; Marchesiello, P.; Menkes, C.E.; Lefèvre, J.; Jourdain, N.C.; Samson, G.; Lengaigne, M. Ocean feedback to tropical cyclones: Climatology and processes. *Clim. Dyn.* **2014**, *43*, 2831–2854. [[CrossRef](#)]
51. Smith, R.K.; Montgomery, M.T.; Van Sang, N. Tropical cyclone spin-up revisited. *Q. J. R. Meteorol. Soc.* **2009**, *135*, 1321–1335. [[CrossRef](#)]
52. Andreas, E.L. Spray Stress Revisited. *J. Phys. Oceanogr.* **2004**, *34*, 1429–1440. [[CrossRef](#)]
53. Doyle, J.D. Coupled Atmosphere–Ocean Wave Simulations under High Wind Conditions. *Mon. Weather Rev.* **2002**, *130*, 3087–3099. [[CrossRef](#)]
54. Andreas, E.L.; Edson, J.B.; Monahan, E.C.; Rouault, M.P.; Smith, S.D. The spray contribution to net evaporation from the sea: A review of recent progress. *Boundary-Layer Meteorol.* **1995**, *72*, 3–52. [[CrossRef](#)]
55. Wang, Y.; Kepert, J.D.; Holland, G.J. The Effect of Sea Spray Evaporation on Tropical Cyclone Boundary Layer Structure and Intensity*. *Mon. Weather Rev.* **2001**, *129*, 2481–2500. [[CrossRef](#)]
56. Liu, B.; Liu, H.; Xie, L.; Guan, C.; Zhao, D. A Coupled Atmosphere–Wave–Ocean Modeling System: Simulation of the Intensity of an Idealized Tropical Cyclone. *Mon. Weather Rev.* **2011**, *139*, 132–152. [[CrossRef](#)]
57. Richter, D.H.; Stern, D.P. Evidence of spray-mediated air-sea enthalpy flux within tropical cyclones. *Geophys. Res. Lett.* **2014**, *41*, 2997–3003. [[CrossRef](#)]
58. Andreas, E.L.; Mahrt, L.; Vickers, D. An improved bulk air-sea surface flux algorithm, including spray-mediated transfer. *Q. J. R. Meteorol. Soc.* **2015**, *141*, 642–654. [[CrossRef](#)]
59. Ovadnevaite, J.; Manders, A.; De Leeuw, G.; Ceburnis, D.; Monahan, C.; Partanen, A.-I.; Korhonen, H.; O’Dowd, C.D. A sea spray aerosol flux parameterization encapsulating wave state. *Atmos. Chem. Phys. Discuss.* **2014**, *14*, 1837–1852. [[CrossRef](#)]
60. Willoughby, H.; Jin, H.-L.; Lord, S.J.; Piotrowicz, J.M. Hurricane structure and evolution as simulated by an ax-isymmetric, nonhydrostatic numerical model. *J. Atmos. Sci.* **1984**, *41*, 1169–1186. [[CrossRef](#)]
61. Lord, S.J.; Willoughby, H.E.; Piotrowicz, J.M. Role of a parameterized ice-phase microphysics in an axisymmetric, nonhydrostatic tropical cyclone model. *J. Atmos. Sci.* **1984**, *41*, 2836–2848. [[CrossRef](#)]
62. Wang, Y. An Explicit Simulation of Tropical Cyclones with a Triply Nested Movable Mesh Primitive Equation Model: TCM3. Part II: Model Refinements and Sensitivity to Cloud Microphysics Parameterization*. *Mon. Weather Rev.* **2002**, *130*, 3022–3036. [[CrossRef](#)]
63. Zhu, T.; Zhang, D.-L. Numerical Simulation of Hurricane Bonnie (1998). Part II: Sensitivity to Varying Cloud Microphysical Processes. *J. Atmos. Sci.* **2006**, *63*, 109–126. [[CrossRef](#)]

64. Li, J.; Wang, G.; Lin, W.; He, Q.; Feng, Y.; Mao, J. Cloud-scale simulation study of Typhoon Hagupit (2008) Part II: Impact of cloud microphysical latent heat processes on typhoon intensity. *Atmos. Res.* **2013**, *120*, 202–215. [[CrossRef](#)]
65. Hoarau, T.; Barthe, C.; Tulet, P.; Claeys, M.; Pinty, J.-P.; Bousquet, O.; Delanoë, J.; Vié, B. Impact of the Generation and Activation of Sea Salt Aerosols on the Evolution of Tropical Cyclone Dumile. *J. Geophys. Res. Atmos.* **2018**, *123*, 8813–8831. [[CrossRef](#)]
66. Bielli, S.; Barthe, C.; Bousquet, O.; Tulet, P.; Pianezze, J. The effect of atmosphere-ocean coupling on the structure and intensity of tropical cyclone Bejisa observed in the southwest Indian ocean. *Atmosphere* **2021**. submitted to this Special Issue.
67. Thompson, C.; Barthe, C.; Bielli, S.; Tulet, P.; Pianezze, J. Projected Characteristic Changes of a Typical Tropical Cyclone under Climate Change in the South West Indian Ocean. *Atmosphere* **2021**, *12*, 232, (this Special Issue). [[CrossRef](#)]
68. Ferrario, F.; Beck, M.W.; Storlazzi, C.D.; Micheli, F.; Shepard, C.C.; Airoidi, L. The effectiveness of coral reefs for coastal hazard risk reduction and adaptation. *Nat. Commun.* **2014**, *5*, 3794. [[CrossRef](#)]
69. Lowe, R.J.; Falter, J.L.; Bandet, M.D.; Pawlak, G.; Atkinson, M.J.; Monismith, S.G.; Koseff, J.R. Spectral wave dissipation over a barrier reef. *J. Geophys. Res. Space Phys.* **2005**, *110*, 04001. [[CrossRef](#)]
70. van Dongeren, A.; Storlazzi, C.D.; Quataert, E.; Pearson, S. Wave dynamics and flooding on low-lying tropical reef-lined coasts. In Proceedings of the Coastal Dynamics, Helsingor, Denmark, 12–16 June 2017; pp. 654–664.
71. Pomeroy, A.; Lowe, R.J.; Symonds, G.; Van Dongeren, A.; Moore, C. The dynamics of infragravity wave transformation over a fringing reef. *J. Geophys. Res. Space Phys.* **2012**, *117*, 11022. [[CrossRef](#)]
72. Baldock, T.; Golshani, A.; Callaghan, D.; Saunders, M.; Mumby, P. Impact of sea-level rise and coral mortality on the wave dynamics and wave forces on barrier reefs. *Mar. Pollut. Bull.* **2014**, *83*, 155–164. [[CrossRef](#)] [[PubMed](#)]
73. Nortek. Wave Measurements Using the PUV Method, TN-19. Doc. No. N4000-720, Nortek AS. 2002. Available online: <http://www.nortek-es.com/lib/technical-notes/puv-wave-measurement> (accessed on 20 March 2021).
74. Hom-Ma, M.; Horikawa, K.; Komori, S. Response Characteristics of Underwater Wave Gauge. *Coast. Eng. Jpn.* **1966**, *9*, 45–54. [[CrossRef](#)]
75. Pomeroy, A.W.M.; Lowe, R.J.; Ghisalberti, M.; Winter, G.; Storlazzi, C.; Cuttler, M. Spatial Variability of Sediment Transport Processes Over Intratidal and Subtidal Timescales Within a Fringing Coral Reef System. *J. Geophys. Res. Earth Surf.* **2018**, *123*, 1013–1034. [[CrossRef](#)]
76. Smithers, S.G.; Hoeke, R.K. Geomorphological impacts of high-latitude storm waves on low-latitude reef is-lands—observations of the December 2008 event on Nukutoa, Takuu, Papua New Guinea. *Geomorphology* **2014**, *222*, 106–121. [[CrossRef](#)]
77. Hoeke, R.K.; McInnes, K.L.; O’Grady, J.G. Wind and Wave Setup Contributions to Extreme Sea Levels at a Tropical High Island: A Stochastic Cyclone Simulation Study for Apia, Samoa. *J. Mar. Sci. Eng.* **2015**, *3*, 1117–1135. [[CrossRef](#)]
78. Friedrich, A.; Krüger, F.; Klinge, K. Ocean-generated microseismic noise located with the Gräfenberg array. *J. Seismol.* **1998**, *2*, 47–64. [[CrossRef](#)]
79. Longuet-Higgins, M.S. A theory of the origin of the microseisms. *Phil. Trans. Roy. Soc.* **1950**, *243*, 1–35.
80. Arduin, F.; Gualtieri, L.; Stutzmann, E. How ocean waves rock the Earth: Two mechanisms explain microseisms with periods 3 to 300 s. *Geophys. Res. Lett.* **2015**, *42*, 765–772. [[CrossRef](#)]
81. Barruol, G.; Reymond, D.; Fontaine, F.R.; Hyvernaud, O.; Maurer, V.; Maamaatuaiahutapu, K. Characterizing swells in the southern Pacific from seismic and infrasonic noise analyses. *Geophys. J. Int.* **2006**, *164*, 516–542. [[CrossRef](#)]
82. Cessaro, R.K. Sources of primary and secondary microseisms. *Bull. Seismol. Soc. Am.* **1994**, *84*, 142–148.
83. Hasselmann, K. A statistical analysis of the generation of microseisms. *Rev. Geophys.* **1963**, *1*, 177–210. [[CrossRef](#)]
84. Arduin, F.; Stutzmann, E.; Schimmel, M.; Mangeney, A. Ocean wave sources of seismic noise. *J. Geophys. Res. Space Phys.* **2011**, *116*, 09004. [[CrossRef](#)]
85. Essen, H.-H.; Krüger, F.; Dahm, T.; Grevemeyer, I. On the generation of secondary microseisms observed in northern and central Europe. *J. Geophys. Res. Space Phys.* **2003**, *108*, 2506. [[CrossRef](#)]
86. Obrebski, M.; Arduin, F.; Stutzmann, E.; Schimmel, M. How moderate sea states can generate loud seismic noise in the deep ocean. *Geophys. Res. Lett.* **2012**, *39*, 11601. [[CrossRef](#)]
87. Davy, C.; Stutzmann, E.; Barruol, G.; Fontaine, F.; Schimmel, M. Sources of secondary microseisms in the Indian Ocean. *Geophys. J. Int.* **2015**, *202*, 1180–1189. [[CrossRef](#)]
88. Reading, A.M.; Koper, K.D.; Gal, M.; Graham, L.S.; Tkalčić, H.; Hemer, M.A. Dominant seismic noise sources in the Southern Ocean and West Pacific, 2000–2012, recorded at the Warramunga Seismic Array, Australia. *Geophys. Res. Lett.* **2014**, *41*, 3455–3463. [[CrossRef](#)]
89. Beucler, É.; Mocquet, A.; Schimmel, M.; Chevrot, S.; Quillard, O.; Vergne, J.; Sylvander, M. Observation of deep water microseisms in the North Atlantic Ocean using tide modulations. *Geophys. Res. Lett.* **2015**, *42*, 316–322. [[CrossRef](#)]
90. Bromirski, P.D. The near-coastal microseism spectrum: Spatial and temporal wave climate relationships. *J. Geophys. Res. Space Phys.* **2002**, *107*, ESE 5-1–ESE 5-20. [[CrossRef](#)]
91. Bromirski, P.D.; Duennebier, F.K.; Stephen, R.A. Mid-ocean microseisms. *Geochem. Geophys. Geosystems* **2005**, *6*, Q04009. [[CrossRef](#)]
92. Chevrot, S.; Sylvander, M.; Benahmed, S.; Ponsolles, C.; Lefèvre, J.M.; Paradis, D. Source locations of secondary microseisms in western Europe: Evidence for both coastal and pelagic sources. *J. Geophys. Res. Space Phys.* **2007**, *112*, B11301. [[CrossRef](#)]
93. Koper, K.D.; Buriaciu, R. The fine structure of double-frequency microseisms recorded by seismometers in North America. *J. Geophys. Res.* **2015**, *120*, 1677–1691. [[CrossRef](#)]

94. Tolman, H.L.; Chalikov, D.V. Source terms in a third-generation wind wave model. *J. Phys. Oceanogr.* **1996**, *26*, 2497–2518. [[CrossRef](#)]
95. Tolman, H.L. Distributed-memory concepts in the wave model WAVEWATCH III. *Parallel Comput.* **2002**, *28*, 35–52. [[CrossRef](#)]
96. Perez, J.; Menendez, M.; Losada, I.J. GOW2: A global wave hindcast for coastal applications. *Coast. Eng.* **2017**, *124*, 1–11. [[CrossRef](#)]
97. Hasselmann, K.; Barnett, T.; Bouws, E.; Carlson, H.; Cartwright, D.E.; Eake, K. *Measurements of Wind-Wave Growth and Swell Decay during the Joint North Sea Wave Project (JONSWAP)*; Deutsches Hydrographisches Institute: Hamburg, Germany, 1973.
98. Harris, L.R.; Nel, R.; Oosthuizen, H.; Meyer, M.; Kotze, D.; Anders, D.; McCue, S.; Bachoo, S. Managing conflicts between economic activities and threatened migratory marine species toward creating a multiobjective blue economy. *Conserv. Biol.* **2017**, *32*, 411–423. [[CrossRef](#)]
99. Swart, N.C.; Lutjeharms, J.R.E.; Ridderinkhof, H.; De Ruijter, W.P.M. Observed characteristics of Mozambique Channel eddies. *Geophys. Res. Lett.* **2010**, *115*, C09006. [[CrossRef](#)]
100. Lutjeharms. *The Agulhas Current*; Springer: Berlin/Heidelberg, Germany, 2006. [[CrossRef](#)]
101. Lellouche, J.-M.; Greiner, E.; Le Galloudec, O.; Garric, G.; Regnier, C.; Drevillon, M.; Benkiran, M.; Testut, C.-E.; Bourdalle-Badie, R.; Gasparin, F.; et al. Recent updates to the Copernicus Marine Service global ocean monitoring and forecasting real-time 1/12° high-resolution system. *Ocean Sci.* **2018**, *14*, 1093–1126. [[CrossRef](#)]
102. Cuyppers, Y.; Le Vaillant, X.; Bourruet-Aubertot, P.; Vialard, J.; McPhaden, M.J. Tropical storm-induced near-inertial internal waves during the Cirene experiment: Energy fluxes and impact on vertical mixing. *J. Geophys. Res. Oceans* **2013**, *118*, 358–380. [[CrossRef](#)]
103. Vialard, J.; Duvel, J.; McPhaden, M.; Bourruet-Aubertot, P.; Ward, P.; Key, E.; Bourras, D.; Weller, R.; Minnett, P.J.; Weill, A.; et al. Cirene: Air Sea Interactions in the Sey-chelles-Chagos thermocline ridge region. *Bull. Am. Met. Soc.* **2009**, *90*, 45–61. [[CrossRef](#)]
104. Jaimes, B.; Shay, L.K. Mixed Layer Cooling in Mesoscale Oceanic Eddies during Hurricanes Katrina and Rita. *Mon. Weather Rev.* **2009**, *137*, 4188–4207. [[CrossRef](#)]
105. Montégut, C.D.B.; Madec, G.; Fischer, A.S.; Lazar, A.; Iudicone, D. Mixed layer depth over the global ocean: An examination of profile data and a profile-based climatology. *J. Geophys. Res. Space Phys.* **2004**, *109*, 1–20. [[CrossRef](#)]
106. Holte, J.; Talley, L. A New Algorithm for Finding Mixed Layer Depths with Applications to Argo Data and Subantarctic Mode Water Formation*. *J. Atmos. Ocean. Technol.* **2009**, *26*, 1920–1939. [[CrossRef](#)]
107. Tomczak, M.; Godfrey, J.S. *Regional Oceanography—An Introduction*; Butler & Tanner: London, UK, 2001.
108. Pickard, G.L.; Emery, W.J. *Descriptive Physical Oceanography*, 5th ed.; Butterworth-Heinemann: Oxford, UK, 1990.
109. Roberts, G.; Burnet, F.; Barrau, S.; Medina, P.; Durand, P.; Gavard, M. A drone over the oceans: The Miriad project. *Météorologie* **2017**, *98*, 9–10. (In French) [[CrossRef](#)]
110. Bevis, M.; Businger, S.; Herring, T.A.; Rocken, C.; Anthes, R.A.; Ware, R.H. GPS meteorology: Remote sensing of atmospheric water vapor using the global positioning system. *J. Geophys. Res. Space Phys.* **1992**, *97*, 15787–15801. [[CrossRef](#)]
111. Beutler, G.; Rothacher, M.; Schaer, S.; Springer, T.; Kouba, J.; Neilan, R. The International GPS Service (IGS): An interdisciplinary service in support of Earth sciences. *Adv. Space Res.* **1999**, *23*, 631–653. [[CrossRef](#)]
112. Guerova, G.; Jones, J.; Douša, J.; Dick, G.; de Haan, S.; Pottiaux, E.; Bock, O.; Pacione, R.; Elgered, G.; Vedel, H.; et al. Review of the state of the art and future prospects of the ground-based GNSS meteorology in Europe. *Atmos. Meas. Tech.* **2016**, *9*, 5385–5406. [[CrossRef](#)]
113. Dvorak, V.F. Tropical Cyclone Intensity Analysis and Forecasting from Satellite Imagery. *Mon. Weather Rev.* **1975**, *103*, 420–430. [[CrossRef](#)]
114. Brennan, M.J.; Hennon, C.C.; Knabb, R.D. The Operational Use of QuikSCAT Ocean Surface Vector Winds at the National Hurricane Center. *Weather Forecast* **2009**, *24*, 621–645. [[CrossRef](#)]
115. Chou, K.-H.; Wu, C.-C.; Lin, S.-Z. Assessment of the ASCAT wind error characteristics by global dropwindsonde observations. *J. Geophys. Res. Atmos.* **2013**, *118*, 9011–9021. [[CrossRef](#)]
116. Mai, M.; Zhang, B.; Li, X.; Hwang, P.A.; Zhang, J.A. Application of AMSR-E and AMSR2 Low-Frequency Channel Brightness Temperature Data for Hurricane Wind Retrievals. *IEEE Trans. Geosci. Remote. Sens.* **2016**, *54*, 4501–4512. [[CrossRef](#)]
117. Zhang, L.; Yin, X.-B.; Shi, H.-Q.; Wang, Z.-Z. Hurricane Wind Speed Estimation Using WindSat 6 and 10 GHz Brightness Temperatures. *Remote. Sens.* **2016**, *8*, 721. [[CrossRef](#)]
118. Reul, N.; Chapron, B.; Zabolotskikh, E.; Donlon, C.; Mouche, A.; Tenerelli, J.; Collard, F.; Piolle, J.-F.; Fore, A.; Yueh, S.; et al. A New Generation of Tropical Cyclone Size Measurements from Space. *Bull. Am. Meteorol. Soc.* **2017**, *98*, 2367–2385. [[CrossRef](#)]
119. Monserrat, O.; Crosetto, M.; Luzi, G. A review of ground-based SAR interferometry for deformation measurement. *ISPRS J. Photogramm. Remote. Sens.* **2014**, *93*, 40–48. [[CrossRef](#)]
120. Fu, L.; Holt, B. *SEASAT Views Oceans and Sea Ice with Synthetic Aperture Radar*; NASA JPL Publ.: La Cañada Flintridge, CA, USA, 1982; pp. 81–120. Available online: https://earth.esa.int/documents/10174/1020083/Seasat_views_Oceans_Sea_Ice_with_SAR.pdf (accessed on 20 March 2021).
121. Li, X.; Zhang, J.A.; Yang, X.; Pichel, W.G.; DeMaria, M.; Long, D.; Li, Z. Tropical Cyclone Morphology from Spaceborne Synthetic Aperture Radar. *Bull. Am. Meteorol. Soc.* **2013**, *94*, 215–230. [[CrossRef](#)]
122. Young, G.; Sikora, T.; Winstead, N. Mesoscale Near-Surface Wind Speed Variability Mapping with Synthetic Aperture Radar. *Sensors* **2008**, *8*, 7012–7034. [[CrossRef](#)]

123. Zhang, B.; Perrie, W. Cross-Polarized Synthetic Aperture Radar: A New Potential Measurement Technique for Hurricanes. *Bull. Am. Meteorol. Soc.* **2012**, *93*, 531–541. [[CrossRef](#)]
124. Mouche, A.; Chapron, B.; Knaff, J.; Zhao, Y.; Zhang, B.; Combot, C. Copolarized and Cross-Polarized SAR Measurements for High-Resolution Description of Major Hurricane Wind Structures: Application to Irma Category 5 Hurricane. *J. Geophys. Res. Oceans* **2019**, *124*, 3905–3922. [[CrossRef](#)]
125. Duong, Q.-P.; Langlade, S.; Payan, C.; Husson, R.; Mouche, A.; Malardel, S. C-band SAR Winds for Tropical Cyclone monitoring and forecast in the South-West Indian Ocean. *Atmosphere* **2021**. accepted pending minor revisions (this Special Issue).
126. Mouche, A.; Chapron, B.; Zhang, B.; Husson, R. Combined co- and cross-polarized SAR measurements under extreme wind conditions. *IEEE Xplore IEEE Trans. Geosci. Remote Sens.* **2017**, *55*, 6476–6755.
127. Sitkowski, M.; Kossin, J.P.; Rozoff, C.M. Intensity and Structure Changes during Hurricane Eyewall Replacement Cycles. *Mon. Weather Rev.* **2011**, *139*, 3829–3847. [[CrossRef](#)]
128. Willoughby, H.; Clos, J.; Shoreibah, M.L. Concentric Eye Walls, Secondary Wind Maxima, and The Evolution of the Hurricane vortex. *J. Atmos. Sci.* **1982**, *39*, 395–411. [[CrossRef](#)]
129. Madec, G.; Bourdallé-Badie, R.; Chanuta, J. *Nemo Ocean Engine. Notes From the Pôle de Modélisation*; Institut Pierre-Simon Laplace: Guyancourt, France, 2019.
130. Barbary, D.; Leroux, M.-D.; Bousquet, O. The orographic effect of Reunion Island on tropical cyclone track and intensity. *Atmos. Sci. Lett.* **2019**, *20*, e882. [[CrossRef](#)]



atmosphere



Article

Cloud Radar Observations of Diurnal and Seasonal Cloudiness over Reunion Island

Jonathan Durand, Edouard Lees, Olivier Bousquet, Julien Delanoë and François Bonnardot



<https://doi.org/10.3390/atmos12070868>

Article

Cloud Radar Observations of Diurnal and Seasonal Cloudiness over Reunion Island

Jonathan Durand ¹, Edouard Lees ¹, Olivier Bousquet ^{1,2,*}, Julien Delanoë ³ and François Bonnardot ⁴

¹ Laboratoire de l'Atmosphère et des Cyclones (UMR8105 LACy), Université de La Réunion, CNRS, Météo-France, 97400 Saint-Denis, France; jonathan.durand@univ-reunion.fr (J.D.); edouard.lees@meteo.fr (E.L.)

² Institute for Coastal Marine Research (CMR), Nelson Mandela University, Port-Elizabeth 6001, South Africa

³ Laboratoire Atmosphère, Milieux et Observations Spatiales (UMR 8190 LATMOS), CNRS/Sorbonne Université/USVQ, 78280 Guyancourt, France; Julien.Delanoë@latmos.ipsl.fr

⁴ Direction Interrégionale de Météo-France pour l'Océan Indien, Saint-Denis, 97490 Sainte-Clotilde, France; francois.bonnardot@meteo.fr

* Correspondence: olivier.bousquet@meteo.fr

Abstract: In November 2016, a 95 GHz cloud radar was permanently deployed in Reunion Island to investigate the vertical distribution of tropical clouds and monitor the temporal variability of cloudiness in the frame of the pan-European research infrastructure Aerosol, Clouds and Trace gases Research InfraStructure (ACTRIS). In the present study, reflectivity observations collected during the two first years of operation (2016–2018) of this vertically pointing cloud radar are relied upon to investigate the diurnal and seasonal cycle of cloudiness in the northern part of this island. During the wet season (December–March), cloudiness is particularly pronounced between 1–3 km above sea level (with a frequency of cloud occurrence of 45% between 12:00–19:00 LST) and 8–12 km (with a frequency of cloud occurrence of 15% between 14:00–19:00 LST). During the dry season (June–September), this bimodal vertical mode is no longer observed and the vertical cloud extension is essentially limited to a height of 3 km due to both the drop-in humidity resulting from the northward migration of the ITCZ and the capping effect of the trade winds inversion. The frequency of cloud occurrence is at its maximum between 13:00–18:00 LST, with a probability of 35% at 15 LST near an altitude of 2 km. The analysis of global navigation satellite system (GNSS)-derived weather data also shows that the diurnal cycle of low- (1–3 km) and mid-to-high level (5–10 km) clouds is strongly correlated with the diurnal evolution of tropospheric humidity, suggesting that additional moisture is advected towards the island by the sea breeze regime. The detailed analysis of cloudiness observations collected during the four seasons sampled in 2017 and 2018 also shows substantial differences between the two years, possibly associated with a strong positive Indian Ocean Southern Dipole (IOSD) event extending throughout the year 2017.

Keywords: cloud radar; BASTA; Indian Ocean Subtropical Dipole; Reunion Island; integrated water vapor; Southwest Indian Ocean; GNSS; cloudiness variability; tropical clouds



Citation: Durand, J.; Lees, E.; Bousquet, O.; Delanoë, J.; Bonnardot, F. Cloud Radar Observations of Diurnal and Seasonal Cloudiness over Reunion Island. *Atmosphere* **2021**, *12*, 868. <https://doi.org/10.3390/atmos12070868>

Academic Editors: Lawrence D. Carey and Filomena Romano

Received: 29 May 2021

Accepted: 29 June 2021

Published: 3 July 2021

Publisher's Note: MDPI stays neutral with regard to jurisdictional claims in published maps and institutional affiliations.



Copyright: © 2021 by the authors. Licensee MDPI, Basel, Switzerland. This article is an open access article distributed under the terms and conditions of the Creative Commons Attribution (CC BY) license (<https://creativecommons.org/licenses/by/4.0/>).

1. Introduction

Because cloudiness plays a major role in distributing the radiative energy available in the atmosphere [1,2], knowledge of cloud properties is crucial for anticipating the impacts of cloud cover and, in particular, low-level cloud feedbacks in climate change projections [3]. A better knowledge of the vertical distribution of clouds is also important for numerical modelling, as errors in the location and vertical structure of clouds, which directly impact the radiative balance, are considered among the main sources of uncertainty in climate and weather numerical weather prediction (NWP) models [4–6].

In the tropics, cloudiness is principally determined by the space–time distribution of the lower-tropospheric moisture, which controls the total water content and buoyancy of

atmospheric parcels. Humidity is essentially driven by the seasonal migration of the Inter-Tropical Convergence Zone (ITCZ), and its associated circulation shifts, as well as by large scale anomalies that influence atmospheric circulation at both intra-seasonal (Madden–Julian Oscillation [7,8]), and interannual (e.g., El Niño Southern Oscillation, Indian Ocean Dipole, Indian Ocean Subtropical Dipole) timescales.

Thanks to their ability to cover vast areas of the globe, spaceborne cloud radars (e.g., CloudSat) have significantly improved our understanding of the spatio-temporal distribution of clouds throughout the planet and are widely considered as one of the most efficient tools to study cloud properties at the global scale [9]. These space-borne observations are nevertheless subject to some limitations, especially at low-level, due to ground (or sea) clutter echoes [10–12] and difficulties to penetrate thick mid-level clouds to observe the low cloud beneath (due to their short wavelength). In this regard, ground-based cloud radars, which feature higher spatio-temporal time resolution than space-borne sensors, are essential to complete (and evaluate) space-borne observations, especially at the local scale [13]. Relatively few studies have however been conducted so far to investigate tropical cloud properties from ground-based cloud radars. Moreover, if one except a few studies conducted from the Atmospheric Radiation Measurement (ARM) Tropical Western Pacific (TWP) sites [14–16], the latter were essentially conducted in the northern hemisphere due to the overall lack of observation facilities available south of the equator. This includes measurements conducted in Niger [17], in the Indian Western Ghats [18], or from the Barbados Cloud Observatory (BCO [19]) to investigate the seasonality and vertical distribution of low-level clouds [20,21]. This lack of observations was further exacerbated in the last few years following the dismantling, in 2013 (Nauru) and 2014 (Darwin and Manus) of the three permanent Pacific ARM TWP sites [22]. As a consequence, the Atmospheric Physics Observatory (OPAR) of Reunion Island, a small (2512 km²) volcanic French overseas territory located in the Southwest Indian Ocean (SWIO), has now become the principal atmospheric research facility in the southern hemisphere.

Due to its location, located both at the edge of the subtropical jet and in the subsidence region of the southern hemisphere Hadley cell, Reunion Island (20.8° S, 55.5° E) is particularly well suited to study tropical and subtropical influences on the general circulation. For this reason, OPAR's instrumentation is principally designed to observe high troposphere—low stratosphere interactions from a unique ensemble of lidars and radiometric sensors deployed at the high-altitude Maïdo observatory [23]. In order to extend cloud and precipitation observation capabilities, a new coastal experimental site was, however, recently integrated to OPAR in the frame of the pan-European research infrastructure “Aerosol, Clouds and Trace gases Research InfraStructure” (ACTRIS, <https://www.actris.eu>, accessed on 1 July 2021), a programme aiming at collecting high-quality observation data to constrain predictive models and improve global forecasts of the atmosphere. This new observation facility, located on the northern coast of the island at Saint-Denis de La Réunion (Figure 1), was notably equipped, in 2016, with a 95 GHz radar BASTA (Bistatic rAdar SysTem for Atmospheric Studies; [24]) to collect cloud observations at high spatial and temporal resolutions. This new site is, in particular, well-adapted to investigate coastal tropical clouds, which are known to occur over different mid-tropospheric conditions than over the open ocean and continental areas due to the combined effects of land–sea breeze interactions [25].

In this study, reflectivity observations collected during the two first years of operation of the cloud radar BASTA are used to investigate the characteristics of cloudiness in Reunion Island as well as its relationship with local and regional tropospheric humidity patterns inferred from radiosounding, Global Navigation Satellite System (GNSS) and high-resolution reanalysis data. Although limited in time, the 2-y cloud radar dataset used in this study allows us to investigate, for the first time in the SWIO, the vertical cloud properties over a remote and climatologically important location of the Southern Hemisphere, which was identified as a key component in the climate system by ACTRIS research infrastructure.

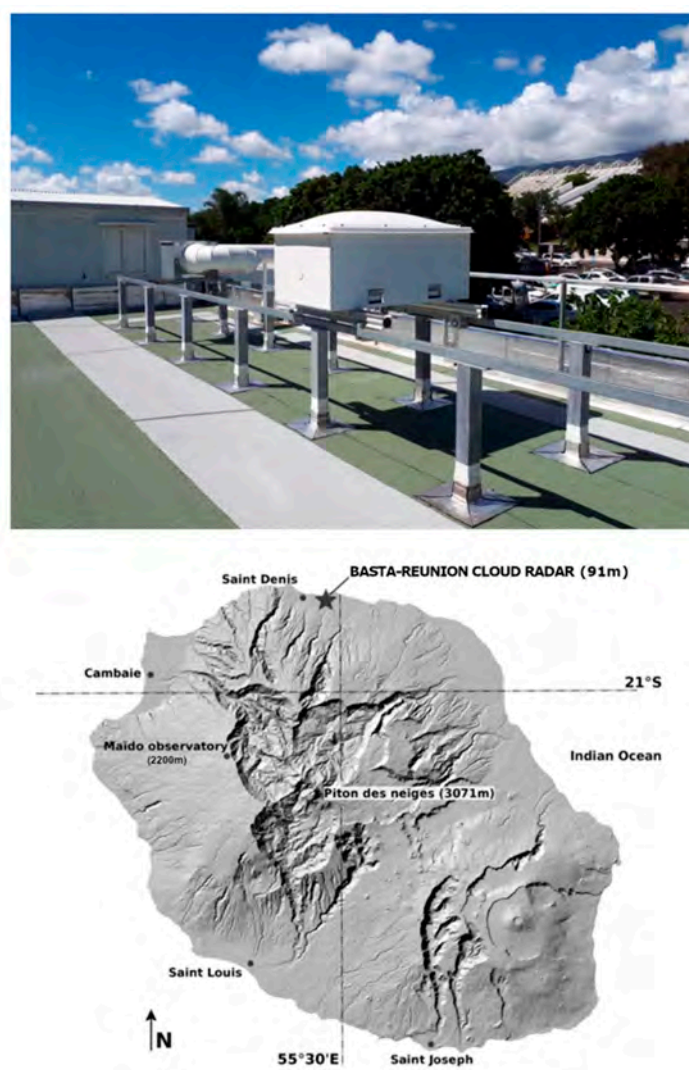


Figure 1. The cloud radar BASTA-REUNION located in Saint-Denis de La Réunion on the rooftop of Reunion University (55.48° E, 20.9° S).

This paper is organized as follows: information about data used in this study are given in Section 2; the distribution and analysis of the seasonal cloud cover over Saint-Denis between November 2016 and October 2018 are presented in Section 3; possible relationships between observed cloud patterns and large-scale environment are thus investigated in Section 4, while Section 5 presents our conclusions and perspectives.

2. Data and Methods

2.1. Cloud Radar Observations

The present study is principally based on continuous observations collected between November 2016 and October 2018 by a cloud radar BASTA. BASTA is a 95 GHz vertically pointing bistatic Doppler radar (distinct antennas for transmission and reception) developed by LATMOS (“Laboratoire Atmosphère, Milieux et Observations Spatiales”) for cloud and fog studies [24,26]. A dedicated version of this radar (referred to as BASTA-REUNION) was deployed in Reunion Island in November 2016 at the main campus facility of Reunion University, located in Saint-Denis approximately 100 m above ground level (Figure 1). BASTA-REUNION provides times series of vertical reflectivity and Doppler velocity profiles up to an altitude of 24 km. Reflectivity profiles consist of a combination of data collected in four distinct operating modes that are each activated over a period of integration of 3 s and later recombined to reconstruct the cloud structure throughout the

tropospheric layer every 12 s. The first operating mode, dedicated to fog and low cloud observations, runs at the resolution of 12.5 m and provides information up to an altitude of 12 km. The second mode, which features a vertical resolution of 25 m, is used to investigate mid-level clouds between 6 km and 18 km. Finally, the last two modes (100 m vertical resolution) are used to sample high-level clouds up to 18 km and 24 km, respectively—the latter mode, which is slightly more sensitive, was specifically implemented for tropical regions. Nearly four million reconstructed vertical reflectivity profiles are used in this study, which represent ~80% of the total number of profiles theoretically expected over a 2-year period.

Due to its operating frequency, BASTA-REUNION can be strongly affected by radar attenuation resulting from the absorption or reflection of transmitted signals in precipitation areas. This phenomenon, which occurs at most radar frequencies, reflects the fact that some of the energy is often lost to scattering and absorption when the radar pulse penetrates in heavy precipitation areas. At 95 GHz, the frequency of BASTA-REUNION, uncertainties can be introduced in the observed cloud properties and occasionally can result in the extinction of the radar signal in a heavy precipitation regime. As will be seen later, this phenomenon nevertheless remains relatively uncommon in the Saint-Denis area and does not significantly affect the statistical analysis of cloud radar data that will be presented hereafter. We thus chose to not discriminate between precipitating and non-precipitating clouds so as to be able to also identify the occurrence of rainfall in radar observations—as fog and low-level stratus never occur over Saint-Denis, radar data collected below 1 km always reflect the presence of precipitation.

During the austral summer, the presence of the Intertropical Convergence Zone (ITCZ) nearby Reunion Island induces low-level convergence of highly buoyant air that favors the development of deep convection. The interactions of these unstable air masses with the complex orography of the island can generate very intense precipitation due, in particular, to the passage of tropical cyclones nearby [27]. In winter, as the ITCZ moves back northwards, the local weather becomes mostly influenced by the subsided southern branch of the Hadley cell. The resulting temperature inversion tends to inhibit atmospheric upward vertical motion above ~3 km [28,29] and is further amplified by the trade wind inversion [30–32]. Due to its complex orography, Reunion Island is also affected all year long by thermally induced sea breeze circulations that can force onshore moist flow at low levels and further favors the development of low-level clouds during daytime [30,33]. Examples of observations collected by BASTA-REUNION in Austral summer (26 March 2017), Austral winter (1 August 2017) as well as during cyclonic conditions (4–6 March 2018) are presented hereafter to illustrate the general cloudiness conditions associated with the various large-scale circulation patterns that drive cloud formation in Reunion Island.

In Austral summer (Figure 2a, 26 March 2017), radar observations show the existence of a strong diurnal cycle characterized by low-level clouds forming early in the morning and eventually dissipating in the late evening. Convective clouds, resulting from the high convective instability that prevails over the tropical SWIO basin during summer, develop in the early afternoon and extend up to the altitude of 10 km (all heights are given above mean sea level). Precipitation, as evidenced by associated time series of collocated rain gauge measurements, is maximised around mid-day (9–11 UTC, 13–15 LST) and dissipates in the early evening. During winter (Figure 2b, 1 August 2017), low-level clouds also form in the early morning (near 03:00 UTC/07:00 LST), but never evolve into deep convective clouds due to the strong capping effect. These low-level clouds, which consist of small, non-precipitating, scattered cumulus, are not advected from the ocean, but develop over the slopes before expanding northwards towards the coast in the middle of the afternoon.

The third example (Figure 3) shows radar observations collected during the passage of tropical cyclone Dumazile over the Mascarene Archipelago in early March 2018. On 4 March (top panel), radar observations were collected within an outer rainband located about 700 km southeast of the TC center. Time series of vertical radar reflectivity profiles show numerous convective cells extending forward and backward up to an altitude of

15 km. On 6 March (bottom panel), radar data are collected within a cirriform region, at the back of the tropical cyclone. Vertical reflectivity profiles collected in this area (indicated by the red circle on the associated MODIS image) show a layer of cirrus clouds extending from 11 to 14 km that is characteristic of pre- and post-convective tropical cyclone regions. As shown by collocated high-resolution (6 min) rainfall measurements, brief but extremely strong rainfall occurred on 4 March around 09:00 UTC (up to 50 mmh^{-1}) and 10:15 UTC (up to 95 mmh^{-1}). These heavy precipitation periods are associated with data gaps in radar observations, which can also be observed in Figure 2a (between 8 and 11 UTC). These gaps reflect the aforementioned attenuation of the radar signal by strong precipitation, which principally occurs for instantaneous rain rates higher than 15 mm h^{-1} (Figures 2a and 3). According to the climatological study of [31], which provides a detailed analysis of the spatio-temporal variability of local rainfall patterns over Reunion Island, such situations are nevertheless uncommon in the Saint-Denis area, and not frequent enough to significantly impact the results that will be presented in the following.

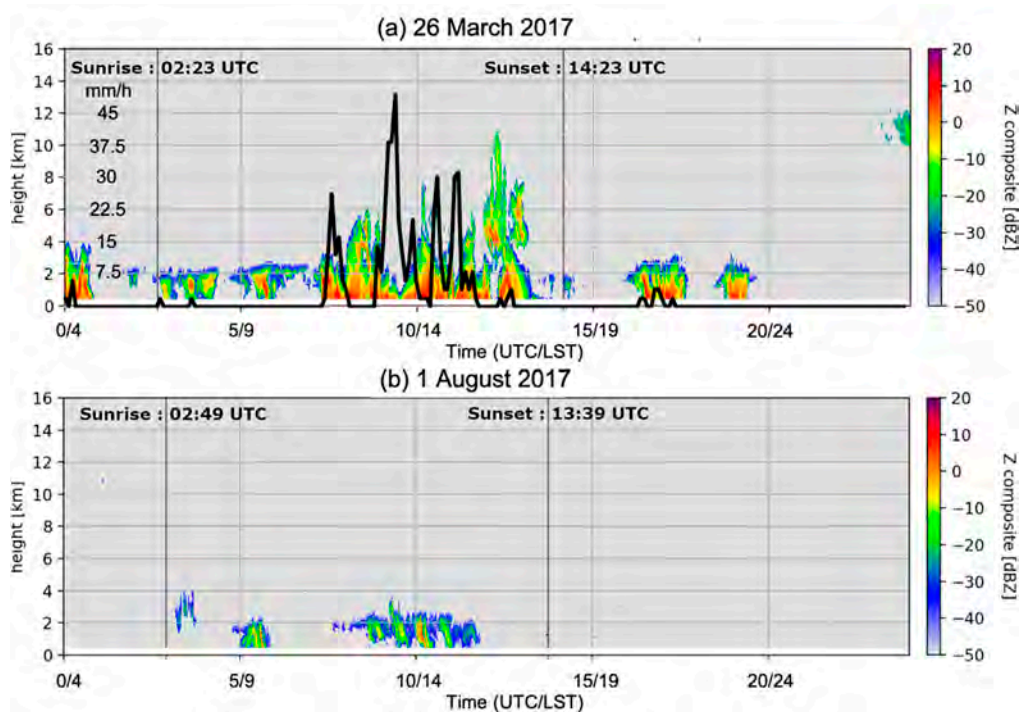


Figure 2. Time series of radar reflectivity vertical profiles (dBZ) collected on (a) 26 March 2017 (summer) and (b) 1 August 2017 (winter). The black line in (a) shows collocated rainfall measurements every 6 min expressed in mmh^{-1} (scale to the left).

2.2. Other Datasets

Additional sources of data are also relied upon to describe the local and regional weather conditions prevailing over Reunion Island and the SWIO basin during the 2-year period of analysis:

- (i) In situ observations of relative humidity inferred from Saint-Denis' airport (20.88° S , 55.51° E) operational daily radiosounding data collected between 2014 and 2018;
- (ii) Time series of integrated water vapor (IWV) columns, inferred from the analysis of GNSS data collected from the IGN (Institut Geographique National) station STDE (20.88° S – 55.51° E) and the International GNSS System (IGS)' station REUN (21.2° S , 55.57° E). GNSS data are processed following the approach used by [34,35] to produce IWV data at various locations in the SWIO basin (a complete description of GNSS IWV retrieval and associated uncertainties can be found in the former papers).

- (iii) Reanalysis data extracted from European Center for Medium-Range Weather Forecast (ECMWF)'s 5th generation reanalysis (ERA5) are used to investigate the regional atmospheric conditions prevailing over the SWIO basin. ERA5 provides hourly estimates of numerous atmospheric, land and oceanic climate variables on a $0.25 \times 0.25^\circ$ horizontal grid [36]. Reanalysis data used in this study consist of wind, humidity, sea level pressure and vertical velocity fields extracted over the period 1990–2020.

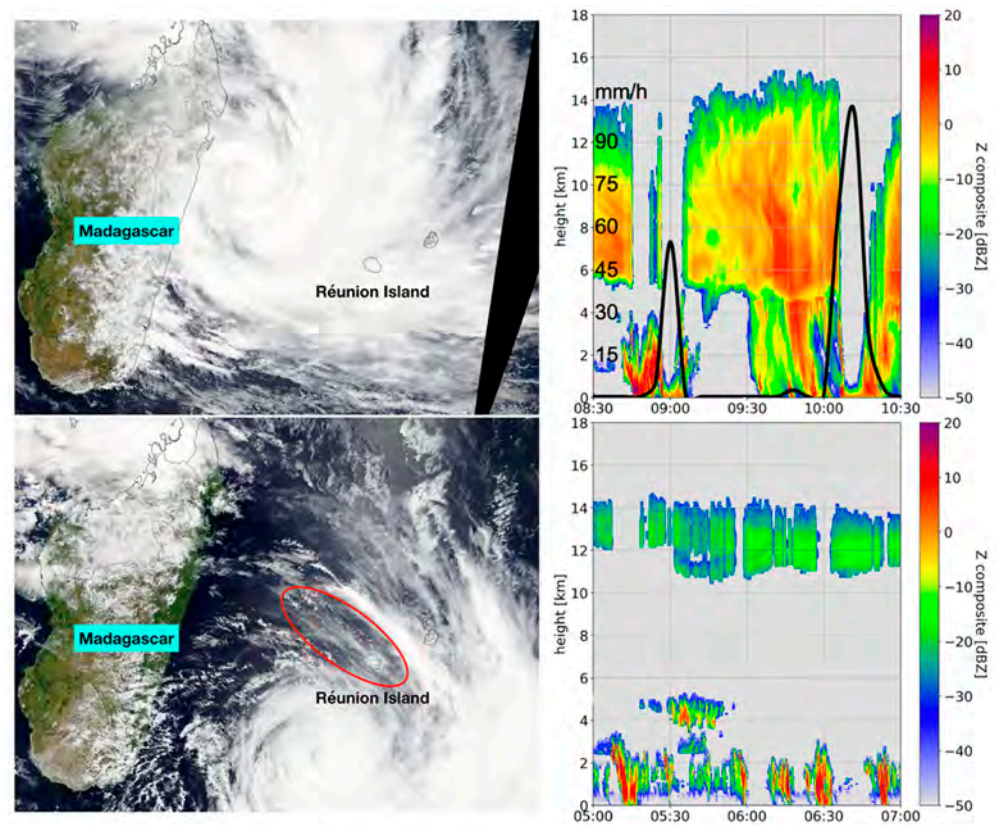


Figure 3. Left panel: Satellite images (MODIS TERRA) of Tropical Cyclone Dumazile, recorded on 4 March 2018 (top, 9:00 UTC) and 6 March 2018 (bottom, 6:00 UTC). Right panel: corresponding time series of BASTA-REUNION vertical radar reflectivity profiles (dBZ, UTC) with superimposed collocated rainfall measurements every 6 min (expressed in mmh^{-1} , scale to the left). The red circle indicates the cirriform region sampled by the radar on 6 March.

3. Diurnal and Seasonal Variability of Cloudiness over Saint-Denis in 2017 and 2018

In the following, reflectivity data collected by BASTA-REUNION are used to investigate the vertical structure of winter and summer clouds over Saint-Denis. For simplicity, the four seasons investigated hereafter will be referred to as summer 2017 (November 2016–March 2017), winter 2017 (June–September 2017), summer 2018 (November 2017–March 2018) and winter 2018 (June–September 2018).

Diurnal Cycle

The seasonal composite analyses of radar reflectivity profiles aggregated over the two sampled summer and the two winter seasons are shown in Figure 4a,b, respectively.

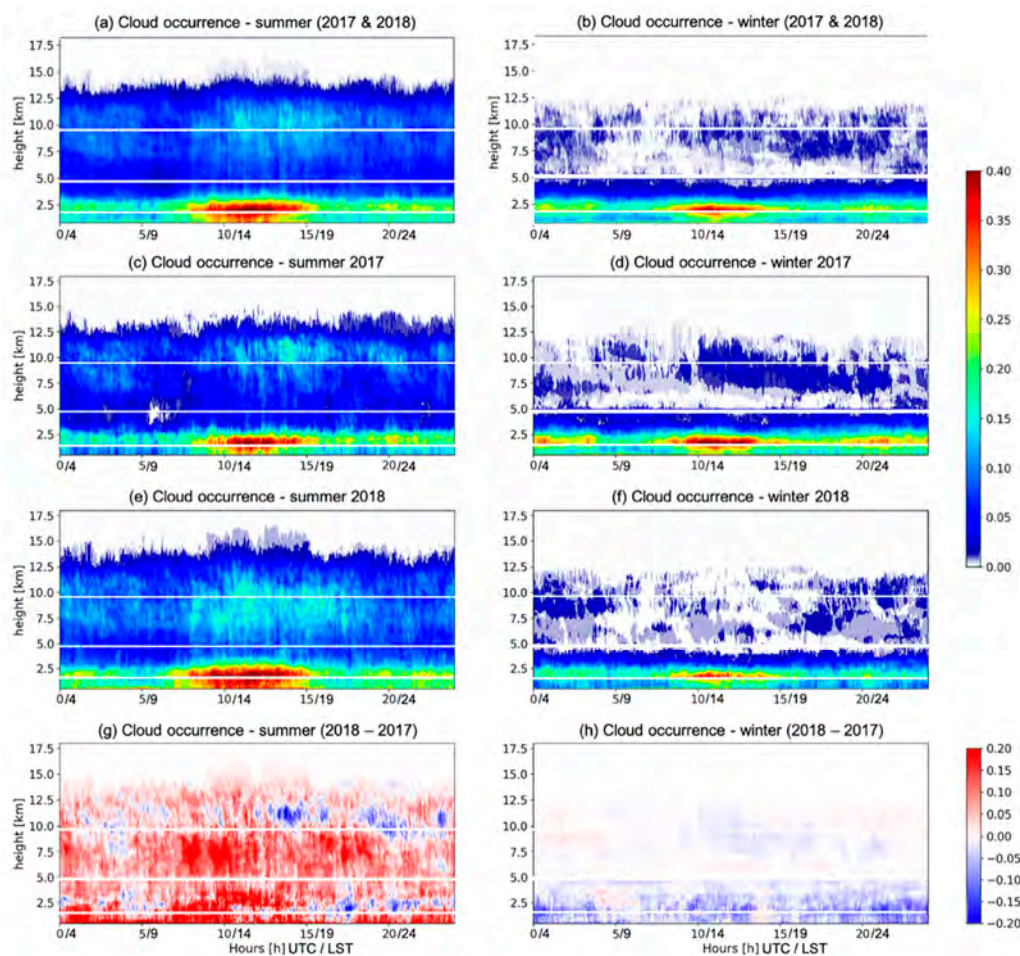


Figure 4. Time series of cloud occurrence (% , normalized to 1) as a function of the time of the day (hours) and altitude (km) for (a) aggregated summer seasons 2017 and 2018, (b) aggregated winter seasons 2017 and 2018, (c) summer 2017, (d) winter 2017, (e) summer 2018, (f) winter 2018, (g) summer 2018 minus summer 2017 and (h) winter 2018 minus winter 2017. White lines near the altitudes 2, 5 and 10 km correspond to data gap layers of ~25–50 m resulting from the recombination of data collected in the different radar acquisition modes.

In summer (Figure 4a), aggregated radar observations show two cloud layers, associated with the diurnal cycle (leading to the formation of low-level cumulus clouds) and convective instability (leading to the development of thunderstorm systems in mid to late afternoon). In the lowest layer, which extends from ~0.5 to 3 km, the maximum cloud occurrence is observed between 08:00 UTC (12 LST) and 15:00 UTC (19 LST) at an altitude of 2 km, with a maximum probability of nearly 45% near 12 UTC (16 LST). The upper layer, comprised between ~6 and 15 km, corresponds to deep convective and ice clouds associated with local storms, as well as tropical storms and cyclones that passed nearby Reunion Island. The probability of occurrence is maximised between 10:00 UTC and 15:00 UTC (14–19 LST) and reaches up to 15% at an altitude of 10 km near 14 UTC (18 LST).

In winter (Figure 4b), one can still observe a layer of low-level clouds extending from approximately 0.5 to 2.5 km. The frequency of cloud occurrence is highest between 09:00 UTC (13 LST) and 14:00 UTC (18 LST), with a maximum probability of about 35% near 2km altitude at 11 UTC (15 LST). While the frequency of occurrence of low-level clouds appears similar during summer and winter periods, the depth of the low-level cloud layer is lower in winter (maximum height of 2.5 km vs. 3 km in summer). High-level clouds are also up to three times less frequent in winter (5% occurrence vs. 15% occurrence in summer) as a result of the stronger stability of the atmosphere during this season.

To further assess the diurnal variability of cloud cover from one year to the next, time series shown in Figure 4a,b were also individually aggregated for each of the four sampled seasons: summer 2017 (Figure 4c) and 2018 (Figure 4e), and winter 2017 (Figure 4d) and 2018 (Figure 4f). From a qualitative standpoint, one can observe strong similarities between both summers and both winters. However, a closer look at the field of differences (Figure 4g,h) shows important disparities from one year to the next. Hence, low-level cloudiness appears significantly higher and deeper in winter 2017 (Figure 4h) than during the following winter season, while significant differences could also be observed throughout the troposphere between the two summer seasons (Figure 4g), with significantly deeper cloud cover in 2018.

Mean vertical profiles of cloud occurrence inferred from the high-resolution BASTA-REUNION profiles collected during the four sampled seasons shown in Figure 4c–f are shown in Figure 5. During summer, the probability of occurrence shows much larger values in 2018 (solid blue line) at both low-level (frequency of cloud/precipitation occurrence below 3 km ranging from 20–22% vs. 15–20% in 2017) and mid-to-high level (frequency of cloud occurrence of 10% vs. 5% in 2017 at 6 km). These differences are even more striking in winter. In 2017 (red dashed line), low-level cloudiness is for instance twice as large as in 2018 (blue-dashed line, 20–22% vs. 10%) and actually bears strong resemblances with that observed during the previous summer (solid blue line). Furthermore, one can also observe large differences occurring at mid-levels. While the vertical cloud extension is more or less limited to 4 km in 2018, in good agreement with previous climatological studies of [30,31], clouds occur in much more significant proportions up to an altitude of 6 km and even beyond (frequency of occurrence of 1% at 8 km) in 2017. In the following, large-scale environmental conditions inferred from the analysis of ERA5 data are investigated in order to understand the possible origins of these differences.

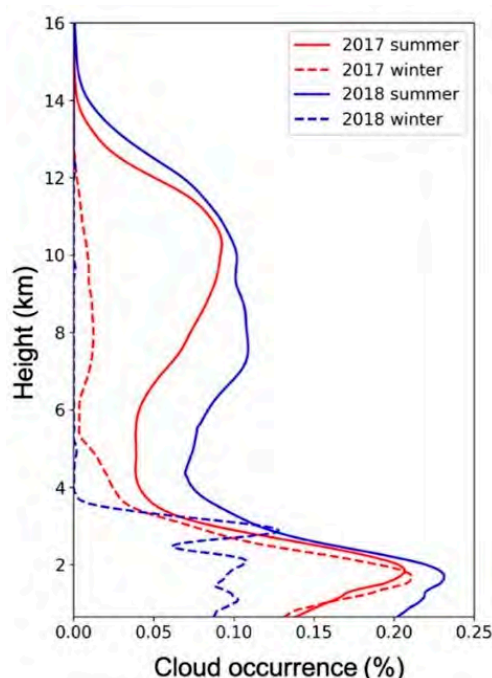


Figure 5. Probability of cloud occurrence (% , normalized to 1) observed during summer (solid line) and winter (dashed line) 2017 (red) and 2018 (blue) as a function of height.

4. Analysis of Local and Large-Scale Environmental Conditions Prevailing in 2017 and 2018

4.1. IOSD Patterns

In the SWIO basin, the main climatic phenomenon that drives large-scale oceanic and atmospheric circulation is the Indian Ocean Subtropical Dipole (IOSD [37]). This climate

anomaly controls the structure of the ocean's surface layer, which, in turn, impacts the atmospheric circulation and rainfall at the regional scale. It is characterized by three distinct phases that are defined by a reference index computed from SST anomaly differences between the western and eastern parts of the basin: a neutral phase, corresponding to the mean state of the ocean, a negative phase and a positive phase. Positive events, which are characterized by above-normal SSTs in the southwestern part of the basin and below-normal SSTs off western Australia, generally start at the beginning of the Austral summer and die off in April/May.

The evolution of the IOSD index from 2013 to 2019 (Figure 6) shows that a particularly strong positive event occurred in early 2017. The latter started in November 2016, peaked in January (with a high index value) and finally died off in late March 2017 (index value of 0.2). However, one can observe that index values started to re-increase significantly at the beginning of the winter, with an average value of ~ 1 throughout the rest of the year, before finally collapsing in early 2018.

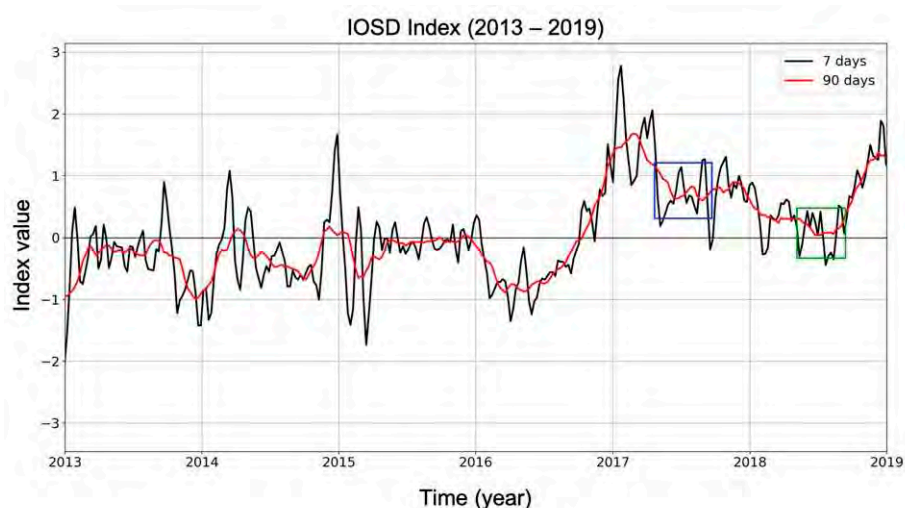


Figure 6. Averaged weekly (black) and quarterly (red) IOSD index between January 2013 and December 2019. Blue and green squares highlight index values during winter 2017 and 2018, respectively.

4.2. Large Scale Anomalies

Corresponding large-scale atmospheric and oceanic anomalies prevailing during summers (DJF) and winters (JJA) 2017 and 2018 are shown in Figures 7 and 8. In good agreement with the occurrence of a positive IOSD event, a positive SST anomaly, centered near 30° S and extending from the East African coast to $\sim 90^{\circ}$ E, can be observed over the SW part of the basin in summer 2017 (Figure 7a). Enhanced midlevel subsidence is also observed over Madagascar and the central part of the basin (Figure 7e), resulting in both positive pressure anomalies (Figure 7c) and dryer conditions in the mid-troposphere (as inferred from IWV anomalies, Figure 7g) in these areas. Over the Mascarenes and Reunion Island, these large-scale conditions result in a slightly positive SST anomaly, of nearly 0.5° C, and a below-normal (negative) humidity anomaly of $\sim 6\text{--}8\text{ kg m}^{-2}$.

During the next summer, a positive SST anomaly can still be observed in the southern part of the basin (Figure 7b). The latter is however shifted southeastwards with respect to summer 2017 and no significant surface pressure (Figure 7d) or mid-level vertical velocity (Figure 7f) anomalies are longer observed over the central part of the basin. A moist tongue extending northwestwards towards Madagascar could be observed, in good agreement with the location of the positive SST anomaly (Figure 7h). Over the Mascarene Archipelago, these large-scale conditions resulted in positive SST and moisture anomalies of up to 1° C and 8 kg m^{-2} , respectively.

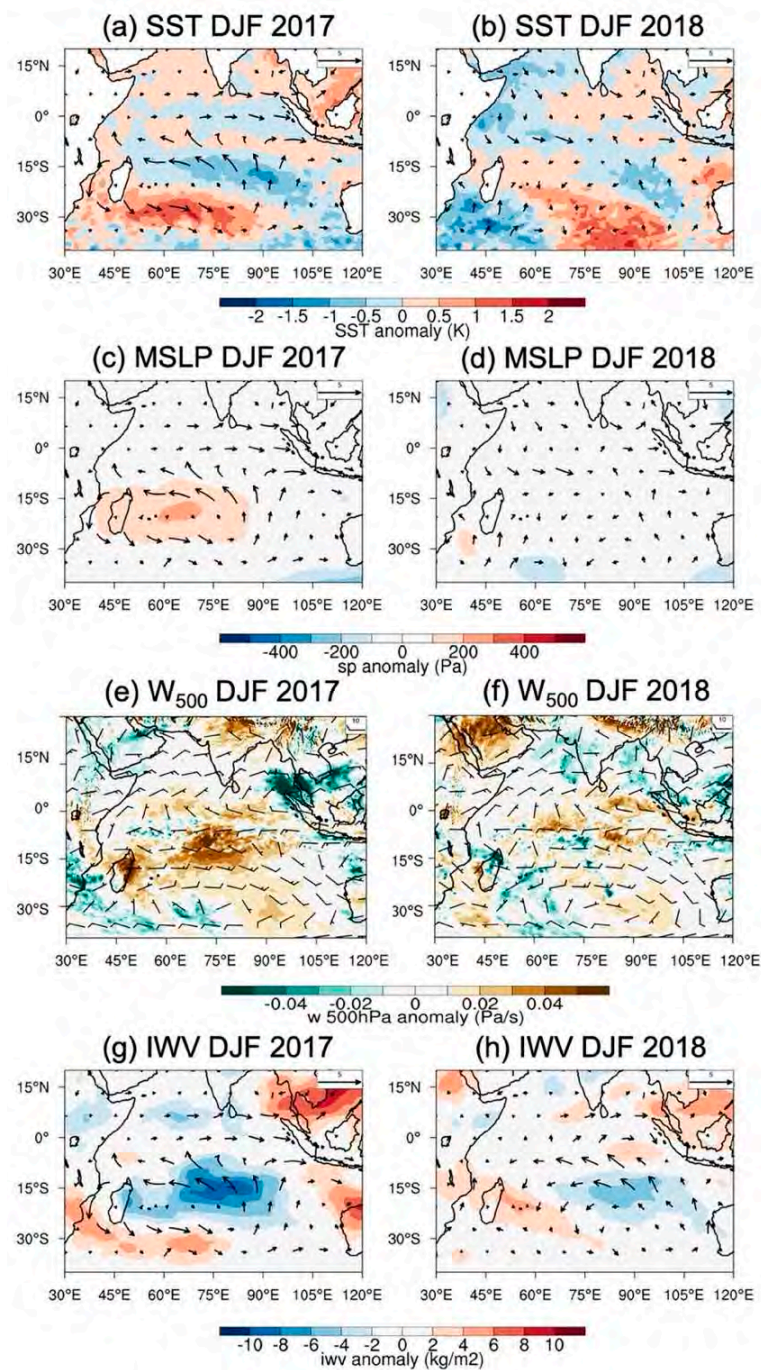


Figure 7. (a,b) Sea Surface Temperature (SST), Mean Sea Level Pressure (MSLP), Vertical velocity at 500 hPa (W) and Integrated Water Vapour (IWV) anomalies in summer (DJF) 2017 (left panel) and 2018 (right panel), computed from ERA5 reanalysis data over the period 1990–2020.

During winter 2017 (Figure 8a), ERA5 data show SST anomalies of up to $1\text{ }^{\circ}\text{C}$ over the Mascarene Archipelago, likely inherited from the IOSD event that started earlier in the year. The Mascarene anticyclone also moved south-eastwards resulting in strong positive pressure anomalies over the central and southern parts of the basin as well as slightly below normal sea level pressures over the Mascarenes (Figure 8c). These anomalies are also accompanied by a decrease in the large-scale midlevel (500 hPa) subsidence over this area (Figure 8e), resulting in higher humidity content at 850 hPa (Figure 8g). While this positive SST anomaly is also present in winter 2018 (Figure 8b), the other atmospheric parameters (Figure 8d,f,h) are nevertheless globally in phase with the climatology.

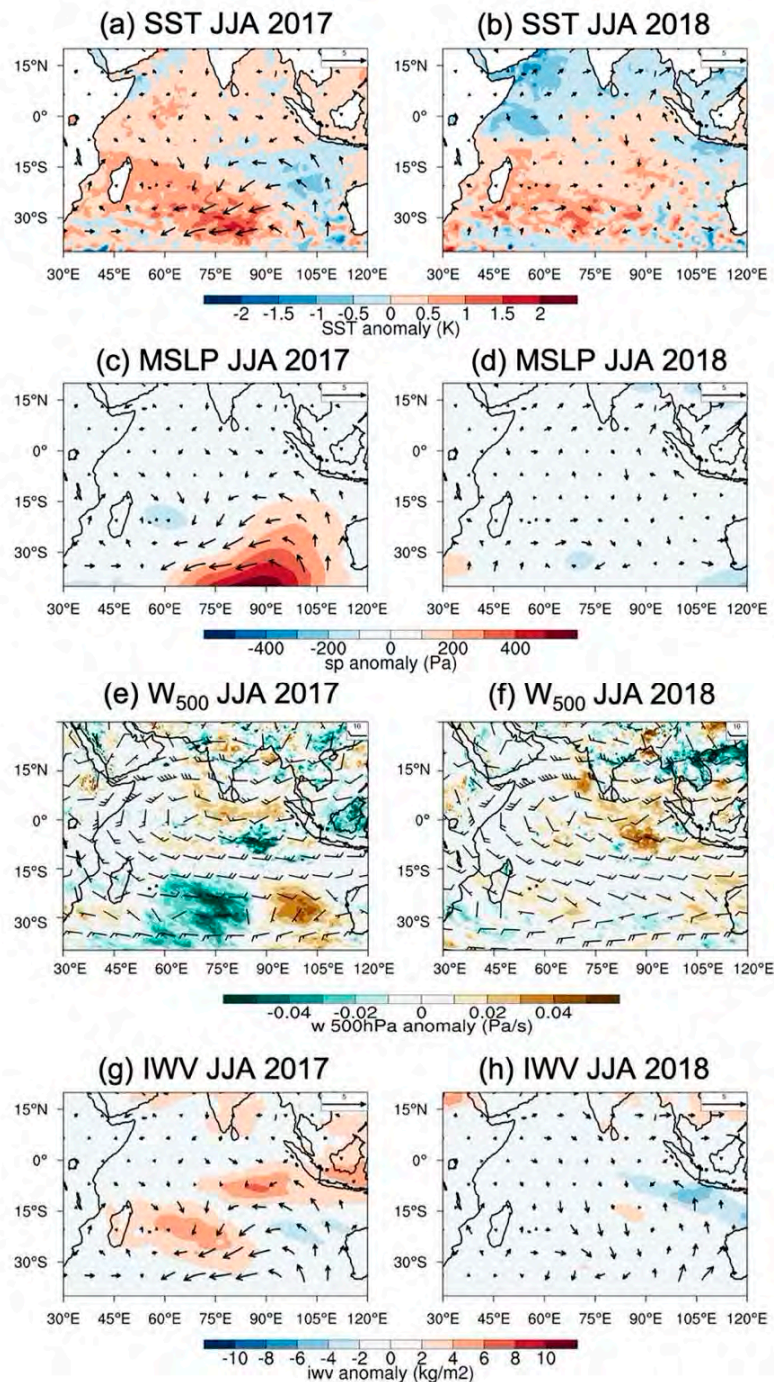


Figure 8. (a,b) Sea Surface Temperature (SST), Mean Sea Level Pressure (MSLP), Vertical velocity at 500 hPa (W) and Integrated Water Vapour (IWV) anomalies in summer (DJF) 2017 (left panel) and 2018 (right panel), computed from ERA5 reanalysis data over the period 1990–2020. As in Figure 7, but for winter (JJA) 2017 and 2018.

4.3. Local Observations

Humidity observations inferred from the analysis of GNSS data collected at the IGS station of REUN (21.2° S, 55.57° E) and radio sounding data collected at Saint-Denis' airport (20.88° S, 55.51° E) are shown in Figure 9. According to time series of monthly averaged GNSS-derived IWV columns (Figure 9a), significantly dryer conditions occurred over Reunion Island during the first 4 months (Nov–March) of the wet season 2017, with differences of up to 12 kg m^{-2} ($+/-30\%$) compared to the same period one year after.

This tendency however inverts at the end of the summer, a period that corresponds to the dying of the 2017 positive IOSD event. GNSS-derived IWV observations also confirm that tropospheric humidity was significantly higher during winter 2017 (JJAS, blue line) than during winter 2018 (red line), with differences of up to 3.5 kg m^{-2} ($\pm 35\%$) between July and September. A strictly similar tendency (not shown) was also observed at other GNSS stations located along the west coast and central area of Reunion Island, indicating that these tropospheric humidity anomalies have impacted the whole island.

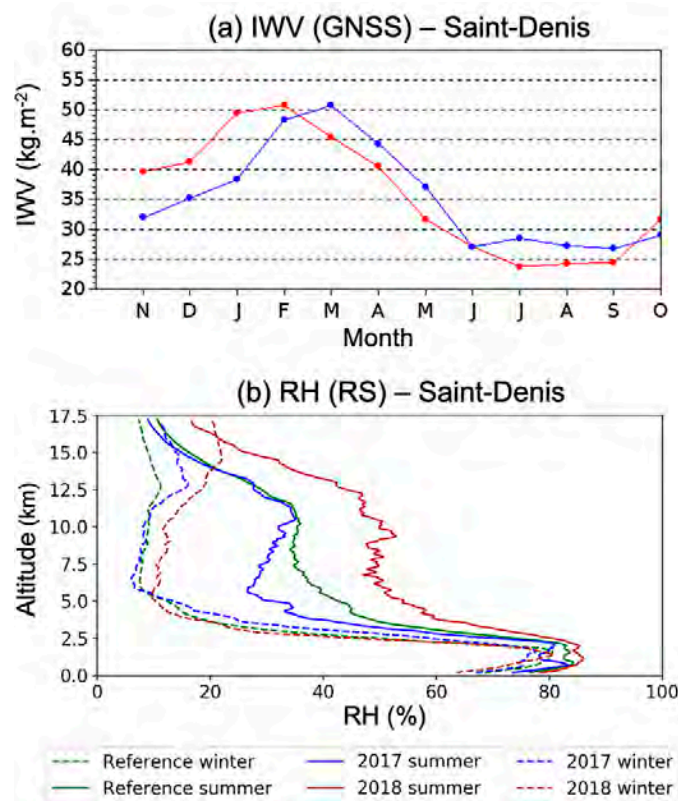


Figure 9. (a) Monthly mean of GNSS-derived IWV content at station REUN in 2017 (blue) and 2018 (red). (b) RS-derived relative humidity at Saint-Denis during summer (plain) and winter (dashed) 2017 (blue) and 2018 (red). The green line in (b) shows corresponding average RH profiles for the period 2014–2018.

According to seasonally averaged relative humidity data inferred from operational radio sounding observations in Saint-Denis (Figure 9b), absolute moisture conditions in summer 2018 (red solid line) were higher throughout the troposphere compared to summer 2017 (blue solid line), with an increase ranging from 10% at low levels to 100% at mid and high levels. The 5-y average (2014–2018) humidity profile (green solid line) also indicates that humidity conditions were significantly below (resp. above) normal in summer 2017 (resp. 2018), in good agreement with moisture anomaly patterns deduced from the analysis of ERA5 data (Figure 7g,h). In winter 2018, the seasonally averaged relative humidity profile (red dashed line) shows good agreement with the climatological mean (green dashed line) up to 6 km, and above normal relative humidity at higher levels. In 2017 (blue-dashed line), one can however observe a significant increase in the low-level relative humidity between 2 and 4 km altitude, ranging from +50% to +80% at a given level.

To further investigate relationships between cloudiness and humidity over Saint-Denis, Figure 10 shows hourly relative anomalies (difference between the hourly value and the daily average, divided by the daily average) of integrated water vapour (IWV, %), radar-derived low- (LLC, 1–3 km) and mid-to-high-level (HLC, 5–10 km) cloudiness (%) as well as insolation, during summer (left panel) and winter (right panel) 2018 (as GNSS

observations collocated with BASTA-REUNION only started to be available in January 2018, we can only compare cloud occurrence and IWV for this year).

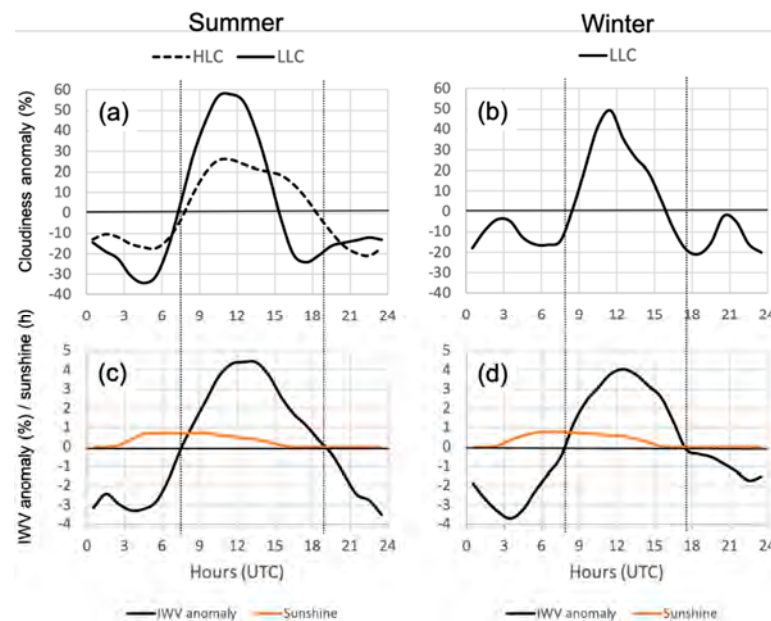


Figure 10. Diurnal cycle of high level (HLC) and low-level (LLC) clouds, Integrated water vapour (IWV) and insolation at Saint-Denis in 2018. Top panel: low-(1–3 km, plain) and mid-(5–10 km, dashed) level cloud anomaly (%) during (a) summer 2018 and (b) winter 2018. Bottom panel: Diurnal cycles of GNSS-derived (STDE station) IWV anomaly (%), black and insolation (hours, orange) during (c) summer 2018 and (d) winter 2018.

The ground starts to heat up in the early morning (3 UTC/7 LST) with sunrise (Figure 10c,d), which increases the air temperature and initiates thermal instability in the boundary layer. As water vapour generated by evapotranspiration starts to condense, a positive cloudiness anomaly appears near 7:30 UTC (11:30 LST) at both low- and mid-to-high levels. A positive IWV anomaly, which remains positive throughout the daytime, can also be observed at nearly the same hour. In both summer (Figure 10c) and winter (Figure 10d) this positive moisture anomaly is maximum near 12 UTC (16 LST) and reaches about 4.5% ($\sim 2 \text{ kg m}^{-2}$ in summer and 1.06 kg m^{-2} in winter). The time of this maximum likely reflects the existence of a sea breeze regime, which is strongest in mid-afternoon, when the difference in temperature between the land and ocean is highest. This IWV anomaly maximum also corresponds to that of the observed maximum in low-level cloudiness anomaly, which reaches up to 60% in summer (Figure 10a) and 50% in winter. This agreement suggests that the sea breeze regime may act to reinforce low-level cloud formation along the slopes through the advection of additional moisture originating from the ocean towards the island.

5. Discussion and Conclusions

The permanent deployment, in 2016, of a 95 GHz vertically pointing cloud radar BASTA in Reunion Island is an important achievement in order to reinforce cloud observations and atmospheric science research capabilities in the SWIO.

Data collected by this radar during its two first years of operation show a strong seasonal cycle with significant variation of cloudiness between summers and winters. During Austral summer, a bimodal mode characterized by two cloud layers extending respectively from 1–3 km (maximum daily frequency of cloud occurrence of 45%) and 8–12 km (maximum daily frequency of cloud occurrence of 15%) is observed. During Austral winter, cloudiness is mostly limited to the low levels (maximum daily probability of occurrence of about 35%) due to both the northward migration of the ITCZ and the

strong trade wind inversion prevailing at this time of the year (which further limits vertical cloud extension). These results are globally in line with those obtained by [19] over the tropical island of Barbados (using ground-based cloud radar data collected over a similar period of two years), which have also shown the existence of a bimodal mode (in the vertical) in summer that disappears in winter due to the circulation shifts accompanying the seasonal migration of the ITCZ. As in [19], we also observed a slight variability in the lower troposphere cloudiness across the seasons on a diurnal scale. In summer, medium and high clouds associated with convective developments over the island's relief show a maximum occurrence between 10 and 15UTC (i.e., between 14 and 19 LST), while low-level clouds are maximised between 8 and 15 UTC (12 and 19 LST) in summer and 9 and 14 UTC (13 and 18 LST) in winter. As in Barbados, this variability appears somewhat more important in summer (maximum value of cloud occurrence of 45% at a height of 2 km at both locations) than during winter (25% in Barbados vs. 35% in Reunion Island at a height of 2 km). The diurnal cycle of the cloudiness is also strongly correlated with the diurnal cycle of IWV regardless of the season and the cloud layer considered.

The comparative analysis of seasonal cloudiness observations collected in 2017 and 2018 also shows strong differences from one year to the next, with significantly higher (resp. lower) cloud cover in winter (resp. summer) 2017 than in 2018. The analysis of ERA5 reanalysis data and local humidity measurements derived from radio soundings and GNSS observations suggests that these differences could be attributed to a different large-scale context between the two years. In summer 2017 a strong positive SST anomaly, which formed in relationship with a positive phase of the subtropical Indian Ocean dipole (SIOD), could be observed south of Madagascar and was accompanied by positive (resp. negative) anomalies of subsidence (resp. humidity) over the center part of the basin. This large-scale subsidence, and associated dry air, acted to limit the vertical extension of clouds and likely explains the significant differences in cloud cover observed between the two summers. The two winter seasons also show important differences in terms of the large-scale environment. In 2017, a zonal dipole of large-scale subsidence anomaly was observed, while conditions were closer to normal in 2018. The eastward shift of high subsidence values resulting from the presence of this dipole resulted in a wet anomaly over the western part of the basin in winter 2017 that was further amplified by a positive SST anomaly over Reunion Island (increased evaporation). As a consequence, the vertical structure of the cloudiness and the probability of cloud occurrence in the lower half of the troposphere were surprisingly similar throughout the year 2017.

According to regional and local humidity data, one can hypothesize that the 2017 IOSD event significantly impacted moisture conditions over Reunion Island throughout the year 2017, resulting in lower (resp. higher) than normal humidity conditions at low- and mid-level in summer (resp. winter). These distinct moisture conditions may have accounted for the large differences observed in terms of cloudiness between Austral summers 2017 and 2018 (Figure 4). The thermodynamic structure of the atmosphere over Reunion Island was also more unstable during Austral winter 2017 than during Austral winter 2018, thus favouring low-level cloud development, which eventually happens to overshoot the trade wind inversion. In this regard, an exceptional and extremely intense storm, which locally produced more than 105 mm of rainfall in one hour in the northeast part of the island, occurred on 29 and 30 August 2017. BASTA-REUNION reflectivity measurements collected at Saint-Denis during this event (Figure 11) show convective cells with vertical development above 7 km altitude, which is extremely uncommon in this season. Instantaneous rainfall data collected next to the radar on 30 August around 1:30 LST confirms that particularly intense rainfall (up to 70 mmh^{-1}) occurred over Saint-Denis even though the rainfall maxima was observed about 15 km SE of the radar. Additionally, note the extinction of the radar signal at the same hour, as already observed in Figures 2 and 3.

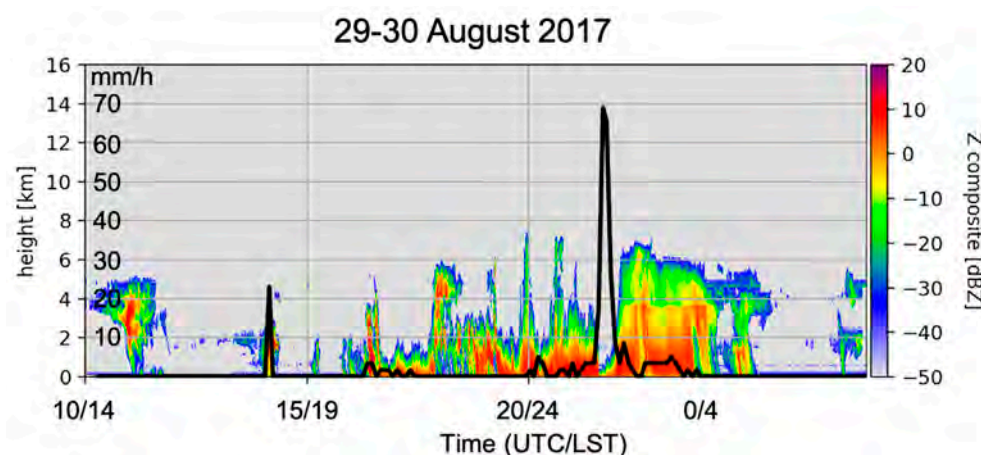


Figure 11. As in Figure 2, but for data collected between 29 August (10 UTC/14 LST) and 30 August (5 UTC/9 LST) 2017.

Decreased moisture at low levels during summer 2017 can also account for the limited development of deep local convective events with respect to 2018. The observed differences in terms of cloudiness were also exacerbated by the significant cyclonic activity that occurred over the Mascarene Archipelago during the wet season 2018. Between January and April 2018 (see Figure 1 in [38]), four tropical cyclones grazed the island (TC Berguitta and Fakir) or passed in its immediate vicinity (TC Ava and Dumazile)—which drained a large amount of mid-to-high level clouds over Reunion Island—whereas only two tropical storms (TS Carlos and Fernando), which passed more than 200 km away from the island, occurred in 2017.

Cloud radar observations are key to investigate the properties and variability of tropical clouds, to evaluate cloud fraction forecasted by NWP systems [39] and derived from space-borne measurements, as well as to evaluate climate model performance [40]. Although limited in time, the preliminary analysis of the 2-y dataset of cloud radar observations analysed in this study already allows us to better understand the various and complex processes that drive cloudiness in the tropical island of the SWIO such as Reunion Island. More efforts are nevertheless obviously needed in order to thoroughly characterize the properties of the clouds in this tropical area as well as to fully exploit the rare observations provided by research cloud radars in the Southern hemisphere.

In this regard, observations of clouds and precipitation in Reunion Island will continue to be reinforced in the frame of ACTRIS through the deployment, in late 2021, of a second, volumetric (i.e., 360° scanning), BASTA cloud radar at the Maïdo observatory. A transportable polarimetric X-band radar, aiming at complementing observations provided by Reunion Island's two operational S-band weather radar systems, will also be installed at Saint-Joseph (southern part of the island) in September 2021, in the frame of the Interreg-V Indian Ocean research project ESPOIRS ("Etude des Systèmes Précipitant de l'Océan Indien par Radars et Satellites" [41]). The deployment of this additional cloud radar, together with the enhancement of the ground-based weather radar network, will allow for further, long-term, studies of the seasonal and inter-annual variability of tropical clouds, but also to benefit from multi-frequency radar observations to better understand the formation and life cycle of clouds and precipitation over this unique tropical area. This new setup will thus permit us to study all sorts of cloud patterns, ranging from orographic, cirrus and low-to-mid level trade clouds to deep convective storms associated with tropical cyclones passing nearby. Altogether, these instruments will also contribute to make OPAR and Reunion Island a precious satellite validation testbed in the southern hemisphere for Earth observation programs, such as the upcoming EARTHCARE [42] space mission.

Author Contributions: Conceptualization J.D. (Jonathan Durand) and O.B.; data acquisition and processing J.D. (Julien Delanoë), J.D. (Jonathan Durand) and O.B.; writing—original draft preparation, J.D. (Jonathan Durand), E.L., F.B. and O.B.; writing—review and editing, all co-authors; supervision, O.B.; project administration, O.B.; funding acquisition, O.B. All authors have read and agreed to the published version of the manuscript.

Funding: This research was funded by the European Union, the Regional Council of Reunion Island and the French state under FEDER projects “BASTA-Reunion” and “ESIEC-RUN” and INTERREG-V Indian Ocean 2014–2020 project “ReNovRisk-Cyclone and Precipitation”.

Institutional Review Board Statement: Not applicable.

Informed Consent Statement: Not applicable.

Data Availability Statement: Data used in this study are available on request from the corresponding author.

Acknowledgments: Authors are grateful to the engineers of the Laboratoire Atmosphère, Milieux et Observations Spatiales (LATMOS) for their help in the setup and operation of the BASTA-REUNION radar.

Conflicts of Interest: The authors declare no conflict of interest.

References

- Liou, K.-N. Influence of Cirrus Clouds on Weather and Climate Processes: A Global Perspective. *Mon. Weather. Rev.* **1986**, *114*, 1167–1199. [CrossRef]
- Hansen, J.; Sato, M.; Ruedy, R. Radiative forcing and climate response. *J. Geophys. Res. Space Phys.* **1997**, *102*, 6831–6864. [CrossRef]
- Klein, S.A.; Hall, A.; Norris, J.R.; Pincus, R. Low-Cloud Feedbacks from Cloud-Controlling Factors: A Review. *Surv. Geophys.* **2017**, *38*, 1307–1329. [CrossRef]
- Bony, S. Marine boundary layer clouds at the heart of tropical cloud feedback uncertainties in climate models. *Geophys. Res. Lett.* **2005**, *32*, 20806. [CrossRef]
- Stephens, G.L. Cloud Feedbacks in the Climate System: A Critical Review. *J. Clim.* **2005**, *18*, 237–273. [CrossRef]
- Nuijens, L.; Stevens, B.; Siebesma, A.P. The Environment of Precipitating Shallow Cumulus Convection. *J. Atmos. Sci.* **2009**, *66*, 1962–1979. [CrossRef]
- Madden, R.; Julian, P. Detection of a 40–50-day oscillation of the zonal wind in the tropical Pacific. *J. Atmos. Sci.* **1971**, *28*, 702–708. [CrossRef]
- Madden, R.; Julian, P. Observations of the 40–50-day tropical oscillation. A review. *Mon. Wea. Rev.* **1994**, *122*, 814–837. [CrossRef]
- Battaglia, A.; Kollias, P.; Dhillon, R.; Lamer, K.; Khairoutdinov, M.; Watters, D. Mind the gap—Part 2: Improving quantitative estimates of cloud and rain water path in oceanic warm rain using spaceborne radars. *Atmos. Meas. Tech.* **2020**, *13*, 4865–4883. [CrossRef]
- Marchand, R.; Mace, G.G.; Ackerman, T.; Stephens, G. Hydrometeor Detection Using Cloudsat—An Earth-Orbiting 94-GHz Cloud Radar. *J. Atmos. Ocean. Technol.* **2008**, *25*, 519–533. [CrossRef]
- Sassen, K.; Wang, Z. Classifying clouds around the globe with the CloudSat radar: 1-year of results. *Geophys. Res. Lett.* **2008**, *35*, 04805. [CrossRef]
- Lamer, K.; Kollias, P.; Battaglia, A.; Preval, S. Mind the gap—Part 1: Accurately locating warm marine boundary layer clouds and precipitation using spaceborne radars. *Atmos. Meas. Tech.* **2020**, *13*, 2363–2379. [CrossRef]
- Kollias, P.; Clothiaux, E.E.; Miller, M.A.; Albrecht, B.A.; Stephens, G.L.; Ackerman, T.P. Millimeter-Wavelength Radars: New Frontier in Atmospheric Cloud and Precipitation Research. *Bull. Am. Meteorol. Soc.* **2007**, *88*, 1608–1624. [CrossRef]
- Long, C.N.; Mather, J.H.; Ackerman, T.P. The ARM Tropical Western Pacific (TWP) Sites. *Meteorol. Monogr.* **2016**, *57*, 7. [CrossRef]
- Thorsen, T.J.; Fu, Q.; Comstock, J. Cloud effects on radiative heating rate profiles over Darwin using ARM and A-train radar/lidar observations. *J. Geophys. Res. Atmos.* **2013**, *118*, 5637–5654. [CrossRef]
- Liu, Z.; Marchand, R.; Ackerman, T. A comparison of observations in the tropical western Pacific from ground-based and satellite millimeter-wavelength cloud radars. *J. Geophys. Res. Space Phys.* **2010**, *115*. [CrossRef]
- Bouniol, D.; Couvreur, F.; Kamsu-Tamo, P.; Leplay, M.; Guichard, F.; Favot, F.; O’Connor, E.J. Diurnal and Seasonal Cycles of Cloud Occurrences, Types, and Radiative Impact over West Africa. *J. Appl. Meteorol. Clim.* **2012**, *51*, 534–553. [CrossRef]
- Sukanya, P.; Kalapureddy, M.C.R. Cloud radar observations of multi-scale variability of cloud vertical structure associated with Indian summer monsoon over a tropical location. *Clim. Dyn.* **2021**, *56*, 1055–1081. [CrossRef]
- Stevens, B.; Farrell, D.; Hirsch, L.; Jansen, F.; Nuijens, L.; Serikov, I.; Brüggemann, B.; Forde, M.; Linné, H.; Lonitz, K.; et al. The Barbados Cloud Observatory: Anchoring Investigations of Clouds and Circulation on the Edge of the ITCZ. *Bull. Am. Meteorol. Soc.* **2016**, *97*, 787–801. [CrossRef]
- Stevens, B.D.; Bony, S.; Farrell, D.; Ament, F. EUREC4A, submitted to Earth. *Sys. Sci. Data.* 2021. Available online: <https://essd.copernicus.org/preprints/essd-2021-18/> (accessed on 29 May 2021).

21. Brueck, M.; Nuijens, L.; Stevens, B. On the Seasonal and Synoptic Time-Scale Variability of the North Atlantic Trade Wind Region and Its Low-Level Clouds. *J. Atmos. Sci.* **2015**, *72*, 1428–1446. [[CrossRef](#)]
22. Kollias, P.; Bharadwaj, N.; Clothiaux, E.E.; Lamer, K.; Oue, M.; Hardin, J.; Isom, B.; Lindenmaier, I.; Matthews, A.; Luke, E.; et al. The ARM Radar Network: At the Leading Edge of Cloud and Precipitation Observations. *Bull. Am. Meteorol. Soc.* **2020**, *101*, E588–E607. [[CrossRef](#)]
23. Baray, J.-L.; Courcoux, Y.; Keckhut, P.; Portafaix, T.; Tulet, P.; Cammas, J.-P.; Hauchecorne, A.; Godin Beekmann, S.; De Mazière, M.; Hermans, C.; et al. Maïdo observatory: A new high-altitude station facility at Reunion Island (21° S, 55° E) for long-term atmospheric remote sensing and in situ measurements. *Atmos. Meas. Tech.* **2013**, *6*, 2865–2877. [[CrossRef](#)]
24. Delanoë, J.; Protat, A.; Vinson, J.-P.; Brett, W.; Caudoux, C.; Bertrand, F.; Du Chatelet, J.P.; Hallali, R.; Barthes, L.; Haeffelin, M.; et al. BASTA: A 95-GHz FMCW Doppler Radar for Cloud and Fog Studies. *J. Atmos. Ocean. Technol.* **2016**, *33*, 1023–1038. [[CrossRef](#)]
25. Bergemann, M.; Jakob, C. How important is tropospheric humidity for coastal rainfall in the tropics? *Geophys. Res. Lett.* **2016**, *43*, 5860–5868. [[CrossRef](#)]
26. Dupont, J.-C.; Haeffelin, M.; Wærsted, E.; Delanoë, J.; Renard, J.-B.; Preissler, J.; O’Dowd, C. Evaluation of Fog and Low Stratus Cloud Microphysical Properties Derived from In Situ Sensor, Cloud Radar and SYRSOC Algorithm. *Atmosphere* **2018**, *9*, 169. [[CrossRef](#)]
27. Quetelard, H.; Bessemoulin, P.; Cerveny, R.S.; Peterson, T.C.; Burton, A.; Boodhoo, Y. Extreme Weather: World-Record Rainfalls During Tropical Cyclone Gamede. *Bull. Am. Meteorol. Soc.* **2009**, *90*, 603–608. [[CrossRef](#)]
28. Taupin, F.G.; Bessafi, M.; Baldy, S.; Bremaud, P.J. Tropospheric ozone above the southwestern Indian Ocean is strongly linked to dynamical conditions prevailing in the tropics. *J. Geophys. Res. Space Phys.* **1999**, *104*, 8057–8066. [[CrossRef](#)]
29. Brémaud, P.; Taupin, F. Cloud influence on ozone diurnal cycle in the marine boundary layer at Réunion Island. *Atmos. Res.* **1998**, *47–48*, 285–298. [[CrossRef](#)]
30. Lesouëf, D.; Gheusi, F.; Delmas, R.; Escobar, J. Numerical simulations of local circulations and pollution transport over Reunion Island. *Ann. Geophys.* **2011**, *29*, 53–69. [[CrossRef](#)]
31. Réchou, A.; Flores, O.; Jumaux, G.; Duflot, V.; Bousquet, O.; Pouppeville, C.; Bonnardot, F. Spatio-temporal variability of rainfall in a high tropical island: Patterns and large-scale drivers in Réunion Island. *Q. J. R. Meteorol. Soc.* **2019**, *145*, 893–909. [[CrossRef](#)]
32. Rechou, A.; Rao, T.N.; Bousquet, O.; Plu, M.; Decoupes, R. Properties of rainfall in a tropical volcanic island deduced from UHF wind profiler measurements. *Atmos. Meas. Tech.* **2014**, *7*, 409–418. [[CrossRef](#)]
33. Jumeaux, G.; Quetelard, H.; Roy, D. Atlas Climatique de La Réunion de Météo-France, Météo-France technical report 2011. (in French). Available online: <http://www.meteofrance.fr/publications/nos-collections/climat-outr-mer/atlas-climatique-de-la-reunion> (accessed on 29 May 2021).
34. Lees, E.; Bousquet, O.; Roy, D.; Leclair, J. Analysis of diurnal to seasonal variability of integrated water vapour in the South Indian Ocean basin using ground-based GNSS and 5th generation ECMWF reanalysis (ERA5) data. *Q. J. R. Meteorol.* **2021**, *147*, 229–248. [[CrossRef](#)]
35. Bousquet, O.; Lees, E.; Durand, J.; Peltier, A.; Duret, A.; Mekies, D.; Boissier, P.; Donal, T.; Fleischer-Dogley, F.; Zakariasy, L. Densification of the Ground-Based GNSS Observation Network in the Southwest Indian Ocean: Current Status, Perspectives, and Examples of Applications in Meteorology and Geodesy. *Front. Earth Sci.* **2020**, *8*. [[CrossRef](#)]
36. Hersbach, H.; Bell, B.; Berrisford, P.; Hirahara, S.; Horanyi, A.; Muñoz-Sabater, J.; Nicolas, J.; Peubey, C.; Radu, R.; Schepers, D.; et al. The ERA5 global reanalysis. *Q. J. R. Meteorol. Soc.* **2020**, *146*, 1999–2049. [[CrossRef](#)]
37. Behera, S.; Yamagata, T. Subtropical SST dipole events in the southern Indian Ocean. *Geophys. Res. Lett.* **2001**, *28*, 327–330. [[CrossRef](#)]
38. Bousquet, O.; Barbary, D.; Bielli, S.; Kebir, S.; Raynaud, L.; Malardel, S.; Faure, G. An evaluation of tropical cyclone forecast in the Southwest Indian Ocean basin with AROME-Indian Ocean convection-permitting numerical weather predicting system. *Atmos. Sci. Lett.* **2019**, *21*, 950. [[CrossRef](#)]
39. Hogan, R.J.; O’Connor, E.J.; Illingworth, A.J. Verification of cloud-fraction forecasts. *Q. J. R. Meteorol. Soc.* **2009**, *135*, 1494–1511. [[CrossRef](#)]
40. Protat, A.; Bouniol, D.; Delanoë, J.; May, P.T.; Plana-Fattori, A.; Hasson, A.; Görsdorf, U.; Heymsfield, A.J. Assessment of Cloudsat Reflectivity Measurements and Ice Cloud Properties Using Ground-Based and Airborne Cloud Radar Observations. *J. Atmos. Ocean. Technol.* **2009**, *26*, 1717–1741. [[CrossRef](#)]
41. Bousquet, O.; Barruol, G.; Cordier, E.; Barthe, C.; Bielli, S.; Calmer, R.; Rindraharisaona, E.; Roberts, G.; Tulet, P.; Amelie, V.; et al. Impact of Tropical Cyclones on Inhabited Areas of the SWIO Basin at Present and Future Horizons. Part 1: Overview and Observing Component of the Research Project RENOVRIK-CYCLONE. *Atmosphere* **2021**, *12*, 544. [[CrossRef](#)]
42. Illingworth, A.J.; Barker, H.W.; Beljaars, A.; Ceccaldi, M.; Chepfer, H.; Clerbaux, N.; Cole, J.; Delanoë, J.; Domènech, C.; Donovan, D.P.; et al. The EarthCARE Satellite: The Next Step Forward in Global Measurements of Clouds, Aerosols, Precipitation, and Radiation. *Bull. Am. Meteorol. Soc.* **2015**, *96*, 1311–1332. [[CrossRef](#)]



Article

Seasonal to Interannual Variability of Vertical Wind Shear and Its Relationship with Tropical Cyclogenesis in the Mozambique Channel

Atanásio João Manhique, Isac Arnaldo Guirruogo, Bernardino João Nhantumbo and Alberto Francisco Mavume

Special Issue

Tropical Cyclones in the Indian Ocean

Edited by
Prof. Dr. Olivier Bousquet



Article

Seasonal to Interannual Variability of Vertical Wind Shear and Its Relationship with Tropical Cyclogenesis in the Mozambique Channel

Atanásio João Manhique ^{1,*}, Isac Arnaldo Guirruogo ¹, Bernardino João Nhantumbo ² 
and Alberto Francisco Mavume ¹ 

¹ Departamento de Física, Faculdade de Ciências, Universidade Eduardo Mondlane, Maputo C.P. 257, Mozambique; isaac.guirruogo@gmail.com (I.A.G.); alberto.mavume@uem.mz (A.F.M.)
² Instituto Nacional de Meteorologia, Maputo C.P. 256, Mozambique; b.nhantumbo@gmail.com
* Correspondence: atanasio.manhique@uem.mz; Tel.: +258-84-305-7356

Abstract: This article explores the relationship between vertical wind shear (VWS) and tropical cyclone (TC) genesis in the Mozambique Channel (MC) for the period 1979–2019. Additionally, SST, low-level relative vorticity, 700 hPa relative humidity and upper-level divergence were also analyzed for the peak cyclogenesis months to explore their relative contributions. The analyses were done using NCEP/NCAR Reanalysis-1 for the atmospheric fields, monthly Optimum Interpolation SST V2, and for the cyclogenesis the TC best track data from the La Reunion–Regional Specialized Meteorological and Joint Typhoon Warning Centre. A total of 43 TCs generated in the MC were observed for the analysed period. The maximum frequency of cyclogenesis in the MC was observed during January and February and the spatial location of maximum TC genesis was coincident with the minimum values of the VWS. The VWS showed significant correlations with TC intensity, particularly when considering the upper atmosphere (200–500 hPa) or the bulk (200–850 hPa) VWS. The mean composites of the cyclogenesis months over the MC of SST, relative humidity at 700 hPa, divergence at upper atmosphere, showed significant values. However, linear correlations between these factors vs. TC genesis frequency and intensity were not significant. Analyses of interannual correlations between VWS and Niño-3.4 (subtropical southwest Indian Ocean dipole-SIOD) showed statistically significant positive (negative) correlations at different lags, suggesting that La Niña and the positive phase of SIOD conditions are favorable to weaker VWS and thus to intensification of TCs in the Mozambique Channel. Thirteen landfall cases were observed with seven over the Madagascar west coast and six over the Mozambique coast. The landfall over the Madagascar (Mozambique) coast was associated with strengthened (weakened) VWS.

Keywords: cyclogenesis; vertical wind shear; Mozambique Channel



Citation: Manhique, A.J.; Guirruogo, I.A.; Nhantumbo, B.J.; Mavume, A.F. Seasonal to Interannual Variability of Vertical Wind Shear and Its Relationship with Tropical Cyclogenesis in the Mozambique Channel. *Atmosphere* **2021**, *12*, 739. <https://doi.org/10.3390/atmos12060739>

Academic Editor: Olivier Bousquet

Received: 18 March 2021

Accepted: 21 May 2021

Published: 9 June 2021

Publisher's Note: MDPI stays neutral with regard to jurisdictional claims in published maps and institutional affiliations.



Copyright: © 2021 by the authors. Licensee MDPI, Basel, Switzerland. This article is an open access article distributed under the terms and conditions of the Creative Commons Attribution (CC BY) license (<https://creativecommons.org/licenses/by/4.0/>).

1. Introduction

The process by which tropical cyclones (TCs) form and intensify, often referred to as tropical cyclogenesis, is strongly dependent on the existence of several environmental conditions. Gray [1] listed six basic conditions favoring TC genesis, namely: (i) sea surface temperature (SST) exceeding 26 °C, (ii) enhanced mid-troposphere (700 hPa) relative humidity, (iii) conditional instability, (iv) enhanced lower troposphere relative vorticity, (v) weak vertical environmental wind shear (VWS) and (vi) a displacement by at least 5° latitude away from the equator. Chan et al. [2] suggested that VWS is one of the main governing factors of both tropical cyclogenesis and tropical cyclone intensity. Moreover, some studies indicate that the uncertainties in forecasting the environmental wind shear values prevent the improvements in TC intensity forecast [3,4]. Over the tropical Pacific, some studies have indicated that VWS is a key environmental variable that determines the TCs development [5,6]. Jones et al. [7] considered the VWS a key predictor of seasonal

TC activity. Although some literature has shown cases of cyclones intensifying under moderate to strong VWS (e.g., [8–10]), in general large values of VWS are considered to be detrimental to the formation as well as the intensification of TCs, due to the “ventilation” effect [1,11–13]. Chan et al. [2] have indicated that the reduction of ventilation above the boundary layer due to vertical alignment is crucial to accumulate the energy within the inner core region of a TC. Nolan and McGauley [6] studied the relationship between VWS and TC genesis events within the latitudes 20° S and 20° N from 1969 to 2008, and found that VWS values in the range of 1.25–5 m/s are the most favorable for TC genesis, although previous studies suggested VWS values between 5–10 m/s (e.g., [14]). Some studies also suggested that there is a VWS threshold value above which TCs may not develop, for example, a threshold value of 12.5 m/s was determined for the western North Pacific by Zehr [15].

The Southwest Indian Ocean (SWIO) is one of the major basins of TCs formation and intensification. TCs forming in this region account for about 14% of the global total, with an average of 12–13 TCs forming each year in the cyclone season running from November to April [16–18]. SWIO TCs, especially those forming in the Mozambique Channel (MC) have been poorly studied so far although they frequently impact island nations and countries on the mainland of southeastern Africa [19–21]. Leroux et al. [21] stated that over the cyclone seasons from 1999/2000 to 2015/16, on average, Mozambique was hit by tropical systems once per year and by TCs about once every 3 years, and that those numbers are even worse for Madagascar, which was hit twice per year by tropical systems and was hit once every 2 years by TCs. These countries are listed as the world’s least developed, with high levels of vulnerability to climatic shocks. This study aims to contribute to the improvement of monitoring and seasonal forecast of TCs in the SWIO and thus to mitigation of the destructive impacts of TCs in the affected countries, which is one of the main objectives of the research project ReNovRisk-Cyclone [22].

Previous studies [23–25] have described several characteristics of the VWS and its association with tropical cyclone activity in the SWIO. Their results showed a band of weak VWS located near the Equator with a tendency to move (south–north) accompanying the displacement of the Inter-Tropical Convergence Zone (ITCZ) which is an important mechanism for tropical cyclogenesis. During the cyclone season in the SWIO, the ITCZ stretches across the MC between 15–20° S and the area of weak VWS along it can enhance the positive vorticity needed for tropical cyclogenesis in the region [18,26,27]. Matyas [28] indicated that given the displacement of the ITCZ in the MC during the cyclone season, TC formation frequency, location and environmental conditions by month. Ho et al. and Kuleshov et al. [17,25] suggested that during the cold phase of El Niño–Southern Oscillation (ENSO), there is a reduction of TC genesis in the western part of the South Indian Ocean (SIO, west of 75° E) and an increase in the eastern part (east of 75° E) as well as displacement of the area favorable for TC genesis further away from the equator and an inverted scenario is observed during the warm phase. The impact of VWS on TC genesis and intensification has been significantly explored globally, however, to our knowledge over the SWIO there are few studies, and none focusing on the MC. The MC has unique environmental conditions for TCs genesis, namely the presence of a summer trough which is associated with moist convection (e.g., [29]) the summer convergence zone, known as the South Indian Convergence Zone, which is associated with zonal wind convergence and moisture convergence [30] and the relative higher SST as compared to the same latitude east of Madagascar [18]. Moreover, the topography of Madagascar has a shielding effect, thus affecting the low-level circulation in the channel (e.g., [31]). Given these peculiarities, it is of interest to explore how the environmental factors contribute to the cyclogenesis in this region. The main objective of this study is to assess the relationship between the seasonal to interannual variability of the VWS and TC genesis frequency and intensity in the MC.

This paper is organized into five sections as follows: Section 1 presents the introduction, Section 2 describes the datasets used and the methodology, Section 3 presents the results and Sections 4 and 5 present the discussions and conclusions, respectively.

2. Data and Methodology

TC intensity and track data were obtained from La Reunion–Regional Specialized Meteorological Centre (LR-RSMC) freely available at <http://www.meteo.fr/temps> (accessed on 16 December 2019) and Joint Typhoon Warning Centre (JTWC) freely available at <http://www.npmoc.navy.mil/jtwc.html> (accessed on 16 December 2019). The data used cover the seasons 1978/79 to 2018/19 (the TC season in the SWIO is considered to be November to April) and the main region of analysis is restricted to the MC (10–27.5° S e 30–50° E). The datasets contain TC centre position (latitude and longitude) and intensity at 6-h intervals. In this study, a cyclogenesis point is defined as the first centre position along a cyclone track where the system reaches storm intensity (i.e., 1 min maximum sustained wind (MSW) > 17 m/s in JTWS data and 10-min maximum sustained wind > 15.4 m/s in LR-RSMC data). These data sets were used to plot the spatial distribution of cyclogenesis events and to analyze the seasonal and interannual frequency of cyclogenesis in the MC and the relationship with VWS. The JTWC dataset was used as the basic sample and the LR-RSMC dataset was used to fill in gaps encountered in JTWC data. A similar approach was previously used for the same region by Mavume et al. [18] and Bessafi and Wheeler [24]. Linear correlations were used to explore the statistical relationship between the number of TC cyclogenesis and VWS and also the maximum intensity and VWS. For years, with more than one TC system only the one with the maximum intensity has been considered, but if all have had the same category then all have been considered.

Monthly mean gridded atmospheric fields are obtained from the National Center for Environmental Prediction/National Centre for Atmospheric Research (NCEP/NCAR) Reanalysis-1 [32]. The datasets include zonal and meridional wind fields at the 200 and 850 hPa pressure levels, 850 hPa relative vorticity, 700 hPa relative humidity and 200 hPa divergence, available on a 2.5-degree global resolution in both latitude and longitude, from January 1948 to the present. Monthly mean Optimum Interpolation Sea Surface Temperature (OI SST) V2 [33] datasets are sourced from the National Oceanic and Atmospheric Administration (NOAA), and are available on a 1.0-degree global resolution in both latitude and longitude, from December 1981 to the present (accessed 10 March 2021).

The wind data were used to calculate the VWS, defined here as the magnitude of the vector difference of the 200 and 850 hPa horizontal winds. The magnitudes here are divided as in Rios-Berios and Torn [34], into three groups: weak ($VWS < 4.5$ m/s), moderate ($4.5 \leq VWS \leq 11$ m/s) and strong ($VWS > 11$ m/s). Mean maps of SST, 850 hPa relative vorticity, 700 hPa relative humidity, and 200 hPa divergence of the months with cyclogenesis in the MC are used to explore their potential contribution to the TC genesis.

Correlation analyses were used to explore the VWS versus El Niño and VWS versus SIOD relationships. The Niño 3.4 index is freely available at https://origin.cpc.ncep.noaa.gov/products/analysis_monitoring/ensostuff/ONI_v5.php (accessed on 22 April 2021), The SIOD index is defined as in Behera and Yamagata [35] and it was computed based on (OI SST) V2. Unless stated, all correlations shown in this study are above the 95% confidence level.

3. Results

The analyses of VWS and TC genesis were particularly focused on the MC for the December–March (Dec–Mar) period. This period covers more than 85% of TC activity in the MC [18,28].

3.1. Spatial and Temporal Variability of Vertical Wind Shear

The mean Dec–Mar VWS for 1979–2019 and the respective circulation are shown in Figure 1. The prominent feature is the area of weak to moderate shear (not exceeding

6 m/s) extending across the SWIO between the latitudes 10–21° S. The VWS values are even smaller (equal or below 3 m/s) in some parts of the strip of low VWS, namely over central SWIO, northern Madagascar, the central Mozambique Channel and central parts of Mozambique.

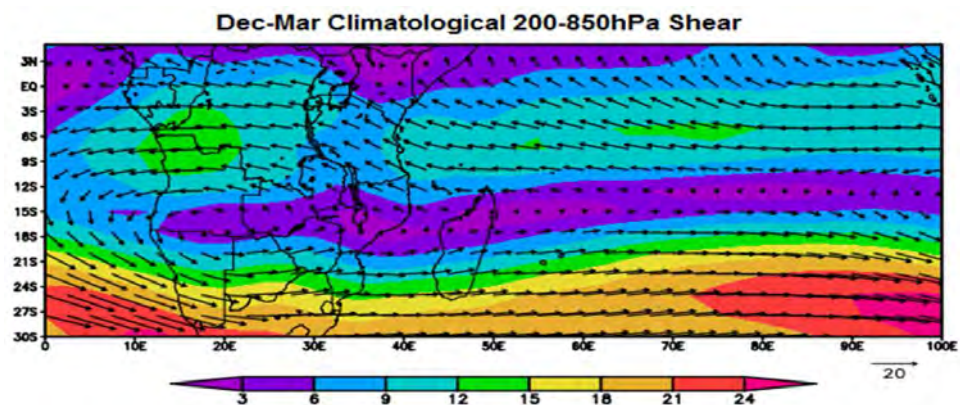


Figure 1. Mean (Dec–Mar 1979–2019) vertical wind shear. Colors indicate the magnitude (m/s) and vectors the direction.

Figure 2 shows the upper and lower-level Dec–Mar wind fields. It is noticeable that the band of weak VWS observed in the mean Dec–Mar (Figure 1) is associated with a band of weak winds at the 200 hPa level which separates the up-level subtropical westerlies and tropical easterlies (Figure 2a). At 850 hPa a similar band of weak winds observed, however, with less latitudinal extension, and with the wind direction on both side of the band reversed, i.e., with the westerlies over the tropical region associated with the cross-equatorial northeasterly monsoons and easterlies over the subtropical region accompanying the southward movement of the Indian Ocean high-pressure cell (see e.g., [29]). Over the MC a region of weak low-level wind associated with the MC trough (e.g., [29]) is observed. This region extends in a diagonal band from the central MC towards northern Mozambique.

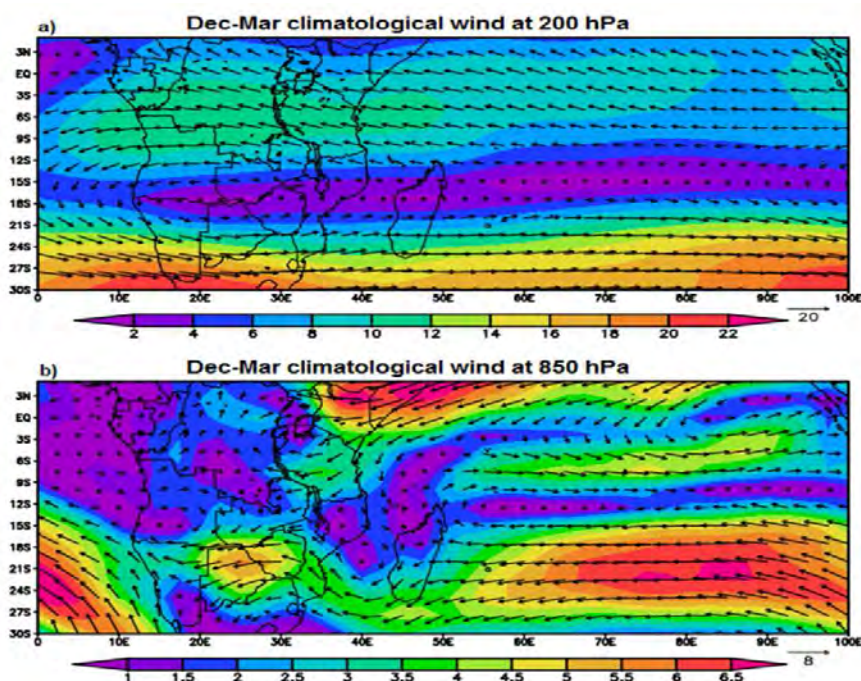


Figure 2. Mean (Dec–Mar 1979–2019) wind fields at 200 (a) and 850 hPa (b). Colors indicate the magnitude (m/s) and vectors the direction.

The seasonal progression of the band of weak VWS is shown in Figure 3. The band moves southward in November and December and reaches its maximum southward position between January and February and then reverses equatorward.

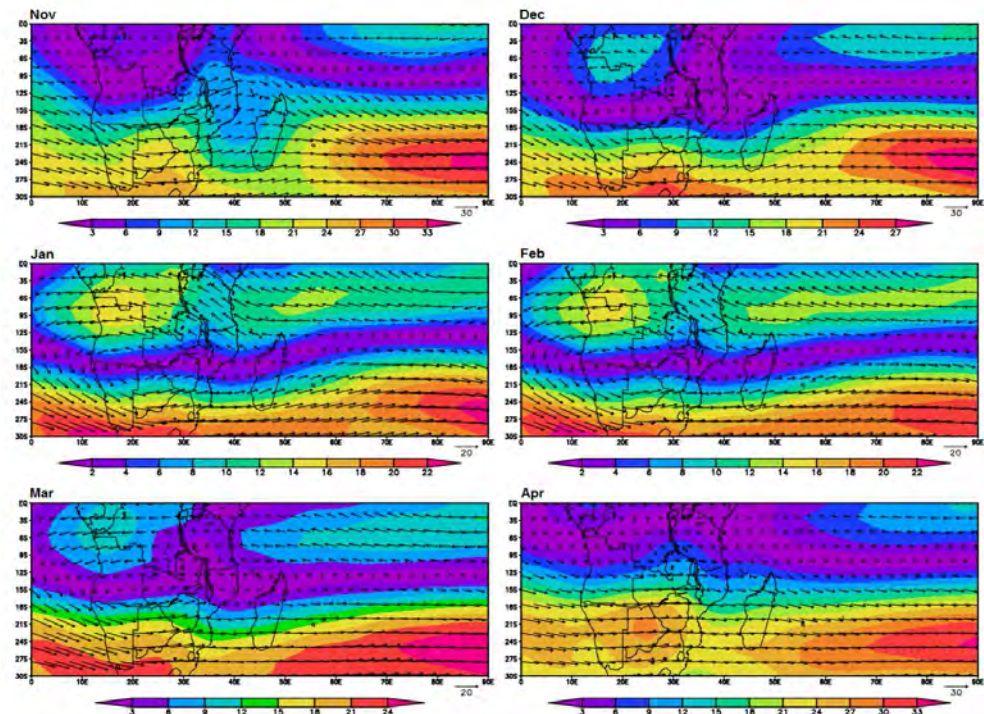


Figure 3. Same as Figure 1, but for mean monthly VWS.

3.2. Correlations between Vertical Wind Shear vs. El Niño and Subtropical Indian Ocean Dipole (SIOD)

Correlations were performed at different lags for December–March VWS (200–850 hPa) vs. Niño-3.4 and SIOD indices. Table 1 shows the correlation coefficients. The Niño-3.4 (SIOD) index showed significant and positive (negative) correlations with 200–850 hPa VWS at different lags.

Table 1. Correlation coefficients of 200–850 hPa VWS vs. Niño-3.4 and SIOD.

Period	Niño-3.4 vs. 200–850 hPa VWS	SIOD vs. 200–850 hPa VWS
September–November (SON)	0.34	
October–December (OND)	0.37	−0.34
November–January (NDJ)	0.40	−0.40
December–February (DJF)	0.43	−0.41
January–March (JFM)	0.50	−0.38

3.3. Vertical Wind Shear vs. Tropical Cyclone Genesis and Intensity

The spatial distribution of TC genesis over the MC for the 1978/1979 to 2018/2019 TC seasons, are presented in Figure 4. TC genesis in the MC is observed between around 12–24° S. A total of 43 TC genesis were observed, with maximum occurrence over the region of weak VWS which coincides with a region of low-level winds (compare with Figure 2b).

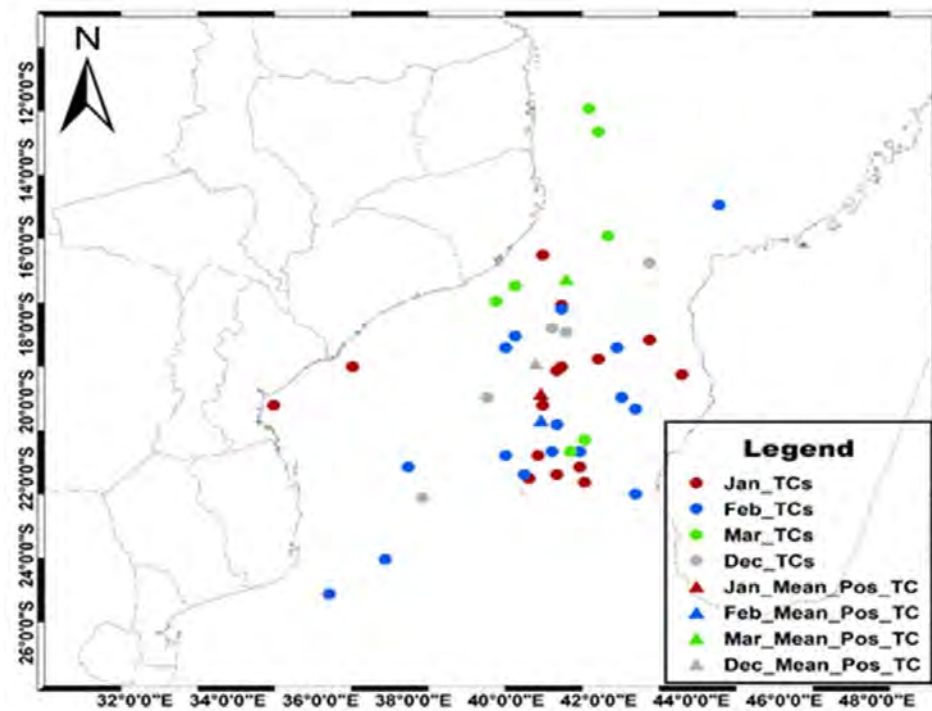


Figure 4. Geographical distribution of tropical cyclogenesis events over the MC during the 1979–2019 period. The colors distinguish the events by month (dots) and the monthly mean position is represented by triangles.

Monthly anomalies of 200–850 hPa VWS were computed together with TC genesis for January to March (Figure 5), to explore their relationship. It is observed from Figure 5 that most TC genesis are located in regions with negative anomalies of VWS. Few cases are observed in regions with positive anomalies, particularly in February, with cases that developed to TC intensity. A total of 15 cases developed to at least TC intensity.

The monthly mean VWS in the MC (10–27.5° S e 30–50° E) and the number of monthly totals of cyclogenesis are shown in Figure 6. The lowest values of VWS and higher number of cyclogenesis are observed between January and February. The average shear for the SWIO cyclone season is 11.64 m/s, and during the cyclone season months, the shear remains below this value, except in November and April. January and February show the lowest values of VWS and are also the most active in terms of tropical cyclogenesis, representing about 72% of the events. Although November and April are part of the cyclone season in the SWIO basin, cyclogenesis is not observed during these months, which is consistent with the observed strong shear.

The interannual variability of Dec–Mar VWS and the number of TC genesis per season in the MC are shown in Figure 7. For the period considered here, the maximum VWS is 10.63 m/s observed in 1992 and the minimum is 5.36 m/s observed in 2017. The number of TC genesis per season is between 0–3, the maximum number of cyclogenesis occurred in 2014, 2015 and 2019, there were fourteen years in which no TCs formed and an average of 1.1 TCs occurred per season.

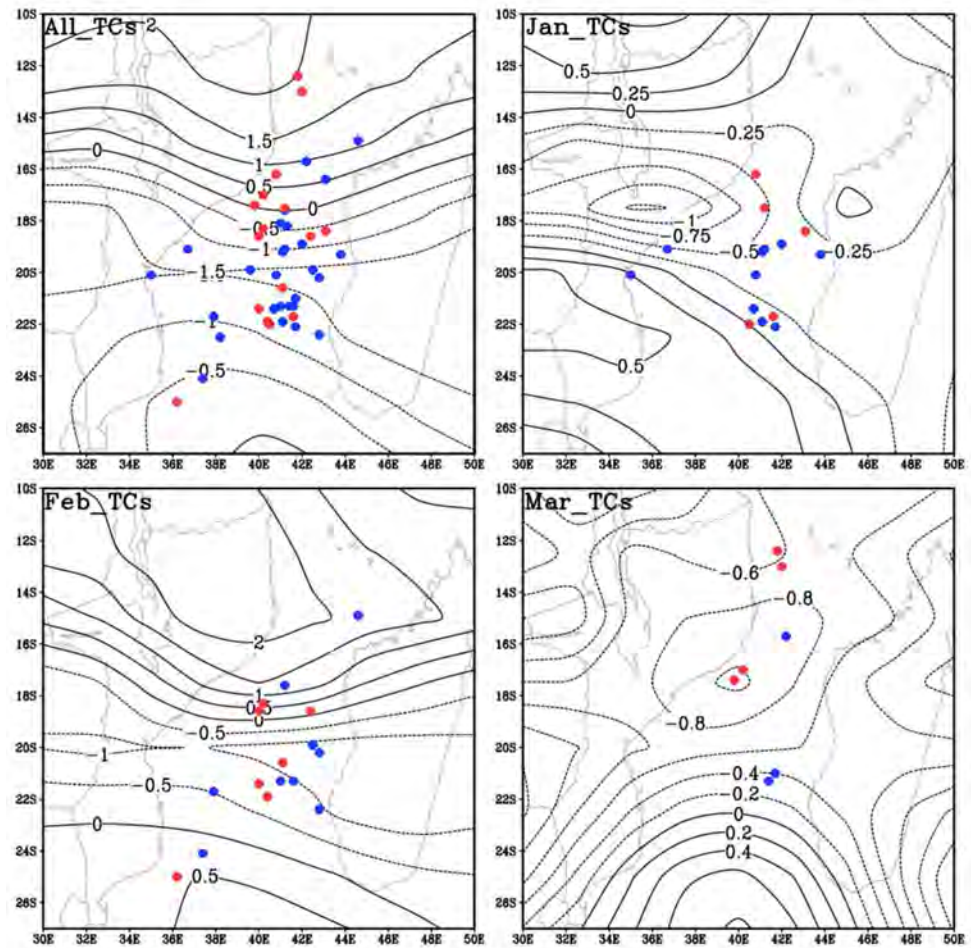


Figure 5. VWS monthly anomaly (contours in m/s) and the geographical distribution of TC genesis events (blue dots indicate monthly distribution and red dots the systems that intensified to at least TC intensity) for the period 1979–2019. Dotted lines indicate negative values.

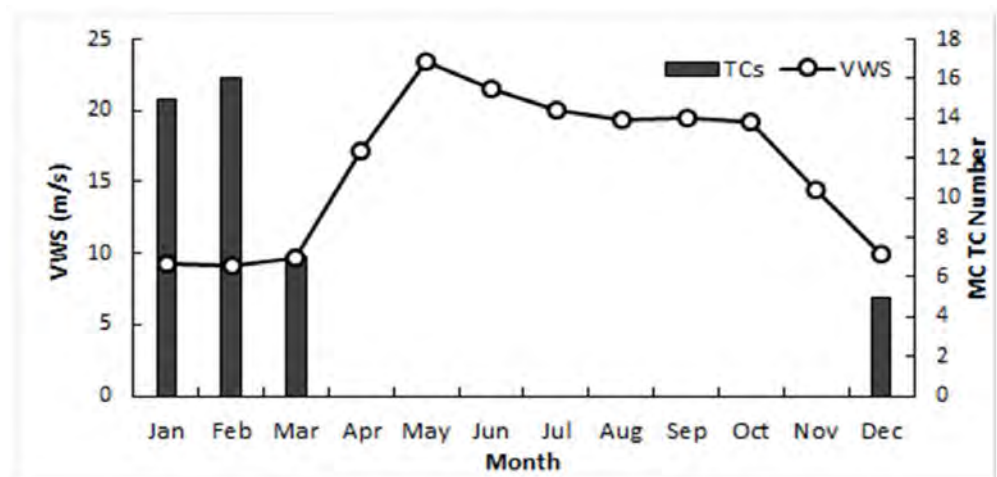


Figure 6. Monthly totals of cyclogenesis events in the MC (bars) and monthly mean VWS (m/s).

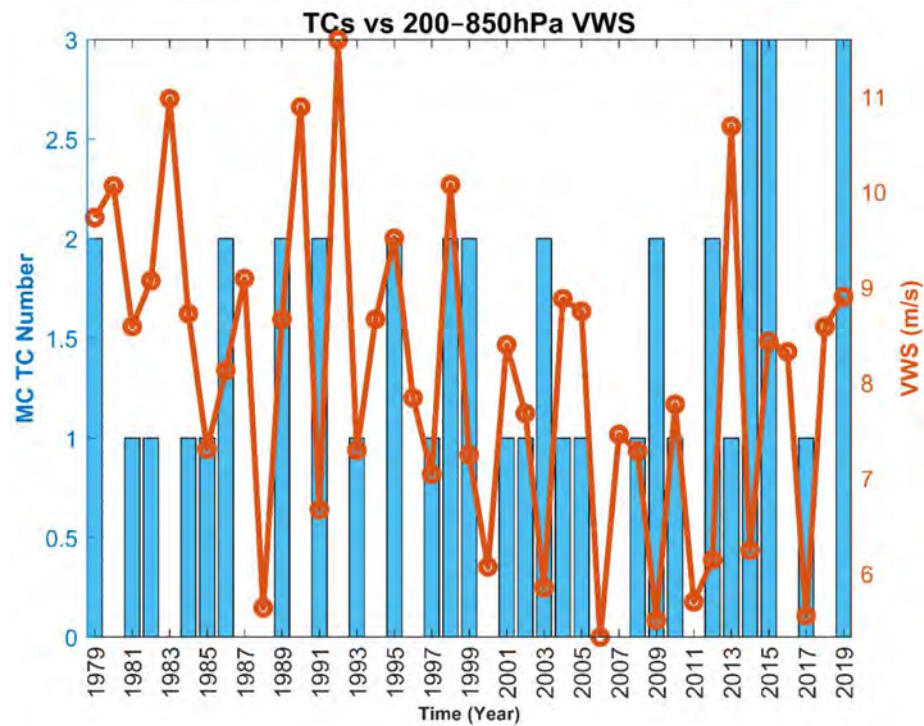


Figure 7. An overlay of the number of cyclones (blue bars) and 200–850 hPa VWS (red solid line) per season (Dec–Mar) over the MC between 1978/1979 and 2018/2019 TC seasons. The long-term linear trend and seasonal cycle have been removed in both time series.

VWS vs. TC Genesis and Intensity Correlations

Correlations were performed between the VWS in different layers and the number of TC genesis in the MC and also between the VWS in different layers and TC maximum intensity. The VWS and number of TC genesis correlations were in general weak. The VWS and TC maximum intensity correlations exhibited significant values for the bulk (200–850 hPa) and upper (200–500 hPa) atmosphere VWS (values above -0.4) while for the lower (500–850) atmosphere there were no significant correlations. Figure 8a,b shows plots of TC max intensity vs. VWS anomalies with the correlation coefficients shown on the top of the panels for 200–850 hPa (a) and 200–500 hPa (b). The long-term linear trend was removed from both time series.

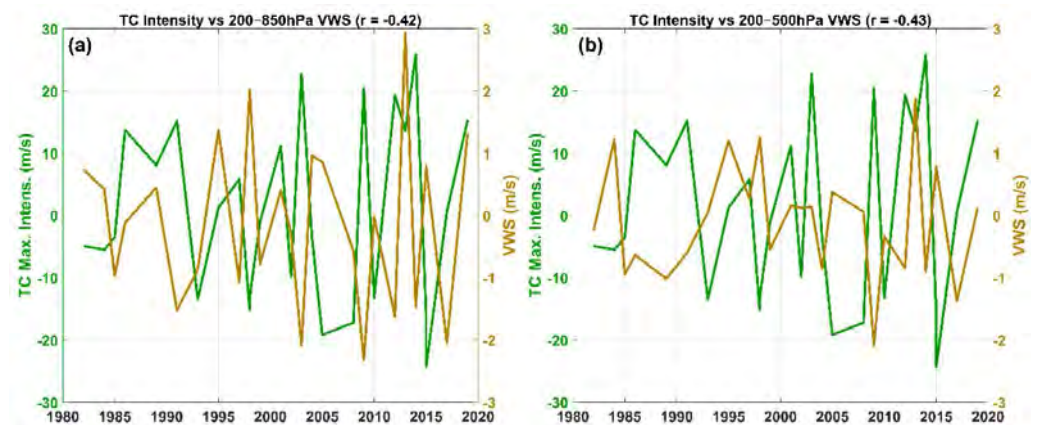


Figure 8. Plots of TC maximum intensity and VWS anomalies for 200–850 layer (a) and 200–500 hPa layer (b) for December–March over the MC. Green and red colors indicate the TC maximum intensity and VWS, respectively. The time series correlation coefficients (at zero lag) are shown on the top of the panel.

3.4. Vertical Wind Shear vs. TC Landfall Coast

During the analyzed period, 13 TC systems formed in the MC made landfall (six over Mozambique coast and seven over Madagascar west coast). Only systems with a storm intensity (equal or greater than 17 m/s) during landfall were considered. Composite anomalies (mean months with TC events making landfall-long term mean) of December–March 200–850 hPa VWS were analyzed to explore the potential role of VWS in the landfall position (Mozambique coast or Madagascar west coast). Figure 9 shows the composite anomalies. The VWS anomalies associated with landfall over Madagascar coast exhibit higher values over the MC, between 4 and 5 m/s (Figure 9a) as compared to values associated with landfall over the Mozambique coast, between 1 to 2 m/s (Figure 9b). The pattern of VWS direction is in general similar for the two cases, however, in case of landfall over Madagascar west coast the VWS is more zonal while for the Mozambique coast a meridional component is also observed. Significant (weak) low level geopotential and wind composite anomalies (figures not shown) are observed when the landfall is over the west coast Madagascar (Mozambique coast).

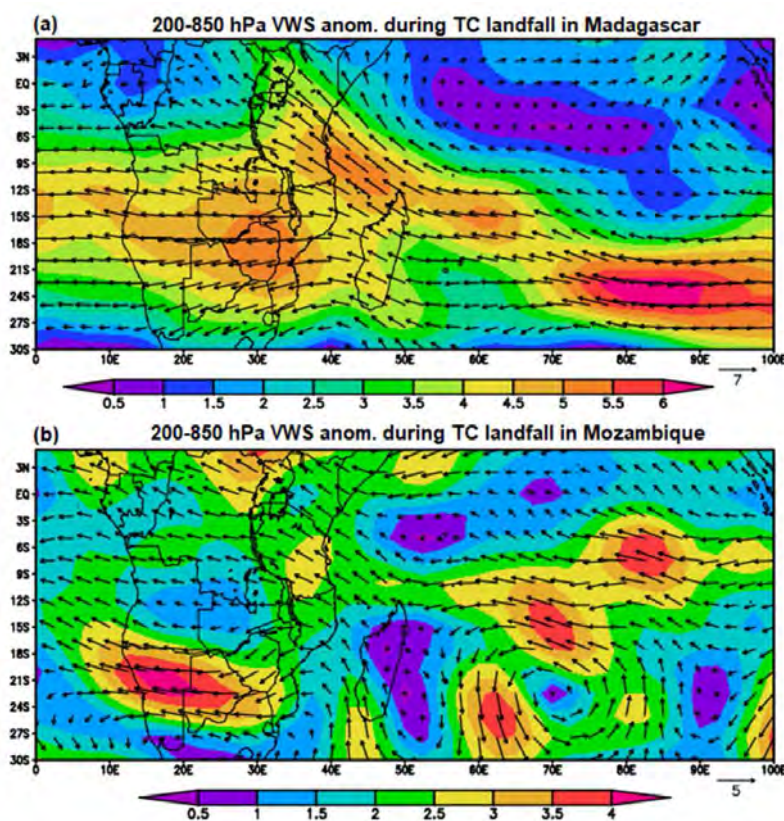


Figure 9. Composite anomalies of December–March 200–850 hPa VWS associated wind landfall over Madagascar west coast (a) and Mozambique coast (b).

3.5. Potential Role of Different Environmental Factors to the Cyclogenesis in the MC

January and February composite mean (only months with cyclogenesis events in the MC) of SST, relative vorticity at 850 hPa, relative humidity at 700 hPa and divergence at 200 hPa were calculated and mapped to explore their potential role on TC genesis over the MC (Figure 10). Mean SST (Figure 10a,b) exhibit high and significant values while the vorticity (Figure 10c,d) values are in general not significant over the MC during cyclogenesis. The relative humidity at 700 hPa (Figure 10e,f) and upper-level divergence (Figure 10g,h) also exhibit significant values ($45\text{--}60\%$ and $2\text{--}3.5 \times 10^{-5} \text{ s}^{-1}$ respectively) over the central and northern parts of the MC. However, correlation analyses between time series of the elements considered here and TC genesis and intensity did not show significant values.

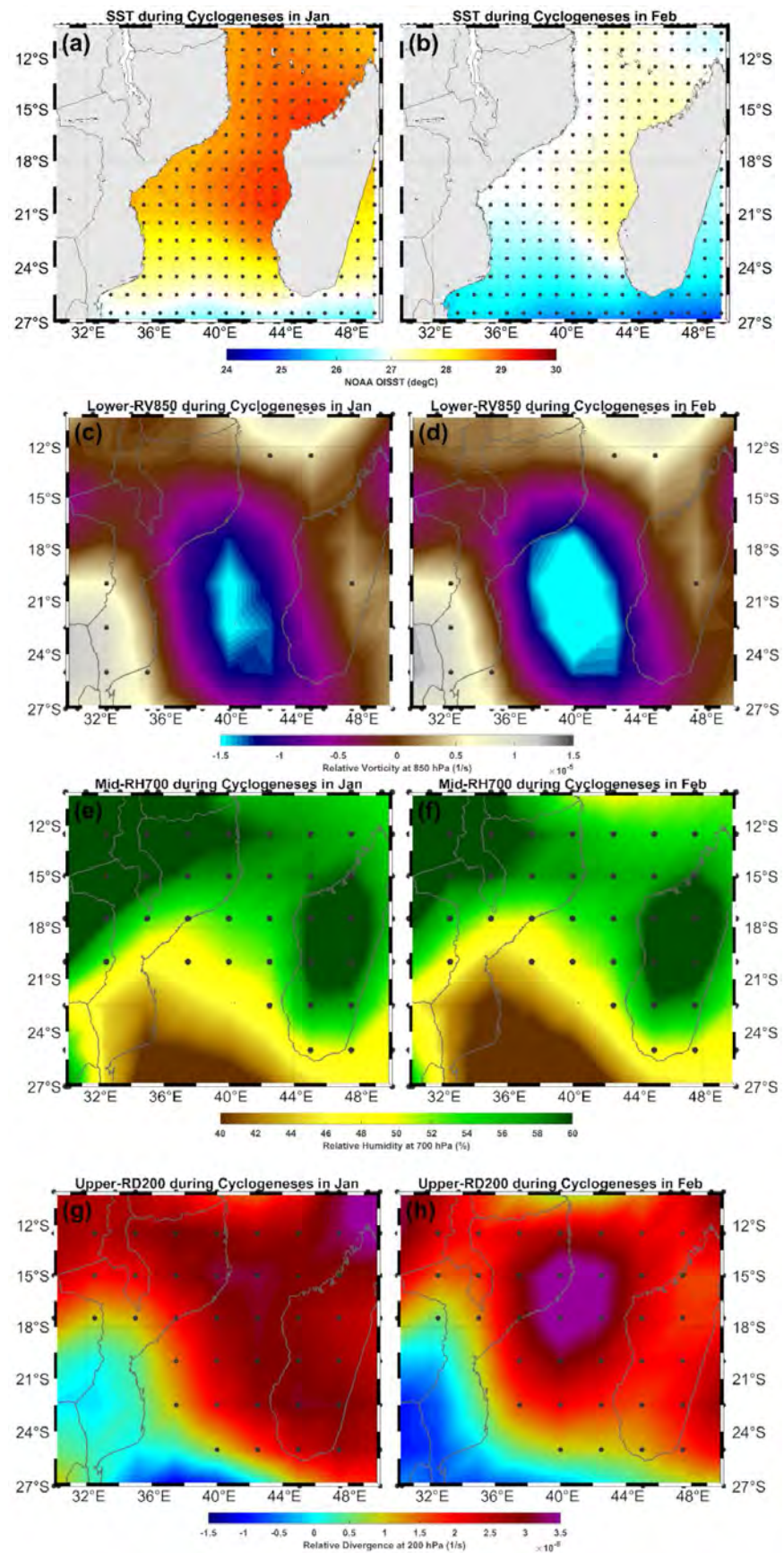


Figure 10. Composite mean of SST (a,b), vorticity at 850 hPa (c,d), relative humidity at 700 hPa (e,f) and divergence at 200 hPa (g,h) for January (left panel) and February (right panel) cyclogenesis (dots indicate 95% *t*-test confidence level).

Scatter plots analyses of January and February are used here to explore the relationship between the VWS and the environmental factors indicated above, averaged over the region ($16\text{--}22^\circ\text{ S}$ and $39\text{--}43^\circ\text{ E}$) of TC genesis maximum occurrence (Figure 11). All the environmental factors show a good and consistent relationship with the 200–850 hPa VWS. The SST and vorticity at 850 hPa show a negative linear relationship while relative humidity at 700 hPa, and divergence at 200 hPa show a positive linear relationship with the VWS.

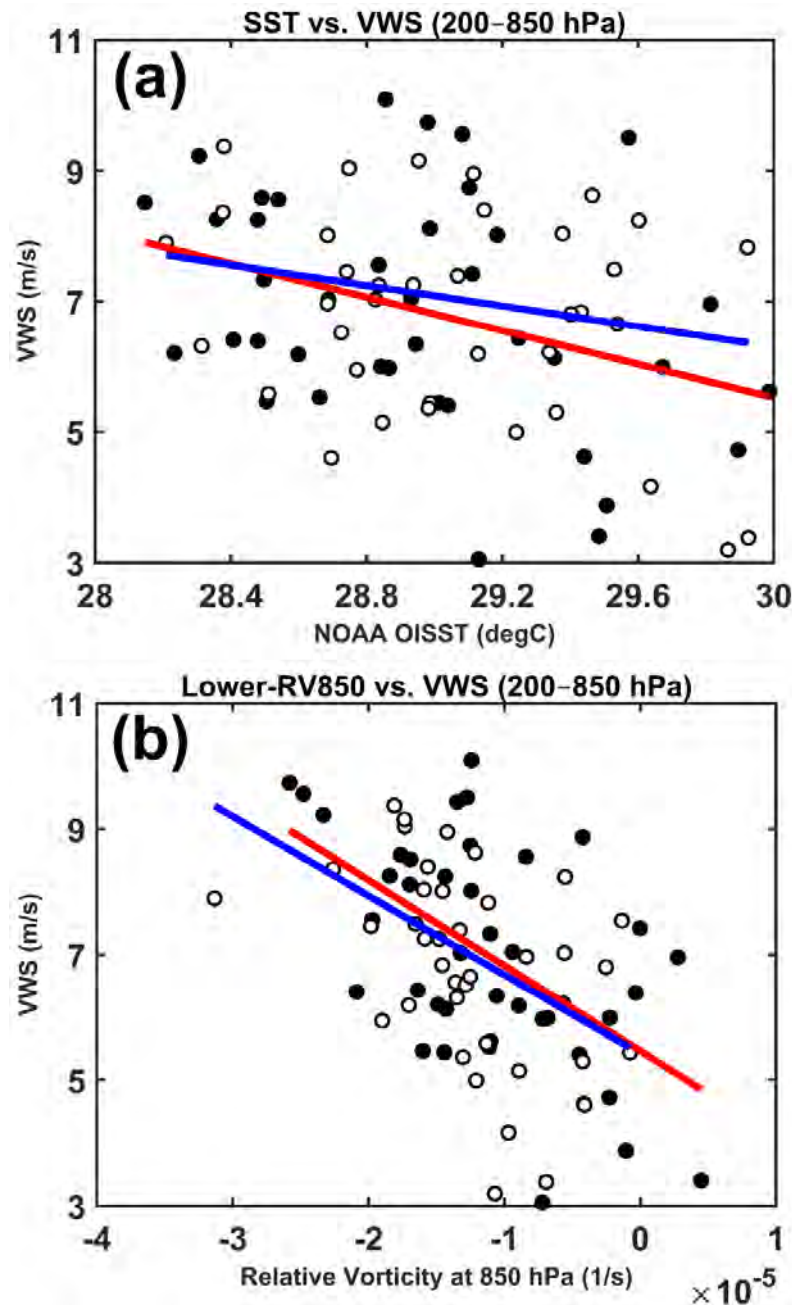


Figure 11. Cont.

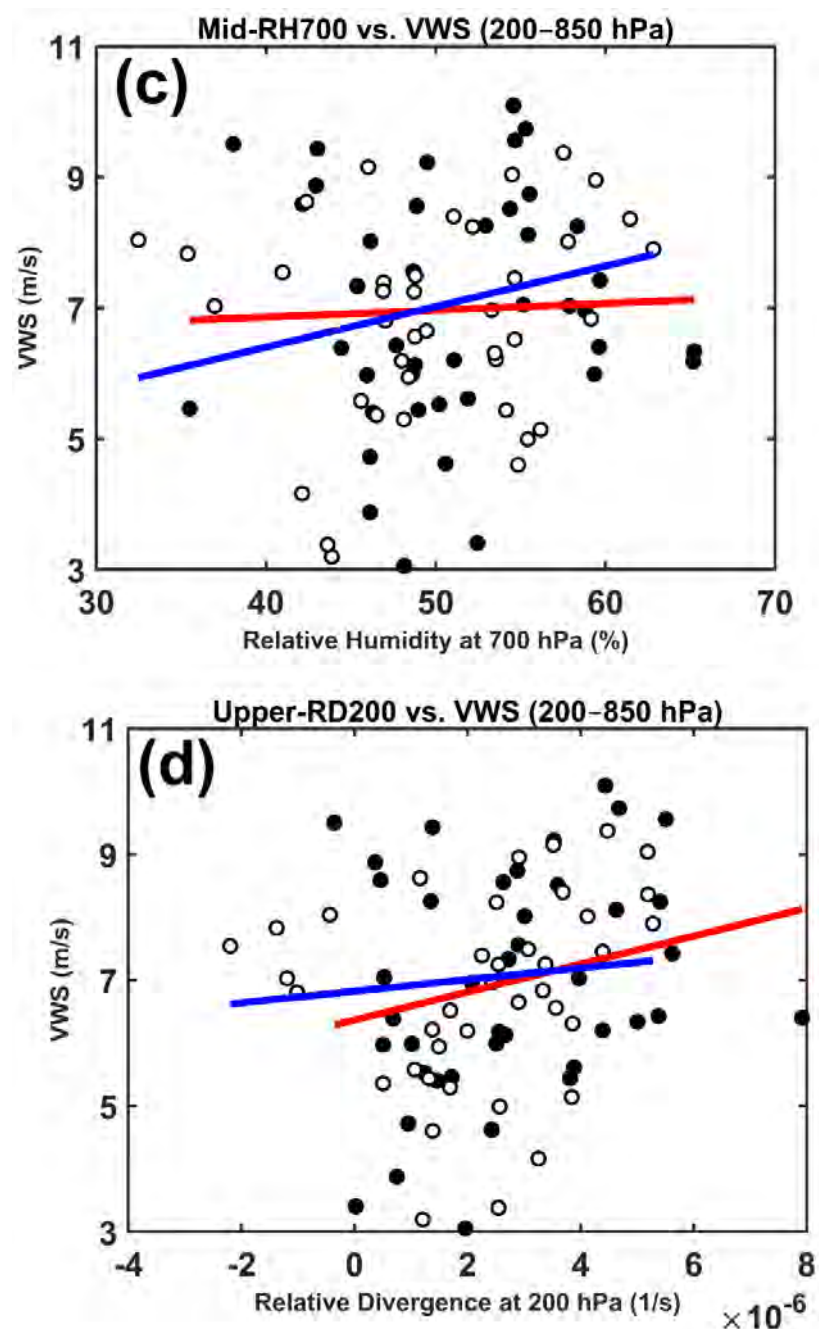


Figure 11. Relationship between VWS and SST (a), vorticity at 850 hPa (b), relative humidity at 700 hPa (c) and divergence at 200 hPa (d) for January (red line and black dots) and February (blue line and white dots).

4. Discussion

Lower values of mean 200–850 hPa VWS over the SWIO are observed during the period December–February, with a distinct band (values below 6 m/s) extending across central South Indian Ocean towards southern Africa. In the MC, the mean position of this band is located between the latitudes 16–22° S. The region is also coincident with the highest cyclogenesis in the MC, above 40 TC formed in the period here considered. January to March monthly VWS anomalies maps, plotted together with TC genesis, show that most TCs are formed in regions of negative anomalies, although some developed to at least TC intensity in regions with positive monthly anomalies. However, it is important to note that the February mean VWS, over the region where all the cyclogenesis was observed, is within the values considered to be favorable for TC genesis (e.g., [5]). The region in the MC

with maximum cyclogenesis events is coincident with the mean location of the center of the MC trough and the months (January and February) with highest events are also coincident with the period of the peak of strength of the trough. Barimalala et al. [29] indicate that the interannual variability in the MCT is associated with moist convection over the MC and is modulated by the location of the warm SST in the south Indian Ocean. These environmental conditions, as indicated in the introduction, are also important for cyclogenesis. Mean composite analyses of SST, relative humidity at 700 hPa and divergence at 200 hPa for January and February (with cyclogenesis) showed significant values, however, at the interannual timescale, no significant correlations were observed with TC genesis and TC maximum intensity. Statistically significant correlations were only observed between TC maximum intensity and VWS (200–850 hPa and 500–200 hPa) suggesting the influence of upper atmosphere vertical wind shear at interannual time scales in the development of TCs.

Correlation analyses of interannual variability of 200–850 hPa VWS (December–March) with Nino 3.4 (SIOD) index at different lags (SON, OND, NDJ, DJF and JFM), shown in Table 1, were significantly positive (negative). This suggests that high values of VWS are associated with El Niño, hence not favorable for TC intensification. Most of the 15 cases of TC that developed to at least TC intensity, developed under La Niña or neutral conditions (six under La Niña, six under neutral and three under El Niño conditions). It is noteworthy that four cases of the neutral condition were under the negative Niño-3.4 index. On the other hand, the negative correlation with the SIOD, suggests that warm SST over SWIO, linked to SIOD, is associated with weaker VWS over the MC. These results may indicate that both La Niña and positive SIOD are favorable to weaker VWS and to intensification of TC in the Mozambique Channel.

Analysis of composite anomalies of 200–850 hPa VWS for landfall events suggest that higher values over the MC are favorable to landfall over Madagascar west coast while weaker values are more favorable to landfall over the Mozambique coast. Composite analyses of low level geopotential height and wind suggest a significantly strengthened MC trough during landfall over the Madagascar west coast.

5. Conclusions

This study analyzed the seasonal to interannual relationship between vertical wind shear and the cyclogenesis and TC development in the Mozambique Channel. The cyclone activity in the MC has not been much studied, particularly the cyclogenesis, however, there is a significant number of cyclones making landfall or affecting Mozambique and Madagascar that are generated in the MC. The VWS over the SWIO is characterized by a band of minima magnitude, propagating southward and reaching its maxima southward position between January and February. Over the MC, the region of minima is associated with the highest number of cyclogenesis. A total of 43 cases of TC genesis were observed in the MC and 15 developed to at least Tropical Cyclone intensity. The VWS showed significant correlations with TC intensity, particularly when considering the upper atmosphere (200–500 hPa) or the bulk (200–850 hPa) VWS. The lower atmosphere VWS (500–850 hPa) did not show statistically significant correlation, a similar result was observed with the correlations between the TC genesis frequency and VWS. Analyses of interannual correlations of VWS and Niño-3.4 (SIOD) showed significant positive (negative) correlations at different lags suggesting that La Niña and positive phase of the SIOD conditions are favorable to weaker VWS and to intensification of TC in the Mozambique Channel. Thirteen landfall cases were observed with seven over the Madagascar west coast and six over the Mozambique coast. The landfall cases over the Madagascar (Mozambique) coast were associated with strengthened (weakened) VWS. The landfall events over Madagascar appear to also be associated with a significantly stronger MC trough.

Author Contributions: Conceptualization A.F.M., A.J.M. and I.A.G.; software, I.A.G., A.F.M. and B.J.N.; data acquisition and processing, I.A.G., A.J.M. and B.J.N.; writing—original draft preparation, I.A.G. and A.J.M.; writing—review and editing, all co-authors; supervision, A.J.M.; project administration, A.J.M.; funding acquisition, A.J.M. All authors have read and agreed to the published version of the manuscript.

Funding: This research work was funded by the European Union, La Réunion Regional Council and the French state under the framework of the INTERREG-5 Indian Ocean 2014–2020 project “ReNovRisk Cyclone and Precipitation”.

Institutional Review Board Statement: Not applicable.

Informed Consent Statement: Not applicable.

Data Availability Statement: Data used here is freely available on the internet and the sources are indicated in the manuscript and referenced in the reference list.

Acknowledgments: The authors would like to thank Eduardo Mondlane University, Faculty of Sciences (UEM-FC) in Maputo, Mozambique, where all computer work was conducted including the software facilities provided by the Department of Physics. The authors would also like to thank the important contribution of the reviewers who through their comments contributed significantly for the improvement of this paper.

Conflicts of Interest: The authors declare no conflict of interest with regard to this work and publication in this journal.

Software: The data analysis and output for this paper was generated using Matlab software, Version [10a], License number 506085, from the Department of Physics, Faculty of Sciences, UEM, Maputo, Mozambique.

References

1. Gray, W.M. Global view of the origin of tropical disturbances and storms. *Mon. Weather Rev.* **1968**, *96*, 669–700. [[CrossRef](#)]
2. Chan, K.T.F.; Wang, D.; Zhang, Y.; Wanawong, W.; He, M.; Yu, X. Does strong vertical wind shear certainly lead to the weakening of a tropical cyclone? *Environ. Res. Commun.* **2019**, *1*, 1–13. [[CrossRef](#)]
3. Emanuel, K.; DesAutels, C.; Holloway, C.; Korty, R. Environmental control of tropical cyclone intensity. *J. Atmos. Sci.* **2004**, *61*, 843–856. [[CrossRef](#)]
4. Finocchio, P.M.; Majumdar, S.J. A Statistical Perspective on Wind Profiles and Vertical Wind Shear in Tropical Cyclone Environments of the Northern Hemisphere. *Mon. Weather Rev.* **2017**, *145*, 361–378. [[CrossRef](#)]
5. Aiyyer, A.R.; Thorncroft, C. Climatology of Vertical Wind Shear over the Tropical Atlantic. *J. Clim.* **2006**, *19*, 2969–2983. [[CrossRef](#)]
6. Nolan, D.S.; McGauley, M.G. Tropical cyclogenesis in wind shear: Climatological relationships and physical processes. In *Cyclones: Formation, Triggers and Control*; Nova Science Publishers, Inc.: New York, NY, USA, 2012; pp. 1–36.
7. Jones, J.J.; Bell, M.M.; Klotzbach, P.J. Tropical and Subtropical North Atlantic Vertical Wind Shear and Seasonal Tropical Cyclone Activity. *J. Clim.* **2020**, *33*, 5413–5426. [[CrossRef](#)]
8. Molinari, J.; Vollaro, D. Rapid Intensification of a Sheared Tropical Storm. *Mon. Weather Rev.* **2010**, *138*, 3869–3885. [[CrossRef](#)]
9. Montgomery, M.T.; Lussier, L.L., III; Moore, R.W.; Wang, Z. The genesis of Typhoon Nuri as observed during the Tropical Cyclone Structure 2008 (TCS-08) field experiment—Part 1: The role of the easterly wave critical layer. *Atmos. Chem. Phys.* **2010**, *10*, 9879–9900. [[CrossRef](#)]
10. Rios-Berrios, R.; Torn, R.D.; Davis, C.A. An Ensemble Approach to Investigate Tropical Cyclone Intensification in Sheared Environments. Part II: Ophelia (2011). *J. Atmos. Sci.* **2016**, *73*, 1555–1575. [[CrossRef](#)]
11. Mundell, D.B. Prediction of Tropical Cyclone Rapid Intensification Events. Master’s Thesis, Colorado State University, Fort Collins, CO, USA, 1990.
12. DeMaria, M. The effect of vertical shear on tropical cyclone intensity change. *J. Atmos. Sci.* **1996**, *53*, 2076–2087. [[CrossRef](#)]
13. Zehr, R.M. Environmental vertical wind shear with Hurricane Bertha (1996). *Weather Forecast.* **2003**, *18*, 345–356. [[CrossRef](#)]
14. Bracken, W.E.; Bosart, L.F. The role of Synoptic-Scale flow during tropical cyclogenesis over the North Atlantic Ocean. *Mon. Weather Rev.* **2000**, *128*, 353–376. [[CrossRef](#)]
15. Zehr, R.M. *Tropical Cyclogenesis in the Western North Pacific*; NOAA Technical Report NESDIS 61; NOAA: St. Petersburg, FL, USA, 1992; p. 181.
16. Fink, H.A.; Speth, P. Tropical cyclones. *Naturwissenschaften* **1998**, *85*, 482–493. [[CrossRef](#)]
17. Ho, C.-H.; Kim, J.-H.; Jeong, J.-H.; Kim, H.-S.; Chen, D. Variation of tropical cyclone activity in the South Indian Ocean: El Niño–Southern Oscillation and Madden-Julian Oscillation effects. *J. Geophys. Res.* **2006**, *111*, 1–9. [[CrossRef](#)]
18. Mavume, A.F.; Rydberg, L.; Rouault, M.; Lutjeharms, J.R.E. Climatology and landfall of tropical cyclones in the SouthWest Indian Ocean. *J. Mar. Sci.* **2009**, *8*, 15–36.

19. Malherbe, J.; Engelbrecht, F.A.; Landman, W.A.; Engelbrecht, C.J. Tropical systems from the southwest Indian Ocean making landfall over the Limpopo River Basin, southern Africa: A historical perspective. *Int. J. Climatol.* **2012**, *32*, 1018–1032. [[CrossRef](#)]
20. WMO. *Global Guide to Tropical Cyclone Forecasting*; Guard, C., Ed.; WMO: Geneva, Switzerland, 2017; p. 399. Available online: <http://www.wmo.int/cycloneguide/pdf/Global-Guide-to-TropicalCyclone-Forecasting.pdf> (accessed on 7 January 2020).
21. Leroux, M.-D.; Meister, J.; Mekies, D.; Dorla, A.-L. A Climatology of Southwest Indian Ocean Tropical Systems: Their Number, Tracks, Impacts, Sizes, Empirical Maximum Potential Intensity, and Intensity Changes. *J. Appl. Meteorol. Climatol.* **2018**, *57*, 1021–1041. [[CrossRef](#)]
22. Bousquet, O.; Barruol, G.; Cordier, E.; Barthe, C.; Bielli, S.; Calmer, R.; Rindraharisaona, E.; Roberts, G.; Tulet, P.; Amelie, V.; et al. Impact of Tropical Cyclones on Inhabited Areas of the SWIO Basin at Present and Future Horizons. Part 1: Overview and Observing Component of the Research Project RENOVRISK-CYCLONE. *Atmosphere* **2021**, *12*, 544. [[CrossRef](#)]
23. Chen, S.S.; Knaff, J.A.; Marks, F.D., Jr. Effects of Vertical Wind Shear and Storm Motion on Tropical Cyclone Rainfall Asymmetries Deduced from TRMM. *Mon. Weather Rev.* **2006**, *134*, 3190–3208. [[CrossRef](#)]
24. Bessafi, M.; Wheeler, M.C. Modulation of South Indian Ocean Tropical Cyclones by the Madden–Julian Oscillation and Convectively Coupled Equatorial Waves. *Mon. Weather Rev.* **2006**, *134*, 638–656. [[CrossRef](#)]
25. Kuleshov, Y.; Ming, F.C.; Qi, L.; Chouaibou, I.; Hoareau, C.; Roux, F. Tropical cyclone genesis in the Southern Hemisphere and its relationship with the ENSO. *Ann. Geophys.* **2009**, *27*, 2523–2538. [[CrossRef](#)]
26. Jury, M.R.; Pathack, B. A study of climate and weather variability over the tropical Southwest Indian Ocean. *Meteorol. Atmos. Phys.* **1991**, *47*, 37–48. [[CrossRef](#)]
27. Jury, M.R. A preliminary study of climatological associations and characteristics of tropical cyclones in the SW Indian Ocean. *Meteor. Atmos. Phys.* **1993**, *51*, 101–115. [[CrossRef](#)]
28. Matyas, C.J. Tropical cyclone formation and motion in the Mozambique Channel. *Int. J. Climatol.* **2015**, *35*, 375–390. [[CrossRef](#)]
29. Barimalala, R.; Blamey, R.C.; Desbiolles, F.; Reason, C.J.C. Variability in the Mozambique Channel Trough and Impacts on Southeast African Rainfall. *J. Clim.* **2020**, *33*, 749–765. [[CrossRef](#)]
30. Cook, H.H. The South Indian Convergence Zone and Interannual Rainfall Variability over Southern Africa. *J. Clim.* **2000**, *13*, 3789–3804. [[CrossRef](#)]
31. Barimalala, R.; Desbiolles, F.; Blamey, R.C.; Reason, C. Madagascar Influence on the South Indian Ocean Convergence Zone, the Mozambique Channel Trough and Southern African Rainfall. *Geophys. Res. Lett.* **2018**, *45*, 11380–11389. [[CrossRef](#)]
32. Kalnay, E.; Kanamitsu, M.; Kistler, R.; Collins, W.; Deaven, D.; Gandin, L.; Iredell, M.; Saha, S.; White, G.; Woollen, J.; et al. The NCEP/NCAR 40-Year Reanalysis Project. *B. Am. Meteorol. Soc.* **1996**, *77*, 437–472. [[CrossRef](#)]
33. Reynolds, R.W.; Rayner, N.A.; Smith, T.M.; Stokes, D.C.; Wang, W. An Improved in Situ and Satellite SST Analysis for Climate. *J. Clim.* **2002**, *15*, 1609–1625. [[CrossRef](#)]
34. Rios-Berrios, R.; Torn, R.D. Climatological Analysis of Tropical Cyclone Intensity Changes under Moderate Vertical Wind Shear. *Mon. Weather Rev.* **2017**, *145*, 1717–1738. [[CrossRef](#)]
35. Bahera, S.K.; Yamagata, T. Subtropical SST dipole events in the southern Indian Ocean. *Geophys. Res. Lett.* **2001**, *28*, 327–330. [[CrossRef](#)]



atmosphere



Article

Analysis of Climate Change Projections for Mozambique under the Representative Concentration Pathways

Alberto F. Mavume, Bionídio E. Banze, Odete A. Macie and António J. Queface

Special Issue

Tropical Cyclones in the Indian Ocean

Edited by

Prof. Dr. Olivier Bousquet



<https://doi.org/10.3390/atmos12050588>

Article

Analysis of Climate Change Projections for Mozambique under the Representative Concentration Pathways

Alberto F. Mavume ^{1,*}, Bionídio E. Banze ¹, Odete A. Macie ¹ and António J. Queface ^{1,2}

¹ Departamento de Física, Faculdade de Ciências, Universidade Eduardo Mondlane, Avenida Julius Nyerere, 3453, Campus Universitário Principal, 257 Maputo, Mozambique; bionidio.banze@uem.mz (B.E.B.); odete.macie@uem.mz (O.A.M.); queface@uem.mz (A.J.Q.)

² Instituto Nacional de Gestão e Redução do Risco de Desastres, Programa de Gestão do Risco de Desastres e Resiliência, Rua Gare de Mercadorias, 690 Maputo, Mozambique

* Correspondence: amavume@uem.mz; Tel.: +258-21-493-377

Abstract: Despite having contributed the least to global warming and having the lowest emissions, the African region is the most vulnerable continent to climate change impacts. To reduce the levels of risk arising from climate change, it is mandatory to combine both mitigation and adaptation. While mitigation can reduce global warming, not all impacts can be avoided. Therefore, adaptation is essential to advance strategic interventions and reduce the impacts. As part of the international effort to cope with changing climate, a set of Coordinated Regional Downscaling Experiment (CORDEX) domains have been established worldwide. The CORDEX-Africa initiative has been developed to analyze downscaled regional climate data over the African domain for climate data analysis techniques and engage users of climate information in both sector-specific and region/space-based applications. This study takes outputs of high-resolution climate multi-models from the CORDEX-Africa initiative constructed at a spatial resolution of 50 km to assess climate change projections over Mozambique. Projected spatial and temporal changes (three 30-year time periods, the present (2011–2040), mid (2041–2070), and the end (2071–2100)) in temperature and precipitation under the Representative Concentration Pathways RCP2.6, RCP4.5, and RCP8.5 are analyzed and compared relative to the baseline period (1961–1990). Results show that there is a tendency toward an increase in annual temperature as we move toward the middle and end of the century, mainly for RCP4.5 and RCP8.5 scenarios. This is evident for the Gaza Province, north of the Tete Province, and parts of Niassa Province, where variations will be T_{max} (0.92 to 4.73 °C), T_{min} (1.12 to 4.85 °C), and T_{mean} (0.99 to 4.7 °C). In contrast, the coastal region will experience less variation (values < 0.5 °C to 3 °C). At the seasonal scale, the pattern of temperature change does not differ from that of the annual scale. The JJA and SON seasons present the largest variations in temperature compared with DJF and MAM seasons. The increase in temperature may reach 4.47 °C in DJF, 4.59 °C in MAM, 5.04 °C in JJA, and 5.25 °C in SON. Precipitation shows substantial spatial and temporal variations, both in annual and seasonal scales. The northern coastal zone region shows a reduction in precipitation, while the entire southern region, with the exception of the coastal part, shows an increase up to 40% and up to 50% in some parts of the central and northern regions, in future climates for all periods under the three reference scenarios. At the seasonal scale (DJF and MAM), the precipitation in much of Mozambique shows above average precipitation with an increase up to more than 40% under the three scenarios. In contrast, during the JJA season, the three scenarios show a decrease in precipitation. Notably, the interior part will have the largest decrease, reaching a variation of –60% over most of the Gaza, Tete, and Niassa Provinces.



Citation: Mavume, A.F.; Banze, B.E.; Macie, O.A.; Queface, A.J. Analysis of Climate Change Projections for Mozambique under the Representative Concentration Pathways. *Atmosphere* **2021**, *12*, 588. <https://doi.org/10.3390/atmos12050588>

Academic Editor: Mohammad Valipour

Received: 10 March 2021

Accepted: 24 April 2021

Published: 1 May 2021

Publisher's Note: MDPI stays neutral with regard to jurisdictional claims in published maps and institutional affiliations.



Copyright: © 2021 by the authors. Licensee MDPI, Basel, Switzerland. This article is an open access article distributed under the terms and conditions of the Creative Commons Attribution (CC BY) license (<https://creativecommons.org/licenses/by/4.0/>).

Keywords: climate change; CORDEX-Africa; RCP; temperature; precipitation; Mozambique

1. Introduction

According to the International Panel on Climate Change (IPCC) Fifth Assessment Report (AR5), climate change warming is unequivocal, while it is extremely likely that

this is a result of anthropogenic activities. For instance, recent climate changes have had widespread impacts on human and natural systems worldwide [1].

Despite having contributed the least to global warming and having the lowest emissions, Africa faces exponential collateral damage, posing systemic risks to its economies, infrastructure investments, water and food systems, public health, agriculture, and livelihoods, threatening to undo its modest development gains and slip into higher levels of extreme poverty. This situation is aggravated by the interaction of ‘multiple stresses’, occurring at various levels and low adaptive capacity [2].

Mozambique is one of the African countries most exposed to climate-related risks, which is and will be exacerbated by climate change. Extreme dangerous and destructive events are remarkable and have been associated with the occurrence of disasters of major socio-economic impacts [3]. Its population was 13 million in 1990, it reached 27.9 million in 2017 and 29.5 million in 2018 with a growth rate of 2.9% per annum [4,5]. The Southern African sub-region (South Africa and Mozambique) is, after Northern Africa, the continent’s most urbanized and is projected to reach a region-wide urban majority around the end of the current decade. South Africa reached an urban majority of 62% in 2011 with Mozambique projected to reach an urban majority by 2050 [6]. The urban population is low (33.4%) and the rural population is high (66.6%), but the wealth distribution is also uneven [7]. About 43% of the population resides within the coastal region of the country. Mozambique has been one of Africa’s fastest growing economies throughout the past years, driven by investments related to the exploration of multiple natural resources. The Mozambique economy generally demonstrated growth in the 2010–2018 period; however the country’s Gross Domestic Product (GDP) per capita has declined over the past decade, from 458 USD in 2007 to 443 USD in 2017, reflecting the country’s population growth [7]. While the population growth numbers and investments are increasing, the vulnerability of the country is also increasing as coastal zones are exposed to a range of coastal hazards such as sea level rise, storm surges, and tropical cyclones. The 2018–2019 southwest Indian Ocean tropical cyclone season was remarkable, being the deadliest and costliest season ever recorded (≈ 1380 deaths and \approx USD 2.3 billion damage). Although the number of cyclones was exceptional across the region, most of the deaths and damage occurred as a result of Intense Tropical Cyclone IDAI. The situation become exacerbated on 25 April, with the appearance of Intense Tropical cyclone Kenneth, which was classified as the strongest cyclone to ever make landfall in Mozambique. This TC struck the Mozambique coast further north, resulting in considerable damage and socio-economic impacts (≈ 45 deaths and \approx USD 100 million damage) [8]. Weather associated with both cyclones affected the central and northern regions of Mozambique, including the neighboring countries of Zimbabwe and Malawi. These destructive cyclones resulted in severe humanitarian impacts, including hundreds of casualties and hundreds of thousands of displaced persons [8–10]. Therefore, vulnerability may increase, as the climate affects human lives, agriculture, water, health, infrastructure, and other aspects of daily life. Extreme weather events such those aforementioned among others including extreme precipitation and floods [11,12] and severe droughts [13], and high extreme temperatures and heat waves [14–16] are predicted to continue and pose significant social and economic pressures within several parts of Africa and elsewhere, while there is mounting evidence suggesting that the frequency and intensity of some events will change in the future due to climate change [17,18].

Post-2015, the Nationally Determined Contributions (NDCs) to the Paris Agreement (PA) have become the main instrument for guiding policy responses to climate change [10]. Three main actions emerged from PA 2015 showing the willingness of national governments to strengthen the global response to the threat of climate change: (i) to keep global temperature rise well below 2 °C above pre-industrial levels, and to pursue determined efforts to limit the temperature increase even further to 1.5 °C; (ii) to strengthen the ability of countries to adapt to climate change and develop low-carbon emission technology; and (iii) to make finance flows consistent with a pathway toward low-carbon emissions and climate-resilient development [19,20]. These two thresholds provided a strong signal for

the governments to take urgent decisions and actions to mitigate the ongoing and future climate change and for the scientific community to assess the various implications that could arise if warming overcomes 1.5–2 °C. A recent study [21] shows considerable global economic gains from complying with the Paris Climate Accord. With the implementation of the NDCs (formerly defined as Intended Nationally Determined Contributions, INDCs), aggregate global emission levels would be lower than in pre-INDC trajectories [21]. These efforts are greatly recognized; however, the translation of these commitments into plausible binding targets of greenhouse gas reductions at the national level is still slow. According to the UN Environment's 2019 Emissions Gap Report, the emissions will continue to increase, even if all national commitments under the Paris Agreement are implemented through the NDC and other regulatory mechanisms. The fact is the world is still on the course for around 3 °C of warming above pre-industrial levels [22,23]. Mozambique's NDC states clearly its adaptation mission to "reduce climate change vulnerability and improve the wellbeing of Mozambicans through the implementation of concrete measures for adaptation and climate risk reduction, promoting mitigation and low-carbon development, aiming at sustainable development, with the active participation of all stakeholders in the social, environmental and economic sectors". Mozambique has committed to reduce about 76.5 metric tons of carbon dioxide equivalent (76.5 MtCO₂eq) from 2020 to 2030, which is conditional on the provision of support from the international community [24].

The two PA thresholds goals are essentially viewed as means to quantify if there is a significant reduction in regional and local climate risks and demonstrating benefits in limiting warming below 1.5 °C [25]. It is likely that negative effects of 0.5 °C increment can be seen in extreme events. For instance, estimates indicate that the chances of an extreme event at 0.5 °C warming is almost two times than that at 1.5 °C [26]. GDP loss estimates per year under global warming scenarios (2, 3, and 4 °C) are expected to be higher, and the relative damages from not complying with the 2 °C target for Southern Africa are particularly severe [21].

Temperature and precipitation are two key indicators that characterize the state of the climate and which have continuously affected living conditions in many geographical locations in Africa [10]. Thus, by changing the temperature and precipitation patterns, climate change becomes a major concern to the survival of the human being as it poses significant risks and impacts on the natural resources, environment, and surrounding assets.

Over Southern Africa, there is a positive sign of change for temperature, with temperature rising faster at 2 °C (1.5–2.5 °C) as compared to 1.5 °C (0.5–1.5 °C) of global warming. On the other hand, the region is projected to face robust precipitation decreases of about 10–20% and increases in the number of consecutive dry days and decrease in the number of consecutive wet days [20]. However, it is likely that some hotspots will face robust precipitation increases in some places. For instance, a projected increase in temperature is expected to influence the multiplication of pests, weeds, and several diseases that would lead to increased costs of crop production and failure in crop yields as well as reduction in food and water resources availability [20,27,28]. Some areas may become drier as a result temperature increases with increasing drought frequency and number of heatwaves [29–31]. Warming will also increase evaporation and transpiration rates that would result reductions in stream flow for hydroelectric power [32,33]. In addition, warming is also likely to increase outbreaks of waterborne diseases and diseases transmitted by rodents [34–38]. The projected increases in rainfall are likely to influence nutrient loss, removal of the top fertile layer of soil and saturation of soil, pests disease outbreaks, and infrastructure damage that would result in low crop yields and disruption of the food supply chain [1,20,36,39,40]. Changes in precipitation patterns are projected to cause severe flooding during the rainy season and severe drought during the dry season [41]. This scenario is likely to affect several business and economic sectors.

Within Southern Africa, Mozambique is one of the hotspots, as it is particularly vulnerable to climate change compounded by high levels of poverty and strong reliance on the rain-fed agriculture sector to drive its economy, employment opportunities, and

food security. The agriculture sector in Mozambique, being largely driven by smallholder farmers, is the primary livelihood basis for 80% of the population and contributes to the overall national economy with approximately 31.5% of the Gross Domestic Product (GDP) [42]. The majority of sectors, particularly agriculture, food security, and water resources, are strongly impacted by variations in temperature and precipitation. The impacts described above are currently happening and causing socio-economic impacts in Mozambique and are likely to be an additional challenge for the country to achieve various sustainable development goals and other national targets.

In this regard, monitoring and understanding the spatial and temporal characteristics of these two indicators (temperature and precipitation) under future climate, along with underlying impacts, at regional and local levels is crucial for strengthening science–policy dialogue and support decision making in the development of effective and science-based adaptation strategies at all levels of governance and sectors.

To perform this exercise, Global Circulation Models also or referred to as Global Climate Models (GCMs) have been used to assess the causes of past changes and for projecting temperature and precipitation changes in the future [43].

GCMs are complex computer models, as well as fundamental tools, designed to provide several important outputs, at a global scale, typically at a spatial scale of 200–330 km, for instance, which is not relevant for studies or applications at regional and local scales [41]. Climate change projections of high quality are performed by downscaling techniques and are often required in climate change impact assessments studies at regional and local scales [25,44,45]. They are also important for informing policy makers and the society on how science-based evidence can contribute to foster actionable mitigation and adaptation measures [46]. Therefore, downscaling of outputs from GCM is a required and important approach to overcome common limitations in the GCM such as coarse spatial resolution and bias [44,47]. The main approaches to downscale outputs from GCMs are (i) statistical downscaling [47,48] and (ii) dynamic downscaling [49]. These approaches result mainly not only from the spatial resolution but also from the more realistic or complete physics representation in Regional Climate Models (RCMs), which allow for obtaining detailed climate information about dynamic processes taking place in specific regions [50]. Dynamic downscaling, which relies on the boundary conditions from GCMs, is seen as the most appropriate approach for the better representation of these processes on climate variables [49]. However, these capabilities are not always available for all, because they demand high computational requirements, particularly if they are of dynamic type [48]. For a comprehensive review about the types and main features of downscaling techniques, see [44]. On the other hand, in regions with low station coverage, weak data infrastructure, and limited modeling capabilities, people are often facing big challenges for conducting their assessments. Currently, there is a significant number of collaborative projects producing climate simulation from dynamic downscaling for model inter-comparisons and impact assessment. Today, thanks to the various collaborative projects around the world, climate simulations derived from dynamic downscaling for model inter-comparisons and impact assessments can be accessed [44]. Some of these projects involve the COordinated Regional Downscaling EXperiment (CORDEX) initiative, which produces dynamically downscaled climate simulations for all continents, including Africa. The CORDEX initiative is the most comprehensive effort ever made in coordinating regional climate projections throughout the world [46] and, for instance, an opening window for the scientific community to access these facilities to get the climate information and skills needed to conduct their own assessments. The CORDEX initiative was pioneered by the World Climate Research Programme (WCRP) to produce high-resolution climate datasets over different parts of the world, of which Africa was the first target region selected for the experiments [51].

Scientific research focusing on GCMs and downscaling techniques to produce climate change projections is receiving more attention in recent years, particularly from research groups of CORDEX community and affiliates. For instance, more than 60 research articles have been published under the CORDEX Africa initiative since 2012 and are publicly

available at the Climate Systems Analysis Group (CSAG), University of Cape Town, South Africa (<http://www.csag.uct.ac.za/cordex-africa/cordex-africa-publications/>, accessed on 12 March 2020). The majority of these studies are either focusing on the CORDEX Africa domain [25,52] or its subregions, namely, East Africa [47,53], West Africa [54,55], Southern Africa [31,56,57], Greater Horn of Africa [58], and the Congo Basin [59]. Some country-level studies have been conducted for Botswana [16], Tanzania [44,60], and Zimbabwe [61], among few others. In general, these publications address various applications providing a comprehensive range of a plausible future within the CORDEX Africa domain or under its subregions or countries. Regional analysis with RCMs in these studies highlighted the indisputable value of the downscaling approach compared to GCMs, as in most cases, it showed good performance in reproducing finer details among other features in both temperature and precipitation projections [25,52].

While some countries might have substantial progress in conducting studies and publishing such results, others have very limited published work, adding to the fact that either GCMs or RCMs downscaling techniques have not been or are poorly implemented and issues such as data infrastructure including the working environment need to be improved and expanded. These limited capabilities elements are common in several countries in Africa, particularly in Mozambique, which is the subject of the current research.

The research entitled “Impact of climate change on disaster risk in Mozambique”, conducted by the National Institute for Disaster Risk Management and Reduction (INGD), former the National Institute for Disaster Management (INGC) was widely cited and became the first to apply climate change models on a regional scale to produce future climate change in Mozambique [62]. The study provided the country with an important view on the possible impacts of climate change on national investment and poverty reduction plans as well as the large sections of the coast characterized by human settlements and investments. The study [3] revealed that climate change and disaster risk go hand in hand because most of the impacts of climate change will be felt in the form of increased risk, spread, intensity, and frequency of natural disasters. Ref. [41] used the statistical downscaling of seven GCMs downscaled to each of the selected 39 station locations. All GCMs were used in the IPCC 4th Assessment Report and forced with SRES A2 emissions scenario (IPCC, 2000—which assumes that society will continue to use fossil fuels at a moderate growth rate, there will be less economic integration, and populations will continue to expand) for the 1960–2005, 2046–2065, and 2080–2100 periods. Ref. [41] found that both maximum and minimum temperatures are projected to increase by 1.5–3 °C in all seasons by all seven GCMs by the middle of the century (2046–2065). Exceptionally, the September–October–November (SON) season will experience the most increase—an increase of 2.5–3 °C. These increases in temperature are expected to be higher more toward inland and less at the coast, partially due to the moderate influence of the ocean. By the end of the century (2081–2100), temperature in the central region will increase by as much as 5–6 °C. Previous studies [29] found the same results, with most of the Southern African region projected to increase between 4 and 6 °C by the 2100s under the A2 SRES emissions scenario. The downscaled projections from seven GCMs [41] suggest an increase in precipitation in the December–May period by the middle of the century and end of this century, particularly in coastal areas considering significant spread between the models, which is indeed a challenge. However, increases in precipitation are likely to be greatest toward the end of the summer season, particularly in the north and coastal regions.

The objective of this work is to use the available CORDEX-Africa archives of regional climate modeled data and make a subset for the Mozambique domain in order to provide a comprehensive range of projected future changes. The study focuses on annual and seasonal temperature and precipitation changes and takes outputs of high-resolution climate ensemble from the CORDEX-Africa Initiative constructed at a spatial resolution of 50 km. It is notably part of the ReNovRisk-Cyclone research program, which aims to assess the impact of climate change on tropical cyclone activity and water resources in the southwest Indian Ocean basin, particularly in the Mozambique Channel region [63]. The

main focus of the analysis is to use the Representative Concentration Pathways scenarios (RCPs, [64,65]) to obtain climate change projections and explore future changes, risks, and impacts. The study assess the performance of model outputs in relation to historical data and the robustness of the projected changes of climate variables through the available simulations and ensembles. Furthermore, the study discusses the implications and usefulness of the projected changes for the various key country targets.

The results are presented and discussed in both regional and local context. Our findings could contribute to the climate adaptation and mitigation actions and NDC efforts in the country. In addition, while this study presents a different methodology, it is also an update of the previous scenario (SRES) applied in previous studies [3,29,41]. The development of RCP emerged from an IPCC request to the scientific community, as the existing scenarios (the so-called Special Emissions Scenarios-SRES) [66] needed to be updated and expanded in scope [64,65].

2. Data and Methods

2.1. Study Area and Climate

Mozambique, the focus domain of this study, is located in the southeastern part of the African Continent, between latitudes $10^{\circ}27' S$ and $26^{\circ}57' S$ and longitudes $30^{\circ}12' E$ and $40^{\circ}51' E$ (Figure 1), which favors the intertropical and subtropical climate conditions. The country has a total surface area of 799,380 km² (of which 98% is land and 2% form inland waters). The country holds a long coastline in the Indian Ocean, covering a total distance of about 2700 km and a continental shelf area of 104,300 km².

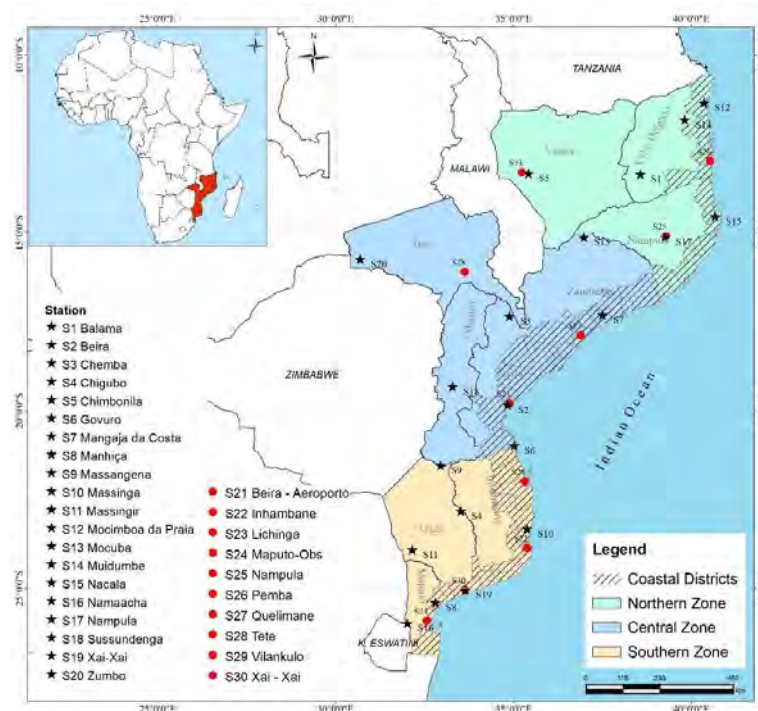


Figure 1. Map of the study area showing the administrative division of Mozambique, the different ground based meteorological stations, and the four sub-regions used in this study as highlighted from the map of the African continent.

Mozambique has a different climatic regime compared to most Southern African countries, given its coastal location, facing the warm Indian Ocean, the varying altitude, and its long latitudinal extension (between approximately 10° and $26^{\circ} S$). Thus, the northern part is dominated by a tropical rainy climate, while the central part is dominated by moderately humid climate modified by altitude. The central part is more prone to floods, tropical weather systems (e.g., tropical cyclones), and epidemics, followed by the north

and south. The southern part is more influenced by mid-latitude systems or by interactions with both. A tropical dry savannah climate is also a common feature in the southern part, which makes it more prone to drought than the center or north. For example, the central and northern regions in Mozambique receive between 400 and 600 mm more annual mean precipitation than the southern part [67]. Other areas in the center of the country and the entire coastal area receive amounts of precipitation ranging from 800 to 1000 mm. Furthermore, a significant number of dry spells is observed in the southern part, while in the northern part, rains are more regular [68].

Mozambique has two seasons: summer, which runs from October to March, and winter, which runs from April to September. The highest average maximum temperatures are found in the country's coastal zone, in the south of Tete province and in the western part of Gaza province [3]. Temperatures in Mozambique are highest during the summer and lowest during the winter. Average temperatures in Mozambique range from 25 to 30 °C (average maximum temperatures) in summer and between 15 and 21 °C (average minimum temperatures) in winter [3]. As for the average minimum temperatures, these have a decreasing pattern from the coast to the interior. The highest average minimum temperatures are found along the north coast, while the lowest are found in the province of Gaza. Extreme temperatures are common both in summer (above 40 °C) and winter (around 15 °C) in some areas.

In general, the precipitation producing systems in Mozambique comprise the Intertropical Convergence Zone (ZCIT), the El Niño-South Oscillation (ENSO), the Tropical Temperate Troughs (TTTs), the tropical cyclones formed in the southwestern Indian Ocean, the Indian Monsoon, the low-pressure systems on the continent, the frontal systems, the Indian Anticyclones, and Atlantic anticyclones. The country precipitation is heavily influenced by ENSO, a global oceanic temperature anomaly [69] that drives local interannual climate variability. The ENSO phenomenon is associated with severe dry conditions over central and southern Mozambique [70]. Conversely, the La Niña phase is associated with periods of heavy, extended precipitation, and it can result in floods. During the rainy season (November to March), precipitation variability in Mozambique is dominated by the ITCZ, a narrow transition belt, where the global northeast and southeast trades converge, inducing upward motion and precipitation [71]. Its influence is predominately felt in the north and center, whereas TTTs, oriented in a northwest-southeast direction, deliver substantial rain over large areas in the southern and central Mozambique and neighboring countries [12]. For instance, these authors hypothesize that a band of rain observed during a convective activity in mid-January 2013 could suggest a strong TTT feature with intense activity over southern Mozambique. TTTs are viewed and accepted as the main summer synoptic rain, producing a system over southern Africa [72] consisting of a combination between a lower-layer tropical perturbation and a mid-latitude trough in the upper atmosphere. Precipitation is the primary factor governing the development and persistence of drought [73]. Low levels of precipitation can have severe impact over Mozambique, which in many areas has a low resilience and limited capacity to mitigate drought effects. Tropical cyclones that generate within the Mozambique Channel (MC) or form and travel into the MC from the wider open waters east of Madagascar Island are occasionally able to make landfall into the African mainland, which is accompanied with heavy precipitation and other associated hazards [74–76]. There are other precipitation episodes of varying duration and intensity that are poorly documented, which are still a challenge for weather forecasters to predict given the short duration and surprising factor when they occur. For example, the interaction between sea breezes and urban heat islands seems to develop mesoscale convective systems that result in short-term heavy rains in some areas of the country. Synoptic-scale winds (e.g., sea breeze) are known to influence the heat island circulation, and their interaction has been studied and confirmed in other parts of the world [77]. Given the limited predicting skills when they occur, the earlier warning systems could not provide the necessary information in a timely and efficiently manner to the residents in order to avoid the consequences.

2.2. Data

2.2.1. Climate Data from Model Simulations Outputs

This study uses three different ensembles of regional climate change simulations outputs from the COordinated Regional Downscaling EXperiment (CORDEX-Africa): one ensemble of 4 simulations (out of which, 5 were not available) based on the representative concentration pathway (RCP) 2.6, one ensemble of 9 simulations based on RCP4.5, and one ensemble of 9 simulations based on RCP8.5. All data for the three ensembles, RCP2.6, RCP4.5 and RCP8.5, included in the analysis were available from the ESGF (Earth System Grid Federation) Swedish datanode (<https://esg-dn1.nsc.liu.se/projects/esgf-liu/>, accessed on 12 March 2020). The Regional Climate Model (RCA4) and the driving GCMs are presented in Table 1.

Table 1. List of driving Global Climate Model—GCMs (nine available for RCP4.5 and RCP8.5, and 4 available for RCP2.6 scenario) along with the RCA4 regional model.

	Project/Initiative	Driving GCMs (Historical)	Driving GCMs (Projections)	RCM	Period
1	CORDEX-Africa	CanESM2	CanESM2	RCA4	1951–2100
2	CORDEX-Africa	CNRM-CM5	CNRM-CM5	RCA4	1951–2100
3	CORDEX-Africa	CSIRO-MK3	CSIRO-MK3	RCA4	1951–2100
4	CORDEX-Africa	GFDL-ESM2M	GFDL-ESM2M	RCA4	1951–2100
5	CORDEX-Africa	HadGEM2-ES	HadGEM2-ES ⁽¹⁾	RCA4	1951–2099
6	CORDEX-Africa	IPSL-CM5A-MR	IPSL-CM5A-MR	RCA4	1951–2100
7	CORDEX-Africa	MIROC5	MIROC5 ⁽¹⁾	RCA4	1951–2100
8	CORDEX-Africa	MPI-ESM-LR	MPI-ESM-LR ⁽¹⁾	RCA4	1951–2100
9	CORDEX-Africa	Nor-ESM1-M	Nor-ESM1-M ⁽¹⁾	RCA4	1951–2100

Driving GCMs Institutes/Centers-1. Canadian Centre for Climate Modelling and Analysis; 2. Centre National de Recherches Météorologiques; 3. Commonwealth Scientific and Industrial Research Organization; 4. Geophysical Fluid Dynamic Laboratory; 5. Met Office Hadley Centre; 6. Institut Pierre Simon Laplace; 7. Tokyo Center for Climate System Research; 8. Max Planck Institute for Meteorology; 9. Bjerkes Centre for Climate Research. RCM Model Center: Swedish Meteorological and Hydrological Institute (SHMI). ¹ Available simulations for RCP2.6.

The data correspond to the 1951–2100 period and cover two of the most important meteorological variables in terms of direct impacts, the temperature and precipitation. The selected variables belong to the Phase I CORDEX simulations and have a spatial resolution of 0.44° (≈50 km). The data are retrieved following specific guiding instructions and steps (<http://www.csag.uct.ac.za/cordex-africa/how-to-download-cordex-data-from-the-esgf/>, accessed on 12 March 2020), which are provided at the ESGF-LiU data node. The regional climate model from which the data were derived is the latest fourth generation Rossby Centre Atmosphere regional climate model (RCA4) at the Swedish Meteorological and Hydrological Institute (SHMI) [78,79].

In practice, SHMI uses RCA4 to dynamically downscale all the GCMs over the Africa CORDEX domain [79]. The RCA4 model has been applied in previous studies in Africa [25] and other parts of the world [80]. Ref. [81] recognize that RCA4 has a number of improved modifications for specific physical parameterizations, which make it ideal and transferrable for applications in African regions. Some common concerns for almost the majority of RCMs in Africa include different convection schemes [82], including the phase of diurnal cycle of precipitation, among others. According to [81], this is an indication that higher resolution does not necessarily lead to a better performance of the RCMs. RCMs model outputs may still produce considerable systematic biases, and their direct use as input for impact assessment models may not be appropriate, since they might lead to inaccurate conclusions [83]. Biases are usually defined as long-term average deviations between simulations and observations [84]. Several bias correction methods have been developed to adjust meteorological variables from the RCMs ranging from simple scaling approaches to sophisticated distribution mapping [85–87]. The GCMs projections are forced by the Representative Concentration Pathways, which are hereafter referred to as RCPs [88]. The RCPs are prescribed greenhouse gas concentration pathways throughout the 21st

century, corresponding to different radiative forcing stabilization levels [64,65]. Three RCP were available for this study: (i) RCP2.6, the *lowest-level scenario* (most ambitious scenario with radical climate mitigation policies) which would slow global warming to 1.5 °C (the peak of the radiative forcing in the middle of the century of $\approx 3 \text{ W/m}^2$) followed by a decline; (ii) RCP4.5, the *mid-level scenario* with strong climate policy (e.g., the Paris Agreement) which would slow global warming to around 2 °C (or $\approx 4.5 \text{ W/m}^2$) by 2100 (RCP4.5), and (iii) RCP8.5, the *highest-level scenario* (business as usual scenario, without either countervailing action or climate policy), which could increase global warming up to 4 °C or 8.5 Wm^2 radiative forcing on the climate system by 2100.

2.2.2. Observed Data

The observed monthly precipitation, maximum temperature, and minimum temperature data from 27 stations were collected from the National Institute of Meteorology (INAM, <https://www.inam.gov.mz/index.php/pt/>, accessed on 12 March 2020) of Mozambique starting from 1961 to 2015. The historical observations were used for performance evaluation against the GCMs historical model outputs in each region of Mozambique.

Due to the inconsistencies in the observed station data, the evaluation was made only for the 1971–2000 period covering 10 stations (Table 2). After the evaluation was made, it was possible to read for each station the associated number of gaps for each variable (precipitation: Prec.; minimum temperature: Tmin.; and maximum temperature: Tmax.). Since the evaluated data showed fewer gaps compared to the initial station data, they are considered more reliable and suitable for the performance evaluation of quantile mapping against the GCMs historical model outputs.

Table 2. Observed stations (10) from the National Institute of Meteorology (INAM) used for the evaluation of model outputs and the related gaps to each data (%).

Station	Prec. Gaps (%)	Tmin Gaps (%)	Tmax Gaps (%)
Xai—Xai	4.11	5.83	7.5
Beira-Aeroporto	1.12	3.06	3.06
Pemba	1.41	5.62	5.62
Lichinga	6.51	1.67	1.67
Nampula	0.56	0.56	1.11
Quelimane	2.56	0.0	0.56
Tete	4.06	3.61	3.89
Maputo-Observatório	0.0	0.0	0.0
Inhambane	2.29	1.67	1.67
Vilanculos	6.21	4.72	5.0

2.3. Methods

2.3.1. Definition of Climate Periods, Seasons, and Subregions

Climate projections for temperature and precipitation are presented for different climate future periods and time scales. Following [53], the years 1961–1990 are defined as the baseline (reference) period or recent past, while the three 30-year period (time-slices), 2011–2040, 2041–2070, and 2071–2100, are representative for the *present*, *mid*, and *end* of the twenty-first century. The climate change projections for Mozambique are presented at annual scale in these periods.

The study also examined temperature and precipitation projections at a seasonal scale considering that large seasonal variations characterize most of Africa and Mozambique in particular [89]. In this context, climate analyses were performed including four seasons, summer (December-January-February (DJF)), late summer (May-June-July (MAM)), winter (June-July-August (JJA)); and early summer (September-October-November (SON)) to explore changes in a seasonal context. Important circulation changes such as El Niño-Southern Oscillation (ENSO), Intertropical Convergence Zone (ITCZ), Mozambique Chanel Trough (MCT), monsoons, and Mascarene High, which alter the climate conditions in

Mozambique, seem to be the most dominant factors that control the seasonal changes. For example, in Southern Africa, the rainy season reaches its peak between December and February (DJF), when 80% of annual rainfall is recorded in the region, with some areas reaching 90% [90]. The influence of El-Niño is felt most in the southeastern part of Southern Africa, reaching a peak at the end of the summer i.e., between January and March (JFM) [91].

For spatial average analysis, the study area is divided in four sub-regions, namely: the coastal, northern, central, and southern regions (see [3]) based on the climatological features and vulnerability in the area (Figure 1 and Table 3).

Table 3. Sample of districts chosen according to vulnerability.

Region	District	Latitude	Longitude	Altitude (m)	Associated Vulnerability Event
Coastal	Govuro	−20.990	35.021	130	Drought/Floods/Cyclones
	Massinga	−23.329	35.382	116	Drought/Cyclones
	Mocimboa da Praia	−11.346	40.357	29	Drought/Cyclones
	Nacala	−14.541	40.672	133	Drought/Floods/Cyclones
	Mangaja da Costa	−17.309	37.508	103	Floods/Cyclones
	Beira	−19.846	34.841	5	Floods/Cyclones
	Xai-Xai	−25.053	33.644	45	Drought/Floods/Cyclones
	Manhiça	−25.401	32.810	37	Drought/Floods/Cyclones
Northern	Muidumbe	−11.823	39.821	504	Drought/Floods/Cyclones
	Balama	−13.348	38.572	591	Drought/Cyclones
	Nampula	−15.120	39.264	414	Floods
	Chimbonila	−13.331	35.423	550	Cyclones
Central	Zumbo	−11.823	30.447	504	Drought/Floods
	Chemba	−13.348	34.894	591	Drought/Floods/Cyclones
	Mocuba	−15.120	36.980	414	Floods
	Sussundenga	−13.331	33.293	550	Floods/Cyclones
Southern	Massangena	−21.545	32.952	120	Drought/Floods
	Chigubo	−22.830	33.523	210	Drought/Floods/Cyclones
	Massingir	−23.920	32.158	191	Drought/Floods
	Namaacha	−25.983	32.018	490	Drought/Floods

2.3.2. Evaluation of Historical CORDEX Model Simulations

The evaluation of historical simulations was made using Taylor diagrams. Taylor diagrams are defined as mathematical diagrams designed to graphically represent which of several approximate representations (or models) of a system, process, or phenomenon is most realistic, and how closely a pattern or a set of patterns matches observations [92,93]. These mathematical diagrams are constructed to assess the performance of model outputs in relation to historical data. Taylor diagrams in this context provide a graphical framework that allows variables from the set of models represented in Table 1 to be compared to our precipitation and temperature historical reference data provided by the INAM.

2.3.3. Calculation of Temporal and Spatial Variations in Climate Projections

The annual time series and spatial variations of temperature and precipitation have been calculated over the entire country as well as in four sub-regions. The multi-model average of simulations (or ensemble approach) is applied to reduce uncertainty associated with individual climate models based on the available Representative Concentration Pathways (RCP2.6, RCP4.5, and RCP8.5). For the temperature, the analysis will focus on the maximum of the change, since we are interested in knowing how much it will heat up until the end of the century. For precipitation, the analysis will focus on the 5th, 50th, and 95th percentiles. The 5th and 95th percentiles are used to indicate the range over which normal values are expected. The 50th percentile indicates the central value, giving the idea of the sign of most of the values.

2.3.4. Robustness of Projected CORDEX Model Simulations

The robustness of the climate projections is based on the combination of two tests, the test of agreement and the significance test, as described by [94]. The test of agreement assesses the robustness of the projections based on the comparison of the signal of each simulation in relation to the signal of the ensemble. The percentage of simulations whose sign of change agrees with the sign of the ensemble will define the level of robustness of the projections. In this study, it is considered that the projection is robust in terms of signal agreement, when over 66% of the simulations agree with the signal of the ensemble. For the significance test, the two-tailed Student t-test based on unequal variances between future and historical data, with a 95% confidence level was used. The significance test assesses the difference in distributions between two series, in this case, the 30 years of the simulated projections in relation to the historical 30 years. Similar to what was done in the test of agreement, the Student t-test was performed for each simulation in such a way that the change is considered statically significant if more than 66% of the simulations show a significant change. The analysis of the robustness of the climate projections is made for the 20 districts of the four regions shown in Table 3.

3. Results

3.1. Evaluation of Historical CORDEX Model Simulations

Taylor diagrams [92] were used to assess the performance of model outputs in relation to historical data in each region of Mozambique. The outputs of the nine models are represented by the letters M1, M2,..., M9, following the sequence shown in Table 1. Despite the evaluation of all model outputs, the analyses are focused on the average of the nine models, which is represented by "ALL".

Regarding temperature (Appendix A, Figure A1), it can be seen that all models show correlations above 0.7, in almost all stations, except in Pemba, where the correlations are above 0.5. The associated errors vary between 0.25 and 2 °C, with the standard deviation not exceeding 3 °C. The average of the models presents the best results in the evaluation, where their correlation reaches more than 0.9 in Beira, Inhambane, Lichinga, Quelimane, Vilanculos, and Xai-Xai.

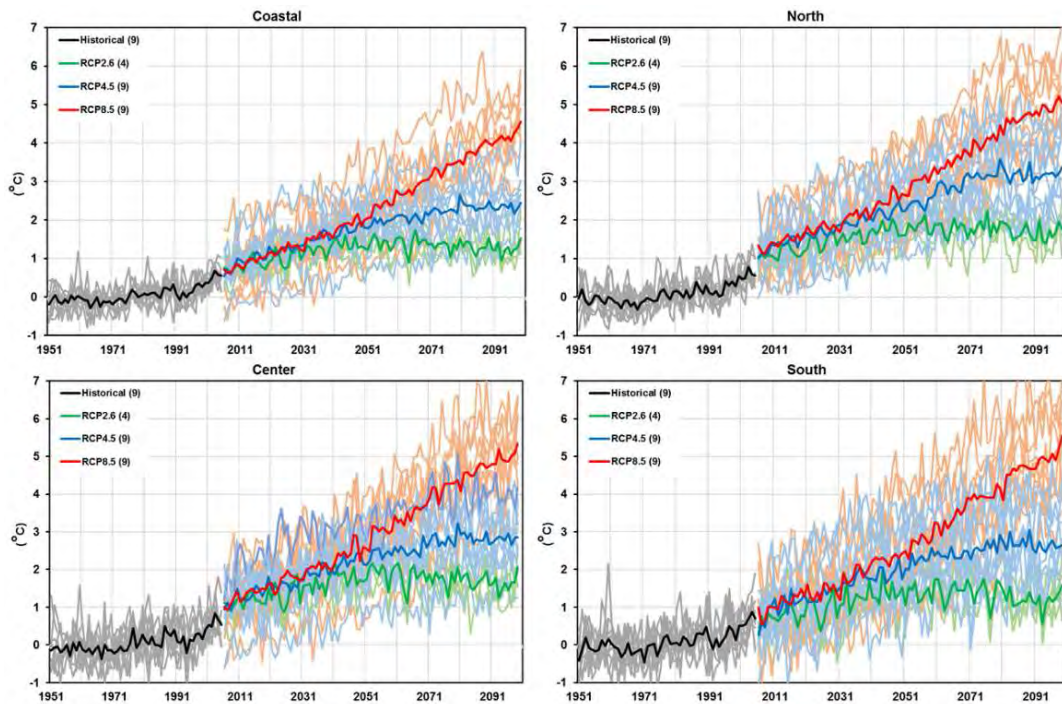
In precipitation (Appendix A, Figure A2), different from temperature, the correlations are relatively lower. In some stations such as Beira, Inhambane, Maputo, Vilanculos, and Xai-Xai, the models show correlations below 0.5. Nampula and Lichinga present correlations that reach 0.75 and 0.77, respectively. The errors vary between 100 and 200 mm. Similar to what was observed in the temperature, the average of the models presents the best results also for precipitation. For the average of the models, only the stations of Inhambane, Maputo, Vilanculos, and Xai-Xai (all from the south) have correlations below 0.5. The rest of the stations show correlations above 0.6, with values reaching 0.79 in Nampula and 0.82 in Lichinga.

3.2. Calculation of Temporal Variations in Climate Projections

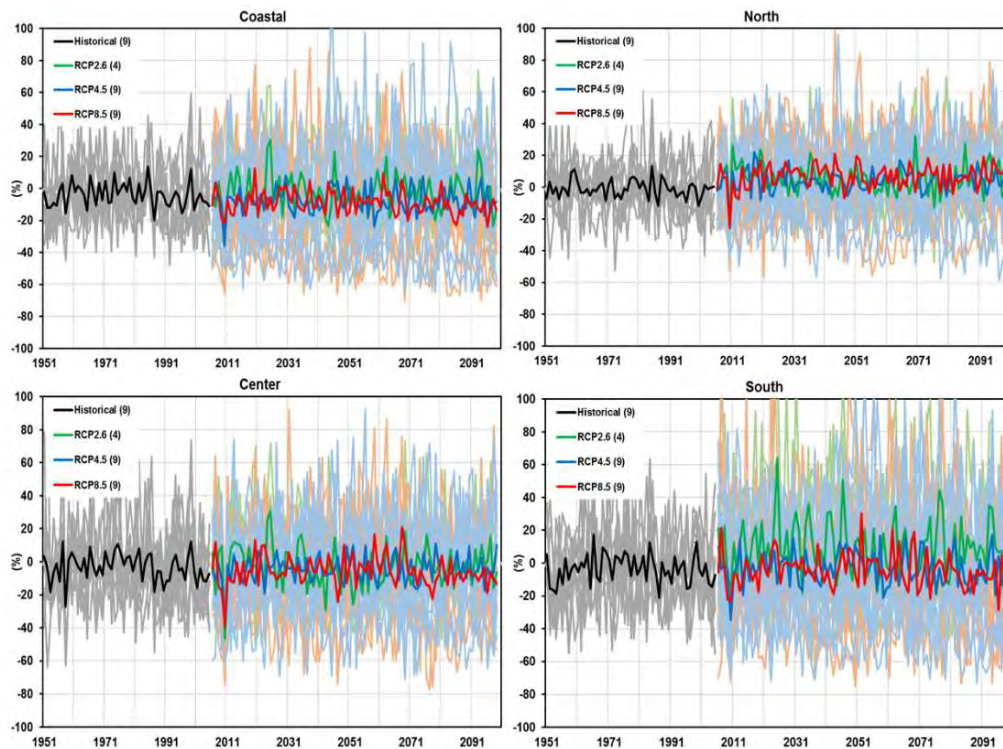
3.2.1. Temporal Variations in Mean Annual Temperature Projections

Figure 2a shows the time series of anomalies (in relation to the 1961-1990 reference period) of the historical and temperature projections for the three RCP scenarios (RCP2.6, RCP4.5, and RCP8.5), for the four regions (coastal, northern, central, and southern) chosen. It is evident that for the more optimistic scenario (RCP2.6), the temperature increase will start to stabilize around 2030, regardless of the region. In the RCP2.6 scenario, the temperature anomaly can reach up to 2 °C in all regions, except the coastal region. This suggests that the coastal region will experience less temperature variation. For the RCP4.5 scenario, the temperature starts to stabilize around 2050, and for this scenario, the temperature anomaly will not exceed 2 °C in the coastal region. In the remaining regions, anomalies associated with RCP4.5 reach 3 °C. The RCP8.5 scenario is the one with the most accentuated increase throughout the 21st century. Anomalies related to this scenario reach

values close to 6 °C in the southern region; on the other hand, in the coastal region, they do not reach 5 °C.



(a)



(b)

Figure 2. (a) Projected time-series of annual mean temperature anomalies with respect to the reference period 1961–1990, for the historical and three RCP simulations (RCP2.6, RCP4.5, and RCP8.5), for the four regions used in this study; (b) Projected time-series of annual precipitation anomalies with respect to the reference period 1961–1990, for the historical and three RCP simulations (RCP2.6, RCP4.5, and RCP8.5), for the four regions used in this study.

3.2.2. Temporal Variations of Annual Precipitation Projections

In the time series of precipitation anomalies (Figure 2b), it is clear that the southern region is the one with the greatest interannual variability. In general, all RCPs present a great annual variability, being that the northern region is the only one with an above average precipitation trend.

3.3. Changes in Mean Annual and Seasonal Temperature Projections over Mozambique

3.3.1. Projected Changes in Mean Annual Temperature

Projected changes for the three periods (2040s, 2070s, and 2100s) show that the average annual temperature (maximum, minimum, and average) will be higher than the average for the reference period (1961–1990), as it is presented in Figures 3–5. There is a tendency toward an increase in temperature as we move toward the middle and end of the century, mainly for the RCP4.5 and RCP8.5 scenarios, with the minimum temperature being the variable that will have the major variation. The coastal region of Mozambique will experience less variation, while the interior will experience greater changes in temperature. This result is consistent with that found by [3]. Some locations (hotspots) stand out for having the major variations regardless of the scenario and the period, such as the cases in the western part of the Gaza Province (near the border with Zimbabwe), the northern Tete Province, and the western part of the Niassa Province. The interior of the Gaza Province is one of the driest regions in Mozambique, while the Tete Province is predominantly the warmest.

Under the RCP2.6 scenario (Figures 3–5, left), during the 2040s, the extreme northeast of Mozambique (Cabo Delgado and Nampula Provinces) is the place that will present the smallest variations (values below 0.5 °C). According to Table 4, the change in maximum, minimum, and average temperatures may reach 0.92, 1.12, and 0.99 °C, respectively, being parts of Gaza and Inhambane (southern region), almost the entire province of Zambézia, and parts of the provinces of Tete, Sofala, and Manica (central region) and parts of the Niassa Province (northern region), the places where the major variation is observed. During the 2070s, the observed patterns do not portray significant differences, with the northernmost part of Mozambique showing variations below 0.5 °C. For this period, projected changes under the same scenario indicate that the maximum, minimum, and average temperature variation may reach 1.39, 1.56, and 1.45 °C, respectively (Table 4), with the provinces of the central region being those that will experience the major increase in the average annual maximum temperature. In the 2100s, in addition to the extreme northeast of Mozambique, the southwestern tip of Maputo Province also stands out as being the place where the change in the average annual maximum temperature does not exceed 0.5 °C. During this period, the temperature variation may reach 1.24 °C for the maximum, 1.4 °C for the minimum, and 1.23 °C for the average, with the central region being the place where the major change will occur.

Table 4. Maximum change in annual temperature for the 2040s (2011–2040), 2070s (2041–2070), and 2100s (2071–2100) with respect to the reference period (1961–1990) for the RCP2.6 scenario. The cells filled with the blue color have values below 2 °C (threshold defined by the Paris Agreement).

Period	Change in 2040s			Change in 2070s			Change in 2100s		
	Tmax	Tmin	Tmean	Tmax	Tmin	Tmean	Tmax	Tmin	Tmean
Annual	0.92	1.12	0.99	1.39	1.56	1.45	1.24	1.40	1.23
DJF	0.87	1.14	0.94	1.46	1.57	1.44	1.46	1.47	1.33
MAM	0.81	1.11	0.83	1.21	1.55	1.31	1.01	1.29	1.08
JJA	1.36	1.53	1.45	1.56	1.69	1.63	1.53	1.69	1.62
SON	1.41	1.33	1.40	1.83	1.78	1.84	1.72	1.67	1.71

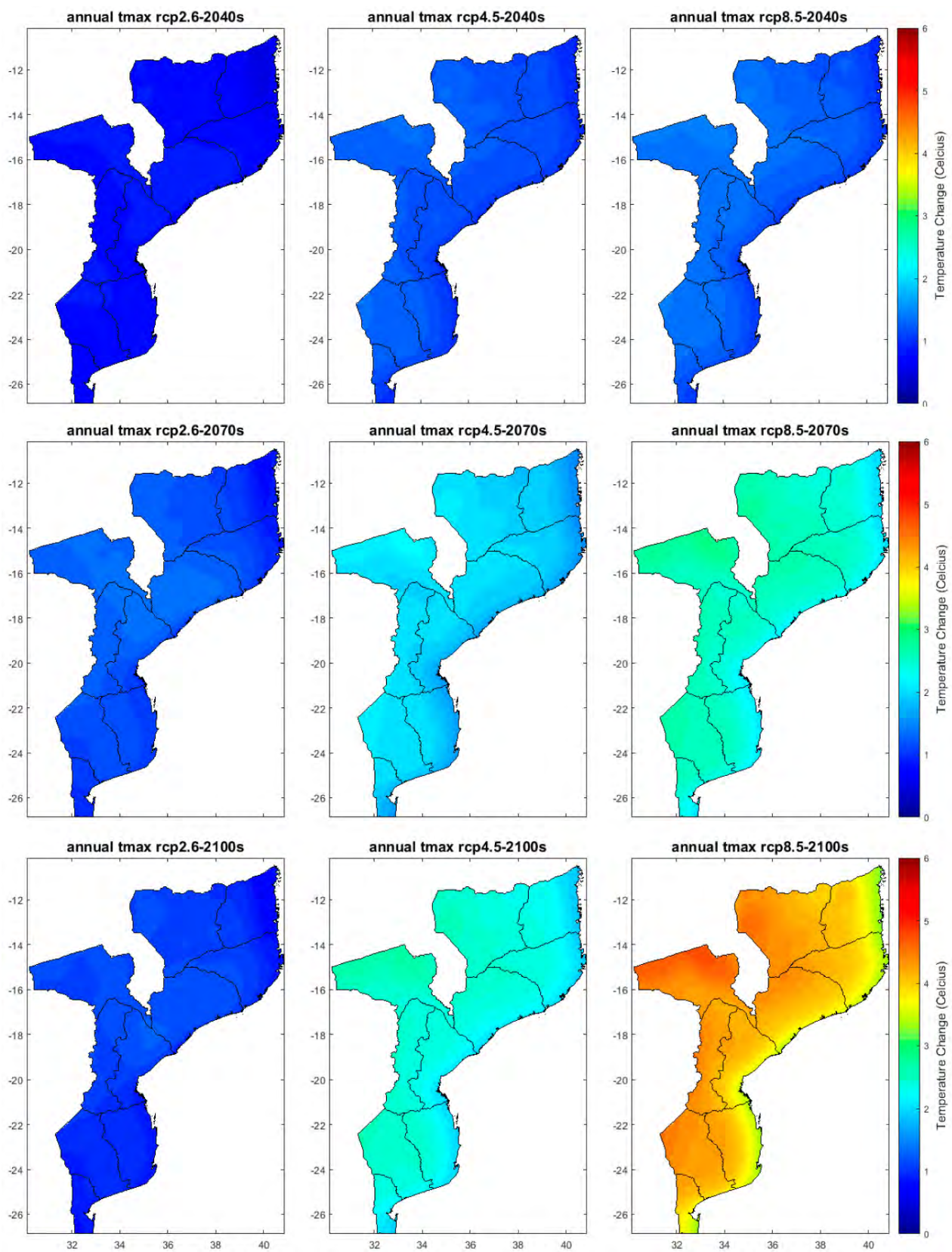


Figure 3. Projected changes of annual maximum temperature for the 2040s (2011–2040), 2070s (2041–2070), and 2100s (2071–2100) with respect to the reference period (1961–1990) for the three RCPs scenarios (RCP2.6, RCP4.5, and RCP8.5).

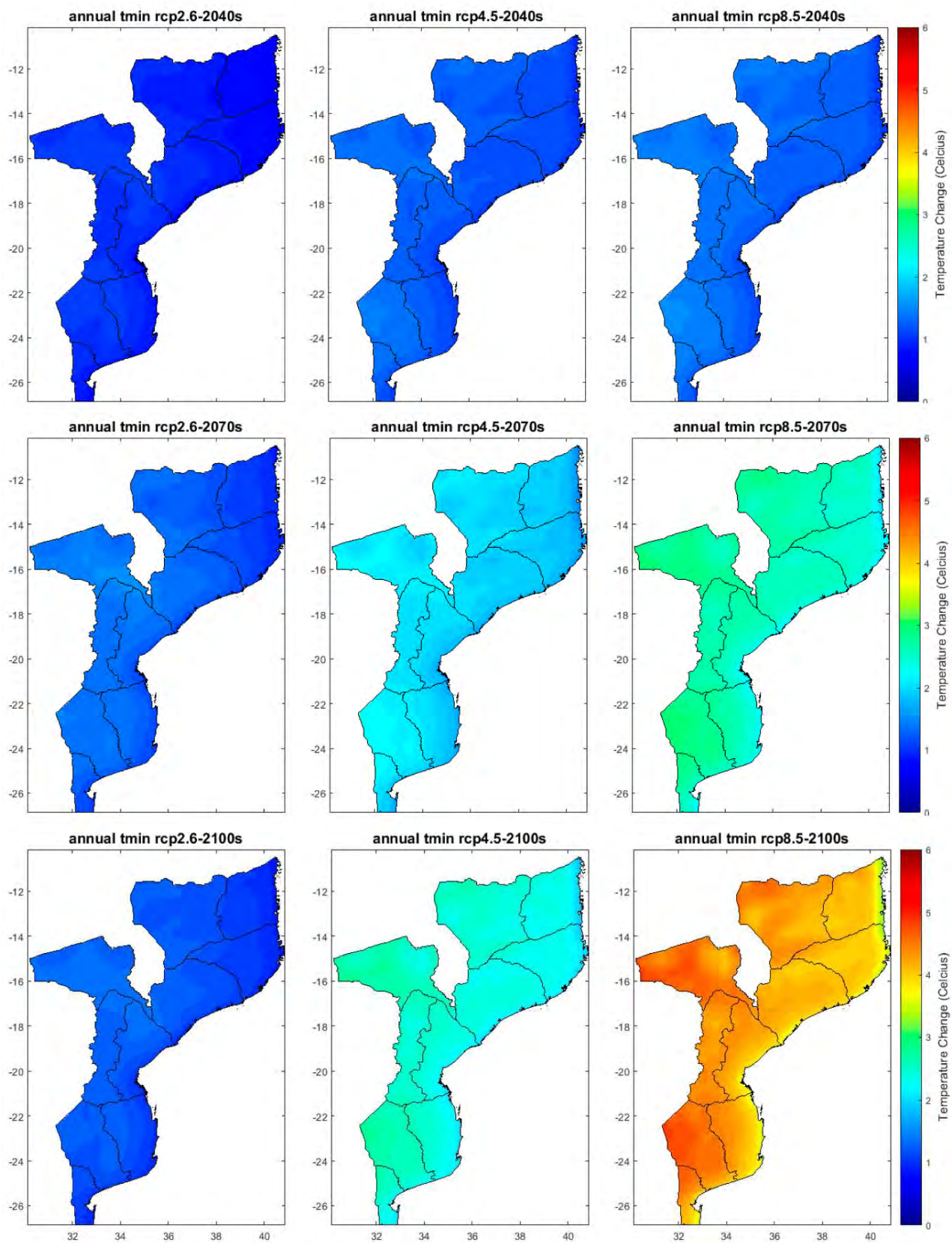


Figure 4. Projected changes of annual minimum temperature for the 2040s (2011–2040), 2070s (2041–2070), and 2100s (2071–2100) with respect to the reference period (1961–1990) for the three RCPs scenarios (RCP2.6, RCP4.5, and RCP8.5).

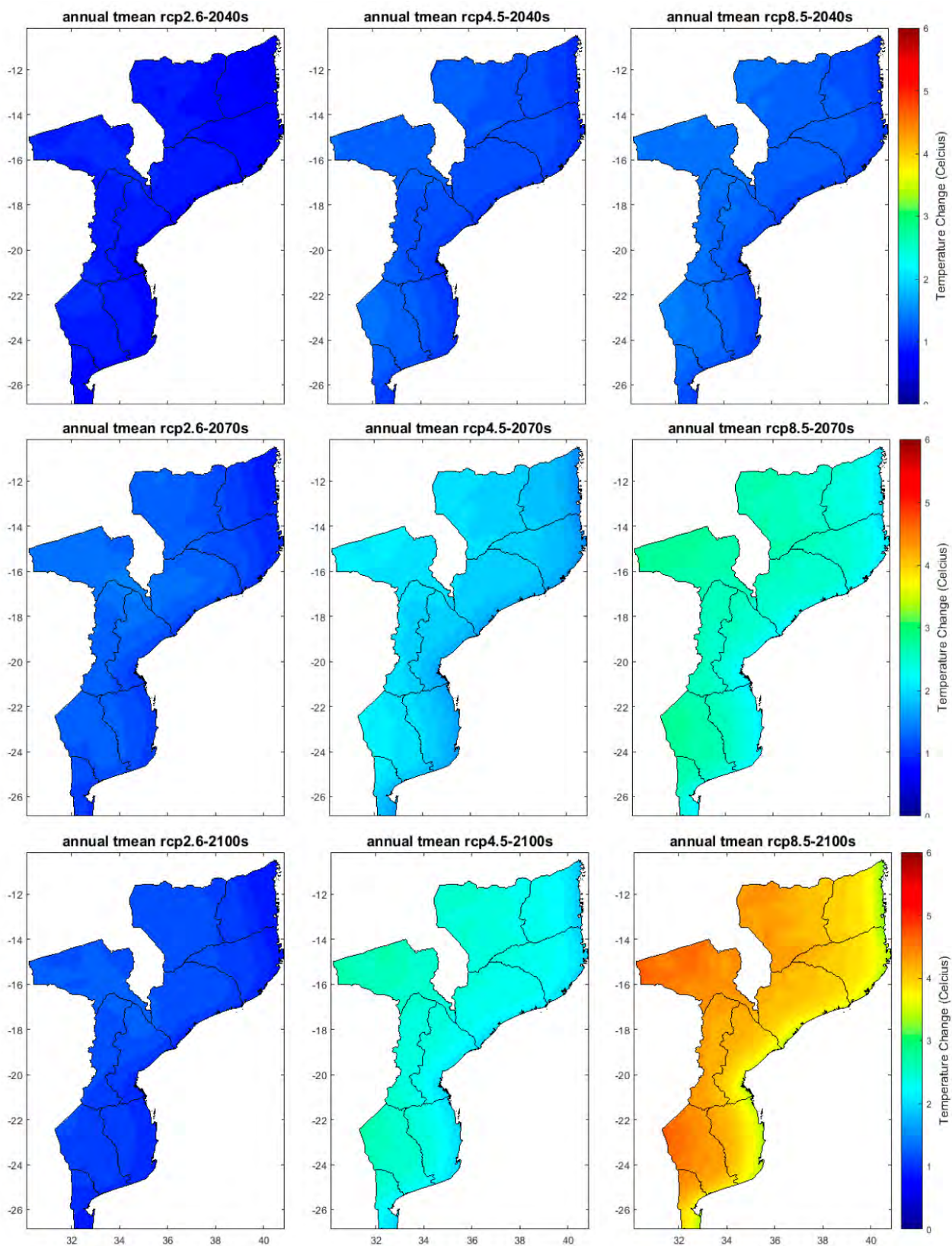


Figure 5. Projected changes of annual mean temperature for the 2040s (2011–2040), 2070s (2041–2070), and 2100s (2071–2100) with respect to the reference period (1961–1990) for the three RCPs scenarios (RCP2.6, RCP4.5, and RCP8.5).

The RCP4.5 scenario presents relatively higher temperature change values compared to RCP2.6 (Figures 3–5, middle). During the 2040s, the entire coastal region showed varia-

tions of less than 0.5 °C. The change in maximum, minimum, and average temperatures can reach 1.35, 1.46, and 1.39 °C (Table 5) with the interior of the Gaza Province, north of the Tete Province, and parts of the Niassa and Zambézia Provinces being the places that experience the major variations. In the 2070s, the temperature variation showed values that exceed 2 °C. The temperature change varies from just over 1 °C in the coastal region to around 2.28 °C in the interior areas. The northern part of the Tete Province is the place where the major variation is observed. During the 2100s, it is evident that for the RCP4.5 scenario, the temperature change is no more than 2 °C in the coastal region. In the interior of Mozambique, the temperature variation exceeds 2 °C, reaching 2.74 °C for the maximum temperature, 2.8 °C for the minimum temperature, and 2.71 °C for the average temperature.

Table 5. Maximum change in annual temperature for the 2040s (2011–2040), 2070s (2041–2070), and 2100s (2071–2100) with respect to the reference period (1961–1990) for the RCP4.5 scenario. The cells filled with the blue color have values below 2 °C (threshold defined by the Paris Agreement), and the cells with orange indicate temperature values between 2 and 4 °C.

Period	Change in 2040s			Change in 2070s			Change in 2100s		
	Tmax	Tmin	Tmean	Tmax	Tmin	Tmean	Tmax	Tmin	Tmean
Annual	1.35	1.46	1.39	2.20	2.28	2.19	2.74	2.80	2.71
DJF	1.47	1.38	1.40	2.19	2.15	2.12	2.57	2.53	2.51
MAM	1.20	1.39	1.27	2.05	2.18	2.01	2.74	2.89	2.69
JJA	1.49	1.55	1.47	2.34	2.39	2.23	2.89	2.91	2.74
SON	1.53	1.53	1.52	2.63	2.51	2.60	3.05	3.03	3.06

The projections under the RCP8.5 scenario (Figures 3–5, right) present a pattern consistent with that observed in both the RCP 2.6 and 4.5 scenarios. For the 2040s, the change is no more than 1 °C in the coastal region. The variation in maximum, minimum, and average temperatures can reach 1.49, 1.56, and 1.48 °C (Table 6), respectively, in which the interior of the Gaza Province, the north of the Tete Province, and parts of the Niassa Province are the places where the major changes are observed. In the 2070s, the coastal parts of the northern and southern regions will experience changes in temperature with values below 2 °C. In the interior areas, the change can reach 3 °C, with the interior of the Gaza Province, north of the Tete Province and parts of the Niassa Province being the most outstanding places. In the last 30 years of the century, projections under the RCP8.5 scenario show that the change in temperature may exceed 4 °C. In the coastal region, the temperature rise has values that reach 3 °C. The change in maximum, minimum, and average temperatures can reach 4.73, 4.85, and 4.7 °C, respectively, with the northern part of the Tete Province and west of the Niassa Province being the places that show the greatest change.

Table 6. Maximum change in annual temperature for the 2040s (2011–2040), 2070s (2041–2070), and 2100s (2071–2100) with respect to the reference period (1961–1990) for the RCP8.5 scenario. The cells filled with the blue color have values below 2 °C (threshold defined by the Paris Agreement), with orange indicating the cells with temperature values between 2 and 4 °C, and finally the red color representing the cells with values above 4 °C.

Period	Change in 2040s			Change in 2070s			Change in 2100s		
	Tmax	Tmin	Tmean	Tmax	Tmin	Tmean	Tmax	Tmin	Tmean
Annual	1.49	1.56	1.48	2.86	3.00	2.86	4.73	4.85	4.70
DJF	1.39	1.40	1.37	2.71	2.78	2.69	4.42	4.47	4.39
MAM	1.50	1.58	1.41	2.68	2.92	2.65	4.65	4.87	4.59
JJA	1.74	1.72	1.63	3.02	3.17	2.92	5.00	5.04	4.70
SON	1.66	1.64	1.64	3.28	3.32	3.28	5.25	5.20	5.20

3.3.2. Projected Changes in Mean Seasonal Temperature

At the seasonal time scale, the pattern of temperature change does not differ from the pattern found in the analysis of projections at the annual scale. The coastal zone has the smallest variations, and the interior has the largest variations. The JJA and SON seasons are the ones that present the largest variations in temperature, with the interior of the Gaza Province and parts of the Tete and Niassa Provinces being the places where the major changes are observed, mainly for the RCP 4.5 and 8.5 scenarios. At this point, due to the high number of variables to be analyzed, the focus will be on the average temperature.

The projections under the RCP2.6 scenario (Table 4) show that the temperature variations will not reach 2 °C, regardless of the period and the season. The spatial distribution of projected changes in temperature, under the RCP2.6 scenario during the DJF season (Figures A3–A5, left), shows that in addition to the coastal region, much of the southern region, including the interior of the Gaza Province, are the places where there will be the lowest variations (values below 0.5 °C). In this season, the variation in the average temperature may reach 0.94 °C in the 2040s, 1.44 °C in the 2070s, and 1.33 °C in the 2100s (Table 4). The northern Tete Province and parts of the Niassa and Zambézia Provinces are the places where the observed warming is largest. During the MAM season (Figures A6–A8, left), the pattern of temperature change is close to the pattern observed in DJF, with the exception of the minimum temperature, which is already beginning to show a significant increase in the interior of the Gaza Province, for the RCP 4.5 and 8.5 scenarios. The change in average temperature may reach 0.83 °C in the 2040s, 1.55 °C in the 2070s, and 1.08 °C in the 2100s (Table 4). The seasons of JJA (Figures A9–A11, left) and SON (Figures A12–A14, left) are the ones that will experience the major changes, with the minimum temperature being the variable that will present the major variation. This suggests that there is a tendency toward a decrease in thermal amplitude, with less cold winters. It is notable that during the 2040s, regardless of the time scale (annual or seasonal), the three temperature variables analyzed show an increase of no more than 1.5 °C except for the minimum temperature, which shows an increase that will reach 1.53 °C during the JJA season (Table 4). The major changes (values above 1 °C) are expected in the interior of the Gaza Province, south of the Manica Province, and north of the Tete Province (central and southern regions) and in parts of the Niassa Province (near the border with Malawi). During the 2070s, the temperature increased slightly compared to the 2040s. In this period (2070s), the change in the minimum temperature presents values above 1.5 °C, with the major change occurring in the SON season (1.78 °C). For the maximum and average temperature, only the JJA and SON seasons have changes above 1.5 °C. For these variables, the major change occurs during the SON season, with values reaching 1.83 °C for the maximum temperature and 1.84 °C for the average temperature. At the end of the century (2100s), projections under the RCP2.6 scenario show a temperature stabilization. The SON season is the one that presents the major changes, with values reaching 1.72, 1.67, and 1.71 °C, for the maximum, minimum, and average temperature, respectively.

For projections under the RCP4.5 scenario (Figures A3–A5, middle), during the DJF season, the coastal region remains the place where the smallest variations are observed. Unlike RCP2.6, for RCP4.5, the interior of the Gaza Province presents the pattern observed on the annual scale, being one of the places where the greatest temperature variations are registered, together with the northern part of the Tete Province and the interior of the Niassa and Zambézia Provinces. The change in average temperature can reach 1.4 °C in the 2040s, 2.12 °C in the 2070s, and 2.51 °C in the 2100s (Table 5). For the MAM station (Figures A6–A8, middle), the change in average temperature may reach 1.27 °C in the 2040s, 2.01 °C in the 2070s, and 2.69 °C at the end of the century. During the JJA and SON seasons (Figures A9–A14, middle), the major changes are also expected in the interior of the Gaza Province, the north of the Tete Province, and in some parts of the Niassa Province. During the 2040s, the change in average temperature only exceeded 1.5 °C in the SON season (Table 5), where it reaches 1.52 °C; in JJA, the average temperature reaches 1.47 °C. In the 2070s, the temperature rise exceeds 2 °C, but it does not reach 3 °C, and the change

in temperature reaches 2.23 °C in JJA and 2.6 °C in SON. For the 2100s period, the RCP4.5 scenario shows that the temperature rise will exceed the 3 °C barrier. Once again, the SON season is the one with the major increase in temperature, reaching 3.05, 3.03, and 3.06 °C, for the maximum, minimum, and average temperature, respectively.

In the RCP8.5 scenario, the same locations mentioned previously (inland Gaza Province, north of the Tete Province, and in some parts of the Niassa Province) are the ones that show the major changes. For the DJF station (Figure A3, Figure A4, Figure A5, right), the average temperature may reach 1.37 °C in the 2040s, 2.69 °C in the 2070s, and 4.39 °C at the end of the century (Table 6). During the MAM season (Figures A6–A8, right), the change in average temperature may reach 1.41 °C in the 2040s, 2.65 °C in the 2070s, and 4.59 °C in 2100s. The temperature increase could rise from 5 °C at the end of the 21st century, mainly during the JJA and SON seasons (Figures A9–A14, right). During the 2040s, RCP8.5 projections show that the average temperature rise will reach 1.63 °C in JJA and 1.64 °C in SON. In the 2070s, the change in average temperature will reach 2.92 °C in JJA and 3.28 °C in SON. At the end of the century, the average temperature change will reach 4.7 °C in JJA and 5.2 °C in SON (Table 6).

3.4. Changes in Annual and Seasonal Precipitation Projections (RCP2.6, RCP4.5, and RCP8.5)

3.4.1. Projected Changes in Annual Precipitation

In general, the behavior of annual precipitation shows a pattern with considerably variability influenced by the type of scenario and period chosen, including the geographic location. All RCPs are consistent in showing that at the annual time scale, there will be a decrease in precipitation in all periods in the coastal zone of the northern region (Figure 6). The projections under the RCP2.6 scenario (Figure 6, left) indicate that there will be an increase in precipitation in much of Mozambique, mainly in the 2040s, where the 5th and 95th percentiles will have values of −7.3% and 30.7%, respectively (Table 7). For almost the entire southern region, with the exception of the coastal part, precipitation may increase by up to 40% compared to the precipitation in the reference period. The same is true in some parts of the central and northern regions, in the northern part of the Tete Province, and some parts of the interior of the Niassa Province, where the increase in precipitation may exceed 50%. During the 2070s, there was a slight decrease in precipitation, with the 5th percentile equal to −16.4% and the 95th percentile equal to 22.1%. At the end of the century, precipitation showed a slight increase in relation to the 2070s, with the entire southern region with precipitation above the average of the reference period.

Table 7. Percentile values of precipitation for the 2040s (2011–2040), 2070s (2041–2070), and 2100s (2071–2100) with respect to the reference period (1961–1990) for the RCP2.6 scenario. The cells filled with different colors differentiate positive and negative anomalies.

Period	Reference Period		Change in 2040s			Change in 2070s			Change in 2100s		
	Average (mm)	Std. Dev.	P5 (%)	P50 (%)	P95 (%)	P5 (%)	P50 (%)	P95 (%)	P5 (%)	P50 (%)	P95 (%)
Annual	1020	246.3	−7.3	10.7	30.7	−16.4	2.1	22.1	−23.3	−8.3	7.2
DJF	186.2	47.6	−7.5	11.6	38.1	−13.8	6.7	31.4	−10.9	4.3	23.0
MAM	86.3	35.6	−1.9	21.5	49.4	−16.6	5.6	24.5	−6.6	17.0	40.4
JJA	23.5	12.6	−56.5	−31.8	1.0	−61.6	−33.4	−15.4	−55.3	−30.9	−6.8
SON	44.5	11.5	−18.2	−1.2	25.1	−26.9	−9.6	9.7	−15.2	2.4	26.2

The RCP4.5 and RCP8.5 scenarios (Figure 6, middle and right) present similar pattern for precipitation in almost all three analysis periods. For these projections, a large part of the southern region will show precipitation within or below the average of the reference period (up to about −30%), except for some parts of the interior of the Inhambane Province and parts of the provinces of the central and northern regions. In these places, the change in precipitation may reach 20%. From Tables 8 and 9, it is clear that projections show a decrease

in precipitation, with RCP4.5 showing the 50th percentile with a negative sign during the 2040s and 2070s periods, while RCP8.5 shows similar behavior for all periods. This shows that for these scenarios, most of the country will experience a decrease in precipitation.

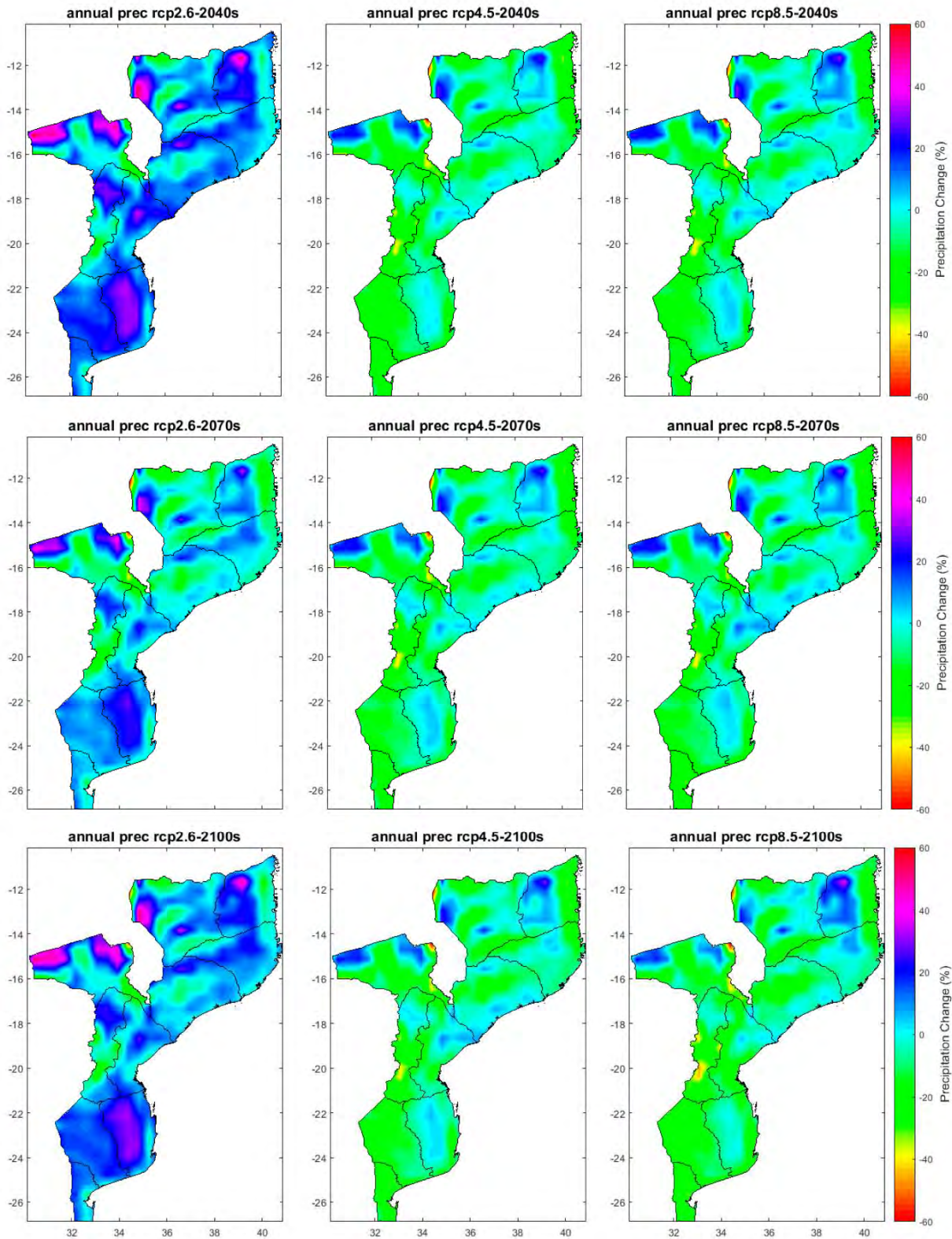


Figure 6. Projected changes in annual precipitation (%) for the 2040s (2011–2040), 2070s (2041–2070), and 2100s (2071–2100) with respect to the reference period (1961–1990) for the three RCPs scenarios (RCP2.6, RCP4.5, and RCP8.5).

Table 8. Percentile values of precipitation for the 2040s (2011–2040), 2070s (2041–2070), and 2100s (2071–2100) with respect to the reference period (1961–1990) for the RCP4.5 scenario. The cells filled with different colors differentiate positive and negative anomalies.

Period	Reference Period		Change in 2040s			Change in 2070s			Change in 2100s		
	Average (mm)	Std. Dev.	P5 (%)	P50 (%)	P95 (%)	P5 (%)	P50 (%)	P95 (%)	P5 (%)	P50 (%)	P95 (%)
Annual	1020	246.3	−23.8	−8.9	7.4	−22.6	−7.9	7.6	−14.5	4.5	23.7
DJF	186.2	47.6	−12.9	3.0	20.3	−10.4	6.0	25.4	−12.2	6.1	26.3
MAM	86.3	35.6	−18.2	3.9	25.1	−16.2	6.7	26.4	−12.8	10.9	31.6
JJA	23.5	12.6	−60.2	−33.4	−14.1	−61.1	−37.3	−19.9	−63.8	−39.5	−23.3
SON	44.5	11.5	−7.6	10.6	37.4	−15.9	2.1	33.5	−21.5	2.3	30.6

Table 9. Percentile values of precipitation for the 2040s (2011–2040), 2070s (2041–2070), and 2100s (2071–2100) with respect to the reference period (1961–1990) for the RCP8.5 scenario. The cells filled with different colors differentiate positive and negative anomalies.

Period	Reference Period		Change in 2040s			Change in 2070s			Change in 2100s		
	Average (mm)	Std. Dev.	P5 (%)	P50 (%)	P95 (%)	P5 (%)	P50 (%)	P95 (%)	P5 (%)	P50 (%)	P95 (%)
Annual	1020	246.3	−22.6	−7.0	9.8	−22.3	−6.6	9.8	−25.0	−10.0	9.5
DJF	186.2	47.6	−10.5	5.6	23.7	−8.2	8.3	26.3	−10.5	7.5	25.3
MAM	86.3	35.6	−15.8	5.6	25.3	−12.8	12.1	30.4	−16.1	5.9	27.9
JJA	23.5	12.6	−60.9	−33.6	−13.1	−63.9	−40.3	−24.9	−67.8	−47.0	−31.1
SON	44.5	11.5	−11.1	11.0	39.2	−16.1	6.1	30.9	−32.6	−6.0	28.6

3.4.2. Projected Changes in Seasonal Precipitation

In general, the behavior of seasonal precipitation shows a variable pattern similar to the pattern of annual precipitation, which is probably influenced by the same factors. All RCP scenarios point to above average precipitation in much of Mozambique during the DJF season (Figure A15), regardless of the period. The projections under the RCP2.6 scenario (Figure A15, left) show that during the DJF season, the entire southern region will show an increase in precipitation, which may exceed the historical average by more than 40%. The 5th and 95th percentile values are −7.5% and 38.1%, in the 2040s, −13.8% and 31.4%, in the 2070s, and −10.9% and 23% at the end of the century (Table 7).

For the RCP 4.5 and 8.5 scenarios (Figure A15, middle and right), there is a decrease in precipitation in the interior of the central and southern regions. For RCP4.5, the 5th and 95th percentiles are −12.9% and 20.3% in the 2040s, −10.4% and 25.4% in the 2070s, and −12.2% and 26.3% in the 2100s (Table 8). The RCP8.5 scenario presents changes in precipitation with values within the same magnitude. At the MAM season (Figure A16), similarly to the DJF season, projections under RCP2.6 point to an increase in precipitation in much of Mozambique, mainly in the 2040s (Figure A16, left) and 2100s. During these periods, the increase in precipitation may reach 60%, mainly in the north of the Tete Province and some parts of the Manica and Niassa Provinces. For the RCP4.5 and RCP8.5 scenarios (Figure A16, middle and right), the pattern is similar to that seen in the DJF season.

During the JJA season (Figure A17), all scenarios show that in almost all of Mozambique, there will be a decrease in precipitation, mainly for scenarios RCP4.5 and 8.5 (Figure A17, middle and right). The north of the Tete Province, the interior of the Niassa Province, and parts of the Cabo Delgado Province are the places where an increase in precipitation is expected, with values not exceeding 30%. The interior part of Mozambique will have a robust decrease in precipitation, reaching a variation of −60% in most of the provinces of Gaza, Tete, and Niassa. In this season, the 5th and 95th percentiles show negative values regardless of the period or scenario, except for the 95th percentile of RCP2.6, which is 1% during the 2040s (Table 7).

For the SON season (Figure A18), the projections under the RCP4.5 and RCP8.5 scenarios (Figure A18, middle and right) show a pattern of increased precipitation in the central and northern regions and of decreased precipitation in the south at the end of the century, where the change in precipitation could reach -40% . On the other hand, the RCP2.6 scenarios (Figure A18, left) show that there will be a decrease in precipitation in central Mozambique in the 2040s and 2100s and a decrease in almost the whole country in the 2070s.

3.5. Robustness of Projected CORDEX Model Simulations

Tables 10–12 show the change in temperature and precipitation projections, including the robustness test for the 20 districts divided by the four sub-regions used in this study. The results in bold are for the places where the change is robust. The results of the change in temperature are in accordance with the analysis in the previous section, with coastal districts having the least variation and districts in the south and center having the greatest variation. For temperature, all districts show robust changes, regardless of RCP and period.

For the precipitation simulations of RCP2.6 (Table 10), it is noticed that most districts present a robustness in the signal agreement, mainly in the districts of the coastal, central, and northern regions. In the districts of the southern region, the fact that none of them passed both tests in the 2070s stands out. In terms of combination, the districts of Beira, in the coastal region, Muidumbe and Chimbonila in the north, and Zumbo in the central region showed a robust change in precipitation in the 2040s. In the 2070s, only the districts of Beira, Muidumbe, and Chimbonila experienced a robust change. In the 2100s, the districts of Mangaja da Costa, Nampula, Chimbonila, Zumbo, and Mocuba show robustness in precipitation change. According to the table, no district in the southern region has a robust change in precipitation for the simulations of RCP2.6.

Table 10. Changes in future projections for RCP2.6 temperature and precipitation simulations. Results in bold show where the changes are robust.

Region	District	Temperature (°C)			Precipitation (%)		
		2040s	2070s	2100s	2040s	2070s	2100s
Coastal	Govuro	0.89	1.23	1.13	24.6	22.0	22.3
	Massinga	0.88	1.21	1.09	30.0	23.9	27.7
	Moc. Praia	0.97	1.29	1.24	26.8	17.0	17.7
	Nacala	0.95	1.23	1.19	14.6	12.7	14.5
	Mang. Costa	0.90	1.29	1.17	26.0	15.9	17.1
	Beira	0.89	1.24	1.13	28.8	20.3	22.9
	Xai-Xai	0.92	1.30	1.16	12.1	8.2	8.8
	Manhiça	0.95	1.31	1.18	7.6	8.4	7.3
Northern	Muidumbe	0.99	1.35	1.29	22.4	14.1	17.3
	Balama	0.96	1.36	1.31	15.1	11.4	12.9
	Nampula	0.96	1.33	1.27	13.6	10.4	12.3
	Chimbonila	1.01	1.41	1.31	7.8	4.3	7.4
Central	Zumbo	1.15	1.62	1.43	20.7	15.0	24.6
	Chemba	1.05	1.52	1.35	14.1	6.5	9.8
	Mocuba	0.93	1.28	1.23	19.6	11.9	15.6
	Sussundenga	1.03	1.45	1.30	11.8	4.4	9.3
Southern	Massangena	1.14	1.52	1.37	9.4	9.8	12.1
	Chigubo	1.09	1.48	1.33	14.8	9.7	11.7
	Massingir	1.08	1.49	1.33	7.6	2.1	4.9
	Namaacha	1.02	1.38	1.25	0.4	1.2	1.4

Table 11. Changes in future projections for RCP4.5 temperature and precipitation simulations. Results in bold show where the changes are robust.

Region	District	Temperature (°C)			Precipitation (%)		
		2040s	2070s	2100s	2040s	2070s	2100s
Coastal	Govuro	1.06	1.72	2.12	−2.4	−1.2	1.3
	Massinga	1.06	1.72	2.10	−12.9	−11.5	−12.3
	Moc. Praia	1.07	1.72	2.12	−25.6	−24.1	−24.6
	Nacala	1.05	1.70	2.10	−7.7	−8.9	−7.8
	Mang. Costa	1.12	1.81	2.22	17.1	14.6	17.1
	Beira	1.07	1.74	2.12	−5.2	−6.3	−4.7
	Xai–Xai	1.13	1.84	2.23	−11.5	−9.7	−12.9
	Manhiça	1.13	1.86	2.24	−21.2	−20.0	−22.1
Northern	Muidumbe	1.10	1.84	2.37	1.2	2.4	1.7
	Balama	1.17	1.99	2.68	20.9	22.3	21.3
	Nampula	1.16	1.95	2.53	6.7	5.4	5.9
	Chimbonila	1.21	2.22	3.18	30.2	28.0	27.1
Central	Zumbo	1.29	2.16	2.55	−31.2	−28.3	−28.7
	Chemba	1.21	1.96	2.41	−7.3	−6.4	−5.4
	Mocuba	1.16	1.90	2.33	7.2	6.9	7.1
	Sussundenga	1.20	1.97	2.42	−12.4	−12.3	−12.8
Southern	Massangena	1.28	2.03	2.52	−9.2	−6.9	−11.5
	Chigubo	1.27	2.02	2.49	−2.1	2.3	−1.3
	Massingir	1.32	2.13	2.56	−0.8	−0.3	−0.5
	Namaacha	1.17	1.96	2.34	2.5	0.6	−0.1

Table 12. Changes in future projections for RCP4.5 temperature and precipitation simulations. Results in bold show where the changes are robust.

Region	District	Temperature (°C)			Precipitation (%)		
		2040s	2070s	2100s	2040s	2070s	2100s
Coastal	Govuro	1.14	2.25	3.49	−2.6	−0.4	−8.4
	Massinga	1.12	2.24	3.65	−12.4	−13.6	−17.4
	Moc. Praia	1.15	2.27	3.72	−23.6	−23.8	−21.5
	Nacala	1.13	2.24	3.64	−4.9	−7.3	−5.4
	Mang. Costa	0.16	1.42	3.72	16.5	17.4	12.7
	Beira	1.16	2.26	3.67	−8.0	−5.1	−11.8
	Xai–Xai	1.20	2.39	3.90	−10.8	−12.6	−16.4
	Manhiça	1.21	2.41	3.93	−20.4	−22.7	−25.7
Northern	Muidumbe	1.20	2.37	3.87	3.9	4.9	8.0
	Balama	1.25	2.48	4.03	24.6	24.5	26.0
	Nampula	1.26	2.49	3.98	8.7	7.6	9.9
	Chimbonila	1.31	2.61	4.24	29.9	30.4	27.2
Central	Zumbo	1.38	2.93	4.60	−28.2	−26.7	−26.7
	Chemba	1.31	2.56	4.21	−6.6	−1.7	−8.1
	Mocuba	1.23	2.51	4.05	7.9	11.0	5.0
	Sussundenga	1.32	2.58	4.06	−13.6	−12.7	−18.9
Southern	Massangena	1.37	2.65	4.37	−10.3	−6.2	−13.8
	Chigubo	1.35	2.67	4.15	−1.9	1.9	−4.2
	Massingir	1.41	2.75	4.51	0.2	0.3	−5.0
	Namaacha	1.28	2.55	3.98	1.5	−0.7	−4.5

For the precipitation simulations of RCP4.5 (Table 11), there is a slight increase in districts that pass the test of significance and a decrease in districts that pass the test of agreement of the sign of change. The fact of having only four simulations of RCP2.6, in relation to nine simulations of RCP4.5, may have contributed to this difference, mainly

with regard to the test of agreement. For the RCP4.5 simulations, no district in the coastal and southern regions passed the combination of the two tests. The districts of Balama and Chimbonila, in the northern region, passed the tests regardless of the period. Still, in the northern region, the districts of Nampula and Muíumbo passed both tests in the 2070s and 2100s, respectively. The district of Sussundenga is the only one that passed both tests, in the central region, in the 2070s.

For the assessment of robustness for the precipitation simulations of RCP8.5 (Table 12), similar to the simulations of RCP2.6 and RCP4.5, no district in the southern region passed the combination of the two tests. The districts of Balama and Chimbonila, in the northern region, passed the tests regardless of the period, while still in this region, the districts of Muíumbo and Nampula passed both tests in the 2040s and 2070s, respectively. In the coastal region, the districts of Beira and Manhiça passed both tests in the 2040s and 2100s. Finally, in the central region, only the district passes the two tests, in the 2070s and 2100s.

4. Discussion and Conclusions

To determine climate change adaptation responses under different future climate projections with reduced uncertainty and particularly at regional, countrywide, or local levels at which important and actionable policy decisions are made requires reliable climate projections. This requires evaluation of climate projection in terms of comparison with other sources of data, also in terms of their robustness and significance [94]. The scarcity of dedicated studies on climate change projections at local levels is an undeniable fact. While efforts are taken to improve the accuracy of climate change projections, publications or studies focusing on regional, countrywide, and local levels should be increased. Publications available to date on climate projections at the aforementioned levels are very limited for Mozambique [3,95].

In this study, we analyzed the results of a multi-model ensemble based on nine models derived from the COordinated Regional Downscaling EXperiment (CORDEX) initiative and examined climate change projections of temperature and precipitation over Mozambique. These changes were calculated and analyzed for Mozambique taking into account its four sub-regions, namely, coastal, northern, central, and southern, considering three 30-year time periods, the 2040s (present 2011–2040), the 2070s (mid 2041–2070), and the 2100s (end 2071–2100) under the Representative Concentration Pathways RCP2.6, RCP4.5, and RCP8.5, relative to the baseline period (1961–1990).

The results show that future warming is not uniform over Mozambique and varies from region to region. Projected temperatures (maximum, minimum, and average) show an upward trend in most of the country in particular for the RCP4.5 and RCP8.5 scenarios.

Under the RCP2.6, for the present (end) period, the maximum temperature increases by 0.8 °C (1.1 °C), the minimum temperature increases by ≈ 1.0 °C (≈ 1.2 °C), and the average temperature increases by ≈ 0.9 °C (≈ 1.2 °C).

Under the RCP4.5, the maximum temperature increases by ≈ 1.2 °C (2.4 °C), the minimum temperature increases by ≈ 1.3 °C (≈ 2.5 °C), and the average temperature increases by ≈ 1.3 °C (≈ 2.4 °C).

Under the RCP8.5, the maximum temperature increases by ≈ 1.2 °C (2.4 °C), the minimum temperature increases by ≈ 1.3 °C (4.1 °C), and the average temperature increases by ≈ 1.3 °C (4.3 °C).

The projected changes in average temperature in this study are consistent with regional estimates (≈ 1.2 °C (≈ 1.3 °C), ≈ 1.4 °C (≈ 2.3 °C), and ≈ 1.7 °C (4.1 °C) under RCP2.6, RCP4.5 and RCP8.5, respectively) obtained from CMIP6 [88] for the sub-region of South East Africa (SEAF) which includes Mozambique.

These increases, especially under the RCPs 4.5 and 8.5 already surpassed the Paris Agreement policy responses to climate change targets [19], which states the need for maintaining temperatures at present levels while assessing the implications that could arise if warming overcomes 1.5–2 °C. These increases in temperature, particularly the maximum

temperature, are expected to impact socio-economic sectors, in particular the agricultural sector.

The largest warming (hotspots) in the country are projected to occur under RCP4.5 and RCP8.5 mainly over parts of Gaza, parts of the central region, and parts of Niassa in the north. These regions are projected to have their maximum temperature increasing by ≈ 0.9 °C (≈ 1.2 °C), minimum temperature increasing by ≈ 1.1 °C (1.4 °C), and average temperature increasing by ≈ 1.0 °C (≈ 1.3 °C) under RCP2.6. Under RCP4.5, the maximum temperature increases by ≈ 1.4 °C (2.7 °C), the minimum temperature increases by ≈ 1.5 °C (≈ 2.8 °C), and the average temperature increases by ≈ 1.4 °C (≈ 2.7 °C). Under RCP8.5, the maximum temperature increases by ≈ 1.5 °C (4.7 °C), the minimum temperature increases by ≈ 1.6 °C (4.9 °C), and the average temperature increases by ≈ 1.5 °C (4.7 °C). The regions of Gaza and central region are predominately semi-arid and experience frequent droughts, and hence, they are the most likely to experience increased risk of inland crop failure, which can be expected to affect a huge number of communities [96] as a result of serious water shortages. The high vulnerability of the population in the arid and semi-arid regions encouraged the Government of Mozambique to initiate several important investments locally. One of these investments was the United Nations Joint Programme (UNJP) on Environmental Mainstreaming and Adaptation to Climate Change for the period between 2008 and 2012 (total of US\$7 million), which identified at the farm and community level adaptive interventions that have been tested and applied as well as showed a positive impact on productivity, broadening of the livelihood basis, and improving resilience to climate change [97]. On the other hand, Niassa is among the most irregular rainfall regimes in the northern region of the country [98]. Increased temperatures due to climate change may result in a decrease soil moisture, which in turn promotes increased evapotranspiration loss from open water bodies, soils, and vegetation [3].

With these projected temperature increases, particularly the hotspots, it is likely that some of the aforementioned areas, particularly in the north, will experience normal to extreme floods more frequently. In contrast, the southern region where the largest warming is expected is likely to deal with more frequent droughts and other induced hazards.

These results are supported to some extent by previous studies [3,31,56,95]. Notably, the magnitude of change in the aforementioned scenarios shows an increase in temperature up to ≈ 5 °C on the interior and less toward the coast of the Mozambique. This result is consistent with the study by [3] in which temperature increased up to 6 °C by 2100 based on an A2 emission scenario (equivalent to the RCP8.5 scenario). The difference in relation to our results can be explained by the outputs of the models used, since there was no downscaling based on local observations for this study. Another result consistent with the study by [3] is related to the fact that at a seasonal time scale, the SON period presents the greatest change in temperature.

One important finding of this study is that projected increases in temperature over most of the country indicate higher values for the worst level case scenario (RCP8.5) than for the medium level case scenario (RCP4.5) and for the low level case scenario (RCP2.6). The latter options have less impact and are more convenient for the world's governments and other institutions for decision making, since they lead to medium/small temperature increases. If the world follows the two pathways, medium/less adaptation will be needed and medium/low costs implications will likely occur.

Projected precipitation changes over Mozambique show substantial spatial and temporal variations. Analysis for the present (end) period presented different patterns under the RCP pathways.

Under the RCP2.6, annual precipitation change is projected to vary from -10 to 30 (-20 to 30)%, with substantial decreases occurring in the northern coastal zone, the interior of the central and northern regions, by -30 (-40)% and the increases occurring optimistically in the southern region and substantial increases in some parts of the central and northern regions by 50 (50)%. The 5th percentile and 95th percentile show values of

−7.3 (−23.3)% and 30.7 (7.2)%, respectively. These results show a tendency of precipitation decrease over time in most of the country.

Under RCP4.5, annual precipitation is projected to decrease over most of Mozambique by −20 (−20)%, with some hotspots showing substantial decreases such as those occurring in the interior of central and Niassa Province by −50 (−60)%, and substantial increases occurring north of Tete Province and parts of the northern region by 25 (30)%. The 5th percentile and 95th percentile show values of −23.8 (−14.5)% and 7.4 (23.7)%, respectively.

Under RCP8.5, annual precipitation is projected to decrease over most of Mozambique by −30 (−30)%, with hotspots indicating substantial decreases for example occurring in the interior of central and Niassa Province by −50 (−60)%, and the highest increases occurring north of the Tete Province and parts of the northern region by 30 (30)%. The 5th percentile and 95th percentile show values of −22.6 (−25)% and 9.8 (9.5)%, respectively.

The results of precipitation analyses point out that under the RCP2.6 scenario, the southern region will experience an increase of precipitation over time. On the other hand, projected precipitation under the RCP4.5 and RCP8.5 scenarios shows that over the southern region, there will be a decrease of precipitation over time, mainly in interior areas. This suggests that long drought periods are likely to be the dominant factor for the southern region climate. The central and northern region results show a complex pattern of projected precipitation change, with a decrease over most of the northern region under the RCP2.6 scenario and an increase under the RCP4.5 and RCP8.5 scenarios. From the point of view of agriculture, the central and northern regions are likely to be more suitable for the cultivation of crops under a precipitation-increasing tendency, while under a precipitation-decreasing tendency, these areas will demand more water for the crops or increase water stress and drought conditions.

Similar findings on projected precipitation changes were also verified by [56], although their analysis was not so localized. Other researchers [31] also found a robust decrease in precipitation accompanied by increases in the number of consecutive dry days and decreases in consecutive wet days over most of the central African subcontinent, including parts of northern Mozambique under RCP8.5.

Studies assessing impacts of hydropower generation in Mozambique found temperature and precipitation to have a critical role since the projected increasing in temperature will increase evaporation, while the projected reduction in precipitation will affect the potential for hydropower generation [33]. Kariba and Cahora Bassa are among the major dams in the Zambezi river system, presenting two vivid examples that will be substantially affected by increased evapotranspiration and decreased precipitation due to climate change.

The assessment of the performance of model outputs in relation to historical data showed that all models have good correlations with the observations (above 0.7) in almost all stations, except in Pemba, where the correlations are above 0.5. The associated errors vary between 0.25 and 2 °C, with the standard deviation not exceeding 3 °C. The average of the models presents the best results in the evaluation, where their correlation reaches more than 0.9. For precipitation, correlations are below 0.5 in most stations; only Nampula and Lichinga present correlations that reach 0.75 and 0.77, respectively. The errors vary between 100 and 200 mm. Similar to what was observed in the temperature, the average of the models presents the best results also for precipitation, reaching 0.79 in Nampula and 0.82 in Lichinga.

Regarding future simulations, the robustness of the change through the combination of the signal agreement and Student t-test was performed. The analysis of the robustness of the change in future simulations is important to assess the level of uncertainty in relation to the projections, mainly of precipitation, which is the variable that presents the great variability, both temporal and spatial. The results show that in all regions and for all periods, the change in temperature is robust. Regarding the change in precipitation, the northern region is the one that presents most of the districts that pass the two robustness tests for the three projection periods (2040s, 2070s, and 2100s). On the other hand, the coastal and southern regions are the ones that have more districts that do not pass the tests,

whereas in the southern region, no district passed the tests in the three periods of analysis. The high spatial and temporal variability of precipitation, and the fact that the simulation was downscaled over the African region, not at the country level, may have influenced the poor robustness of the precipitation projections.

A special highlight derived from the analysis goes to the central region, which is extremely vulnerable to all types of natural disasters and weather-related events, which are likely induced by ongoing climate change. The complexity of the climate patterns in this region calls for profound climate risk monitoring, risk preparedness, and resilience actions as well as more dedicated climate studies.

This study is perhaps among the first of its kind using CORDEX Climate model ensemble outputs to assess climate projections over Mozambique (countrywide), based on the Representative Concentration Pathways (RCPs) to update previous studies conducted with Special Emission Scenarios (SRES), among others. This piece of work represents a contribution aiming to respond to the impacts of climate change already happening in Mozambique and elsewhere. The significance of this work lies in the fact that this information is particularly needed to support decision making at different levels: policy, government sectors, scientific community, associations, civil society, and other types of organizations. In particular, the expanded uncertainties associated with the increasing climate variability and climate change (global warming) make such decisions and public participation even more daunting. This fact points to the need for more reliable, tailored climate information to adequately attend different and specific user needs.

In this paper, we show that improved climate information of high resolution freely available from web portals can be used to study the behavior of our climate system with an eye to the past, present, and future changes over time in a specific domain, particularly under but not limited to the human influence. This is crucial, because accessing this information, which contains key indicators that characterize the state of the climate represents an open window for the scientific community to conduct timely and systematic assessments on the patterns of change, thus improving our understanding of how climate change becomes a major concern to the survival of human beings as it poses significant risks and impacts on the natural resources, environment, and surrounding assets. Finally, we are able to discuss and present results that can be used as reference material for decisions processes, climate change projects, interventions, and also for education purposes.

Author Contributions: Conceptualization, A.F.M., B.E.B. and A.J.Q.; methodology, A.F.M., B.E.B. and O.A.M.; software, A.F.M. and B.E.B.; validation, A.F.M., A.J.Q. and B.E.B.; formal analysis, A.F.M., B.E.B., O.A.M. and A.J.Q.; investigation, A.F.M., B.E.B., O.A.M. and A.J.Q.; resources, A.F.M.; data curation, A.F.M. and B.E.B.; writing—original draft preparation, A.F.M. and B.E.B.; writing—review and editing, A.F.M., B.E.B., O.A.M. and A.J.Q.; visualization, B.E.B.; supervision, A.F.M., B.E.B., O.A.M. and A.J.Q.; project administration, A.F.M.; funding acquisition, A.F.M. All authors have read and agreed to the published version of the manuscript.

Funding: This research work was funded by the European Union, La Réunion Regional Council and the French state under the framework of the INTERREG-5 Indian Ocean 2014–2020 project “ReNovRisk-Cyclone and Precipitation”.

Institutional Review Board Statement: Not applicable.

Informed Consent Statement: Not applicable.

Data Availability Statement: The numerical models outputs (CanESM2, CNRM-CM5, CSIRO-MK3, GFDL-ESM2M, HadGEM2-ES, IPSL-CM5A-MR, MIROC5, MPI-ESM-LR, Nor-ESM1-M) used in this study can be downloaded following specific guiding instructions and steps available at <http://www.csag.uct.ac.za/cordex-africa/how-to-download-cordex-data-from-the-esgf>. Other data presented in this study are not publicly available. These data are available on request from INAM (Instituto Nacional de Meteorologia, Maputo, Moçambique).

Software: The data analysis and output for this paper was generated using (i) [ArcGIS] software, Version [10.5.1], from the Department of Geology, Faculty of Sciences, Eduardo Mondlane University (UEM), Maputo, Mozambique; (ii) ENVI 5.1 and IDL software, Version [8.5.], License number 406564

(student version), from Stockholm University, Sweden, and (iv) Matlab software, Version [10a], License number 506085, from the Department of Physics, Faculty of Sciences, UEM, Maputo, Mozambique.

Acknowledgments: The authors thank Eduardo Mondlane University, Faculty of Sciences (UEM-FC) in Maputo, Mozambique, where all computer work was conducted. including the software facilities provided by the Departments of Geology and Physics. They also give thanks to the National Institute of Meteorology for providing station data for validation analysis. The authors also thanks the climate modeling groups and their respective institutions (aforementioned in Table 1) and the COordinated Regional Downscaling EXperiment (CORDEX) for producing and making their model output archived via Earth System Grid Federation (ESGF) Swedish datanode (<https://esg-dn1.nsc.liu.se/projects/esgf-liu/>) and freely available (access on February 2020).

Conflicts of Interest: The authors declare no conflict of interest with regard to this work and publication in this journal.

Appendix A

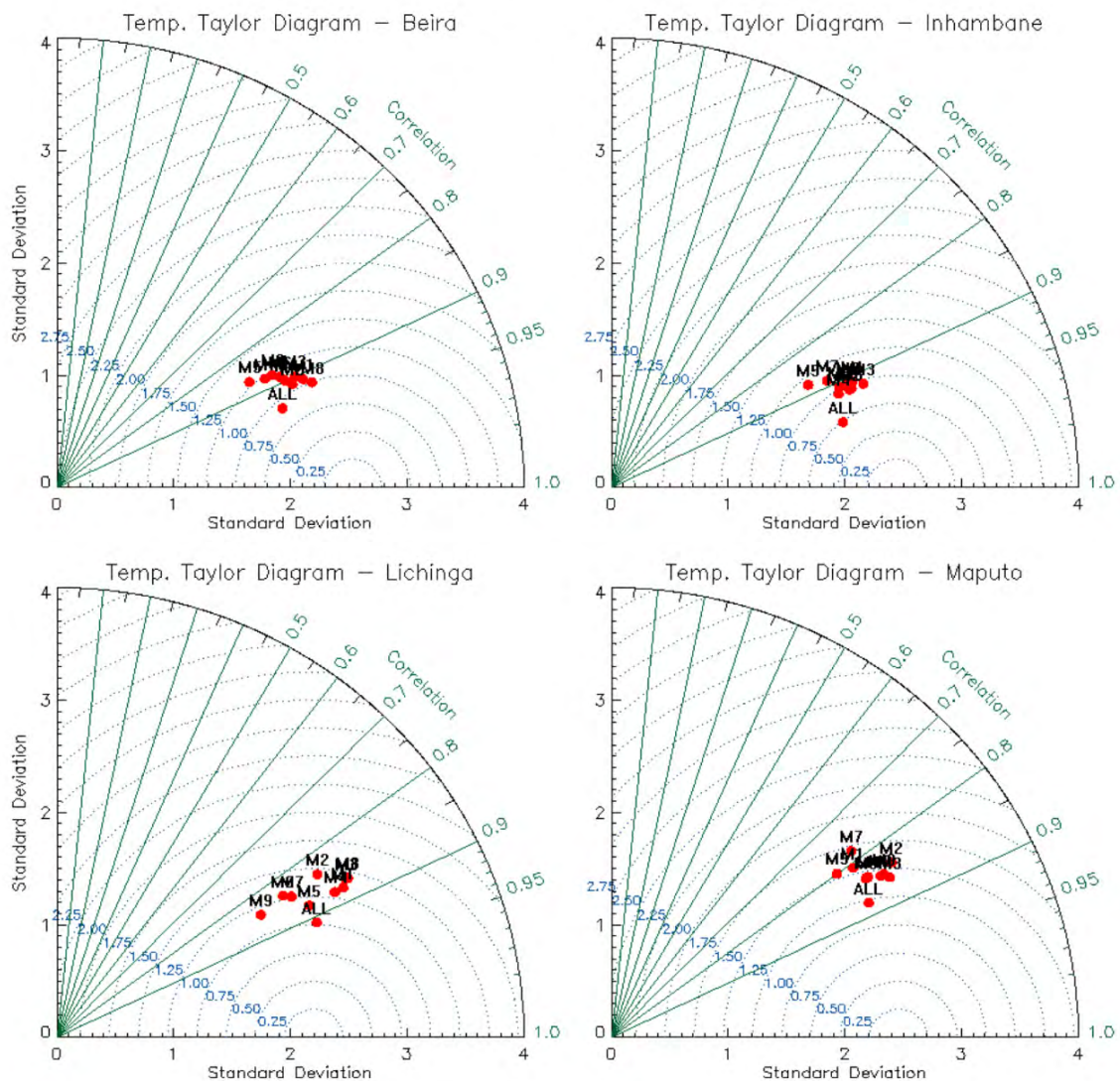


Figure A1. Cont.

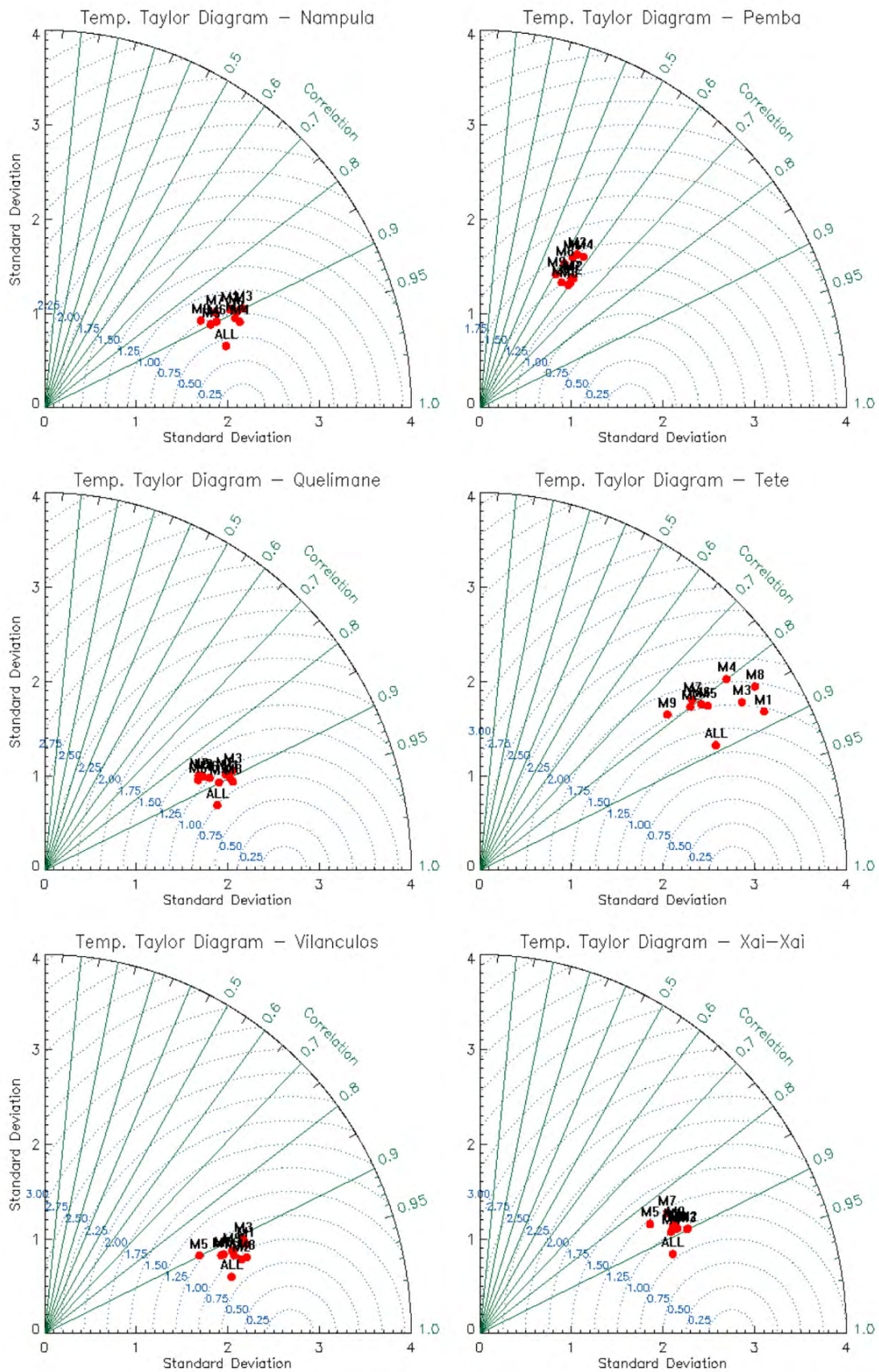


Figure A1. Taylor diagrams for temperature evaluation in Beira, Inhambane, Lichinga, and Maputo stations; Nampula, Pemba, Quelimane, Tete, Vilanculos, and Xai-Xai stations.

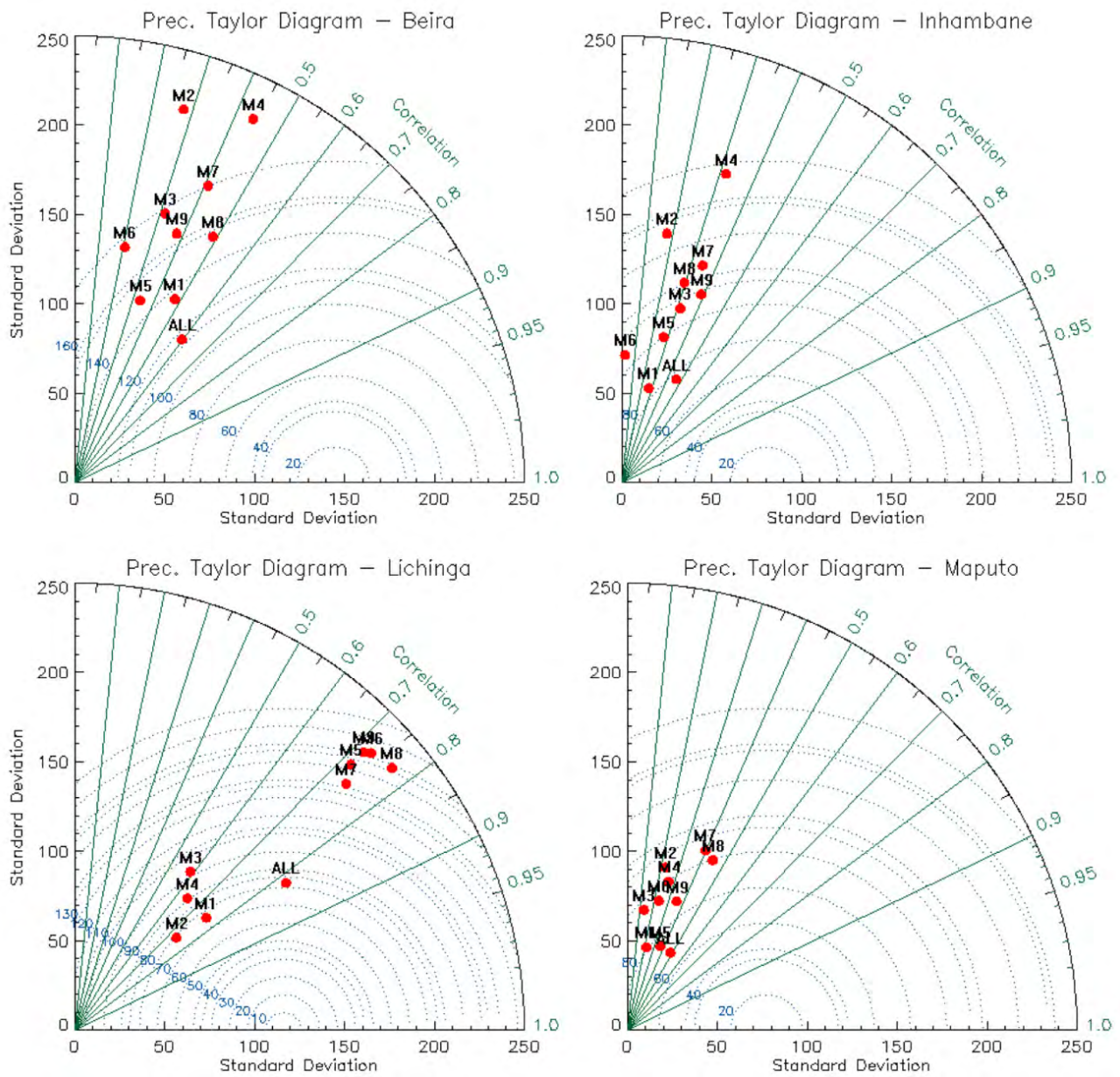


Figure A2. Cont.

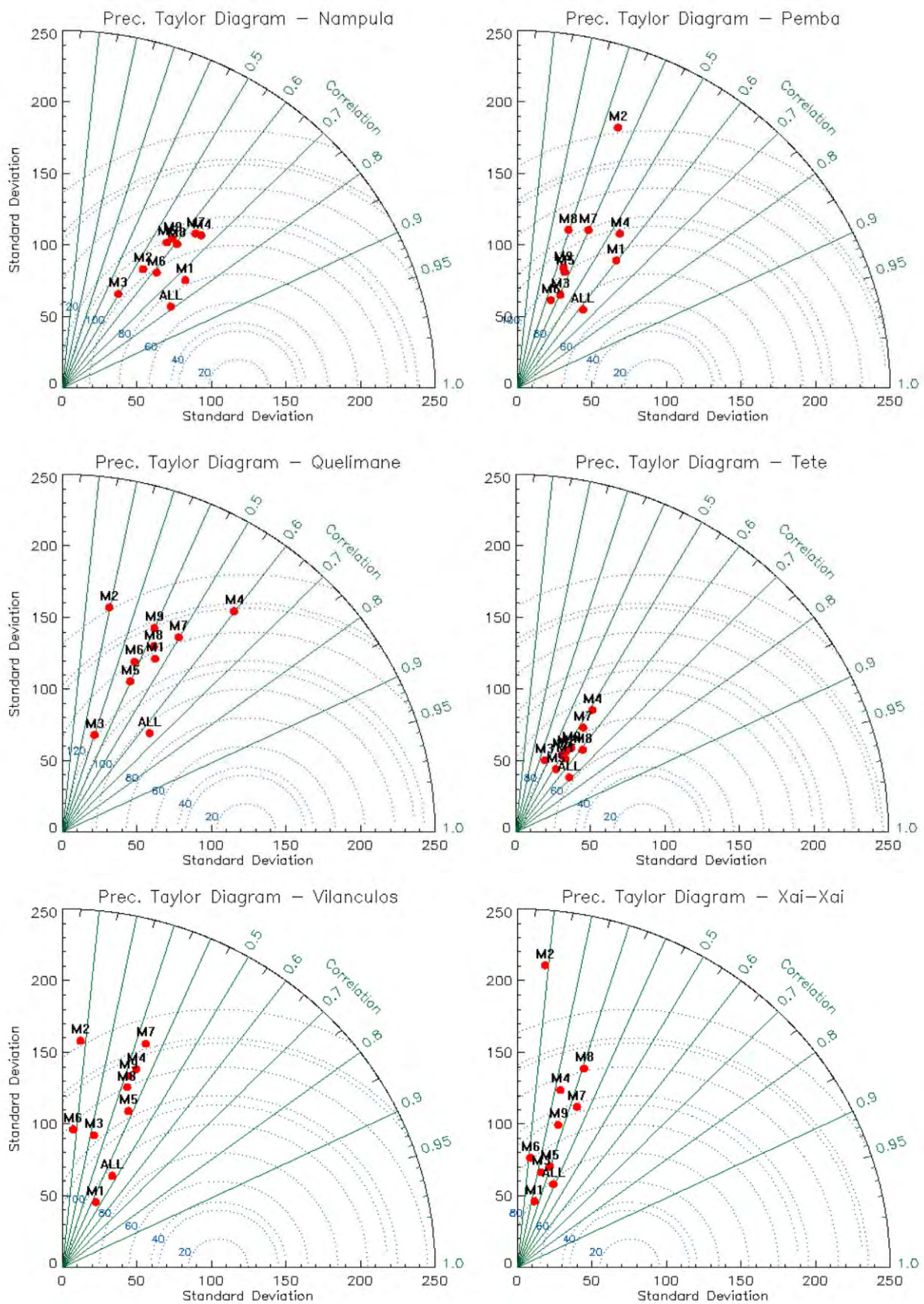


Figure A2. Taylor diagrams for precipitation evaluation in Beira, Inhambane, Lichinga, and Maputo stations; Nampula, Pemba, Quelimane, Tete, Vilanculos, and Xai-Xai stations.

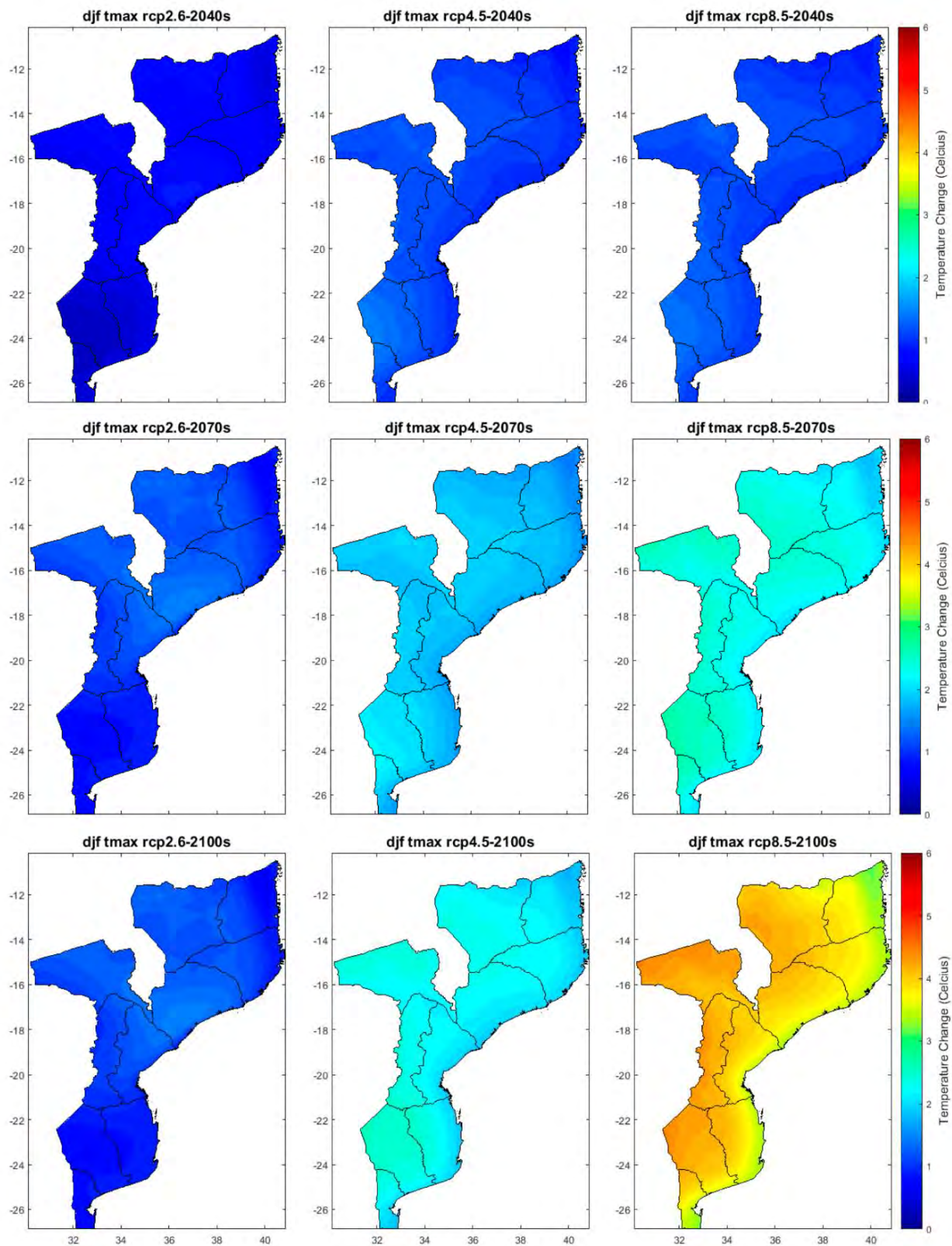


Figure A3. Projected changes of DJF maximum temperature for the 2040s (2011–2040), 2070s (2041–2070), and 2100s (2071–2100) with respect to the reference period (1961–1990) for the three RCP emission scenarios (RCP2.6, RCP4.5, and RCP8.5).

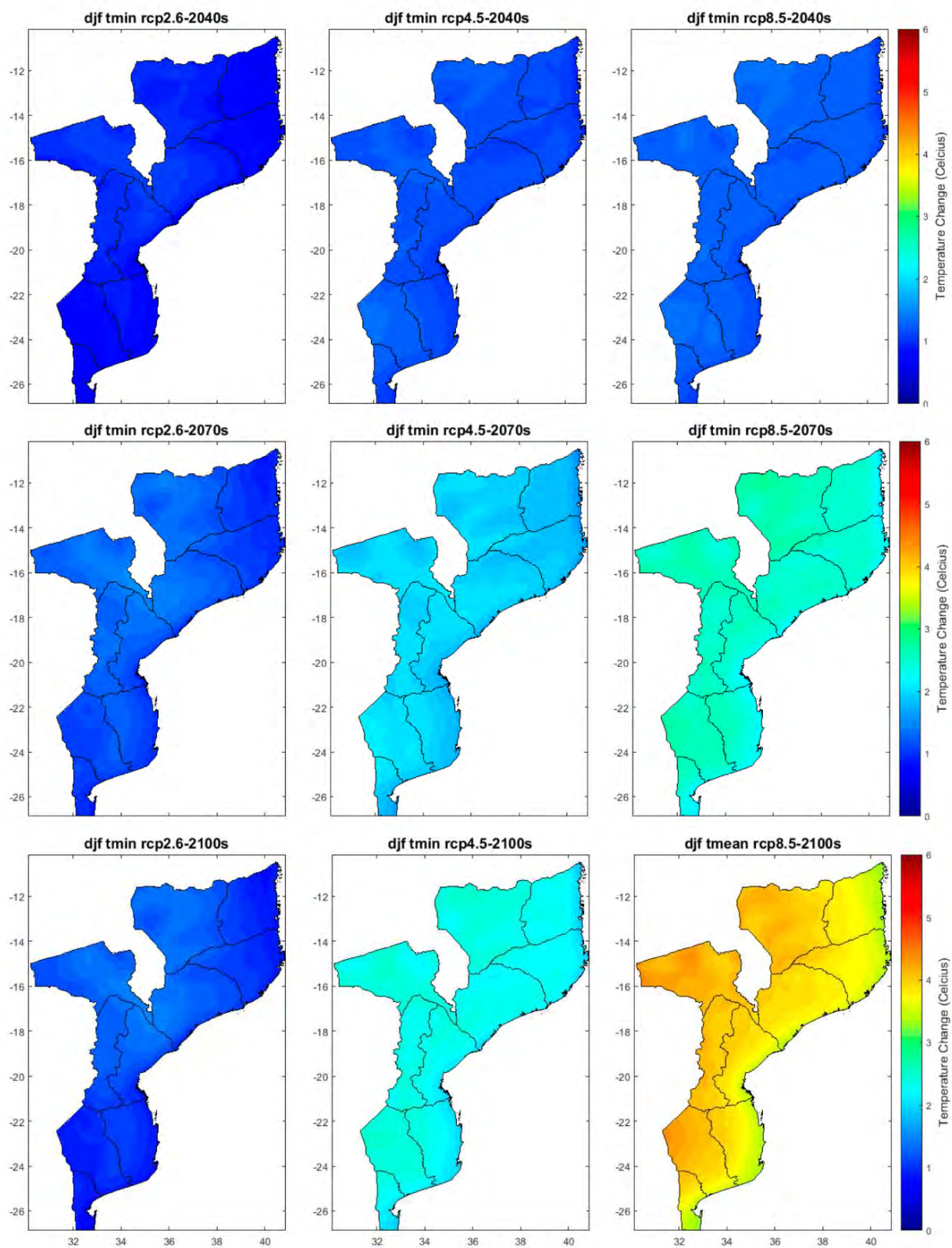


Figure A4. Projected changes of DJF minimum temperature for the 2040s (2011–2040), 2070s (2041–2070), and 2100s (2071–2100) with respect to the reference period (1961–1990) for the three RCP emission scenarios (RCP2.6, RCP4.5, and RCP8.5).

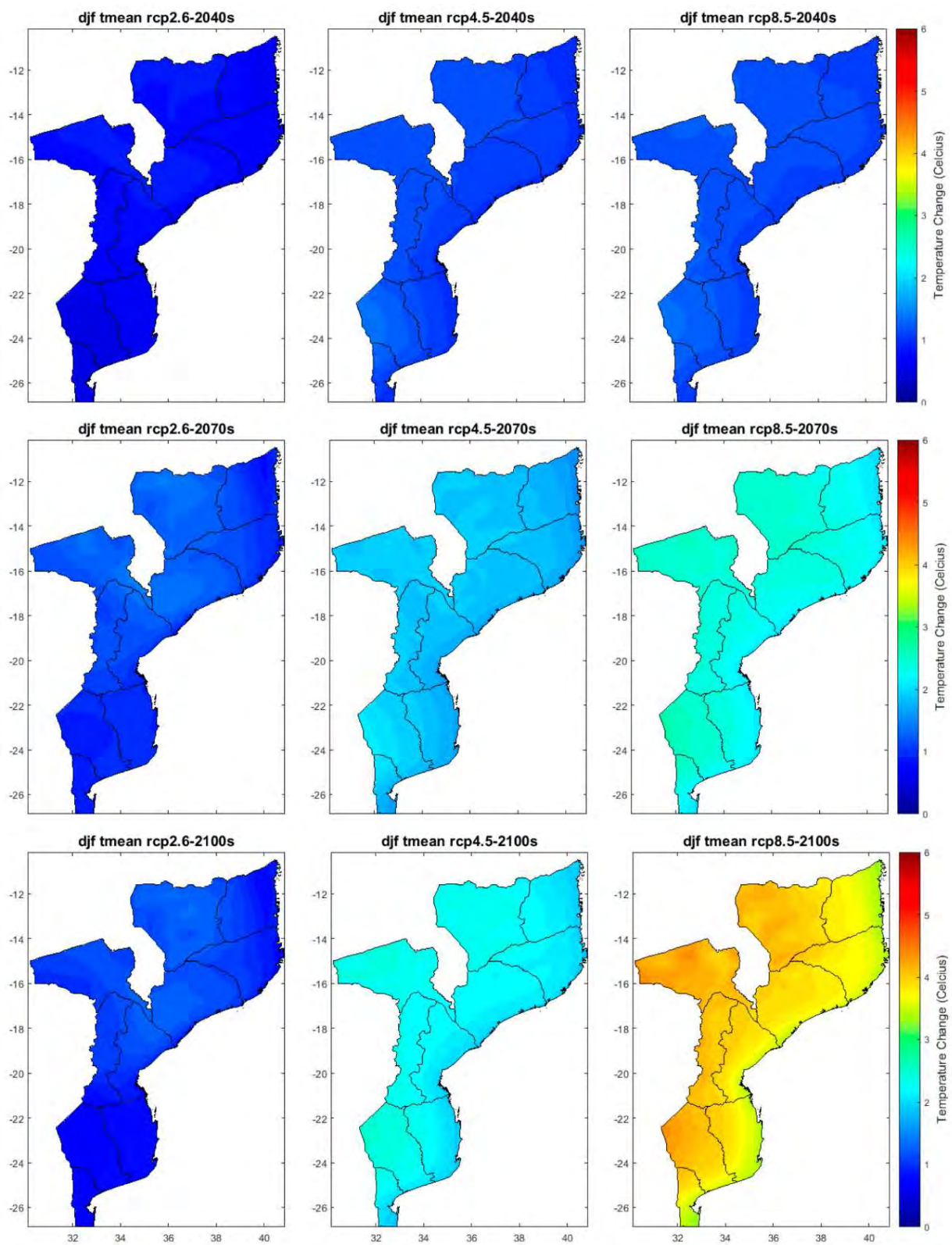


Figure A5. Projected changes of DJF mean temperature for the 2040s (2011–2040), 2070s (2041–2070), and 2100s (2071–2100) with respect to the reference period (1961–1990) for the three RCP emission scenarios (RCP2.6, RCP4.5, and RCP8.5).

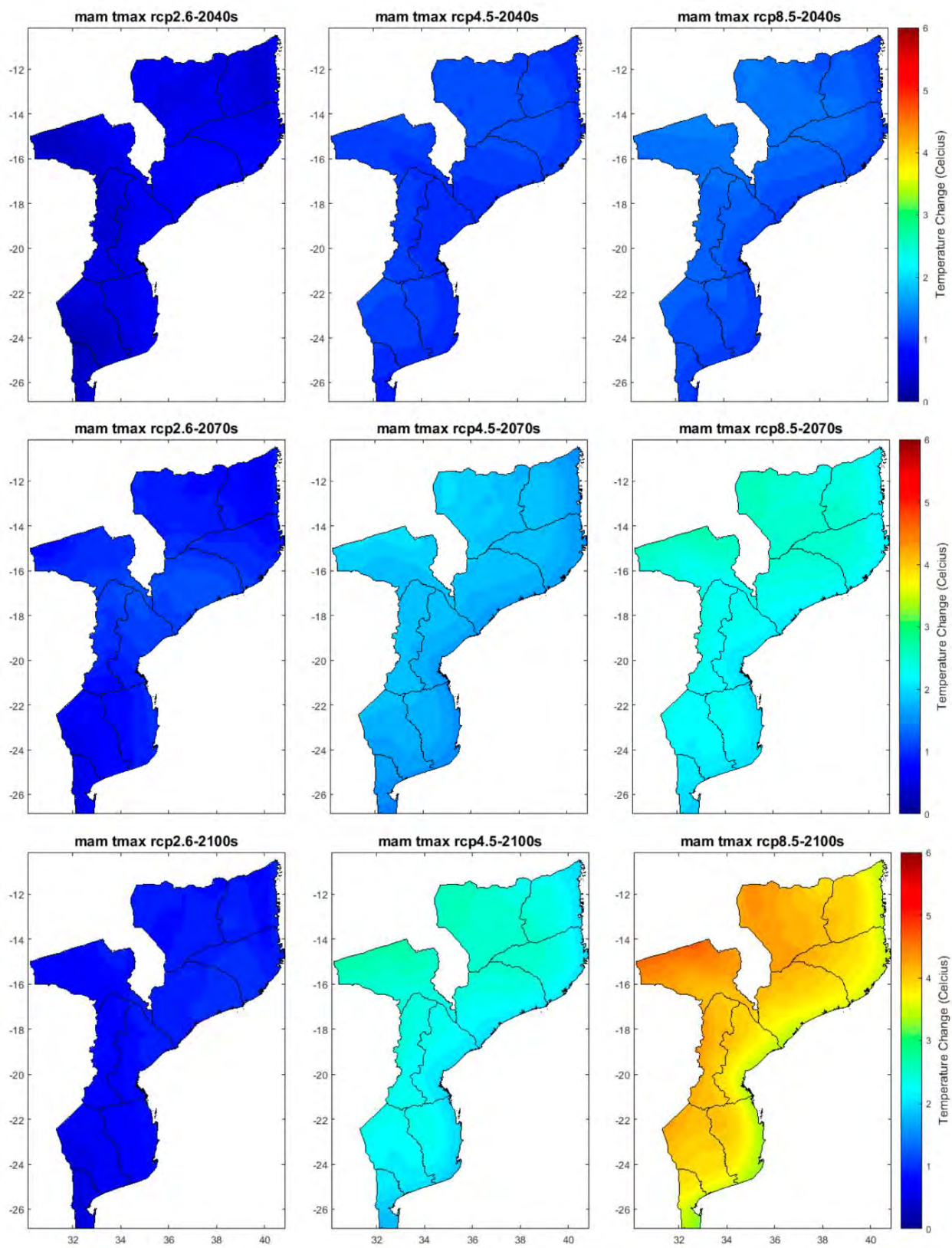


Figure A6. Projected changes of the MAM maximum temperature for the 2040s (2011–2040), 2070s (2041–2070), and 2100s (2071–2100) with respect to the reference period (1961–1990) for the three RCP emission scenarios (RCP2.6, RCP4.5, and RCP8.5).

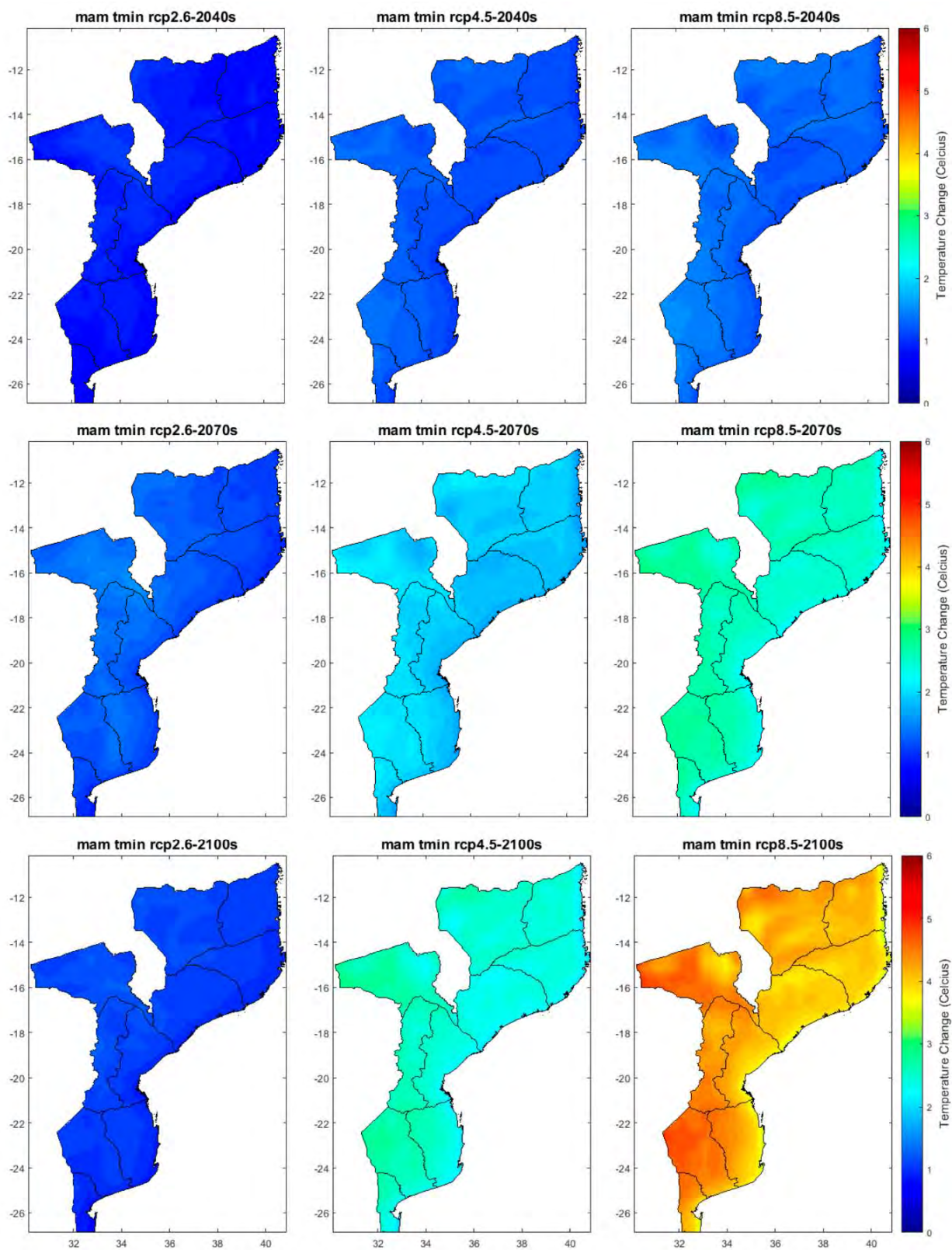


Figure A7. Projected changes of MAM minimum temperature for the 2040s (2011–2040), 2070s (2041–2070), and 2100s (2071–2100) with respect to the reference period (1961–1990) for the three RCP emission scenarios (RCP2.6, RCP4.5, and RCP8.5).

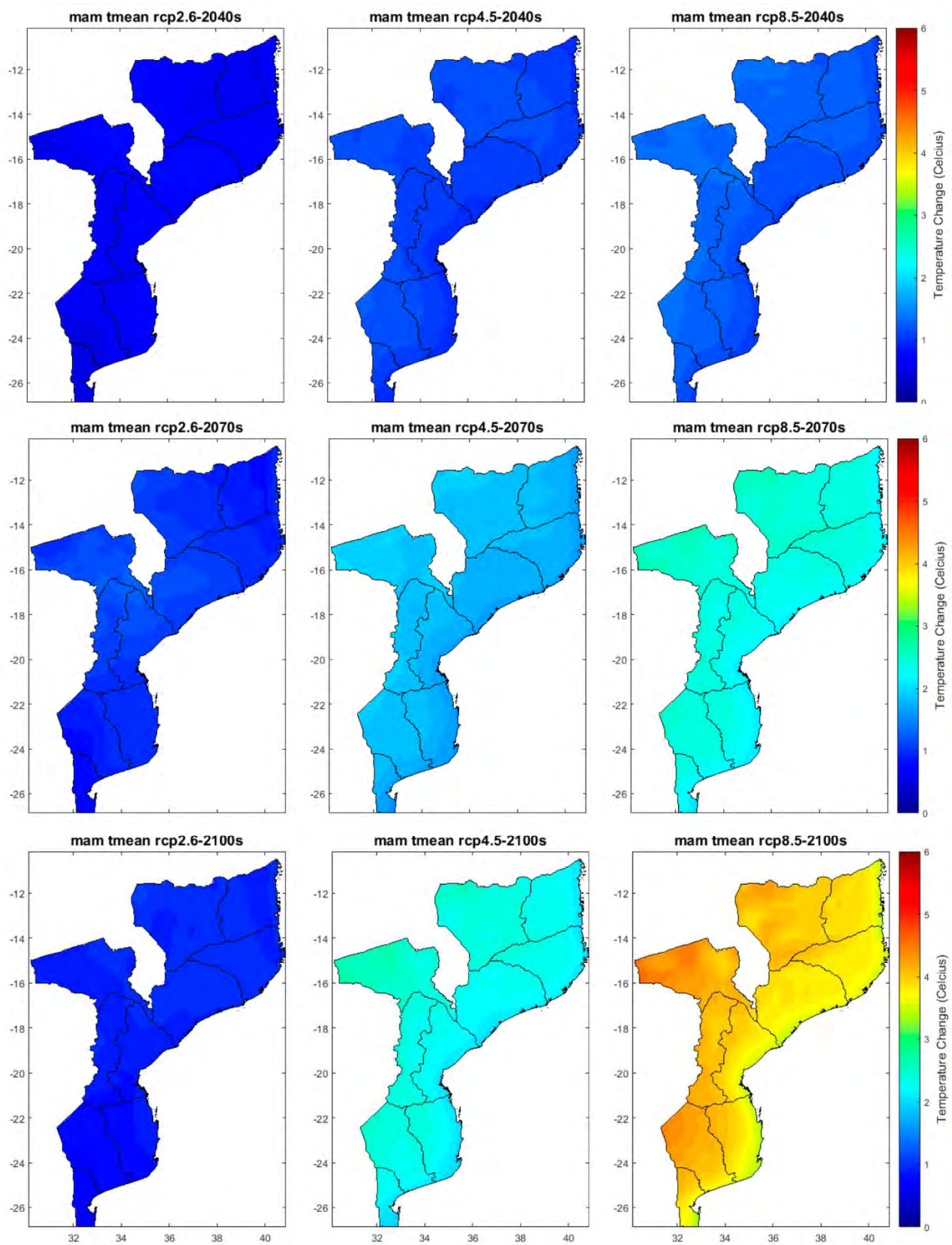


Figure A8. Projected changes of MAM mean temperature for the 2040s (2011–2040), 2070s (2041–2070), and 2100s (2071–2100) with respect to the reference period (1961–1990) for the three RCP emission scenarios (RCP2.6, RCP4.5, and RCP8.5).

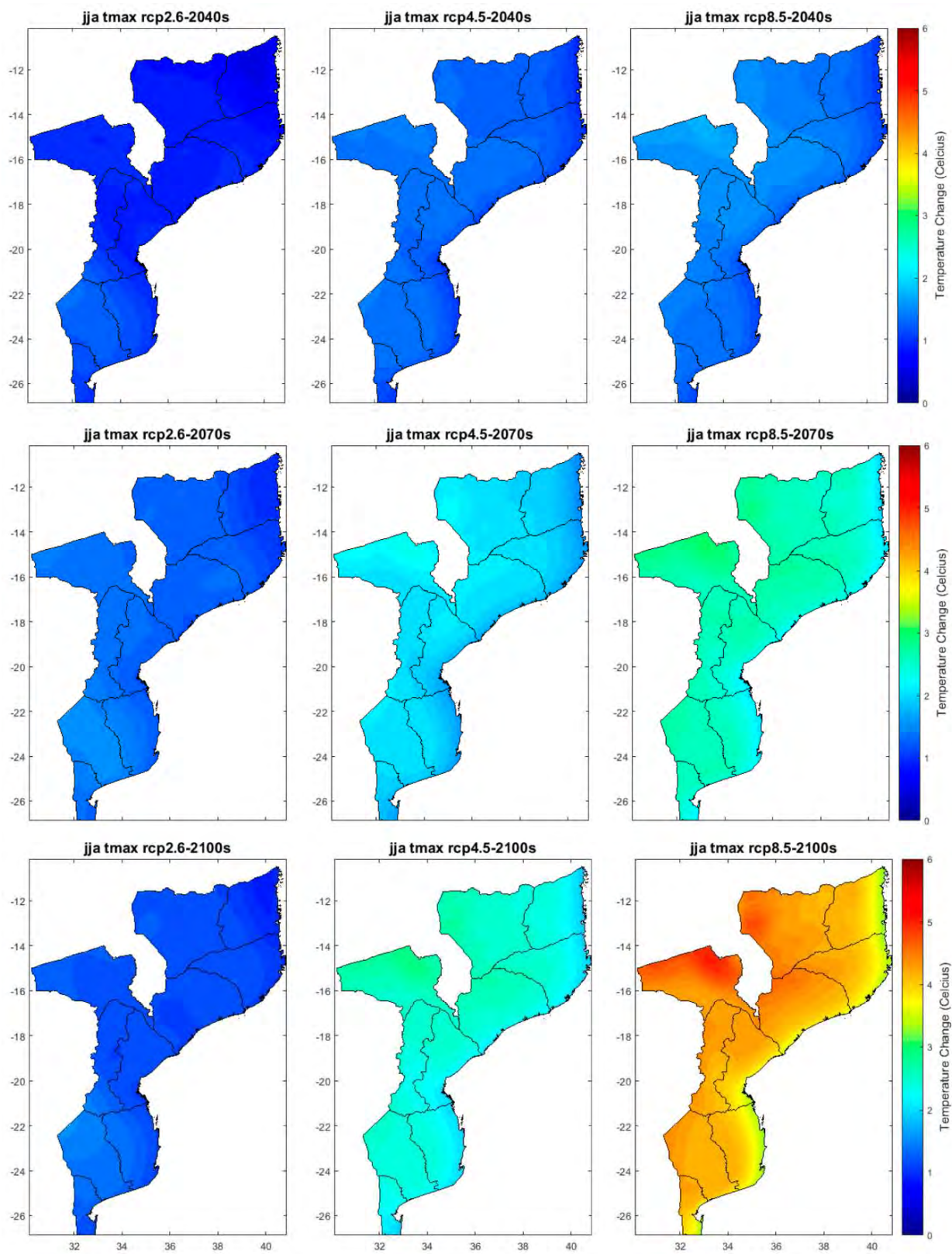


Figure A9. Projected changes of JJA maximum temperature for the 2040s (2011–2040), 2070s (2041–2070), and 2100s (2071–2100) with respect to the reference period (1961–1990) for the three RCP emission scenarios (RCP2.6, RCP4.5, and RCP8.5).

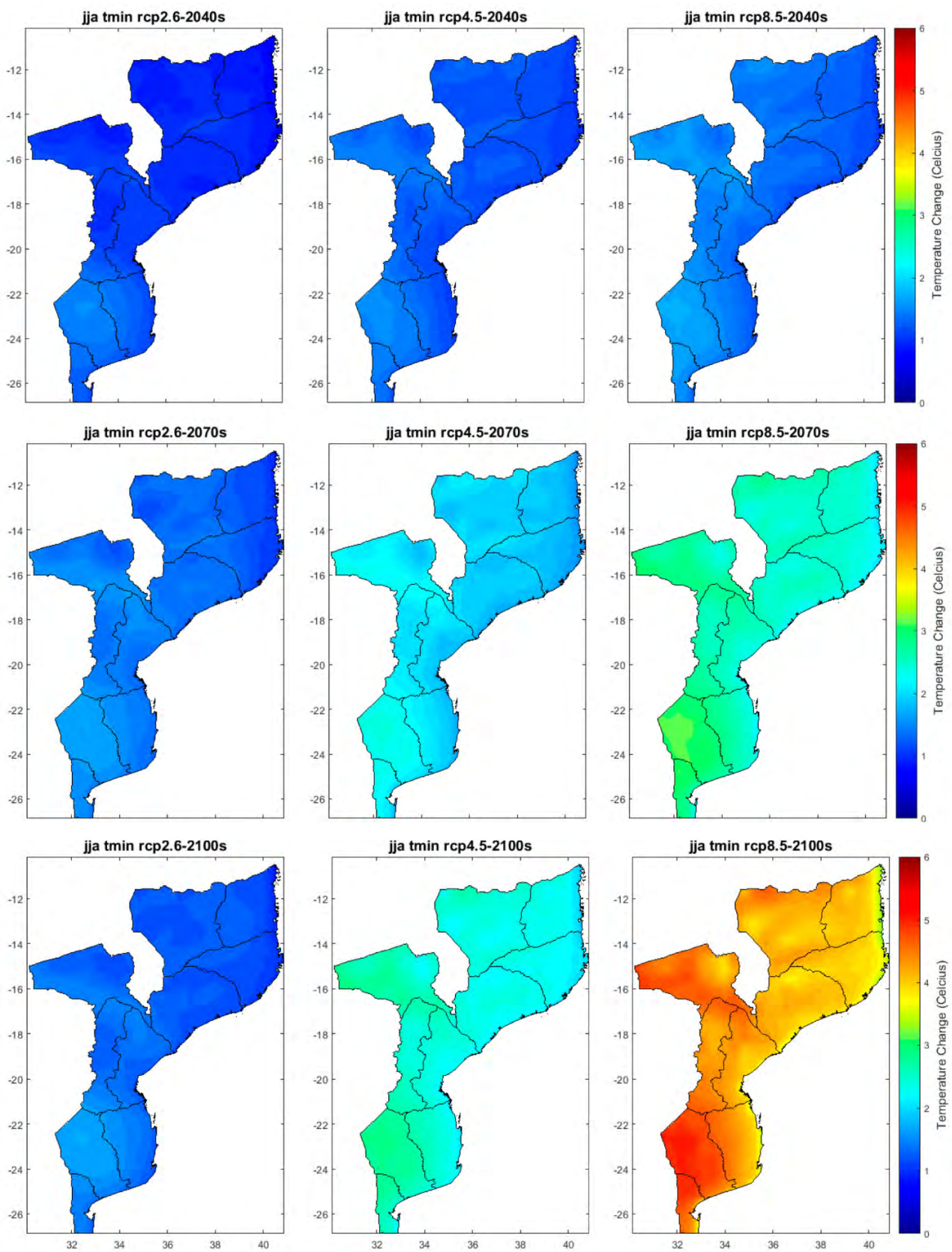


Figure A10. Projected changes of JJA minimum temperature for the 2040s (2011–2040), 2070s (2041–2070), and 2100s (2071–2100) with respect to the reference period (1961–1990) for the three RCP emission scenarios (RCP2.6, RCP4.5, and RCP8.5).

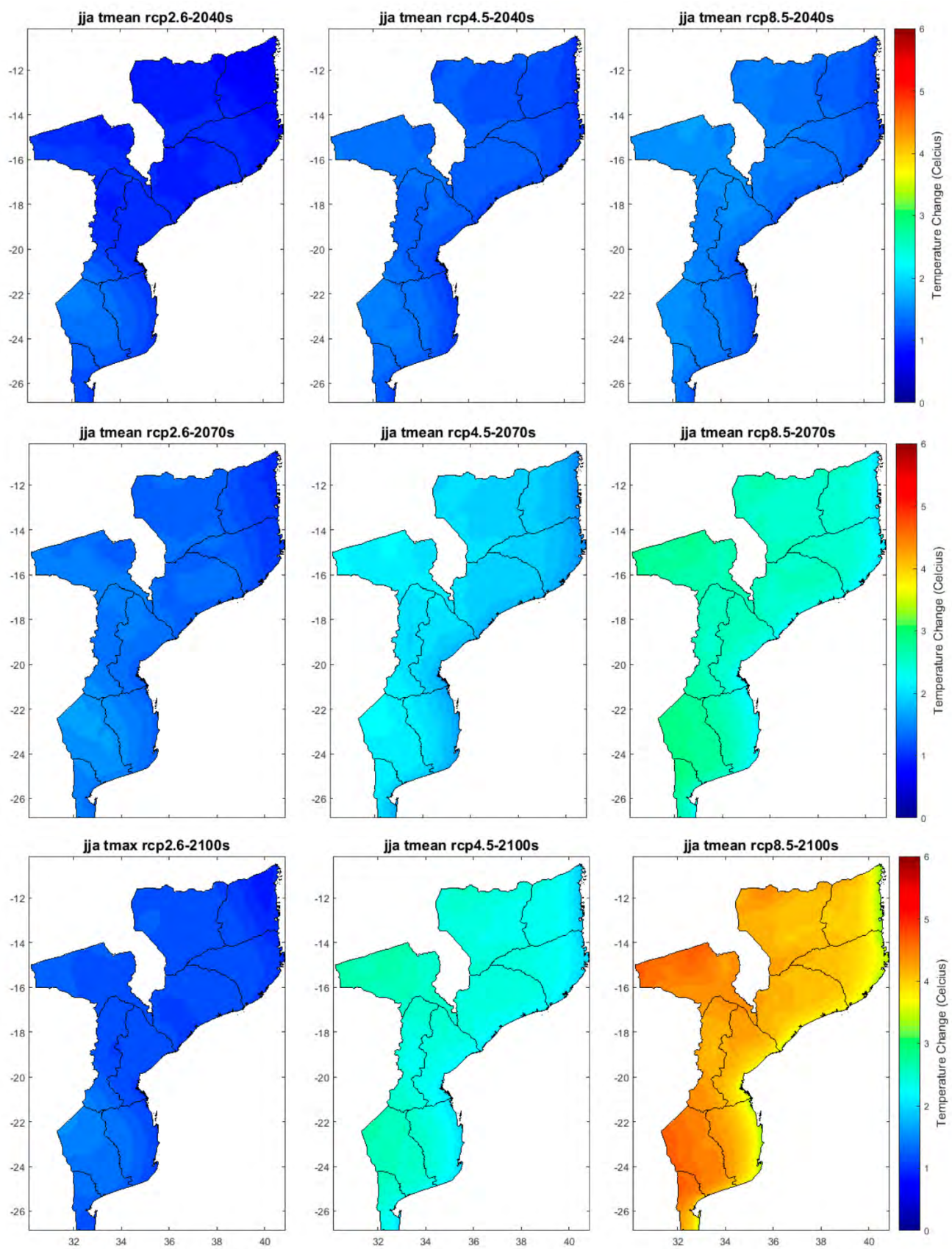


Figure A11. Projected changes of JJA mean temperature for the 2040s (2011–2040), 2070s (2041–2070), and 2100s (2071–2100) with respect to the reference period (1961–1990) for the three RCP emission scenarios (RCP2.6, RCP4.5, and RCP8.5).

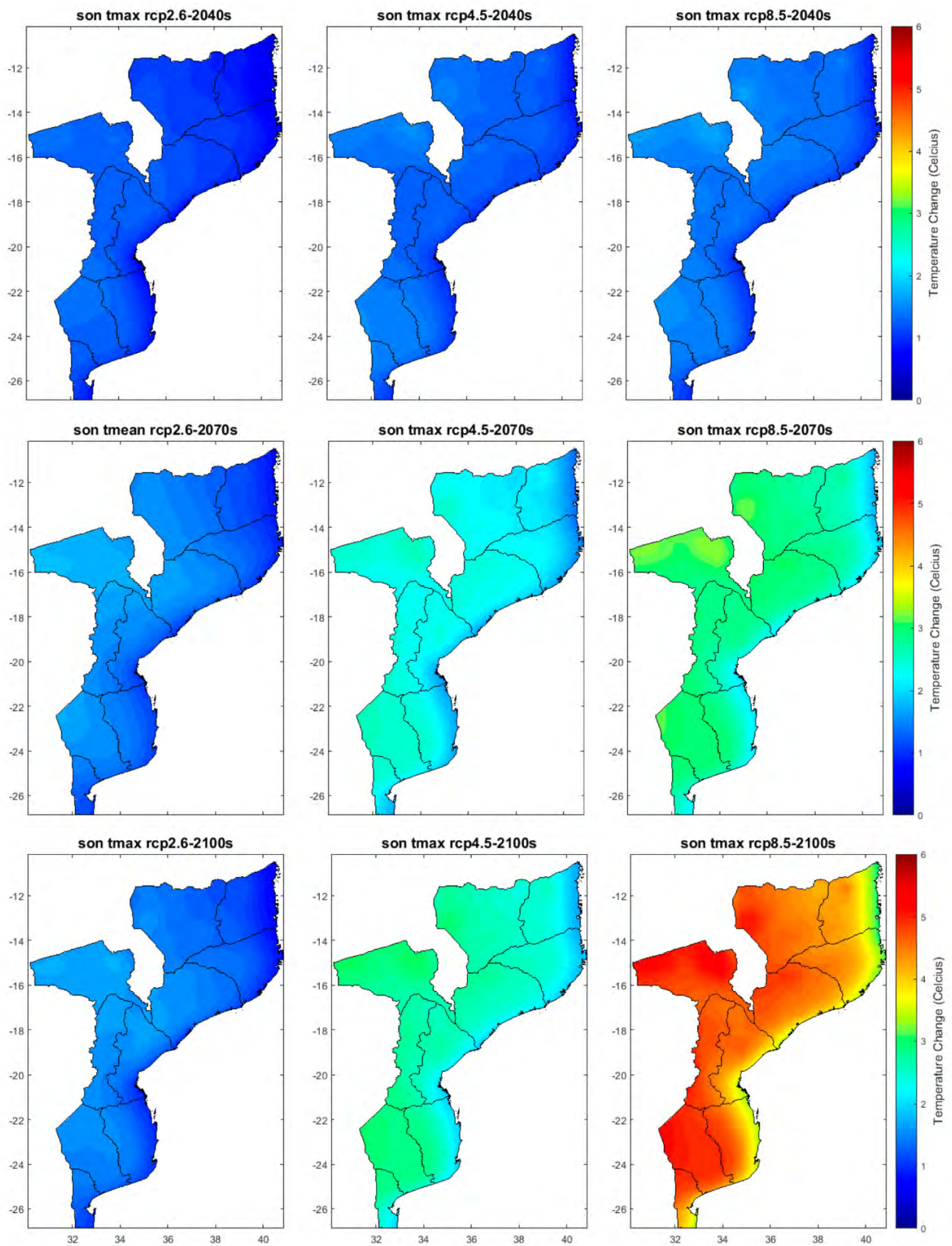


Figure A12. Projected changes of SON maximum temperature for the 2040s (2011–2040), 2070s (2041–2070), and 2100s (2071–2100) with respect to the reference period (1961–1990) for the three RCP emission scenarios (RCP2.6, RCP4.5, and RCP8.5).

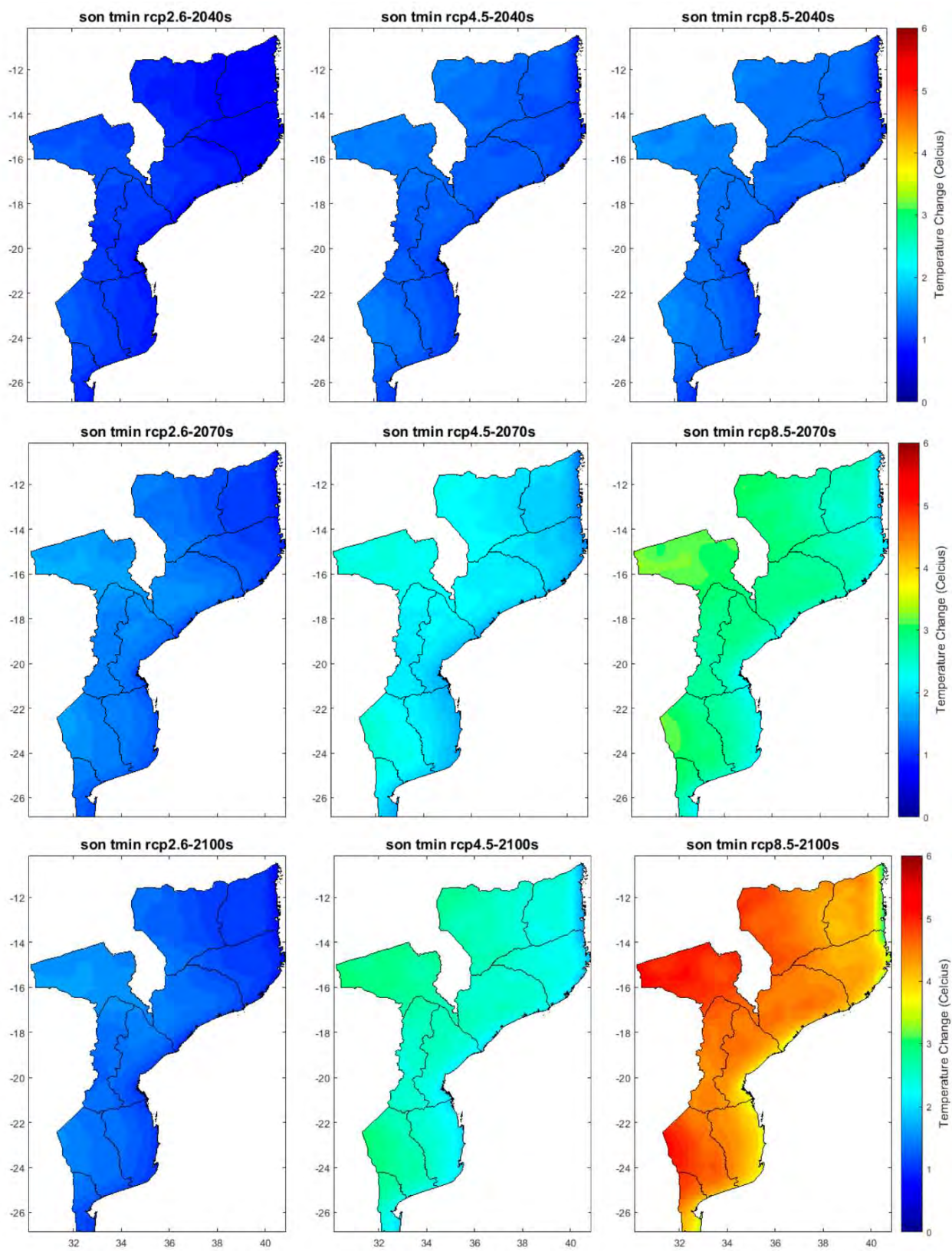


Figure A13. Projected changes of SON minimum temperature for the 2040s (2011–2040), 2070s (2041–2070), and 2100s (2071–2100) with respect to the reference period (1961–1990) for the three RCP emission scenarios (RCP2.6, RCP4.5, and RCP8.5).

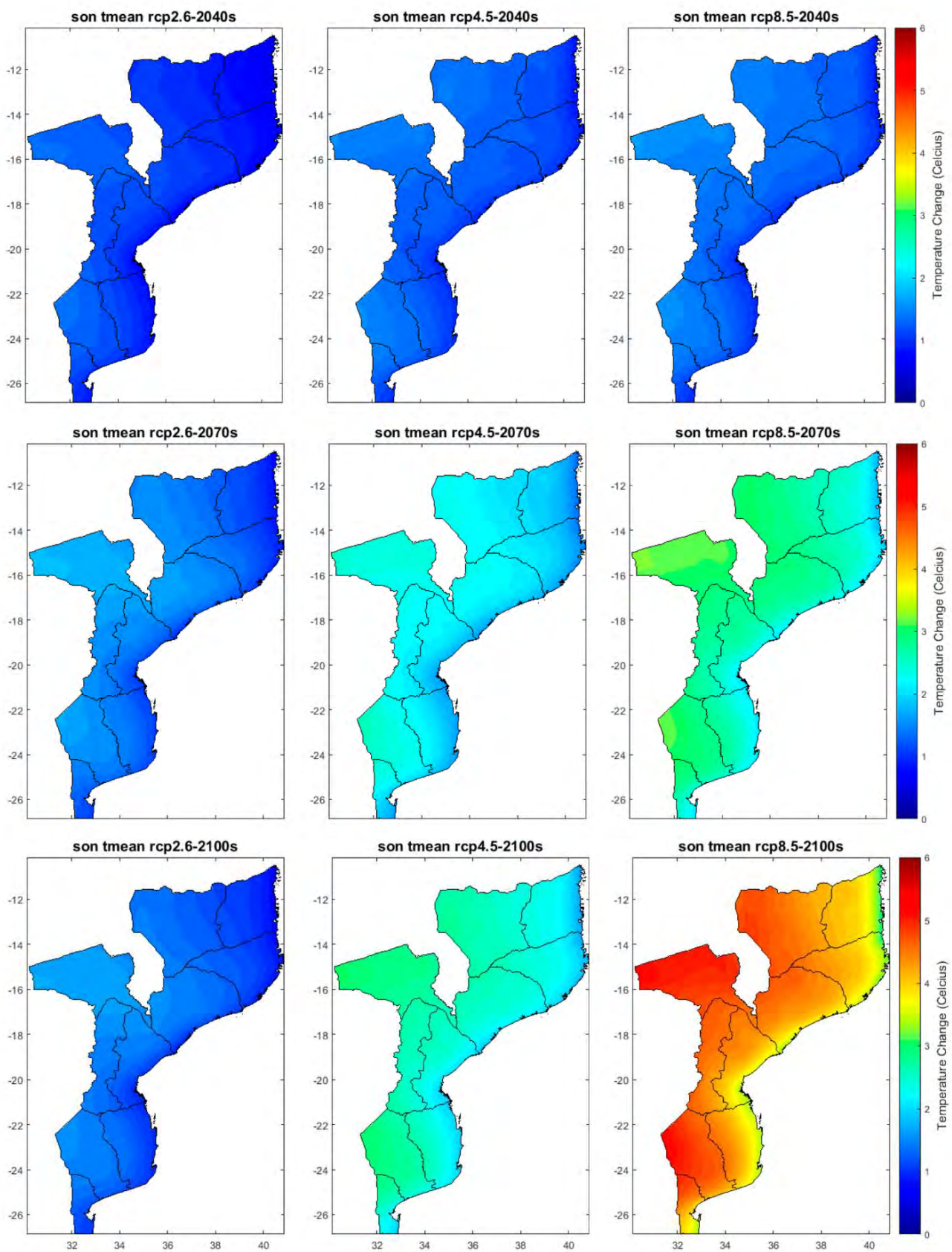


Figure A14. Projected changes of SON mean temperature for the 2040s (2011–2040), 2070s (2041–2070), and 2100s (2071–2100) with respect to the reference period (1961–1990) for the three RCP emission scenarios (RCP2.6, RCP4.5, and RCP8.5).

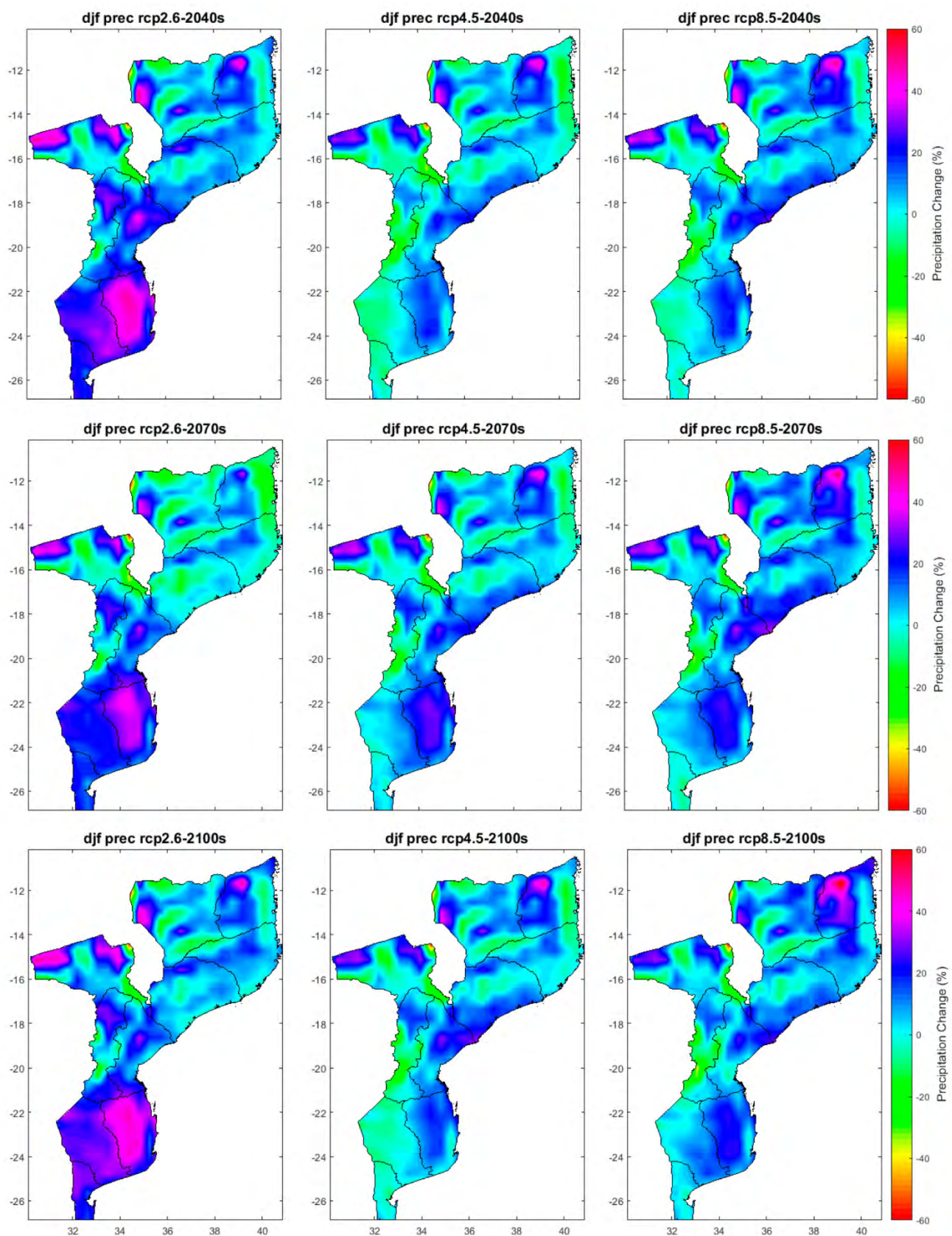


Figure A15. Projected changes of DJF precipitation (%) for the 2040s (2011–2040), 2070s (2041–2070), and 2100s (2071–2100) with respect to the reference period (1961–1990) for the three RCP emission scenarios (RCP2.6, RCP4.5, and RCP8.5).

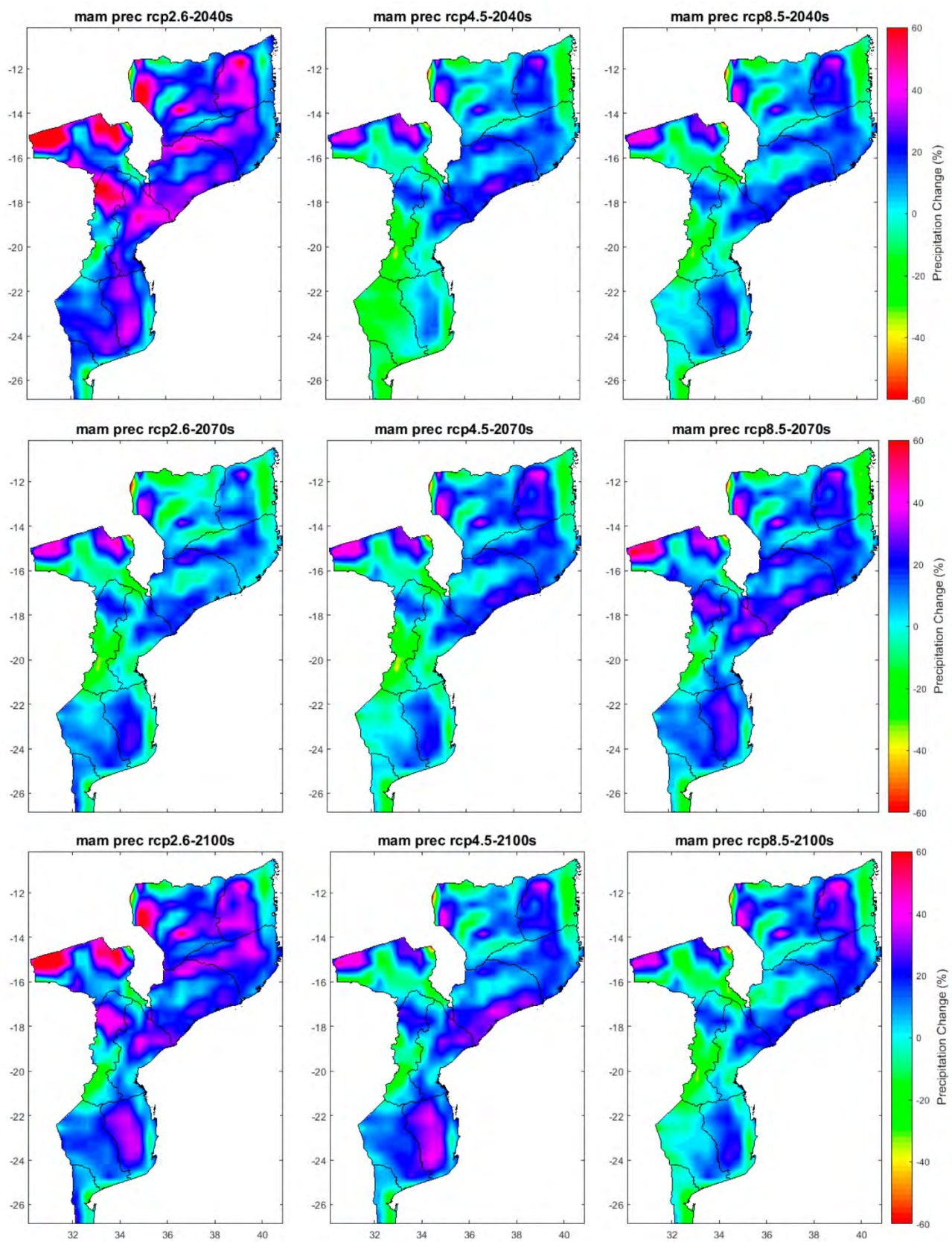


Figure A16. Projected changes of MAM precipitation (%) for the 2040s (2011–2040), 2070s (2041–2070), and 2100s (2071–2100) with respect to the reference period (1961–1990) for the three RCP emission scenarios (RCP2.6, RCP4.5, and RCP8.5).

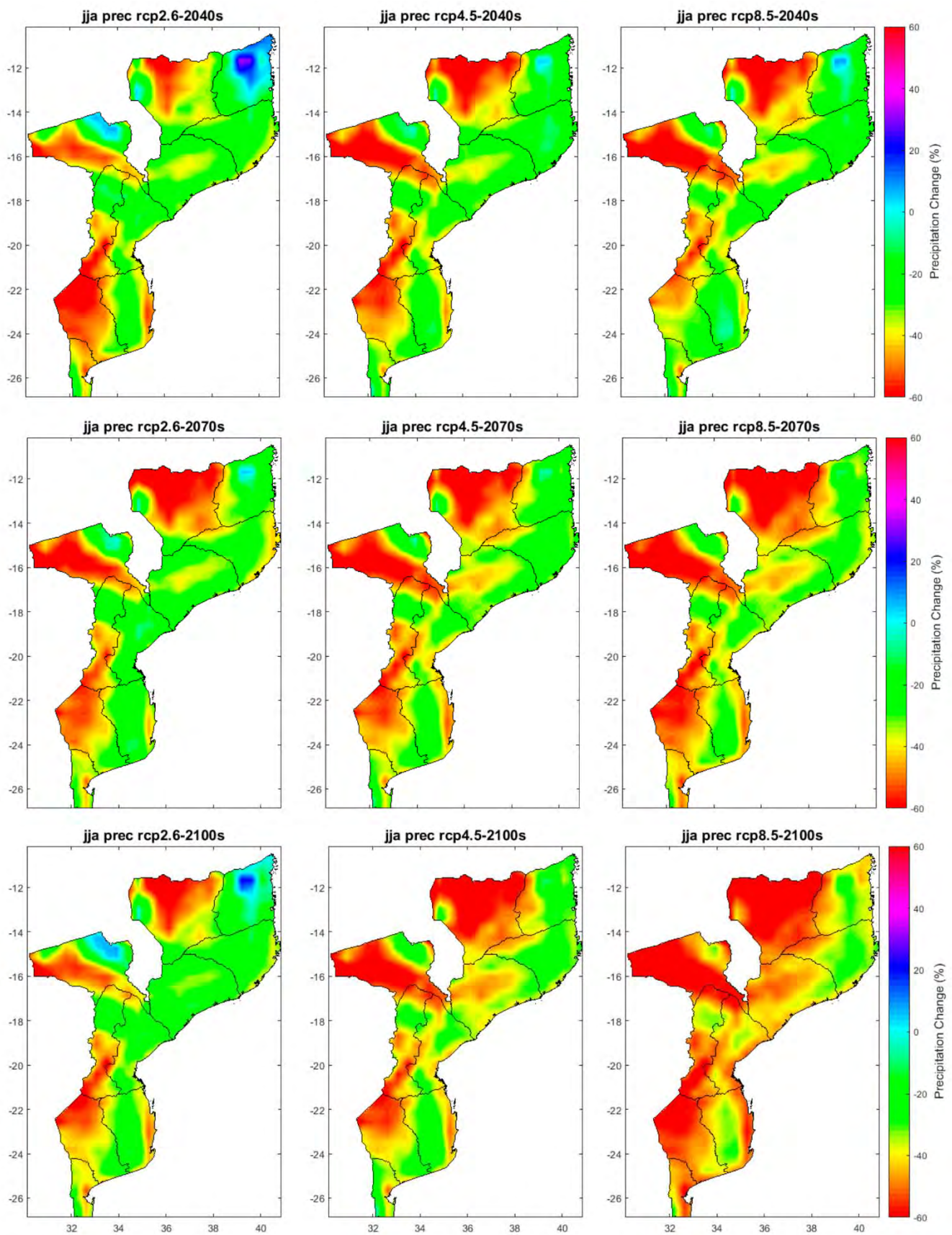


Figure A17. Projected changes of JJA precipitation (%) for the 2040s (2011–2040), 2070s (2041–2070), and 2100s (2071–2100) with respect to the reference period (1961–1990) for the three RCP emission scenarios (RCP2.6, RCP4.5, and RCP8.5).

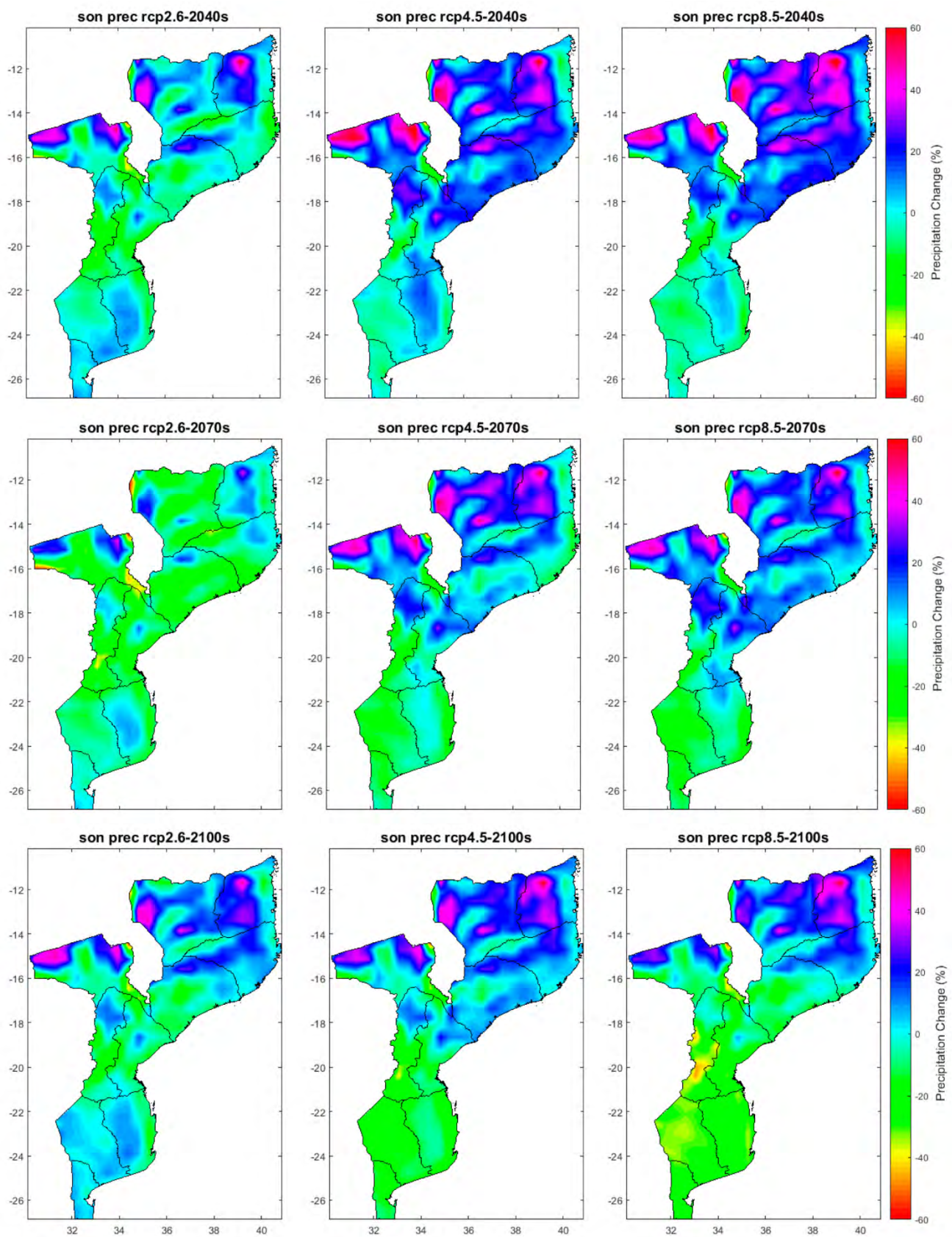


Figure A18. Projected changes of SON precipitation (%) for the 2040s (2011–2040), 2070s (2041–2070), and 2100s (2071–2100) with respect to the reference period (1961–1990) for the three RCP emission scenarios (RCP2.6, RCP4.5, and RCP8.5).

References

1. IPCC. Climate Change 2014: Synthesis Report. In *Contribution of Working Groups I, II and III to the Fifth Assessment Report of the Intergovernmental Panel on Climate Change*; Pachauri, R.K., Meyer, L.A., Eds.; IPCC: Geneva, Switzerland, 2014; p. 151.
2. Boko, M.; Niang, I.; Nyong, A.; Vogel, C.; Githeko, A.; Medany, M.; Osman-Elasha, B.; Tabo, R.; Yanda, P. *Contribution of Working Group II to the Fourth Assessment Report of the Intergovernmental Panel on Climate Change. Climate Change 2007: Impacts, Adaptation and Vulnerability*; Parry, O.F., Canziani, J.P., Palutikof, P.J., van der Linden, Eds.; Cambridge University Press: Cambridge, UK, 2007; pp. 433–467.
3. INGC. *Main Report: INGC Climate Change Report: Study on the Impact of Climate Change on Disaster Risk in Mozambique*; Asante, K., Brundrit, G., Epstein, P., Fernandes, A., Marques, M.R., Mavume, A., Metzger, M., Patt, A., Queface, A., Sanchez del Valle, R., et al., Eds.; INGC: Maputo, Mozambique, 2009.
4. INE. *Statistical Yearbook 2018—Mozambique*; National Statistics Institute: Newport, UK, 2018.
5. World Bank. *Population Growth Rate (Annual %)—Mozambique*; World Bank: Washington, DC, USA, 2019.
6. UN-HABITAT. *The State of African Cities 2014: Re-Imagining Sustainable Urban Transitions*; UN-Habitat: Nairobi, Kenya, 2014.
7. INE. *Statistical Yearbook 2019—Mozambique*; National Statistics Institute: Newport, UK, 2019.
8. Mawren, D.; Hermes, J.; Reason, C.J.C. Exceptional Tropical Cyclone Kenneth in the Far Northern Mozambique Channel and Ocean Eddy Influences. *Geophys. Res. Lett.* **2020**, *47*, e2020GL088715. [[CrossRef](#)]
9. PDNA. *Mozambique Cyclone Idai Post Disaster Needs Assessment: Full Report (2019)*; PDNA: Maputo, Mozambique, 2019.
10. WMO. *State of the Climate in Africa 2019*; WHO: Geneva, Switzerland, 2020.
11. Reason, C.J.C. Tropical cyclone Dera, the unusual 2000/01 tropical cyclone season in the South West Indian Ocean and associated rainfall anomalies over Southern Africa. *Theor. Appl. Clim.* **2007**, *97*, 181–188. [[CrossRef](#)]
12. Manhique, A.J.; Reason, C.J.C.; Silinto, B.; Zucula, J.; Raiva, I.; Congolo, F.; Mavume, A.F. Extreme rainfall and floods in southern Africa in January 2013 and associated circulation patterns. *Nat. Hazards* **2015**, *77*, 679–691. [[CrossRef](#)]
13. Rouault, M.; Richard, Y. Intensity and spatial extent of droughts in southern Africa. *Geophys. Res. Lett.* **2005**, *32*. [[CrossRef](#)]
14. New, M.; Hewitson, B.; Stephenson, D.B.; Tsigas, A.; Kruger, A.; Manhique, A.; Gomez, B.; Coelho, C.A.S.; Masisi, D.N.; Kululanga, E.; et al. Evidence of trends in daily climate extremes over southern and west Africa. *J. Geophys. Res. Space Phys.* **2006**, *111*, 111. [[CrossRef](#)]
15. Ceccherini, G.; Russo, S.; Ameztoy, I.; Marchese, A.F.; Carmona-Moreno, C. Heat waves in Africa 1981–2015, observations and reanalysis. *Nat. Hazards Earth Syst. Sci.* **2017**, *17*, 115–125. [[CrossRef](#)]
16. Nkemelang, T.; New, M.; Zaroug, M.A.H. Temperature and precipitation extremes under current, 1.5 °C and 2.0 °C global warming above pre-industrial levels over Botswana, and implications for climate change vulnerability. *Environ. Res. Lett.* **2018**, *13*, 065016. [[CrossRef](#)]
17. Davis-Reddy, C.L.; Vincent, K. *Climate Risk and Vulnerability: A Handbook for Southern Africa*, 2nd ed.; Council for Scientific and Industrial Research: Pretoria, South Africa, 2017.
18. Muthige, M.S.; Malherbe, J.; A Englebrecht, F.; Grab, S.; Beraki, A.; Maisha, T.R.; Van Der Merwe, J.; A Engelbrecht, F. Projected changes in tropical cyclones over the South West Indian Ocean under different extents of global warming. *Environ. Res. Lett.* **2018**, *13*, 065019. [[CrossRef](#)]
19. UNFCCC. *Paris Agreement*; UNFCCC: Bonn, Germany, 2015.
20. IPCC. 2018: Summary for Policymakers. In *Global warming of 1.5 °C. An IPCC Special Report on the Impacts of Global Warming of 1.5 °C above Pre-Industrial Levels and Related Global Greenhouse Gas Emission Pathways, in the Context of Strengthening the Global Response to the Threat of Climate Change, Sustainable Development, and Efforts to Eradicate Poverty*; Masson-Delmotte, V., Zhai, P., Pörtner, H.O., Roberts, D., Skea, J., Shukla, P.R., Pirani, A., Moufouma-Okia, W., Péan, C., Pidcock, R., et al., Eds.; World Meteorological Organization: Geneva, Switzerland, 2018.
21. Kompas, T.; Pham, V.H.; Che, T.N. The Effects of Climate Change on GDP by Country and the Global Economic Gains From Complying With the Paris Climate Accord. *Earth's Futur.* **2018**, *6*, 1153–1173. [[CrossRef](#)]
22. Rogelj, J.; Elzen, M.D.; Höhne, N.; Fransen, T.; Fekete, H.; Winkler, H.; Schaeffer, R.; Sha, F.; Riahi, K.; Meinshausen, M. Paris Agreement climate proposals need a boost to keep warming well below 2 °C. *Nat. Cell Biol.* **2016**, *534*, 631–639. [[CrossRef](#)]
23. UNEP. *UN Environment, Emissions Gap Report 2019 (Nairobi: UN Environment, 2019)*; UNEP: Nairobi, Kenya, 2019.
24. INDC. *Intended Nationally Determined Contribution (INDC) of Mozambique to the United Nations Framework Convention on Climate Change (UNFCCC)*; UNFCCC: Rio de Janeiro, Brazil, 2015.
25. Nikulin, G.; Lennard, C.; Dosio, A.; Kjellström, E.; Chen, Y.; Hänsler, A.; Kupiainen, M.; Laprise, R.; Mariotti, L.; Maule, C.F.; et al. The effects of 1.5 and 2 degrees of global warming on Africa in the CORDEX ensemble. *Environ. Res. Lett.* **2018**, *13*, 065003. [[CrossRef](#)]
26. Fischer, E.M.; Knutti, R. Anthropogenic contribution to global occurrence of heavy-precipitation and high-temperature extremes. *Nat. Clim. Chang.* **2015**, *5*, 560–564. [[CrossRef](#)]
27. Marques, M.R. Impacts of Climate Change and socio economic developments on Land Use and Land Cover-Potential effects on crop yields. In *INGC. (2009). Main Report: INGC Climate Change Report: Study on the Impact of Climate Change on Disaster Risk in Mozambique*; Asante, K., Brundrit, G., Epstein, P., Fernandes, A., Marques, M.R., Mavume, A., Metzger, M., Patt, A., Queface, A., Sanchez del Valle, R., et al., Eds.; INGC: Maputo, Mozambique, 2009.

28. Assante, K.; Vilankulos, A. Future impacts of climate change on river flow, floods, saline intrusion. In *INGC. (2009). Main Report: INGC Climate Change Report: Study on the Impact of Climate Change on Disaster Risk in Mozambique*; Asante, K., Brundrit, G., Epstein, P., Fernandes, A., Marques, M.R., Mavume, A., Metzger, M., Patt, A., Queface, A., Sanchez del Valle, R., et al., Eds.; INGC: Maputo, Mozambique, 2009.
29. Engelbrecht, F.; Adegoke, J.; Bopape, M.-J.; Naidoo, M.; Garland, R.; Thatcher, M.; McGregor, J.; Katzfey, J.; Werner, M.; Ichoku, C.; et al. Projections of rapidly rising surface temperatures over Africa under low mitigation. *Environ. Res. Lett.* **2015**, *10*, 085004. [[CrossRef](#)]
30. Dosio, A. Projection of temperature and heat waves for Africa with an ensemble of CORDEX Regional Climate Models. *Clim. Dyn.* **2017**, *49*, 493–519. [[CrossRef](#)]
31. Maure, G.A.; Pinto, I.; Ndebele-Murisa, M.R.; Muthige, M.; Lennard, C.; Nikulin, G.; Dosio, A.; Meque, A.O. The southern African climate under 1.5 °C and 2 °C of global warming as simulated by CORDEX regional climate models. *Environ. Res. Lett.* **2018**, *13*, 065002. [[CrossRef](#)]
32. Kling, H.; Stanzel, P.; Preishuber, M. Impact modelling of water resources development and climate scenarios on Zambezi River discharge. *J. Hydrol. Reg. Stud.* **2014**, *1*, 17–43. [[CrossRef](#)]
33. Uamusse, M.M.; Tussupova, K.; Persson, K.M. Climate Change Effects on Hydropower in Mozambique. *Appl. Sci.* **2020**, *10*, 4842. [[CrossRef](#)]
34. Epstein, P. Preliminary health analysis. In *Main Report: INGC Climate Change Report: Study on the Impact of Climate Change on Disaster Risk in Mozambique*; Asante, K., Brundrit, G., Epstein, P., Fernandes, A., Marques, M.R., Mavume, A., Metzger, M., Patt, A., Queface, A., Sanchez del Valle, R., et al., Eds.; INGC: Maputo, Mozambique, 2009.
35. Salau, O.R.; Adeleye, O.A.; Adeleye, F.A.; Américo, F. The Links between Climate and Malaria Disease in Ekiti State, Nigeria. *Intern. J. Prev. Med. Res.* **2018**, *4*, 60–67.
36. WHO. Cholera in 1997. *Week. Epidem. Rec.* **1998**, *73*, 201–208.
37. Bateman, C. Mozambique cholera will affect region. *S. Afr. Med. J.* **2002**, *92*, 104–106.
38. Gudo, E.S.; Pinto, G.; Weyer, J.; Le Roux, C.; Mandlaze, A.; José, A.F.; Muianga, A.; Paweska, J.T. Serological evidence of rift valley fever virus among acute febrile patients in Southern Mozambique during and after the 2013 heavy rainfall and flooding: Implication for the management of febrile illness. *Virol. J.* **2016**, *13*, 96. [[CrossRef](#)] [[PubMed](#)]
39. WHO. *Fact Sheet: World Malaria Report 2016*; World Health Organization: Geneva, Switzerland, 2016.
40. Colborn, K.L.; Giorgi, E.; Monaghan, A.J.; Gudo, E.; Candrinho, B.; Marrufo, T.J.; Colborn, J.M. Spatio-temporal modelling of weekly malaria incidence in children under 5 for early epidemic detection in Mozambique. *Sci. Rep.* **2018**, *8*, 9238. [[CrossRef](#)]
41. Tadross, M. Climate Change modelling and future analysis. In *INGC. (2009). Main report: INGC Climate Change Report: Study on the Impact of Climate Change on Disaster Risk in Mozambique*; Asante, K., Brundrit, G., Epstein, P., Fernandes, A., Marques, M.R., Mavume, A., Metzger, M., Patt, A., Queface, A., Sanchez del Valle, R., et al., Eds.; INGC: Maputo, Mozambique, 2009.
42. Hunter, R.; Afonso, F.; Mavume, A.; New, M. *Problems and Solutions for Climate Change Resilience and Adaptation in Mozambique: State of Adaptation Knowledge, Policies and Practices to support Conservation Agriculture*; Universidade Eduardo Mondlane: Maputo, Mozambique, 2011.
43. Hayhoe, K.; Edmonds, J.; Kopp, R.E.; Le Grande, A.N.; Sanderson, B.M.; Wehner, M.F.; Wuebbles, D.J. Climate models, scenarios, and projections. In *Climate Science Special Report: Fourth National Climate Assessment*; U.S. Global Change Research Program: Washington, DC, USA, 2017; Volume I, pp. 1–470.
44. Luhunga, P.M.; Kijazi, A.L.; Chang’A, L.; Kondowe, A.; Ng’Ongolo, H.; Mtongori, H. Climate Change Projections for Tanzania Based on High-Resolution Regional Climate Models From the Coordinated Regional Climate Downscaling Experiment (CORDEX)-Africa. *Front. Environ. Sci.* **2018**, *6*, 6. [[CrossRef](#)]
45. Pinto, I.; Jack, C.; Hewitson, B. Process-based model evaluation and projections over southern Africa from Coordinated Regional Climate Downscaling Experiment and Coupled Model Intercomparison Project Phase 5 models. *Int. J. Clim.* **2018**, *38*, 4251–4261. [[CrossRef](#)]
46. Zittis, G.; Hadjinicolaou, P.; Klangidou, M.; Proestos, Y.; Lelieveld, J. A multi-model, multi-scenario, and multi-domain analysis of regional climate projections for the Mediterranean. *Reg. Environ. Chang.* **2019**, *19*, 2621–2635. [[CrossRef](#)]
47. Gebrechorkos, S.H.; Hülsmann, S.; Bernhofer, C. Statistically downscaled climate dataset for East Africa. *Sci. Data* **2019**, *6*, 1–8. [[CrossRef](#)] [[PubMed](#)]
48. Hewitson, B.; Crane, R. Climate downscaling: Techniques and application. *Clim. Res.* **1996**, *7*, 85–95. [[CrossRef](#)]
49. Giorgi, F.; Gutowski, W.J. Regional Dynamical Downscaling and the CORDEX Initiative. *Annu. Rev. Environ. Resour.* **2015**, *40*, 467–490. [[CrossRef](#)]
50. Liang, X.-Z.; Kunkel, K.E.; Meehl, G.A.; Jones, R.G.; Wang, J.X.L. Regional climate models downscaling analysis of general circulation models present climate biases propagation into future change projections. *Geophys. Res. Lett.* **2008**, *35*, 1–5. [[CrossRef](#)]
51. Giorgi, F.; Jones, C.; Asrar, G. Addressing Climate Information Needs at the Regional Level: The CORDEX Framework. *World Meteor. Organiz. Bull.* **2009**, *58*, 175–183. Available online: http://wcrp.ipsl.jussieu.fr/RCD_Projects/CORDEX/CORDEX_giorgi_WMO.pdf (accessed on 12 March 2020).
52. Buontempo, C.; Mathison, C.; Jones, R.; Williams, K.; Wang, C.; McSweeney, C. An ensemble climate projection for Africa. *Clim. Dyn.* **2014**, *44*, 2097–2118. [[CrossRef](#)]

53. Gebrechorkos, S.H.; Hülsmann, S.; Bernhofer, C. Regional climate projections for impact assessment studies in East Africa. *Environ. Res. Lett.* **2019**, *14*, 044031. [[CrossRef](#)]
54. Klutse, N.A.B.; Ajayi, V.O.; Gbobaniyi, E.; Egbebiyi, T.S.; Kouadio, K.; Nkrumah, F.; Quagrain, K.A.; Olusegun, C.; Diasso, U.; Abiodun, B.J.; et al. Potential impact of 1.5 °C and 2 °C global warming on consecutive dry and wet days over West Africa. *Environ. Res. Lett.* **2018**, *13*, 055013. [[CrossRef](#)]
55. Dosio, A.; Turner, A.G.; Tamoffo, A.T.; Sylla, M.B.; Lennard, C.; Jones, R.G.; Terray, L.; Nikulin, G.; Hewitson, B. A tale of two futures: Contrasting scenarios of future precipitation for West Africa from an ensemble of regional climate models. *Environ. Res. Lett.* **2020**, *15*, 064007. [[CrossRef](#)]
56. Pinto, I.; Lennard, C.; Tadross, M.; Hewitson, B.; Dosio, A.; Nikulin, G.; Panitz, H.-J.; Shongwe, M.E. Evaluation and projections of extreme precipitation over southern Africa from two CORDEX models. *Clim. Chang.* **2015**, *135*, 655–668. [[CrossRef](#)]
57. Lennard, C.; Nikulin, G.; Dosio, A.; Moufouma-Okia, W. On the need for regional climate information over Africa under varying levels of global warming. *Environ. Res. Lett.* **2018**. [[CrossRef](#)]
58. Osima, S.; Indasi, V.S.; Zaroug, M.; Endris, H.S.; Gudoshava, M.; Misiani, H.O.; Nimusiima, A.; Anyah, R.O.; Otieno, G.; Ogwang, B.A.; et al. Projected climate over the Greater Horn of Africa under 1.5 °C and 2 °C global warming. *Environ. Res. Lett.* **2018**, *13*, 065004. [[CrossRef](#)]
59. Tamoffo, A.T.; Dosio, A.; Vondou, D.A.; Sonkoué, D. Process-Based Analysis of the Added Value of Dynamical Downscaling Over Central Africa. *Geophys. Res. Lett.* **2020**, *47*. [[CrossRef](#)]
60. Luhunga, P.; Botai, J.; Kahimba, F. Evaluation of the performance of CORDEX regional climate models in simulating present climate conditions of Tanzania. *J. South. Hemisph. Earth Syst. Sci.* **2016**, *66*, 32–54. [[CrossRef](#)]
61. Sibanda, S.; Grab, S.W.; Ahmed, F. An evaluation of the CORDEX regional climate models in simulating future rainfall and extreme events over Mzingwane catchment, Zimbabwe. *Theor. Appl. Clim.* **2019**, *140*, 91–100. [[CrossRef](#)]
62. Van Logchem, B.; Queface, A.J. *Responding to Climate Change in Mozambique: Synthesis Report*; INGC: Maputo, Mozambique, 2012.
63. Bousquet, O.; Barruol, G.; Cordier, E.; Barthe, C.; Bielli, S.; Calmer, R.; Rindraharisaona, E.; Roberts, G.; Tulet, P.; Amelie, V.; et al. Impact of Tropical Cyclones on Inhabited Areas of the SWIO Basin at Present and Future Horizons. Part 1: Overview and Observing Component of the Research Project RENOVRISKCYCLONE. *Atmosphere* **2021**, *12*, 544. [[CrossRef](#)]
64. Van Vuuren, D.P.; Stehfest, E.; Elzen, M.G.J.D.; Kram, T.; Van Vliet, J.; Deetman, S.; Isaac, M.; Goldewijk, K.K.; Hof, A.; Beltran, A.M.; et al. RCP2.6: Exploring the possibility to keep global mean temperature increase below 2 °C. *Clim. Chang.* **2011**, *109*, 95–116. [[CrossRef](#)]
65. van Vuuren, D.P.; Carter, T.R. Climate and socio-economic scenarios for climate change research and assessment: Reconciling the new with the old. *Clim. Chang.* **2014**, *122*, 415–429. [[CrossRef](#)]
66. Nakicenovic, N.; Swart, R. *Special Report on Emissions Scenarios: A Special Report of Working Group III of the Intergovernmental Panel on Climate Change*; Cambridge University Press: Cambridge, UK, 2000; p. 599.
67. Manhique, A. The South Indian Convergence Zone and Relationship with Rainfall Variability in Mozambique. Ph.D. Thesis, University of Cape Town, Western Cape, South Africa, 2008.
68. Usman, M.; Reason, C. Dry spell frequencies and their variability over southern Africa. *Clim. Res.* **2004**, *26*, 199–211. [[CrossRef](#)]
69. Lindesay, J.A.; Vogel, C.H. Historical evidence for Southern Oscillation-southern African rainfall relationships. *Int. J. Clim.* **1990**, *10*, 679–689. [[CrossRef](#)]
70. Rocha, A.; Simmonds, I.A.N. Interannual variability of south-eastern African summer rainfall. Part 1: Relationships with air-sea interactions processes. *Int. J. Climatol.* **1997**, *17*, 235–265. [[CrossRef](#)]
71. Tyson, P.D.; Preston-Whyte, R.A. *The Weather and Climate of Southern Africa*; Oxford University Press: Oxford, UK, 2000; p. 396.
72. Reason, C.J.C.; Landman, W.; Tennant, W. Seasonal to Decadal Prediction of Southern African Climate and Its Links with Variability of the Atlantic Ocean. *Bull. Am. Meteorol. Soc.* **2006**, *87*, 941–956. [[CrossRef](#)]
73. Edossa, D.C.; Woyessa, Y.E.; Welderufael, W.A. Analysis of Droughts in the Central Region of South Africa and Their Association with SST Anomalies. *Int. J. Atmos. Sci.* **2014**, *2014*, 1–8. [[CrossRef](#)]
74. Reason, C.J.C.; Keibel, A. Tropical Cyclone Eline and its unusual penetration and impacts over the southern Africa mainland. *Weather Forecast.* **2004**, *19*, 789–805. [[CrossRef](#)]
75. Mavume, A.F.; Rydberg, L.; Rouault, M.; Lutjeharms, J.R.E. Climatology of Tropical Cyclones in the South-West Indian Ocean; landfall in Mozambique and Madagascar. *West. Indian Ocean J. Mar. Sci.* **2009**, *8*, 15–36.
76. Leroux, M.-D.; Meister, J.; Mekies, D.; Dorla, A.-L.; Caroff, P. A Climatology of Southwest Indian Ocean Tropical Systems: Their Number, Tracks, Impacts, Sizes, Empirical Maximum Potential Intensity, and Intensity Changes. *J. Appl. Meteorol. Clim.* **2018**, *57*, 1021–1041. [[CrossRef](#)]
77. Freitas, E.D.; Rozoff, C.M.; Cotton, W.R.; Dias, P.L.S. Interactions of an urban heat island and sea-breeze circulations during winter over the metropolitan area of São Paulo, Brazil. *Bound.-Layer Meteorol.* **2006**, *122*, 43–65. [[CrossRef](#)]
78. Jones, C.G.; Wyser, K.; Ullerstig, A.; Willén, U. The Rossby Centre Regional Atmospheric Climate Model Part II: Application to the Arctic Climate. *AMBIO A J. Hum. Environ.* **2004**, *33*, 211–220. [[CrossRef](#)]
79. Samuelsson, P.; Jones, C.G.; Willén, U.; Ullerstig, A.; Gollvik, S.; Hansson, U.; Jansson, C.; Kjellström, C.; Nikulin, G.; Wyser, K. The Rossby Centre Regional Climate model RCA3: Model description and performance. *Tellus A Dyn. Meteorol. Oceanogr.* **2011**, *63*, 4–23. [[CrossRef](#)]

80. Collazo, S.; Lhotka, O.; Rusticucci, M.; Kysely, J. Capability of the SMHI-RCA4 RCM driven by the ERA-Interim reanalysis to simulate heat waves in Argentina. *Int. J. Clim.* **2017**, *38*, 483–496. [[CrossRef](#)]
81. Wu, M.; Nikulin, G.; Kjellström, E.; Belušić, D.; Jones, C.; Lindstedt, D. The impact of regional climate model formulation and resolution on simulated precipitation in Africa. *Earth Syst. Dyn.* **2020**, *11*, 377–394. [[CrossRef](#)]
82. Kalognomou, E.-A.; Lennard, C.; Shongwe, M.; Pinto, I.; Favre, A.; Kent, M.; Hewitson, B.; Dosio, A.; Nikulin, G.; Panitz, H.-J.; et al. A Diagnostic Evaluation of Precipitation in CORDEX Models over Southern Africa. *J. Clim.* **2013**, *26*, 9477–9506. [[CrossRef](#)]
83. Switanek, M.B.; Troch, P.A.; Castro, C.L.; Leuprecht, A.; Chang, H.-I.; Mukherjee, R.; DeMaria, E.M.C. Scaled distribution mapping: A bias correction method that preserves raw climate model projected changes. *Hydrol. Earth Syst. Sci.* **2017**, *21*, 2649–2666. [[CrossRef](#)]
84. Wilcke, R.A.I.; Mendlik, T.; Gobiet, A. Multi-variable error correction of regional climate models. *Clim. Chang.* **2013**, *120*, 871–887. [[CrossRef](#)]
85. Mendez, M.; Maathuis, B.; Hein-Griggs, D.; Alvarado-Gamboa, L.-F. Performance Evaluation of Bias Correction Methods for Climate Change Monthly Precipitation Projections over Costa Rica. *Water* **2020**, *12*, 482. [[CrossRef](#)]
86. Mehan, S.; Gitau, M.W.; Flanagan, D.C. Reliable Future Climatic Projections for Sustainable Hydro-Meteorological Assessments in the Western Lake Erie Basin. *Water* **2019**, *11*, 581. [[CrossRef](#)]
87. Teutschbein, C.; Seibert, J. Is bias correction of Regional Climate Model (RCM) simulations possible for non-stationary conditions? *Hydrol. Earth Syst. Sci.* **2013**, *17*, 5061–5077. [[CrossRef](#)]
88. Moss, R.H.; Edmonds, J.A.; Hibbard, K.A.; Manning, M.R.; Rose, S.K.; Van Vuuren, D.P.; Carter, T.R.; Emori, S.; Kainuma, M.; Kram, T.; et al. The next generation of scenarios for climate change research and assessment. *Nature* **2010**, *463*, 747–756. [[CrossRef](#)]
89. Almazroui, M.; Saeed, F.; Saeed, S.; Islam, M.N.; Ismail, M.; Klutse, N.A.B.; Siddiqui, M.H. Projected Change in Temperature and Precipitation Over Africa from CMIP6. *Earth Syst. Environ.* **2020**, *4*, 455–475. [[CrossRef](#)]
90. Hobbs, J.E.; Lindesay, J.A.; Bridgman, H.A. *Climate of the Southern Continents: Present, Past and Future*; Wiley: Hoboken, NJ, USA, 1998; p. 318.
91. Lindesay, J.A. South African rainfall, the Southern Oscillation and a Southern Hemisphere semi-annual cycle. *J. Clim.* **1988**, *8*, 17–30. [[CrossRef](#)]
92. Taylor, K.E. Summarizing multiple aspects of model performance in a single diagram. *J. Geophys. Res. Atmos.* **2001**, *106*, 7183–7192. [[CrossRef](#)]
93. Ashaley, J.; Anornu, G.K.; Awotwi, A.; Gyamfi, C.; Anim-Gyampo, M. Performance evaluation of Africa CORDEX regional climate models: Case of Kpong irrigation scheme, Ghana. *Spat. Inf. Res.* **2020**, *28*, 735–753. [[CrossRef](#)]
94. Pfeifer, S.; Bülow, K.; Gobiet, A.; Hänsler, A.; Mudelsee, M.; Otto, J.; Rechid, D.; Teichmann, C.; Jacob, D. Robustness of Ensemble Climate Projections Analyzed with Climate Signal Maps: Seasonal and Extreme Precipitation for Germany. *Atmosphere* **2015**, *6*, 677–698. [[CrossRef](#)]
95. McSweeney, C.; New, M.; Lizcano, G.; Lu, X. The UNDP Climate Change Country Profiles. *Bull. Am. Meteorol. Soc.* **2010**, *91*, 157–166. [[CrossRef](#)]
96. Salite, D.; Poskitt, S. Managing the impacts of drought: The role of cultural beliefs in small-scale farmers' responses to drought in Gaza Province, southern Mozambique. *Int. J. Disaster Risk Reduct.* **2019**, *41*, 101298. [[CrossRef](#)]
97. Midgley, S.; Dejene, A.; Mattick, A. *Mozambique Adaptation to Climate Change in Semi-Arid Environments: Experience and Lessons from Mozambique*; FAO: Rome, Italy, 2012; ISBN 978-92-5-107135-9.
98. INAM. *Atlas de Precipitação de Moçambique*; INAM: Maputo, Mozambique, 2012.

Projected Changes in the Southern Indian Ocean Cyclone Activity Assessed from High-Resolution Experiments and CMIP5 Models

JULIEN CATTIAUX AND FABRICE CHAUVIN

Centre National de Recherches Météorologiques, Université de Toulouse, CNRS, Météo-France, Toulouse, France

OLIVIER BOUSQUET, SYLVIE MALARDEL, AND CHIA-LUN TSAI

Laboratoire de l'Atmosphère et des Cyclones, Université de la Réunion, CNRS, Météo-France, Saint-Denis, France

(Manuscript received 2 August 2019, in final form 7 March 2020)

ABSTRACT

The evolution of tropical cyclone activity under climate change remains a crucial scientific issue. Physical theory of cyclogenesis is limited, observational datasets suffer from heterogeneities in space and time, and state-of-the-art climate models used for future projections are still too coarse (~100 km of resolution) to simulate realistic systems. Two approaches can nevertheless be considered: 1) perform dedicated high-resolution (typically <50 km) experiments in which tropical cyclones can be tracked and 2) assess cyclone activity from existing low-resolution multimodel climate projections using large-scale indices as proxies. Here we explore these two approaches with a particular focus on the southern Indian Ocean. We first compute high-resolution experiments using the rotated-stretched configuration of our climate model (CNRM-CM6-1), which is able to simulate realistic tropical cyclones. In a 2-K warmer world, the model projects a 20% decrease in the frequency of tropical cyclones, together with an increase in their maximum lifetime intensity, a slight poleward shift of their trajectories, and a substantial delay (about 1 month) in the cyclone season onset. Large-scale indices applied to these high-resolution experiments fail to capture the overall decrease in cyclone frequency, but are able to partially represent projected changes in the spatiotemporal distribution of cyclone activity. Last, we apply large-scale indices to multimodel CMIP5 projections and find that the seasonal redistribution of cyclone activity is consistent across models.

1. Introduction

Understanding how climate change may influence tropical cyclone (TC) activity remains a challenging scientific issue (Knutson et al. 2010; Walsh et al. 2016). As TCs cause local devastating impacts and play a crucial role in maintaining regional water resources, this question also receives particular public attention.

Detecting potential trends in observational data is limited by the quality of historical records and the difficulty to disentangle the climate change signal from the noise of internal variability. A few studies have analyzed the International Best Track Archive for Climate Stewardship (IBTrACS) database, which compiles the best track datasets from diverse centers (Knapp et al. 2010). Various trends have been reported, such as an increase and a poleward shift in the TC lifetime

maximum intensity (Kossin et al. 2013; Holland and Bruyère 2014) or a slowdown of the translation speed (Kossin 2018), but it remains unclear whether these trends result from data heterogeneities (e.g., introduction of new satellites), natural variability, or anthropogenic forcings. Therefore, so far, most assessments regarding the evolution of TCs in a warmer world have been made from theoretical and/or modeling studies.

There is a theoretical expectation that a warmer climate would undergo stronger TCs, in line with higher sea surface temperatures (SST) and increased potential intensity (Emanuel 1988). However, no such robust conclusion exists for changes in TC frequency due to the lack of a generally accepted theory for cyclogenesis, even if progress has been made on identifying the environmental conditions favoring cyclone activity (e.g., Held and Zhao 2011; Peng et al. 2012; Sugi et al. 2012).

Modeling studies addressing the evolution of TCs under climate change face an implacable issue: grid resolution must be high enough to simulate realistic

Corresponding author: Julien Cattiaux, julien.cattiaux@meteo.fr

DOI: 10.1175/JCLI-D-19-0591.1

© 2020 American Meteorological Society. For information regarding reuse of this content and general copyright information, consult the [AMS Copyright Policy](https://www.ametsoc.org/PUBSReuseLicenses) (www.ametsoc.org/PUBSReuseLicenses).

TCs and experiments must be long enough—or enroll enough ensemble members—to isolate climate change from natural variability. The current generation of global models used for future climate projections—i.e., participants of the phase 5 of the Coupled Model Intercomparison Project (CMIP5)—have a horizontal grid spacing of about 100 km or greater (Taylor et al. 2011), which is too coarse to simulate realistic TCs (Camargo 2013); interestingly, the upcoming generation (CMIP6) will include a few models with higher resolutions (typically 50 km or higher). So far two approaches have thus been traditionally considered for studying TCs: (i) perform additional dedicated experiments at a higher resolution, or (ii) use the existing multimodel low-resolution climate projections to assess how large-scale environmental conditions favorable to cyclone activity may evolve in a warmer climate.

The first approach has been undertaken by a growing, but still limited, number of modeling centers that can afford the computer cost of high-resolution climate projections. Most of the performed experiments project a future reduction in the overall frequency of TCs, but an increase in the frequency of the strongest TCs (Walsh et al. 2016, and references therein). Also commonly reported are projected increases in associated phenomena, such as rainfall amounts and storm surges (Knutson et al. 2015; Woodruff et al. 2013).

The second approach consists of determining statistical relationships between cyclone activity and large-scale environmental factors, including dynamical (e.g., vertical and horizontal wind shear, low-tropospheric vorticity) and thermodynamical (e.g., midtropospheric humidity, sea surface temperature) variables. Combinations of these variables allow us to build cyclogenesis indices (CGIs), that have been shown to represent both the seasonal and geographical distribution of cyclone activity fairly well (Menkes et al. 2012). (Previous authors have used the abbreviation “GPIs” as the generic term for these indices, but since “GPI” is also an abbreviation used for one specific index used in this paper, here we use “CGIs.”) Using CGIs to quantify potential changes in the cyclone activity is, however, questionable, as it assumes that statistical relationships established for present-day climatological features remain valid in a climate change context. In particular, it has been shown that CGIs fail to capture the decrease in TC frequency when applied to high-resolution climate projections (Camargo et al. 2014; Wehner et al. 2015; Chauvin et al. 2020), which may explain why attempts to apply CGIs to CMIP5 future projections have mostly remained inconclusive so far (Camargo 2013). However, the

ability of CGIs to capture other potential changes in the cyclone activity (e.g., changes in the spatiotemporal distribution) has not been documented so far. In addition, since CGIs can be broken down into dynamical and thermal components, they can provide useful insights for the physical understanding of the projected changes in TC tracks.

Here we apply and compare both high-resolution and CGIs approaches to assess projected changes in cyclone activity and explore whether the two approaches can be reconciled on some aspects. We use the same methodology as in Chauvin et al. (2020) but we focus over the SIO basin, which has been seldom studied so far. Among the eight IBTrACS basins, it ranks third in terms of overall number of reported TCs (after the western and eastern Pacific basins). Even if less highly populated regions are exposed to TC hazards than in other basins, SIO TCs can still have dramatic impacts in Western Australia and southeastern Africa, including Madagascar and the Mascarene Islands (La Réunion, Mauritius, and Rodrigues), as recently illustrated by the devastating cyclone Idai.¹ In the western part of the SIO, the death toll associated with TCs averages to 20 fatalities per year over the last 19 years with 9 seasons above 100 fatalities according to the European Commission Joint Research Centre.² Long-term climate trend analysis in the SIO basin is particularly challenging due to the introduction of the *Meteosat-5* geostationary satellite into the region in 1998, which causes a temporal heterogeneity in observational and reanalysis products (Kuleshov et al. 2010; Kossin et al. 2013). Evidences for an observed increase in the number of severe TC days have nevertheless been reported in the western part of the SIO (Kuleshov et al. 2010; Malan et al. 2013). High-resolution climate projections suggest that SIO TCs follow the global behavior: a decrease in the overall frequency and an increase in the intensity (e.g., Murakami et al. 2012; Walsh et al. 2016).

The paper is structured as follows. Observations, reanalyses, high-resolution experiments, and CMIP5 models used in this study are presented in section 2. Methodologies including the tracking algorithm applied to high-resolution data and the cyclogenesis indices applied to lower-resolution data are detailed in section 3. Section 4 contains our main findings while discussion and conclusions are provided in sections 5 and 6.

¹ <https://public.wmo.int/en/media/news/tropical-cyclone-idai-hits-mozambique>.

² Emergency Reporting 23: <http://www.gdacs.org/Public/download.aspx?type=DC&id=161>.

TABLE 1. Observations, reanalyses, and CNRM-CM experiments used in this study. Time periods correspond to Southern Hemisphere convention for cyclone seasons (i.e., 1980 is July 1979–June 1980).

Abbreviation	Name	Details	Resolution (km)	Time period	TC tracks
IBTr	IBTrACS	TC track observations	—	1980–2016	×
ERA1	ERA-Interim	Reanalysis	80	1980–2016	
ERA5	ERA-5	Reanalysis	30	1980–2016	×
T127	CNRM-CM5	Historical simulation	155	1976–2005	
T359	CNRM-CM6-HR	AMIP simulation	55	1980–2010	×
SIO-P	CNRM-CM6-HR r.-s.	Experiment forced by historical SST	10–50	1971–2014	×
SIO-F	CNRM-CM6-HR r.-s.	Experiment forced by RCP8.5 SST	10–50	2051–94	×

2. Data

a. Observations and reanalyses

Observations and reanalyses used in this study are summarized in Table 1. Observational TC data are taken from the IBTrACS, version 4, dataset released in April 2019 that provides best track characteristics (e.g., position, sea level pressure, maximum sustained winds) on a 3-hourly basis (<https://www.ncdc.noaa.gov/ibtracs/>, Knapp et al. 2010). For consistency with model and reanalysis data used in this study, we restrict IBTrACS data to the period July 1979–June 2016 (i.e., cyclone seasons 1980–2016) and the hours 0000, 0600, 1200, and 1800 UTC. We only use information provided by the World Meteorological Organization (WMO) Regional Specialized Meteorological Centres (RSMCs): Météo-France La Réunion and the Australian Bureau of Meteorology (BoM) for the SIO basin. We only consider systems that are indicated as “TS” (tropical storms) in the metadata and that reach the official *moderate tropical storm* (category 1) stage according to Météo-France (BoM) classifications (i.e., 10-min sustained winds above 18 m s^{-1}) at least once in their lifetime. (Note that we use the terminology of the local RSMCs in this paper, not the Saffir–Simpson scale.)

ERA-5 data (30-km resolution, Hersbach et al. 2018) are used for both TC tracking and computing CGIs. ERA-Interim data (80-km resolution, Dee et al. 2011) are also used for computing CGIs, which allows for a fair comparison with CMIP5 models as they do not simulate realistic TCs (contrarily to ERA-5). Both datasets are downloaded from the European Centre for Medium-Range Weather Forecasts (<https://www.ecmwf.int/en/forecasts/datasets/browse-reanalysis-datasets>), on a regular $0.5^\circ \times 0.5^\circ$ longitude–latitude grid and at a 6-hourly frequency over the period July 1979–June 2016 (i.e., cyclone seasons 1980–2016).

b. High-resolution experiments

We use the same experimental setup as in Chauvin et al. (2020), which consists in performing atmosphere-only

present-day and future experiments with the Centre National de Recherches Météorologiques Coupled Global Climate Model (CNRM-CM) in its rotated-stretched configuration. The atmospheric component of CNRM-CM (ARPEGE) has indeed the particularity to enable a deformation of its horizontal grid: the pole can be placed over a location of interest (here, the SIO), and a stretching factor can be applied to progressively increase (decrease) the resolution around the pole (the antipode). The advantage of this configuration is that it provides high-resolution simulations over the area of interest, while preserving the consistency of the large-scale dynamics between global and regional scales. This technique has been extensively validated as it is routinely utilized by Météo-France for operational numerical weather prediction over Europe and has also been used in numerous studies of TCs over the North Atlantic basin (e.g., Chauvin et al. 2006; Daloz et al. 2012; Chauvin et al. 2020).

In the present study, the stretching is applied to a T359 grid (720×360 points), the pole is located at 12.5°S , 55°E , and the stretching factor is 3.5, resulting in a 14–50-km effective resolution within the SIO domain (defined as $0^\circ\text{--}30^\circ\text{S}$, $30^\circ\text{--}120^\circ\text{E}$; see Fig. 1a). The choice of the exact grid pole location was made in order to have the highest-resolution increase in the area under the responsibility of the Météo-France RSMC on La Réunion Island. The model is run with a 15-min time step. We use the same version of ARPEGE as in Chauvin et al. (2020) (i.e., a version close to the one participating to CMIP6 through CNRM-CM6-1 and CNRM-ESM2 models). A comprehensive description of this version, including details on convection, microphysics, and turbulence parameterizations, can be found in Voldoire et al. (2019), together with an evaluation of the CNRM-CM6-1 model.

Similarly to Chauvin et al. (2020), two experiments are conducted with the rotated-stretched configuration: a present-day simulation over the period 1971–2014 (named SIO-P), using historical SST and radiative forcings, and a future simulation over the period 2051–94

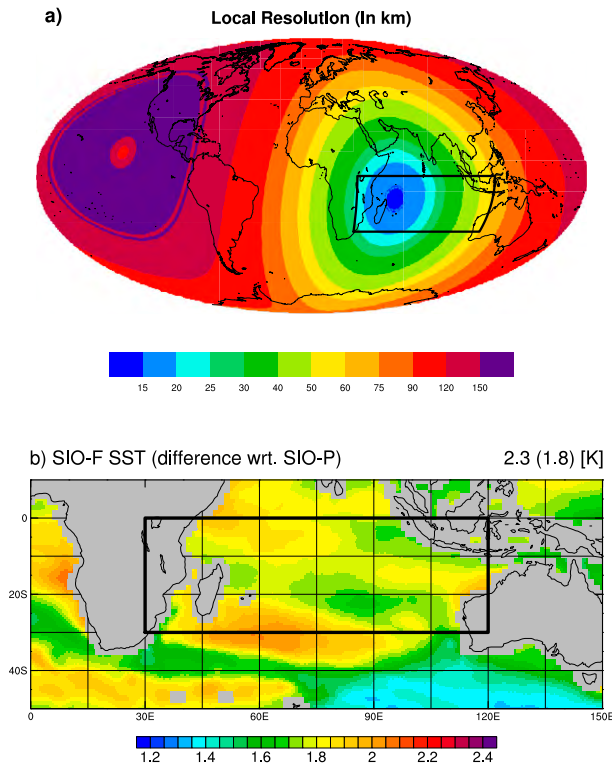


FIG. 1. (a) Effective grid resolution (km) of the rotated–stretched experiments. (b) Mean difference between prescribed SST (K) of SIO-F and SIO-P experiments.

(named SIO-F), using future SST and radiative forcings corresponding to the 8.5 W m^{-2} radiative concentration pathway (RCP8.5). Prescribed SST are taken from a member of CNRM-CM5 historical 1 RCP8.5 simulations (namely, the run r1i1p1; Voldoire et al. 2013), and are bias corrected over the present-day period with respect to the HadISST dataset (Rayner et al. 2003). Further methodological details, including the treatment of sea ice,

are provided in Chauvin et al. (2020). The time-averaged SST difference between the two experiments is a generalized warming ranging from 1.6 to 2 K over the SIO domain with a field average of 1.8 K (Fig. 1b); CNRM-CM5 is close to the CMIP5 multimodel mean on this aspect (not shown). To assess the potential benefits of the rotated–stretched configuration in simulating cyclones, a third experiment with a uniform T359 grid (denoted T359) is conducted over 1980–2010 using prescribed SST from HadISST.

c. CMIP5 simulations

We use monthly outputs of atmospheric temperature (ta), wind (ua, va), specific humidity (hus), convective precipitation (prc), sea level pressure (psl), and sea surface temperature (ts) from the historical + RCP8.5 simulations of 14 CMIP5 models (Table 2). This ensemble includes the CNRM-CM5 simulation from which SST are taken to perform the high-resolution experiments, which will be denoted T127 in the following. All fields are interpolated from the native model grid onto a common $2.5^\circ \times 2.5^\circ$ longitude–latitude grid prior to any diagnostic computation. This is also the case for ERA-5 and ERA-Interim data when they are compared with CMIP5 data.

3. Methods

a. Tracking algorithm

As in Daloz et al. (2012) and Chauvin et al. (2020), we use the algorithm introduced and detailed in Chauvin et al. (2006) to track TCs in ERA-5 and SIO-P, SIO-F, and T359 experiments. The tracker is applied to 6-hourly outputs, and in this paper all the data are first interpolated onto a common $0.5^\circ \times 0.5^\circ$ longitude–latitude

TABLE 2. CMIP5 models used in this study.

Abbreviation	Name	Country	Lon \times lat	Resolution (km)
BCC	BCC-CSM1.1	China	$2.8^\circ \times 2.8^\circ$	310
CCCMA	CanESM2	Canada	$2.8^\circ \times 2.8^\circ$	310
CNRM	CNRM-CM5	France	$1.4^\circ \times 1.4^\circ$	155
CSIRO	CSIRO-Mk3.6.0	Australia	$1.9^\circ \times 1.9^\circ$	210
GFDL	GFDL-ESM2M	United States	$2.0^\circ \times 2.5^\circ$	250
GISS	GISS-E2-R	United States	$2.0^\circ \times 2.5^\circ$	250
INM	INM-CM4	Russia	$1.5^\circ \times 2.0^\circ$	195
IPSL	IPSL-CM5A-LR	France	$1.9^\circ \times 3.8^\circ$	300
MIROC	MIROC-ESM	Japan	$2.8^\circ \times 2.8^\circ$	310
MOHC	HadGEM2-ES	United Kingdom	$1.3^\circ \times 1.9^\circ$	180
MPIM	MPI-ESM-LR	Germany	$1.9^\circ \times 1.9^\circ$	210
MRI	MRI-CGCM3	China	$1.1^\circ \times 1.1^\circ$	120
NCAR	CCSM4	United States	$0.9^\circ \times 1.3^\circ$	120
NCC	NorESM1	Norway	$1.1^\circ \times 1.1^\circ$	120

grid (i.e., the effective grid of the T359 experiment and the resolution chosen for the download of ERA-5 data) in order to allow for a fair comparison. The tracking algorithm involves three steps:

- 1) At each time step, grid points potentially concerned by a TC are identified, based on the main criteria that depict TCs: sea level pressure is a local minimum (low pressure system), 850-hPa vorticity exceeds a threshold (strong vortex), 10-m wind speed exceeds a threshold (strong winds), mean 700–300-hPa temperature local anomaly exceeds a threshold (warm core), tangential wind speed is higher at 850 hPa than at 300 hPa (stronger winds at low levels due to the thermal wind relationship), temperature local anomaly is higher at 300 hPa than at 850 hPa (warmer core at high levels). (Thresholds are discussed below.) Note that there is no latitude criterion, so that the detection can potentially occur outside the tropics.
- 2) TC points identified in step 1 are connected across consecutive time steps to build TC tracks. The association procedure is described in detail in Chauvin et al. (2006).
- 3) Tracks are completed before and after the TC stage in order to include cyclogenesis and cyclolysis. This is done by relaxing all criteria except vorticity and rerunning the algorithm backward (forward) from the first (last) point of the previously identified TC track. This step also ensures that a system reaching the TC stage twice (or more) in its lifetime is counted as a unique system.

The algorithm is highly sensitive to the thresholds used in step 1 that primarily depend on the data resolution. Here, the thresholds have been calibrated by repeating the tracking procedure on ERA-5 over 2011–16 with various combinations of thresholds and comparing the resulting tracks to IBTrACS. The retained values are $20 \times 10^{-5} \text{ s}^{-1}$ for vorticity, 13 m s^{-1} for wind speed, and 1 K for local temperature anomaly. With these values, the algorithm detects most of IBTrACS trajectories in ERA-5, with a limited number of false or missed tracks (see example of cyclone season 2015 in Fig. 2 and further details in section 4). Note that a perfect correspondence between IBTrACS and ERA5 tracks was not expected due to (i) IBTrACS specificities, (ii) potential model errors, and (iii) potential impacts of data assimilation on TCs.

We distinguish three stages in the tracks resulting from the algorithm: the development stage [from the system initiation (or cyclogenesis) to its intensification into a TC], the TC stage (encompassing all TC points with possible temporary interruptions), and the cyclolysis stage (from the last TC point to the end of the track). For consistency, we also distinguish these three stages in

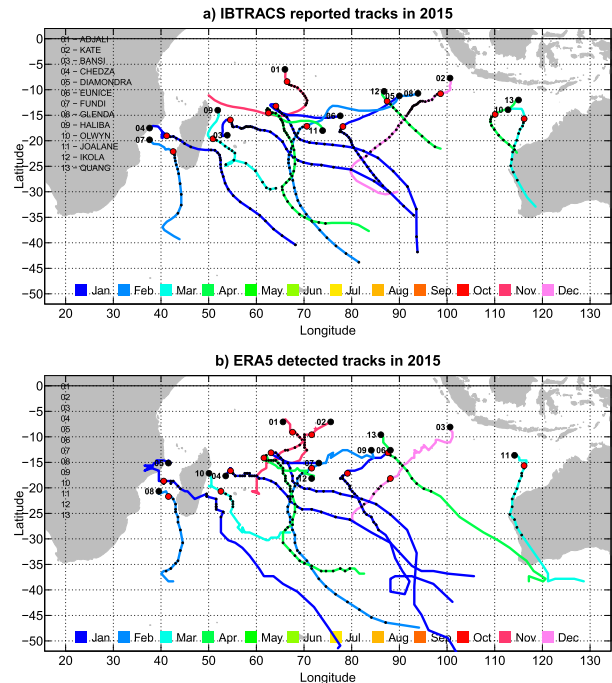


FIG. 2. (a) TC tracks reported in IBTrACS for the 2015 season. (b) TC tracks resulting from the tracking algorithm applied to ERA5 for the 2015 season. Dots along trajectories indicate TC points, with thick black dots for the first point of the system (genesis point) and thick red dots for the first point of the TC stage (intensification point). Track colors indicate the month of the track starting point (genesis).

IBTrACS, but on the basis of the 18 m s^{-1} wind speed threshold: development stage from the track start to the first exceedance, then TC stage until the last exceedance, then cyclolysis stage.

b. Cyclogenesis indices (CGIs)

The link between cyclone activity and large-scale environmental conditions is assessed using CGIs from the existing literature. We use the three indices evaluated on seasonal and interannual time scales by Menkes et al. (2012), and used separately by Royer and Chauvin (2009), Camargo (2013), and Chauvin et al. (2020) in a climate change perspective:

- the CYGP index introduced by Royer et al. (1998), after Gray (1975);
- the GPI index introduced by Emanuel and Nolan (2004);
- the TCS index introduced by Tippett et al. (2011) (hereafter referred as TIPP in order to avoid confusion with the TCs acronym used for “tropical cyclones”).

All indices are computed at the gridpoint scale and on a monthly basis (i.e., calculated with monthly mean climate data). They are constructed as multiplicative functions of dynamical and thermal variables that result

from empirical fits between observed cyclone activity and reanalyzed large-scale variables. Dynamical variables are the same for the three indices used in this paper (low-level vorticity and vertical wind shear) while thermal variables differ. More precisely, the indices are as follows:

$$\text{CYGP} = \beta_{\text{CYGP}} \times \underbrace{|f| \left(\frac{\zeta_r}{|f|} + 5 \right) (V_{\text{shear}} + 3)^{-1}}_{\text{Dynamical}} \times \underbrace{\max(P_c^* - 3, 0)}_{\text{Thermal}}, \quad (1)$$

$$\text{GPI} = \beta_{\text{GPI}} \times \underbrace{|10^5 \zeta|^3 (1 + 0.1V_{\text{shear}})^{-2}}_{\text{Dynamical}} \times \underbrace{\left(\frac{H}{50} \right)^3 \left(\frac{V_{\text{pot}}}{70} \right)^3}_{\text{Thermal}}, \quad (2)$$

$$\text{TIPP} = \beta_{\text{TIPP}} \times \underbrace{\cos(\varphi) \exp(1.03\zeta - 0.15V_{\text{shear}})}_{\text{Dynamical}} \times \underbrace{\exp(0.05H + 0.56\text{SST}_{\text{loc}})}_{\text{Thermal}}, \quad (3)$$

where f is the Coriolis parameter, φ is the latitude, ζ (ζ_r) is the absolute (relative) vorticity at 850 hPa, $V_{\text{shear}} = \Delta V/\Delta p$ is the vertical wind shear between 850 and 200 hPa, P_c^* is the convective precipitation, H is the relative humidity at 600 hPa, $\text{SST}_{\text{loc}} = \text{SST} - \text{SST}^{(20\text{S}-20\text{N})}$ is the local SST anomaly relative to the tropics (20°S–20°N), and V_{pot} is the TC potential intensity introduced by Emanuel (1988) that we calculate using the `pmin_2013.f` routine distributed by K. Emanuel.³ For the three indices, the β coefficient is a scaling factor that allows to interpret global maps of CGIs as densities of TCs; here we systematically tune these scaling factors so that the global sum of CGIs equals 84 (TCs per year over the globe) over the present-day period, and we keep the same β for computing indices over future periods. More details about the computation of these three indices can be found in the appendix of Menkes et al. (2012).

It is important to note that in this paper, we use the exact same equations for all reanalysis or model data on which we compute CGIs. In particular the numerical constants that are present in the above equations are the ones used by Menkes et al. (2012), and they correspond to the ones originally introduced by the respective authors. Camargo et al. (2014) suggest that CGIs perform better in capturing climate-related changes in cyclone

activity when they are refitted for the model of interest (including the selection of predictors). Here we consider that such a model-dependent computation of CGIs is outside the scope of our study, and that using the exact same definition for CGIs allows for a fair comparison between models. Last, for the sake of simplicity, results are mainly shown for the average of the three indices (hereafter the aggregate CGI), and behaviors of individual indices are only mentioned in the text when they substantially differ from the mean. Considering the average of CGIs also tends to emphasize signals that are common—thus robust—across individual indices.

As CGIs are written as multiplicative functions, differences between time averages over two periods of time (typically present-day vs future) can be broken down into individual contributions of dynamical versus thermal components. Indeed, for each calendar month, if x_i (y_i) denotes the dynamical (thermal) component of the CGI for year i , and x'_i and y'_i denotes their anomalies relative to their time averages \bar{x} and \bar{y} , the time-averaged CGI over either the present-day (P) or the future (F) period is

$$\overline{\text{CGI}} = \overline{x_i y_i} = (\overline{x + x'_i})(\overline{y + y'_i}) = \bar{x} \bar{y} + \overline{x'_i y'_i}. \quad (4)$$

Thus, the $F - P$ difference (denoted Δ) in time-averaged CGI is

$$\Delta \overline{\text{CGI}} = \overline{\text{CGI}}^F - \overline{\text{CGI}}^P = \overline{x^F y^F} - \overline{x^P y^P} + \underbrace{\overline{x'_i y'_i{}^F} - \overline{x'_i y'_i{}^P}}_{\varepsilon}, \quad (5)$$

with ε the residual term resulting from dependencies between monthly anomalies of x_i and y_i . Finally, since $\overline{x^F} = \bar{x}^P + \Delta \bar{x}$ and $\overline{y^F} = \bar{y}^P + \Delta \bar{y}$, one can write

$$\Delta \overline{\text{CGI}} = \underbrace{\overline{y^P \Delta x}}_{\text{Dynamical}} + \underbrace{\overline{x^P \Delta y}}_{\text{Thermal}} + \underbrace{\Delta \bar{x} \Delta \bar{y} + \varepsilon}_{\text{Residual}}, \quad (6)$$

where $\overline{y^P \Delta x}$ is the contribution of dynamical changes only, and $\overline{x^P \Delta y}$ is the contribution of thermal changes only. In the following, the last two terms $\Delta \bar{x} \Delta \bar{y}$ and ε are grouped into a single residual term, which is systematically shown in the figures but not commented in the text. The decomposition is performed for each calendar month separately and then averaged over the season or the year.

4. Results

a. Analysis of high-resolution experiments

1) REALISM OF SIMULATED TCs

To assess the realism of TCs simulated by the different model configurations, we first analyze the statistical

³ <ftp://texmex.mit.edu/pub/emanuel/TCMAX/>.

distribution of the annual minimum of sea level pressure in the SIO basin (Fig. 3a). Observed values are taken from IBTrACS assuming that annual minima of sea level pressure systematically occur within TCs. Over 1980–2016 the median is found to be 915 hPa; this means that such a low pressure is reached by at least one system over the SIO basin every 2 years on average. ECMWF reanalyses are unable to simulate pressures lower than 950 hPa, although a notable improvement is seen in ERA-5 relative to ERA-Interim (likely due to the increase in resolution). Uniform CNRM-CM configurations (T127 and T359) also fail to simulate extremely low pressures, although one outlying system reaches 905 hPa in the T359 experiment. The CNRM-CM5 (CNRM-CM6-1) model nevertheless simulates lower pressures than ERA-Interim (ERA-5) while it has a slightly coarser resolution; one reason could be that in reanalyses, data assimilation tends to spatially smooth low pressure systems when centers of action are slightly shifted between assimilated observations and forecast background. The added value of the rotated-stretched configuration in the present-day climate (SIO-P) is evident from Fig. 3a: this experiment is able to simulate lower pressures than observed (e.g., below 900 hPa), even if the median of the annual minimum pressure distribution remains slightly higher than observed (~930 hPa).

Once the tracking is done, the realism of resulting TCs is evaluated from the statistical relationship between the minimum sea level pressure and the maximum wind speed along the track (Fig. 3b). Both variables are indeed strongly correlated, as evidenced in TC observations (IBTrACS) and shown by Atkinson and Holliday (1977). Such a relationship is well captured by present-day model experiments (T359, SIO-P), although the model exhibits stronger winds than IBTrACS for a given pressure especially in the rotated-stretched configuration. The uniform experiment (T359) nevertheless struggles to simulate strong TCs (only two systems with pressure below 930 hPa and wind speed above 50 m s^{-1}) while the rotated-stretched experiment (SIO-P) can generate stronger TCs than the most intense TC recorded in IBTrACS. This result was also found by Chauvin et al. (2020) over the North Atlantic basin. Despite its fine resolution, ERA-5 fails to reproduce the strength of observed TCs. Note that a fair comparison between winds of IBTrACS, ERA-5, and ARPEGE experiments is, however, difficult since one compares wind output at a given time step and grid point (model) with 10-min sustained winds at the local cyclone scale (IBTrACS).

Finally, a first evaluation of the projected changes in TC characteristics can be assessed from these diagnostics: here we find no clear difference in the pressure–wind relationship between the SIO-P and the SIO-F

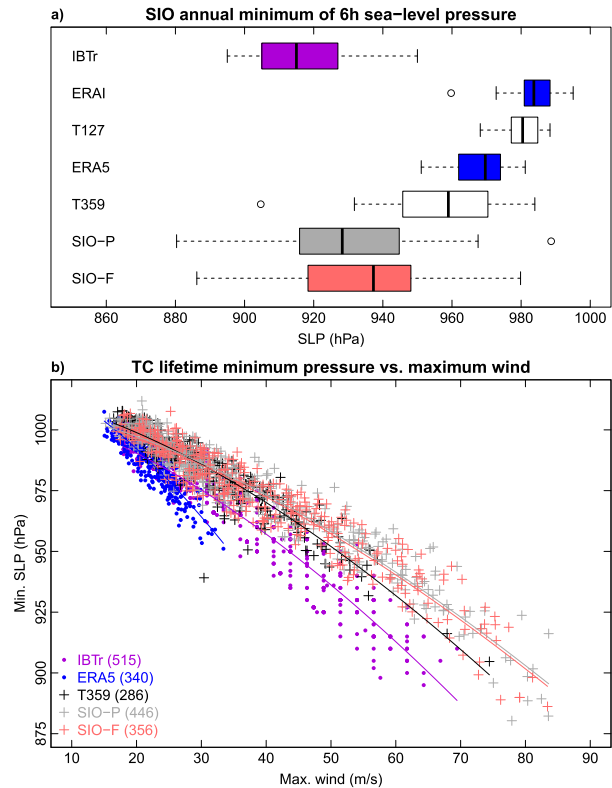


FIG. 3. (a) Distribution of the annual minimum of 6-h SLP (hPa) across the SIO domain (0° – 30° S, 30° – 120° E) for IBTrACS (1980–2016, violet), ERAI and ERA5 (1980–2016, blue), T127 (1976–2005) and T359 (1981–2010) uniform experiments (white), and SIO-P (1971–2014, gray) and SIO-F (2051–94, red) rotated-stretched experiments. In all boxplots used in this paper, the box represents the first and third quartiles, the band inside is the median, the whiskers expand to the largest values still within the 1.5 interquartile range from the box, and the small circles indicate outliers. (b) Lifetime minimum SLP (p) as function of lifetime maximum wind (V) for all TCs reported in IBTrACS and detected in ERA5, T359, SIO-P, and SIO-F [periods and colors are as in (a)]. Fits are added following Atkinson and Holliday (1977) (i.e., assuming $p = a + bV^{1/0.644}$ with a and b the coefficients to be fitted).

experiments (Fig. 3b), and although the SIO-F distribution of the annual minimum of sea level pressure seems slightly shifted toward higher pressures than SIO-P (Fig. 3a), the difference between the two samples is not statistically significant (p value of about 0.5). Changes in TC characteristics are thus more carefully scrutinized in the following.

2) ANALYSIS OF TC FREQUENCY

On average, 13.9 TCs per year are reported in the SIO domain by IBTrACS (Fig. 4a). As the average number of TC days per system is found to be 5.2 days, it leads to an annual number of TC days of 73 days (Fig. 4b). The tracking algorithm has been calibrated on ERA-5 over 2011–16 (section 3); on average over these years, it

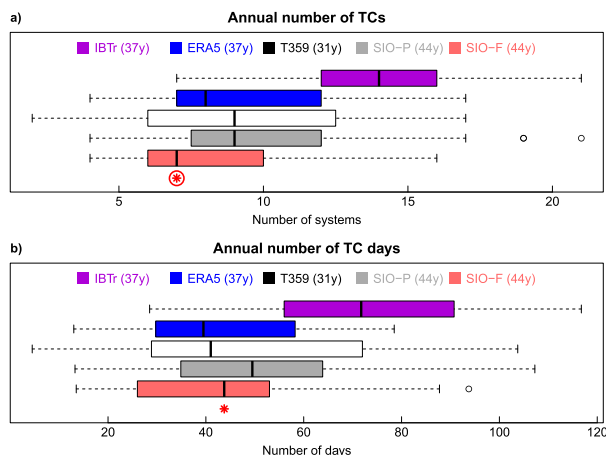


FIG. 4. (a) Distribution of the annual number of TCs in the SIO domain for IBTrACS (violet), ERA5 (blue), T359 (white), SIO-P (gray), and SIO-F (red). (b) As in (a), but for the annual number of TC days. Red (circled) asterisks indicate differences between SIO-P and SIO-F averages that are significant at the 90% (95%) level following a t test.

detects 11 TCs and 54 TC days per year (vs 12.5 TCs and 63 TC days per year in IBTrACS). Over the whole time period 1980–2016, the tracking algorithm applied to ERA-5 more substantially underestimates the observed number of both TCs (9 vs 13.9 yr^{-1}) and TC days (42 vs $73 \text{ TC days yr}^{-1}$). This inconsistency is the strongest at the beginning of the time period and progressively decreases with time (not shown), which questions the temporal homogeneity of IBTrACS and/or ERA-5 over the SIO. However, a more detailed evaluation is left for future studies.

T359 and SIO-P experiments simulate a similar amount of TCs (9.2 and 10.1 on average, distribution in Fig. 4a) and TC days (51 vs 52 on average, distribution in Fig. 4b). This suggests that the uniform 50-km resolution of the T359 experiment is potentially sufficient to generate a realistic number of TCs, albeit with weaker intensity than in the rotated-stretched configuration (see previous section and Fig. 3). The SIO-F experiment produces about 20% less TCs than the SIO-P experiment (8.1 yr^{-1} on average), which is qualitatively consistent with the broadly reported future decrease in TC frequency (e.g., Walsh et al. 2016) and quantitatively agrees with results of Murakami et al. (2012). This 20% decrease in the frequency is significant at the 95% level; as it is associated with a slight increase in TC duration (5.5 vs 5.1 TC days per system), the decrease in the annual number of TC days is less statistically significant (90% level, 44 vs 52 days). (This increase in TC duration is further detailed below with the TC intensity.)

In the SIO, TCs preferably develop close to the center of the basin (10° – 15°S , 60° – 80°E), the Mozambique

channel, and close to the Australian shore (Fig. 5a). This spatial pattern is well captured by ERA-5, confirming that the tracking algorithm applied to the reanalysis is able to detect part of the TCs reported in IBTrACS (Fig. 5b, spatial correlation of 0.90 with Fig. 5a). T359 and SIO-P experiments tend to simulate too little (much) TC intensification in the center (south) of the basin (Figs. 5c,d, spatial correlations of 0.62 and 0.51 with Fig. 5a). This might reflect a systematic bias of the CNRM-CM6-1 model since a similar behavior was reported by Chauvin et al. (2020) over the North Atlantic basin; future studies will investigate the origins of this geographical bias. The rotated-stretched configuration (SIO-P) results in an enhanced number of TCs in the SIO relative to the uniform configuration; symmetrically, less systems are simulated in other basins. A few systems have their intensification point outside the tropics (even south of 30°S) in the model; these can be either systems that have developed in the tropics and reached the TC stage after an extratropical transition, or systems that have developed outside the tropics but still meet the criteria to be detected as TC by the tracking algorithm. We have decided not to filter these systems out; in particular the use of a fixed latitude criterion would have been questionable in a climate change context. A small number of such extratropical systems is also detected in ERA-5 by the tracking algorithm.

In agreement with Fig. 4, SIO-F simulates globally fewer TCs than SIO-P, especially northeast of the Mascarene Islands (Fig. 5e). Although the signal is noisy due to the limited number of systems (446 in SIO-P vs 356 in SIO-F), more TC intensification is observed south of the Mozambique and west of Australia. Similar conclusions arise from analyzing densities of full TC tracks that are smoother due to the greater number of points included (Figs. 5f–j). In particular, the SIO-F versus SIO-P difference reveals a general northwest–southeast dipole (with the exception of the Mozambique channel), consistent with a poleward shift of TC tracks superimposed with a general decrease in the number of TCs.

3) ANALYSIS OF TC INTENSITY

Consistent with Fig. 3b, TCs simulated by the uniform T359 experiment are weaker than reported in IBTrACS, as illustrated by both the lifetime minimum pressure (983 vs 962 hPa on average, Fig. 6a) and maximum wind speed (31 vs 36 m s^{-1} on average, Fig. 6b). This bias is partly corrected in the rotated-stretched configuration (SIO-P, 975 hPa and 37 m s^{-1} on average). TC intensity is significantly increased in the SIO-F experiment (971 hPa and 39 m s^{-1} on average), which is again in line with the existing literature (e.g., Walsh et al. 2016). Interestingly, most of this increase in intensity arises

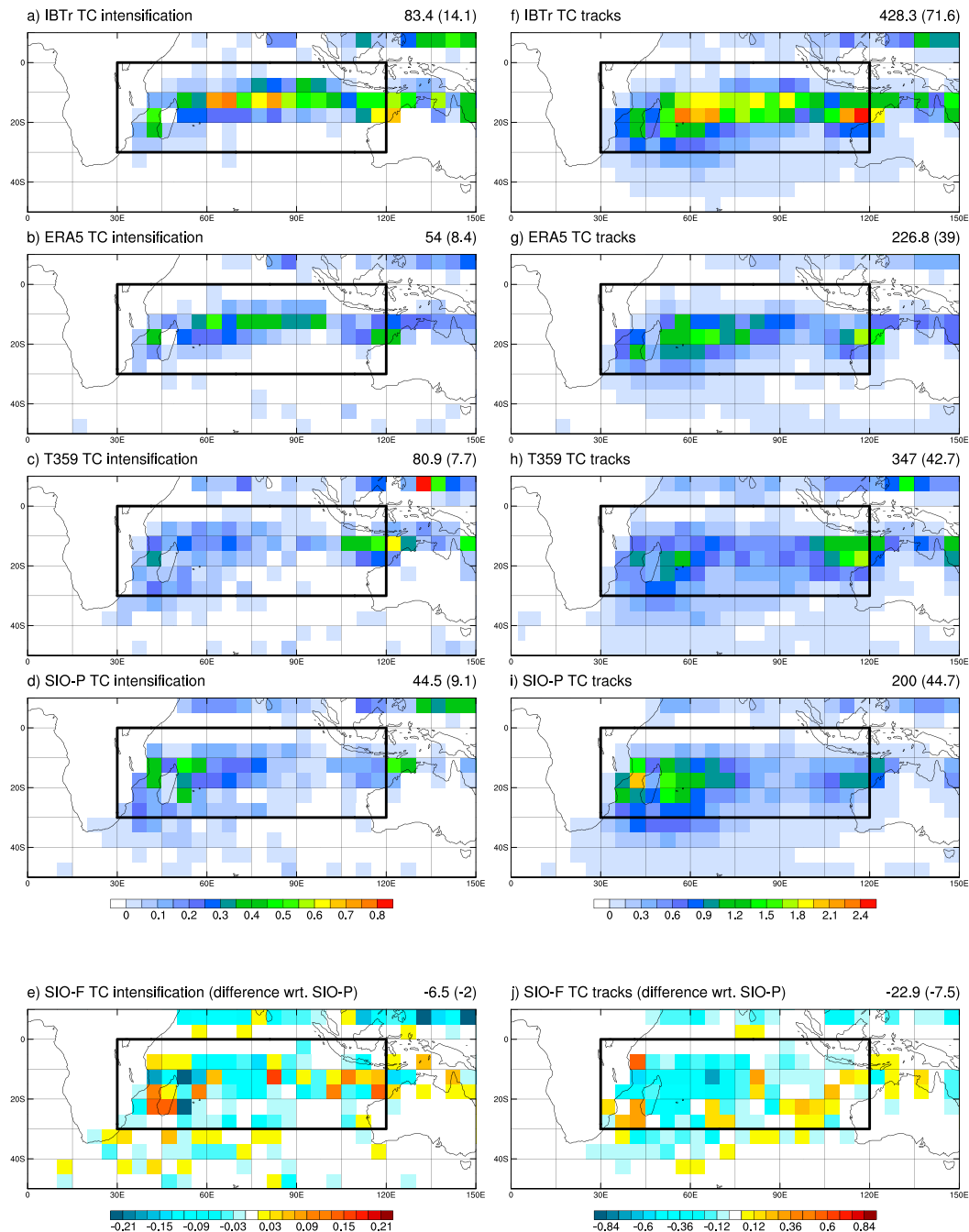


FIG. 5. (a)–(e) Frequency of TC intensification points (i.e., first TC point for each trajectory) (in number of points per year and per 5° × 5° grid box) for (a) IBTrACS, (b) ERA5, (c) T359, (d) SIO-P, and (e) SIO-F represented as a difference relative to (d). (f)–(j) As in (a)–(e), but for TC tracks (i.e., all TC points for each trajectory). Sums over the globe and for the SIO domain (in parentheses) are indicated in the top-right corner of each panel.

from the core of the distribution: TCs with an intensity below the median of the present-day distribution occur less frequently in the future experiment (40% of TCs in SIO-F vs 50% in SIO-P by definition), while TCs with an intensity between the 60th and 80th percentiles of the present-day distribution are more frequent (30% vs

20% by definition). (Values are similar for both minimum pressure and maximum wind.) Extremely intense TCs also contribute to the intensity increase: about 6%–7% of the future TCs exceeds the 95th percentile of the present-day intensity distribution (low pressure or high winds), so that even if the overall number of TCs

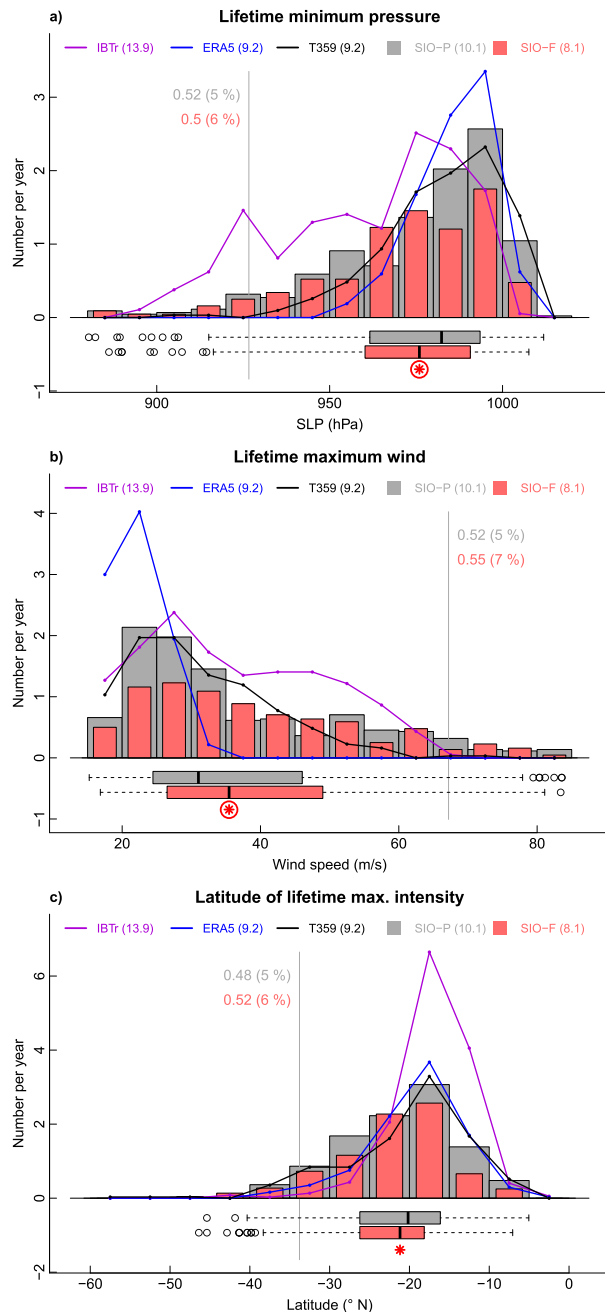


FIG. 6. (a) Frequency histogram (in number of systems per year) of the TC lifetime minimum pressure (hPa) for IBTrACS (violet line), ERA5 (blue line), T359 (black line), SIO-P (gray bars), and SIO-F (red bars). (b) As in (a), but for the lifetime maximum wind (m s^{-1}). (c) As in (a), but for the latitude of the lifetime minimum pressure ($^{\circ}\text{N}$). For SIO-P and SIO-F, probability distributions are also represented (boxplots). Red (circled) asterisks indicate differences between SIO-P and SIO-F averages that are significant at the 90% (95%) level following a t test.

decreases by 20% (Fig. 4), the number of extremely intense TCs remains constant (about 0.5 yr^{-1} with this definition). Similar results are obtained from the accumulated cyclone energy (not shown).

The increase in TC intensity in the rotated-stretched experiments is associated with a 90% level significant poleward shift of the lifetime maximum intensity (Fig. 6c). Although this is qualitatively consistent with the literature (e.g., Kossin et al. 2013), here we find a relatively weak shift of about 1°S in 80 years (22.3°S for SIO-F vs 21.3°S for SIO-P on average). This shift is related to a poleward extension of the tracks: while latitudes of genesis and intensification do not change significantly, the latitude of cyclolysis is shifted by 1.4°S on average (26.9° vs 25.5°S). Model biases in the spatial density of tracks (Fig. 5) are reflected in the distribution of the latitude of maximum lifetime intensity: too many (few) tracks at high (low) latitudes. Part of the discrepancy between model experiments and IBTrACS could arise from the tracking algorithm, since the ERA-5 distribution shows a similar poleward displacement.

Last, the increase in TC intensity is also related to a slightly longer TC stage (5.7 vs 5.4 days on average) that incorporates more TC days (5.5 vs 5.1 on average). Over the whole system lifetime, this increase is compensated by decreases in the duration of both development (1.9 vs 2.1 days) and cyclolysis (2.4 vs 2.5 days) stages; however, only the shorter development stage is statistically significant at the 95% level (not shown). (The terminology of the different stages is defined in section 3a.)

4) ANALYSIS OF SEASONAL CYCLE

An interesting feature revealed by the rotated-stretched experiments is that the cyclone season is found to be shorter under future climate conditions (Fig. 7). In the SIO-P experiment, the first (last) TC of the season—July to June—starts on average on 12 November (28 April), so that the cyclone season—defined here as the difference between these two dates—lasts on average 172 days. These values are very close to the uniform T359 experiment (12 November to 21 April, 165 days) and to the IBTrACS observations (7 November to 28 April, 177 days). In the SIO-F experiment, the season begins on average 32 days later (14 December), ends 9 days earlier (19 April), and thus lasts 41 days less than in SIO-P. The later onset and the shorter duration of the season are significant at the 95% level. These changes result from a strong decrease in the number of TCs occurring in the austral winter: in SIO-P, 17 TCs (3.8% on the total number) are detected during the months of June–September and 16 (3.6%) in October, versus 2 (0.6%) and 3 (0.8%), respectively, in SIO-F. Note that such wintertime systems are realistic: 9 systems are recorded over 1980–2016 in IBTrACS in

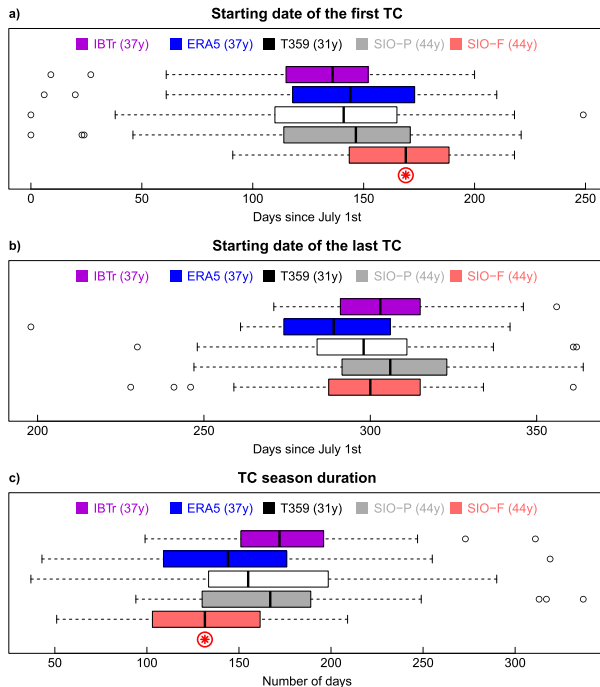


FIG. 7. As in Fig. 4, but for (a) the date of the first TC intensification within the season, (b) the date of the last TC intensification within the season, and (c) the TC season duration measured as the difference between (b) and (a).

June–September and 11 in October (i.e., 1.7% and 2.1% of the total number), with 6 systems reaching at least the *severe tropical storm* (category 2) stage (winds above 25 m s^{-1}), including one *tropical cyclone* (category 3) system (33 m s^{-1} ; Oscar in October 1983) and two *intense tropical cyclone* (category 4) systems (47 m s^{-1} ; Bellamine in October 1996 and Anais in October 2012) according to Météo-France (BoM) classifications (again, we use the terminology of the local RSMCs in this paper, not the Saffir–Simpson scale.). As a consequence of the winter decrease, the relative fraction of TCs occurring during the austral summer increases, especially during the months of February, March, and April (57% of TCs in SIO-F vs 51% in SIO-P). Further elements about this seasonal redistribution of TCs are discussed later.

b. Analysis of cyclogenesis indices

1) CGIs IN HIGH-RESOLUTION EXPERIMENTS

Previous studies have shown that CGIs can capture the geographical distribution of cyclone activity fairly well (e.g., Menkes et al. 2012). This is verified here over the SIO basin by comparing the aggregate index (average of CGIs, see section 3) computed on the ERA-5 data (Fig. 8a) with observed TC track densities (Figs. 5a,f). CGIs are indeed able to represent both the fraction of

global cyclone activity that occurs within the SIO basin (12.5 out of 84 TCs yr^{-1} on average, similar to IBTrACS values) and its spatial distribution within the basin with a local maximum around 10°S , 75°E (spatial correlation of 0.73 between Figs. 5a and 8a when remapped onto the same $5^{\circ} \times 5^{\circ}$ grid). The agreement between indices and actual track densities is less clear for the SIO-P experiment: CGIs suggest that cyclone activity should preferably occur within a latitudinally narrow area expanding from Madagascar to Indonesia similarly to ERA-5 (Fig. 8b) whereas TC tracks were detected more uniformly in the western part of the basin (Figs. 5d,i, spatial correlation of 0.54 between Figs. 5b and 8d). Possible reasons for this discrepancy can be that (i) the native resolution in SIO-P is nonuniform across the basin, (ii) CGIs were fitted on observations and reanalysis, so that coefficients used in their computation do not reflect the model characteristics, and (iii) the model (and the tracking algorithm) seem to have difficulties to simulate (detect) TCs at low latitudes, as reported in section 4a and Fig. 5.

CGIs fail to capture the 20% decrease in TC frequency between SIO-P and SIO-F that is observed in Figs. 5e,j (Fig. 8c). They instead indicate an unchanged cyclone activity on average over the SIO basin (difference of $+0.4 \text{ TCs yr}^{-1}$). This result is consistent with results of Chauvin et al. (2020) over the North Atlantic basin and also agrees with Camargo et al. (2014), who compared CGIs and actual TC tracks in high-resolution experiments from another model. Within the basin, the spatial pattern of changes in CGIs mostly consists in a poleward shift of the cyclone activity area, which is qualitatively consistent with changes in densities of tracks (Figs. 5e,j, spatial correlation of 0.25 between Figs. 5e and 8c) and with the poleward displacement of the location of lifetime maximum intensity (Fig. 6c). CGIs also support an increased cyclone activity north of Madagascar and in the Mozambique channel, as seen in the TC tracks. In other words, CGIs miss the overall decrease in TC frequency but seem to capture part of the changes in the regional distribution of TC tracks.

Further, breaking down changes in CGIs into dynamical and thermal components indicates that both contribute almost equally to the poleward shift of the cyclone activity area (Figs. 8d–f). They differ the most in the western part of the basin, especially north of the Mascarene Islands, where dynamical variables support a decrease in cyclone activity—consistent with the decrease in the number of TC tracks (Fig. 5j)—which is almost entirely compensated by the thermal contribution. One could interpret such a decrease in the dynamical component as less favorable conditions for cyclogenesis (i.e., decreased TC frequency), while the

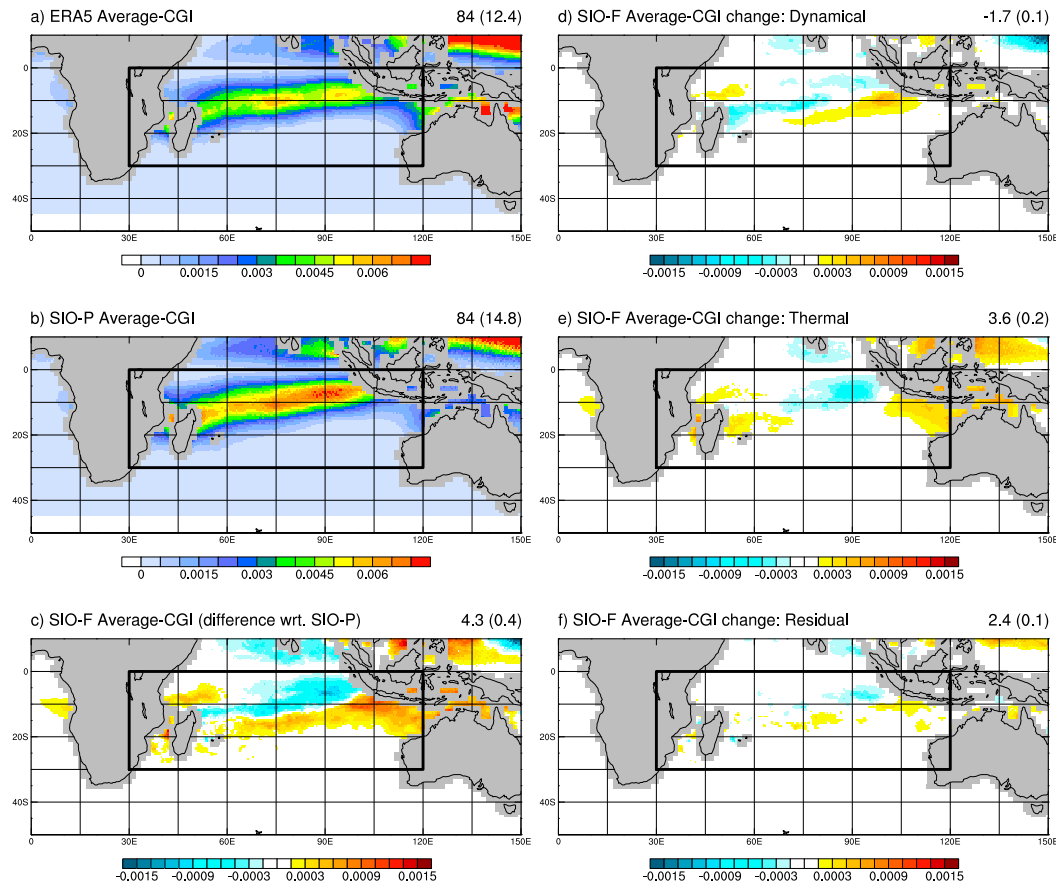


FIG. 8. (left) Annual mean of averaged CGIs (in number of TCs yr^{-1} and per $0.5^\circ \times 0.5^\circ$ grid box) for (a) ERA5, (b) SIO-P, and (c) SIO-F represented as a difference relative to (b). (right) Contributions of (d) dynamical components, (e) thermal components, and (f) residuals to (c). Sums over the globe and for the SIO domain (in parentheses) are indicated in the top-right corner of each panel.

increase in the thermal component could be indicative of more favorable conditions for intensification (i.e., increased TC intensity). However, this simple interpretation should be moderated by the fact that dynamical predictors can also be important for intensification (e.g., the vertical wind shear modulates the TC intensity), while thermal predictors can also be important for cyclogenesis (e.g., the midlevel relative humidity is relevant to spinning up the midlevel vortex in the early development). The CGI increase in the Mozambique channel solely arises from the thermal contribution, in line with a greater SST increase in this area compared to the rest of the basin (Fig. 1). The residual contribution is generally small but can be substantial especially in the eastern part of the basin.

Last, while results discussed above are based on the aggregate CGI, similar conclusions can be drawn from each index taken separately (not shown). In particular the spatial pattern of the SIO-F versus SIO-P difference (Fig. 8c) is common to all indices, albeit the spatial

average over the domain differs (+0.4, +1.3, and -0.6 TCs per year for CYGP, GPI, and TIPP, respectively). As all the three indices share the same dynamical variables, there is little interindex dispersion in the dynamical contribution presented in Fig. 8d. Discrepancies in the thermal contribution, that is strongly positive for the GPI and slightly negative for the TIPP, therefore explain most of the differences between indices, suggesting that some thermal variables are more relevant than others to capture climate-related changes in cyclone activity.

2) CGIS IN CMIP5 MODELS

Here we assess whether changes in CGIs obtained in high-resolution CNRM-CM6-1 experiments are representative of changes in CGIs obtained in low-resolution multimodel CMIP5 projections. In the following we indicate CMIP5 ensemble-mean values together with the 10th and 90th percentiles of CMIP5 distribution between parentheses—as the ensemble contains 14

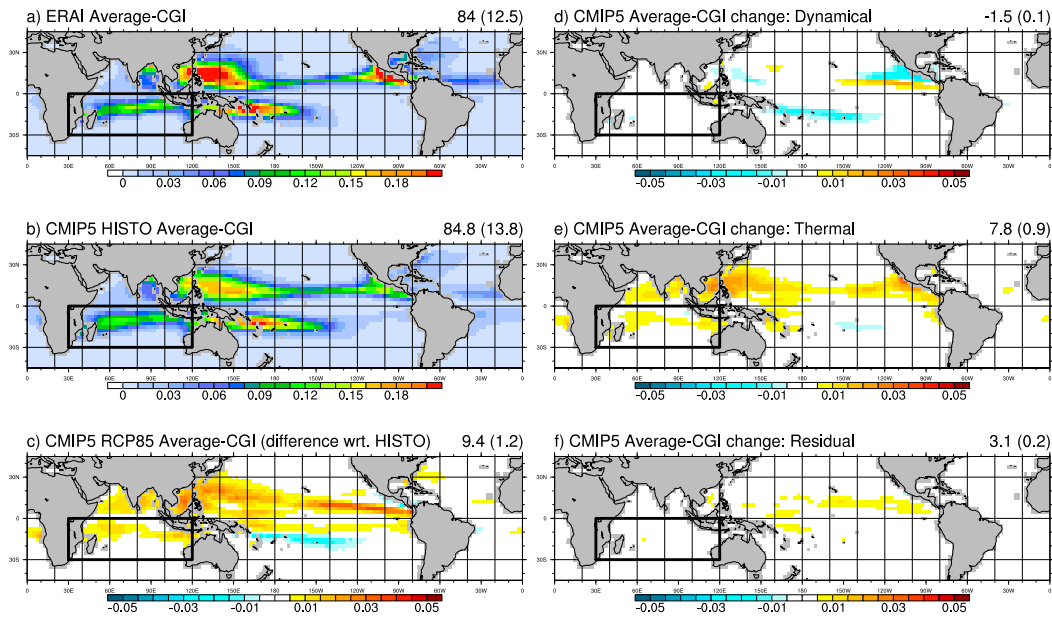


FIG. 9. (left) Annual mean of averaged CGIs (in number of TCs yr^{-1} and per $2.5^\circ \times 2.5^\circ$ grid box) for (a) ERAI, (b) CMIP5 ensemble mean historical simulations over 1976–2005, and (c) CMIP5 ensemble-mean RCP8.5 simulations over 2070–99 represented as a difference relative to (b). (right) Contributions of (d) dynamical components, (e) thermal components, and (f) residuals to (c). Sums over the globe and for the SIO domain (in parentheses) are indicated in the top-right corner of each panel.

models, this range excludes the two lowest and two highest values.

First, comparing ERA-Interim (80-km resolution, interpolated onto a 2.5° grid, Fig. 9a) with ERA-5 (30-km resolution, interpolated onto a 0.5° grid, Fig. 8a) shows that the resolution has little effect on the computation of CGIs; this was expected since these indices are designed to account for large-scale conditions. Both reanalyses indeed result in a similar fraction of cyclone activity in the SIO (about 15% of the global activity) and a similar spatial pattern within the basin. CMIP5 models have been shown to represent the geographical climatology of several CGIs fairly well (Camargo 2013), which is here confirmed by our aggregate CGI (Fig. 9b), although the ensemble averaging tends to smooth hotspots of cyclone activity due to intermodel dispersion in the exact location of local maxima. On average, about 16% [14%–20%] of the global cyclone activity occurs in the SIO, which is consistent with reanalyses. [A more detailed analysis of individual CMIP5 model biases can be found in Camargo (2013) and is considered to be beyond the scope of this paper.] Importantly, we have verified that our SIO-P high-resolution experiment lies within the range of CMIP5 models in terms of representation of present-day climatology of CGIs (not shown).

In future RCP8.5 projections, CMIP5 models simulate an overall increase in CGIs, slightly less pronounced

over the SIO (+9% [–8% to 20%]) than globally (+11% [–2% to 20%], Fig. 9c). Our results based on an aggregate CGI are consistent with the GPI analysis reported in Camargo (2013), although the GPI is the index that projects the strongest ensemble-mean increase: +16.3 (+2.8) TCs per year at global scale (in the SIO basin) versus +7.7 (+0.2) and +4.1 (+0.6) for the CYGP and the TIPP, respectively.

The global increase in CGIs projected by CMIP5 models (+11%, i.e., +9.4 TCs per year) arises from the thermal contribution (+7.8 TCs per year), while the dynamical component exhibits a small decrease (–1.5, Figs. 9d–f). The latter is robust across indices (–2, –1.2, and –1.3 for CYGP, GPI, and TIPP, respectively), while the former is the strongest for GPI (+14.7) and the lowest for TIPP (+3). This is consistent with CGIs applied to high-resolution experiments and supports the idea that changes in dynamical conditions could be related to changes in TC frequency (e.g., less favorable weather for cyclogenesis), while changes in thermal conditions could be related to changes in TC intensity (e.g., more available energy for intensification). This may be particularly the case for the GPI that includes the potential intensity introduced by Emanuel (1988) in its thermal component (Emanuel and Nolan 2004). Again, this interpretation should nevertheless be moderated because the relationship between dynamical versus thermal components and TC genesis versus intensification is not straightforward.

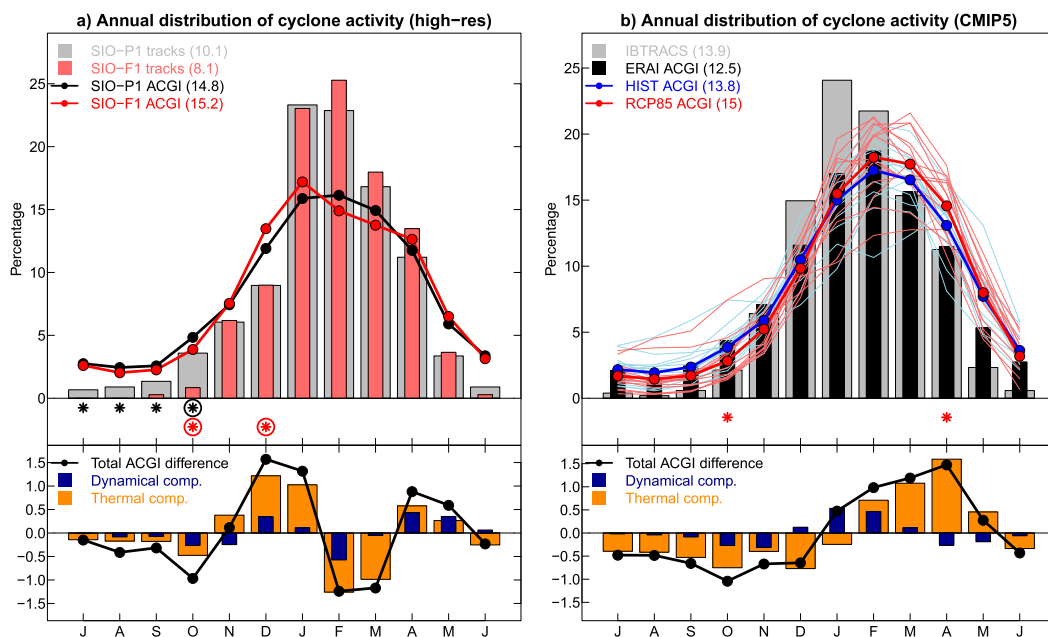


FIG. 10. (a) Annual distribution of SIO-P (gray bars) and SIO-F (red bars) TCs, and SIO-P (black line) and SIO-F (red line) aggregate CGI. Black (circled) asterisks indicate differences between bars that are significant at the 90% (95%) level; red (circled) asterisks indicate differences between lines that are significant at the 90% (95%) level. (b) Annual cycle of IBTrACS TCs (gray bars), and ERA-Interim (black bars), CMIP5 historical (blue lines), and RCP8.5 (red lines) averaged CGIs, with thick lines for ensemble means. Red (circled) asterisks indicate differences between ensemble means that are significant at the 90% (95%) level. All cycles are normalized and represented in percent per month. (bottom) Decomposition of the total aggregate CGI difference (black line) into dynamical (blue bars) and thermal (orange bars) components.

With a +0.4 TCs per year increase in the SIO (Fig. 8c), the SIO-F versus SIO-P difference is consistent with the range of CMIP5 projections. A fair comparison is, however, difficult since time periods used to evaluate changes differ. Interestingly, spatial patterns of CGI changes in the SIO are similar between high-resolution CNRM-CM6-1 experiments and the CNRM-CM5 experiment included in the CMIP5 ensemble (not shown). This is not completely surprising since SIO-P and SIO-F experiments use SST taken from this CNRM-CM5 simulation, but suggests that changes in large-scale environmental variables associated with cyclone activity are robust across the two versions of the atmospheric model and the two grid configurations. The poleward shift of cyclone activity suggested by CNRM-CM6-1 aggregate CGIs is, however, not representative of the CMIP5 ensemble that rather projects a reinforcement of cyclone activity close to the equator (Fig. 9c). This highlights that changes in the geographical distribution of cyclone activity captured by CGIs can be model dependent (e.g., Camargo 2013).

3) ANALYSIS OF CGIS' ANNUAL CYCLE

Globally, CGIs have been shown to represent the annual cycle of TC occurrence fairly well, although

with a weaker seasonal amplitude (Menkes et al. 2012). This is confirmed here by our high-resolution experiments: in the SIO-P experiment, 90% of the TC tracks occur from November to May while the aggregate CGI would indicate 78% (Fig. 10a). As discussed above (Fig. 7), we find a dramatic decrease in TC frequency during the austral winter in the SIO-F experiment, which translates into a significant decrease in the relative TC occurrence from June to October, counterbalanced by an increase—albeit not significant—from February to April. This redistribution is partly explained by CGIs, which also support a relative decrease of cyclone activity in winter (significant in October) and a relative increase in summer (significant in December). The fact that relative changes disagree between TC tracks and CGIs in February and March could be due to sampling uncertainty since they are not statistically significant.

Annual cycles of both TC occurrence and CGIs simulated by the SIO-P experiment are consistent with IBTrACS and ERA-Interim, respectively (Fig. 10b). In particular, 94% of IBTrACS TCs occur from November to May while the ERA-Interim aggregate CGI would indicate 82%. CMIP5 historical simulations are generally consistent with ERA-Interim in that aspect,

although they tend to underestimate (overestimate) the proportion of cyclone activity in early (late) summer: 49% (41%) from November to February (March to June) on average over the ensemble versus 54% (35%) in ERA-Interim. Projected changes in the RCP8.5 simulations are indicative of relative decrease of cyclone activity from June to December (significant in October) counterbalanced by a relative increase from January to May (significant in April). Such a seasonal redistribution of cyclone activity is fully consistent with results from our high-resolution experiments, suggesting that this feature of TC changes could be robust across models. Last, both dynamical and thermal components contribute to reshaping the annual cycle of CGIs, although monthly contributions differ: for instance, in CMIP5, the CGI relative increase in summer is mostly explained by the dynamical component in January, by the thermal component in March and April, and by both in February.

5. Discussion

In this paper we have tried to assess projected changes in the SIO cyclone activity from two complementary approaches: (i) high-resolution experiments with our in-home model (CNRM-CM6-1) that simulates realistic TCs and allows for a statistical analysis of TC characteristics and (ii) low-resolution multimodel climate projections in which cyclone activity can only be estimated from empirical indices built on large-scale environmental variables. Although we have shown that robust results emerge, both approaches used in this study suffer from clear limitations.

First, our high-resolution experiments are performed in an atmosphere-only framework (i.e., with prescribed SST), whereas the atmosphere strongly interacts with the near-surface ocean during TCs. Daloz et al. (2012) have shown that the ocean–atmosphere coupling can modify the simulation of TCs by the rotated-stretched configuration of the CNRM-CM model, the impact being sensitive to the coupling frequency. However, in their review paper, Walsh et al. (2016) assess that atmosphere–ocean coupling only has a limited effect on climate change experiments. In addition, using an atmosphere-only framework allows us to correct for potential biases in SST (as done in our experimental design).

Second, results obtained with the rotated-stretched configuration might be sensitive to the arbitrary choice of the grid pole location (Daloz et al. 2012). In the present study, the focus has been intentionally made on the western part of the SIO, in order to better assess potential changes in TCs over the area enclosing Mozambique, Madagascar, and the Mascarene Islands

[i.e., the region under the responsibility of Météo-France (local RSMC)]. In exchange, the resolution was not dramatically increased at the other side of the SIO (Australian shore) compared to the uniform T359 grid. We are nevertheless confident (from our expertise with the rotated-stretched configuration) that a small displacement of the grid pole would not have altered the results significantly. The fact that the uniform T359 experiment (50 km) simulates reasonable TCs gives us additional confidence that results of rotated-stretched experiments are robust across the whole SIO basin. Last, our results share some similarities with Chauvin et al. (2020), which suggests that the main conclusions could be robust among oceanic basins, although a more systematic analysis would be needed.

A third limitation of our experimental protocol is that it only includes one member per experiment, which could raise questions about our ability to disentangle climate change signal from the noise of internal variability. More ensemble members would probably have smoothed the changes in track densities presented in Fig. 5; we were nevertheless able to detect a few statistically significant changes at the basinwide scale, such as the decrease in the overall number of TCs or the reduction in the duration of the cyclone season. In their analysis of the North Atlantic basin, Chauvin et al. (2020) performed five members per experiment and concluded that although this provides robustness in results obtained at regional scale, one member of 50 years is sufficient for the large-scale signal to emerge.

A follow-up question is the sensitivity of our results to the unique model used to perform high-resolution experiments (CNRM-CM6-1). Here we have shown that (i) our results are quantitatively similar to other high-resolution modeling studies (e.g., Murakami et al. 2012) and that (ii) large-scale environmental changes simulated by CNRM-CM6-1 lie in the range of CMIP5 uncertainties. However, the issue of model dependency will not be properly tackled until multimodel ensembles of high-resolution climate projections exist, and the upcoming HighResMIP exercise (Haarsma et al. 2016) can be considered as a promising first step to that regard.

Last, statistical tools used to analyze both high-resolution experiments (TC tracking algorithm) and multiple low-resolution model datasets (computation of CGIs) can be questioned. The TC tracking algorithm uses several arbitrary thresholds (winds, vorticity, temperature) that clearly affect the number of systems detected; however, we have verified that our main findings remain unchanged when using slightly different thresholds (not shown). The computation of CGIs is also problematic as the choice of the predictors (environmental variables) and the fit of their coefficients are likely to be model

sensitive; using 3 indices and 14 models was a way to take this source of uncertainty into account, and building more sophisticated and possibly model-dependent CGIs is left for future work.

6. Conclusions

The aim of this study was to assess projected changes in the SIO tropical cyclone (TC) activity from both high-resolution CNRM-CM6-1 dedicated experiments and CMIP5 multimodel climate projections. Our main findings can be summarized as follows:

- the uniform T359 (50 km) configuration of the CNRM-CM6-1 model is able to simulate realistic TCs in terms of frequency and pressure–wind relationship, although with a weaker intensity than observed. The rotated-stretched configuration improves the realism of simulated TCs (especially in terms of intensity) over the area of interest.
- Rotated-stretched high-resolution experiments project a 20% decrease in the SIO TC frequency between 1965–2014 and 2045–94 in the RCP8.5 scenario. In the meantime, they indicate an increase in the maximum lifetime intensity, and a slight poleward extension of the TC tracks. As a consequence, the frequency of the strongest TCs is projected to remain nearly constant.
- Rotated-stretched high-resolution experiments project a substantial reduction of the cyclone season duration; in particular the first TC of the season is projected to occur 1 month later on average (mid-December vs mid-November). Although the raw number of TCs is projected to decrease for all individual months, cyclone activity is redistributed within the season, with a smaller (greater) relative proportion of cyclones occurring in early (late) summer. This result may be important for Regional Specialized Meteorological Centres and local administrations in charge of TC monitoring and alertness.
- Cyclogenesis indices (CGIs) applied to high-resolution experiments fail to capture the projected decrease in overall TC frequency. However, they are able to partially represent changes in the spatiotemporal distribution of cyclone activity, such as the poleward shift and the seasonal redistribution. This may not be surprising as CGIs are designed to represent not the total number of TCs but their spatiotemporal distribution.
- Changes in CGIs obtained from CNRM-CM6-1 lie in the range of CMIP5 projections. In particular the seasonal redistribution of cyclone activity is consistent across models.

Future work will involve further understanding of the decreasing TC frequency in CNRM-CM6-1 experiments: whether this results from less frequent initiations of

small-scale vortices or from less favorable conditions to intensification into TCs will be particularly scrutinized in the light of the work of Duvel (2015). Besides, the computation of CGIs in high-resolution experiments can be viewed as a first step into the physical understanding of changes in cyclone activity, and future analyses will further explore how they relate to changes in large-scale environmental features such as the Indian monsoon, the Madden–Julian oscillation, and/or the Hadley–Walker circulation. Impact studies may also be conducted to assess consequences of the projected changes in cyclone activity on associated phenomena such as rainfall or storm surges. Expanding the analysis to the new generation of climate models (CMIP6)—especially those with sufficiently high resolutions to simulate realistic TCs—will also be naturally considered for future work.

Finally, a promising perspective of this study is to pursue the efforts to reconcile results on TCs derived from high-resolution experiments with CGIs computed on low-resolution climate projections. In this paper we have shown that although CGIs miss the overall decrease in the number of TCs, they partially capture changes in their spatiotemporal distribution. Further, we have shown that the future increase in CGIs is mostly driven by their thermal component, while their dynamical component slightly decreases. The fact that these indices are empirically fitted on present-day cyclone activity features might give too much weight to the thermal component in a climate change context. Future research may therefore focus on the development of cyclogenesis indices that remain relevant for assessing climate change, taking advantage of high-resolution climate projections distributed within CMIP6 and possibly using more comprehensive statistical learning techniques.

Acknowledgments. This work has been partly supported by the ReNovRisk-C3 project within the Indian Ocean INTERREG-V Programme 2014–20. J.C. thanks all people at LACy and Météo-France La Réunion for their welcome and fruitful discussions, and Rémy Lee-Ah-Siem for technical support.

REFERENCES

- Atkinson, G., and C. Holliday, 1977: Tropical cyclone minimum sea level pressure/maximum sustained wind relationship for the western North Pacific. *Mon. Wea. Rev.*, **105**, 421–427, [https://doi.org/10.1175/1520-0493\(1977\)105<0421:TCMSLP>2.0.CO;2](https://doi.org/10.1175/1520-0493(1977)105<0421:TCMSLP>2.0.CO;2).
- Camargo, S., 2013: Global and regional aspects of tropical cyclone activity in the CMIP5 models. *J. Climate*, **26**, 9880–9902, <https://doi.org/10.1175/JCLI-D-12-00549.1>.

- , M. Tippett, A. Sobel, G. Vecchi, and M. Zhao, 2014: Testing the performance of tropical cyclone genesis indices in future climates using the HiRAM model. *J. Climate*, **27**, 9171–9196, <https://doi.org/10.1175/JCLI-D-13-00505.1>.
- Chauvin, F., J.-F. Royer, and M. Déqué, 2006: Response of hurricane-type vortices to global warming as simulated by ARPEGE-Climat at high resolution. *Climate Dyn.*, **27**, 377–399, <https://doi.org/10.1007/s00382-006-0135-7>.
- , R. Pilon, P. Palany, and A. BelMadani, 2020: Future changes in Atlantic hurricanes with the rotated-stretched ARPEGE-Climat at very high resolution. *Climate Dyn.*, **54**, 947–972, <https://doi.org/10.1007/s00382-019-05040-4>.
- Daloz, A. S., F. Chauvin, and F. Roux, 2012: Impact of the configuration of stretching and ocean–atmosphere coupling on tropical cyclone activity in the variable-resolution GCM ARPEGE. *Climate Dyn.*, **39**, 2343–2359, <https://doi.org/10.1007/s00382-012-1561-3>.
- Dee, D., and Coauthors, 2011: The ERA-Interim reanalysis: Configuration and performance of the data assimilation system. *Quart. J. Roy. Meteor. Soc.*, **137**, 553–597, <https://doi.org/10.1002/qj.828>.
- Duvel, J.-P., 2015: Initiation and intensification of tropical depressions over the southern Indian Ocean: Influence of the MJO. *Mon. Wea. Rev.*, **143**, 2170–2191, <https://doi.org/10.1175/MWR-D-14-00318.1>.
- Emanuel, K., 1988: The maximum intensity of hurricanes. *J. Atmos. Sci.*, **45**, 1143–1155, [https://doi.org/10.1175/1520-0469\(1988\)045<1143:TMIOH>2.0.CO;2](https://doi.org/10.1175/1520-0469(1988)045<1143:TMIOH>2.0.CO;2).
- , and D. Nolan, 2004: Tropical cyclone activity and the global climate system. Preprints, *26th Conf. on Hurricanes and Tropical Meteorology*, Miami, FL, Amer. Meteor. Soc., 240–241.
- Gray, W. M., 1975: Tropical cyclone genesis. Atmospheric Science Paper 234, Colorado State University, 121 pp.
- Haarsma, R., and Coauthors, 2016: High Resolution Model Intercomparison Project (HighResMIP v1.0) for CMIP6. *Geosci. Model Dev.*, **9**, 4185–4208, <https://doi.org/10.5194/gmd-9-4185-2016>.
- Held, I., and M. Zhao, 2011: The response of tropical cyclone statistics to an increase in CO₂ with fixed sea surface temperatures. *J. Climate*, **24**, 5353–5364, <https://doi.org/10.1175/JCLI-D-11-00050.1>.
- Hersbach, H., and Coauthors, 2018: Operational global reanalysis: Progress, future directions and synergies with NWP. ERA Rep. Series 27, 65 pp, <https://doi.org/10.21957/tkic6g3wm>.
- Holland, G., and C. Bruyère, 2014: Recent intense hurricane response to global climate change. *Climate Dyn.*, **42**, 617–627, <https://doi.org/10.1007/s00382-013-1713-0>.
- Knapp, K., M. Kruk, D. Levinson, H. Diamond, and C. Neumann, 2010: The International Best Track Archive for Climate Stewardship (IBTrACS). *Bull. Amer. Meteor. Soc.*, **91**, 363–376, <https://doi.org/10.1175/2009BAMS2755.1>.
- Knutson, T., and Coauthors, 2010: Tropical cyclones and climate change. *Nat. Geosci.*, **3**, 157–163, <https://doi.org/10.1038/ngeo779>.
- , J. Sirutis, M. Zhao, R. Tuleya, M. Bender, G. Vecchi, G. Villarini, and D. Chavas, 2015: Global projections of intense tropical cyclone activity for the late twenty-first century from dynamical downscaling of CMIP5/RCP4.5 scenarios. *J. Climate*, **28**, 7203–7224, <https://doi.org/10.1175/JCLI-D-15-0129.1>.
- Kossin, J., 2018: A global slowdown of tropical-cyclone translation speed. *Nature*, **558**, 104–107, <https://doi.org/10.1038/s41586-018-0158-3>.
- , T. Olander, and K. Knapp, 2013: Trend analysis with a new global record of tropical cyclone intensity. *J. Climate*, **26**, 9960–9976, <https://doi.org/10.1175/JCLI-D-13-00262.1>.
- Kuleshov, Y., R. Fawcett, L. Qi, B. Trewin, D. Jones, J. McBride, and H. Ramsay, 2010: Trends in tropical cyclones in the South Indian Ocean and the South Pacific Ocean. *J. Geophys. Res.*, **115**, D01101, <https://doi.org/10.1029/2009JD012372>.
- Malan, N., C. Reason, and B. Loveday, 2013: Variability in tropical cyclone heat potential over the Southwest Indian Ocean. *J. Geophys. Res. Oceans*, **118**, 6734–6746, <https://doi.org/10.1002/2013JC008958>.
- Menkes, C., M. Lengaigne, P. Marchesio, N. Jourdain, E. Vincent, J. Lefèvre, F. Chauvin, and J.-F. Royer, 2012: Comparison of tropical cyclogenesis indices on seasonal to interannual time-scales. *Climate Dyn.*, **38**, 301–321, <https://doi.org/10.1007/s00382-011-1126-x>.
- Murakami, H., and Coauthors, 2012: Future changes in tropical cyclone activity projected by the new high-resolution MRI-AGCM. *J. Climate*, **25**, 3237–3260, <https://doi.org/10.1175/JCLI-D-11-00415.1>.
- Peng, M., B. Fu, T. Li, and D. Stevens, 2012: Developing versus nondeveloping disturbances for tropical cyclone formation. Part I: North Atlantic. *Mon. Wea. Rev.*, **140**, 1047–1066, <https://doi.org/10.1175/2011MWR3617.1>.
- Rayner, N. A., D. Parker, E. Horton, C. Folland, L. Alexander, D. Rowell, E. Kent, and A. Kaplan, 2003: Global analyses of sea surface temperature, sea ice, and night marine air temperature since the late nineteenth century. *J. Geophys. Res.*, **108**, 4407, <https://doi.org/10.1029/2002JD002670>.
- Royer, J.-F., and F. Chauvin, 2009: Response of tropical cyclogenesis to global warming in an IPCC AR4 scenario. *Hurricanes and Climate Change*, J. Elsner and T. Jagger, Eds., Springer, 213–234, https://doi.org/10.1007/978-0-387-09410-6_12.
- , —, B. Timbal, P. Araspin, and D. Grimal, 1998: A GCM study of the impact of greenhouse gas increase on the frequency of occurrence of tropical cyclones. *Climatic Change*, **38**, 307–343, <https://doi.org/10.1023/A:1005386312622>.
- Sugi, M., H. Murakami, and J. Yoshimura, 2012: On the mechanism of tropical cyclone frequency changes due to global warming. *J. Meteor. Soc. Japan*, **90A**, 397–408, <https://doi.org/10.2151/JMSJ.2012-A24>.
- Taylor, K., R. Stouffer, and G. Meehl, 2011: An overview of CMIP5 and the experiment design. *Bull. Amer. Meteor. Soc.*, **93**, 485–498, <https://doi.org/10.1175/BAMS-D-11-00094.1>.
- Tippett, M., S. Camargo, and A. Sobel, 2011: A Poisson regression index for tropical cyclone genesis and the role of large-scale vorticity in genesis. *J. Climate*, **24**, 2335–2357, <https://doi.org/10.1175/2010JCLI3811.1>.
- Voldoire, A., and Coauthors, 2013: The CNRM-CM5.1 global climate model: Description and basic evaluation. *Climate Dyn.*, **40**, 2091–2121, <https://doi.org/10.1007/s00382-011-1259-y>.
- , and Coauthors, 2019: Evaluation of CMIP6 DECK experiments with CNRM-CM6-1. *J. Adv. Model. Earth Syst.*, **11**, 2177–2213, <https://doi.org/10.1029/2019MS001683>.
- Walsh, K., and Coauthors, 2016: Tropical cyclones and climate change. *Wiley Interdiscip. Rev.: Climate Change*, **7**, 65–89, <https://doi.org/10.1002/WCC.371>.
- Wehner, M., Prabhat, K. A. Reed, D. Stone, W. D. Collins, and J. Bacmeister, 2015: Resolution dependence of future tropical cyclone projections of CAM5.1 in the U.S. CLIVAR Hurricane working group idealized configurations. *J. Climate*, **28**, 3905–3925, <https://doi.org/10.1175/JCLI-D-14-00311.1>.
- Woodruff, J., J. Irish, and S. Camargo, 2013: Coastal flooding by tropical cyclones and sea-level rise. *Nature*, **504**, 44–52, <https://doi.org/10.1038/nature12855>.



ReNovRisk: a multidisciplinary programme to study the cyclonic risks in the South-West Indian Ocean

Pierre Tulet¹ · Bertrand Aunay² · Guilhem Barruol^{3,4} · Christelle Barthe¹ · Remi Belon² · Soline Bielli¹ · François Bonnardot⁵ · Olivier Bousquet¹ · Jean-Pierre Cammas^{1,6} · Julien Cattiaux⁷ · Fabrice Chauvin⁷ · Idriss Fontaine⁸ · Fabrice R. Fontaine^{3,9} · Franck Gabarrot⁶ · Sabine Garabedian⁸ · Alicia Gonzalez^{3,4} · Jean-Lambert Join³ · Florian Jouvenot¹⁰ · David Nortes-Martinez⁸ · Dominique Mékiès¹ · Pascal Mouquet¹⁰ · Guillaume Payen⁶ · Gwenaëlle Pennober¹⁰ · Joris Pianezze¹ · Claire Rault² · Christophe Revillion¹⁰ · Elisa J. Rindraharisaona^{3,4} · Kevin Samyn² · Callum Thompson¹ · Hélène Vérémes^{1,6}

Received: 13 October 2020 / Accepted: 3 February 2021 / Published online: 10 March 2021
© The Author(s) 2021

Abstract

Today, resilience in the face of cyclone risks has become a crucial issue for our societies. With climate change, the risk of strong cyclones occurring is expected to intensify significantly and to impact the way of life in many countries. To meet some of the associated challenges, the interdisciplinary ReNovRisk programme aims to study tropical cyclones and their impacts on the South-West Indian Ocean basin. This article is a presentation of the ReNovRisk programme, which is divided into four areas: study of cyclonic hazards, study of erosion and solid transport processes, study of water transfer and swell impacts on the coast, and studies of socio-economic impacts. The first transdisciplinary results of the programme are presented together with the database, which will be open access from mid-2021.

Keywords Tropical cyclone · Cyclonic hazards · Interdisciplinary programme · Indian Ocean

1 Introduction

The South-West Indian Ocean (SWIO) is the second-to-third most active tropical cyclone basin in the world. Approximately 10%–12% of the world's total cyclonic activity takes place in the SWIO, where two regions are particularly involved: the Mozambique Channel and the open ocean east of Madagascar (Neumann et al. 1993). Mavume et al. (2008) and Leroux et al. (2018) confirmed this high activity and showed that the basin has an annual average of 9 to 10 tropical storms, half of which develop into

✉ Pierre Tulet
pierre.tulet@univ-reunion.fr

Extended author information available on the last page of the article

tropical cyclones (TC). Particularly intense TCs have developed in this part of the world recently. Very Intense Tropical Cyclone (VITC, WMO (2016), maximum of the average wind speed greater than 60 m s^{-1} ; Hellen (2014)) and Intense Tropical Cyclone (ITC, maximum of the average wind speed between 46 and 59 m s^{-1} ; Kenneth (2020)) were the two most intense tropical cyclones ever observed in the Mozambique Channel. More recently, ITC Idai (2019) caused more than 1000 deaths in Mozambique. VITC Fantala (2016) was the second most intense tropical cyclone ever recorded in the whole basin and devastated the Farquhar archipelago of the Seychelles. VITC Gafilo (2004) made landfall first on the north-eastern region of Madagascar and then on its south-western part, affecting more than 200 000 people and killing more than 350. In 2017, ITC Enawo also landed in North-East Madagascar and killed ~ 50 people (more than 300 000 people affected).

Two essential elements make the SWIO particularly sensitive to cyclonic risks. The first is large number of developing countries with fragile infrastructures and food and water supply systems, where a significant proportion of the population is living in extreme poverty. The second is due to the topography of some regions in the basin. Several islands of volcanic origin have steep slopes that locally reinforce convection, wind channelling effects and precipitation. Reunion Island, for instance, lays claim to several world records for cumulative rainfall: 1.1 m and 1.8 m over 12 h and 24 h, respectively, for TC Denise in 1966 (Holland 1993), and 3.9 m and 4.9 m over 72 h and 96 h, respectively, for TC Gamède in 2007 (Quetelard et al. 2007). Its orography has been shown to significantly influence the track and intensity of TCs passing nearby (Barbary et al. 2019). Terry et al (2013) also showed that in January and February a large proportion of storms in the SWIO had curving and sinuously moving trajectories. This track sinuosity is found to increase the storm longevity and the difficulties in forecasting, which reinforce the exposure of the territories.

Such intense precipitation generates landslides, ground movements and flash floods. In general, following the passage of a cyclone, several hundreds of landslides can impact the infrastructures (more than 200 landslides, rock falls or erosion phenomena were counted during TC Berguita (2018) in Reunion Island (Aunay et al. 2018)). Sudden slope collapses and accelerations of slow-moving landslides are driven by the duration and intensity of precipitation (e.g. Caine 1980; Iverson 2000). Beyond the number of landslides, the moving masses involved can be considerable: two landslides of over 350 Mm^3 each, in the Salazie area of Reunion Island, move up to 1 m per year and more than 1,000 people live directly on their surfaces (Belle et al. 2014).

In some regions of Mozambique and Madagascar, which have vast plains or highlands as well as catchment areas sensitive to flooding, the impact of cyclonic rainfall can be particularly tragic. In 2019, for instance, floods caused by the landfall of TC Idai affected more than 2.6 million people in Mozambique, Malawi and Zimbabwe, with a devastating cost in human lives (more than 1000 deaths and 2450 persons declared missing), as well as significant economic damage (2 billion dollars estimated in 2019). Furthermore, TCs induce indirect economic impacts—both in time and space, and throughout the different levels of the economic fabric—whose magnitudes may compete with direct ones (Camargo and Hsiang 2015; Meyer et al. 2013). Such phenomena are especially relevant in the context of the SWIO insofar as the combination of both kinds of economic impacts has the potential to compromise a given country's long-term capacity to grow and develop (Hsiang and Jina 2014).

Regarding the strong impact of cyclonic hazards on lives and territories of the SWIO, a crucial question arises concerning the evolution of this risk with climate change. One

key aspect is the expected increase in ocean temperatures, future projections for which are described by the Intergovernmental Panel for Climate Change (IPCC). According to their scenario RCP8.5 describing "business-as-usual" high emissions, CMIP5 and CMIP6 climate models (i.e. those in the Coupled Model Intercomparison Project Phases 5 and 6) predict a global average increase in ocean surface temperatures of 2.6 °C–4.8 °C by 2100 (ICCP, 2013). In the SWIO basin, this increase could exceed 4 °C in the northern Mozambique Channel and have the direct consequence of significantly increasing the energy available for TCs. Associated with this temperature evolution, the tropical band delineated by the seasonal displacement of the inter-tropical convergence zone is expanding by 0.25°–0.5° latitude per decade (Lu et al. 2009; Staten et al. 2018, 2020). This expansion significantly widens the geographical zones conducive to cyclogenesis and thus increases the potential for cyclonic impacts on territories that are currently at low risk. It also affects the evolution of cyclone intensity. Kosin et al. (2014) highlight a year-on-year poleward shift in the latitude at which cyclones reach their lifetime maximum intensity. More recently, based on an analysis of 39 years of data, Kosin et al. (2020) have shown an 8% increase per decade in the occurrence of the most intense cyclones (categories 3–5 on the Saffir–Simpson scale).

High-resolution numerical modelling studies that re-simulate historical cyclones using projected future climates also point to an increase in cyclone risk. Most studies highlight an increase in intensity of the order of 10 hPa and an increase in precipitation of 15%–27% (Lackmann 2015; Parker et al. 2018; Mittal et al. 2019). However, to date, no regional or mesoscale studies have been carried out to study the climatic evolution of cyclone hazard in the SWIO basin.

With regard to future cyclone risk, in its AR5 report of 2014 (Impacts, Adaptation and Vulnerability, <https://www.ipcc.ch/report/ar5/wg2/>), the IPCC recommends (i) strengthening early warning capabilities, (ii) developing cyclone and flood shelters, (iii) improving building codes and practices, (iv) strengthening transport systems and road infrastructure, and (v) developing rainwater and wastewater management.

In response to some of these challenges, the ReNovRisk programme (REunion NOvative research on cyclonic RISks, € 6 M) was launched in 2017. It is funded by the European Union (FEDER and INTER-REG5 funds), Région Reunion, the French government (CPER funds), the BRGM (French Geological Survey), and the CNRS (French National Centre for Scientific Research). ReNovRisk is developing an integrated study of the various risks associated with tropical cyclones in the SWIO basin by integrating mapping and economic analysis of the damage.

Coordinated by the Université de La Reunion, BRGM and IRD (French Research Institute for Development), ReNovRisk brings together a large consortium of research laboratories and scientific institutes from several countries in the western Indian Ocean, including France, Madagascar, the Seychelles, Mozambique, and Mauritius. Drawing on this wide pool of resources and expertise, the objectives of the ReNovRisk programme are multiple: (i) to improve observations and numerical forecasting systems for tropical cyclones in the SWIO, (ii) to study the cyclonic risks associated with winds, rainfall, ground movements, floods, submersion and swell over several target regions, and (iii) to develop a methodology suited to the SWIO that can estimate the direct and indirect economic costs associated with cyclonic damage.

This article is intended to present an overview of the ReNovRisk programme by detailing the presentation and strategy of its sub-programmes (Sect. 2). Some preliminary results from the various sub-programmes are presented in Sect. 3, and the ReNovRisk open databases are described in Sect. 5.

2 Organization and strategy of ReNovRisk programmes

The ReNovRisk programme is divided into four interactive sub-programmes (Fig. 1). ReNovRisk-Cyclone (RNR-C) is divided into two components referred to as “Cyclones and Climate Change” and “Cyclones and Precipitation”. It aims to (i) improve the spatial coverage of TC observations over the SWIO, (ii) develop high-resolution TC forecasting models and (ii) analyse future TC activity at both basin and local scale from high-resolution climate and mesoscale simulations. The RNR-C outputs feed the other ReNovRisk programmes with swell fields, high-resolution winds and precipitation and also climate projections on the intensity and occurrence of cyclones. The aim of ReNovRisk-Erosion (RNR-E) is to study landslides, floods and solid transport in two sensitive catchment areas of Reunion Island. ReNovRisk-Transfer (RNR-T) analyses the transfer and connection of cyclonic risks across the western volcanic plateau of Reunion Island, which slopes down through temporary semi-urbanized ravines (flood risks) to the coastline of either the ocean or the back reef lagoon (risks of sediment transport, erosion, and submersion). RNR-T also provides other ReNovRisk programmes with high-resolution maps of rainfall over Reunion Island. ReNovRisk-Impacts (RNR-I) aims at mapping and analysing the economic vulnerability of, and the damage caused by TC in Reunion Island and Madagascar. Furthermore, RNR-I also approaches societal impacts of TC. The geographic area of the ReNovRisk programmes is shown in Fig. 2.

2.1 ReNovRisk-cyclone (RNR-C)

Given the colossal impact of TCs on local populations, infrastructures and economic development in the SWIO, it is essential to improve the prediction of cyclonic events at all spatial and temporal scales in order to adapt public development policies to the present and future risks faced by the territories. In this respect, research work carried out in recent decades has significantly improved the prediction of TCs at all time scales (DeMaria et al. 2014). The advent of coupled ocean–atmosphere models, in particular, constitutes a major step forward in assessing the impact of cyclonic activity at the

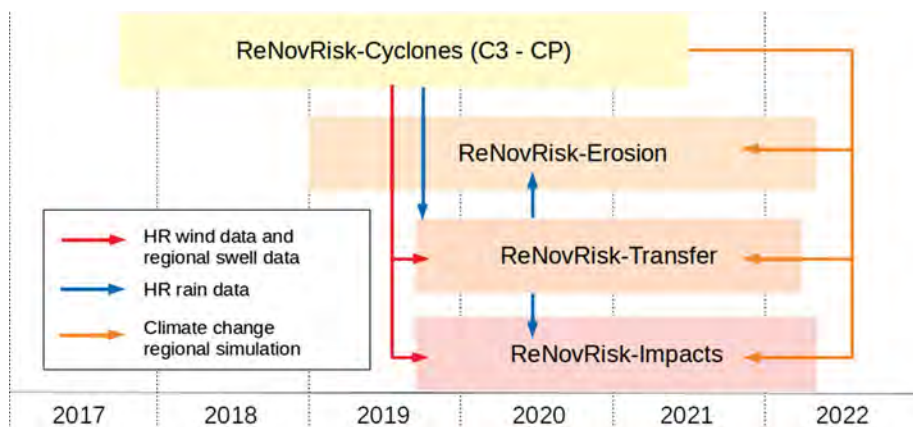


Fig. 1 Scheme of development times of the various ReNovRisk sub-programmes and data-feeding links between them

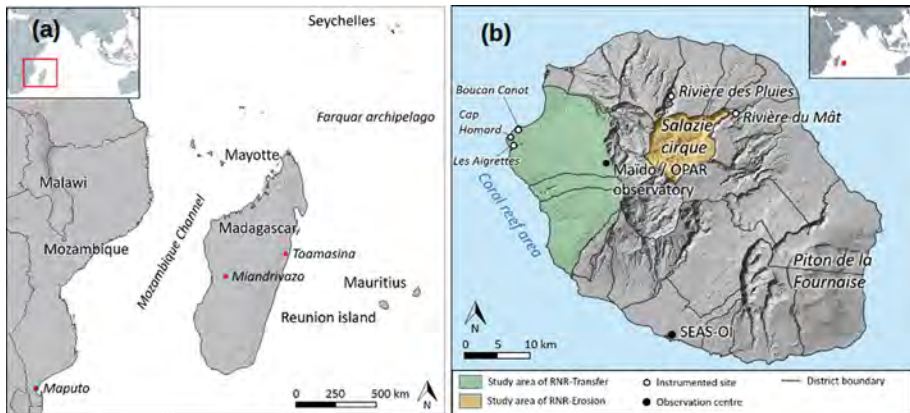


Fig. 2 Geographic area of the ReNovRisk programmes. **a** SWIO domain of ReNovRisk. **b** Reunion Island map and locations cited in the text

regional level (e.g. Eyring et al. 2016; Vitart et al. 2017). Nevertheless, it is commonly agreed that current models do not yet have the technicality and sophistication required to accurately assess the impact of TCs at the local scale.

Coupled numerical weather prediction (NWP) and climate models also require extensive observations to constrain and thoroughly assess the performance of their atmospheric and oceanic components. Because TCs develop, evolve and propagate primarily over oceanic areas, which are generally poorly equipped with conventional observing systems, collecting observations in TC basins can be extremely difficult. Due to the small proportion of land masses and also to the difficulties of sustainably operating observation systems in this poor area, the SWIO is the least instrumented of the six TC basins. Although satellite imagery has now made it possible to track the trajectories and general evolution of TCs all around the world, additional measurements are still urgently needed to study the mechanisms governing the evolution and impacts of low-pressure tropical systems in this particularly active basin.

In this respect, RNR-C has been built along three principal lines:

- An observation component, aimed at providing additional TC observations to calibrate, initialize and evaluate the performance of coupled models in this particularly under-instrumented region;
- A modelling component, aiming at developing a coupled, high-resolution (0.5 km–2 km), ocean–wave–atmosphere modelling system to represent the interactions between a TC and its environment as exhaustively as possible;
- A climate component, aiming at assessing the consequences of climate change on the properties (trajectories, intensity and structure) and potential impacts of tropical cyclones at both local and basin scales.

2.1.1 Observations

The observation component of RNR-C aims to provide accurate observations of TCs and their environments by reinforcing regional- and local-scale observing capabilities in the SWIO. To achieve this objective, RNR-C was built around three approaches.

The first is a conventional and ideally sustainable approach, based on the deployment of regional observation networks and the acquisition of new satellite observations of wind and sea swell in the SWIO. Regarding ground-based observations, a water vapour observing network composed of Ground-based Navigation Satellite System (GNSS) receivers and weather stations was deployed throughout the western part of the basin from November 2017 to September 2020 within the framework of the RNR-C's sub-programme "Indian Ocean GNSS Applications for Meteorology" (IOGA⁴MET). This important achievement has significantly enhanced water vapour observation capabilities in the SWIO and provides a new tool to thoroughly investigate the water vapour cycle in this area (Lees et al. 2020; Bousquet et al. 2020a).

Regarding space-borne observations, a collaboration with ESA (European Space Agency) and IFREMER (Institut Français de Recherche pour l'Exploitation de la MER) has enabled a unique set of high-resolution (1 km) satellite images of sea surface wind and roughness to be collected from synthetic aperture radars (SAR) deployed onboard the Sentinel 1A/1B satellites of the European Earth Observation programme Copernicus. Throughout 2018 to 2020, SAR data have been acquired on demand (with 48 h notice) for about two-thirds of the TCs that developed in the basin over this period. (About one hundred images were collected, nearly half of which were acquired in the eye-wall regions of TCs and tropical storms.)

The second, an experimental approach, is based on the temporary deployment of various atmospheric and oceanic observation systems at different points in the basin. Several temporary atmospheric and oceanographic observing campaigns have been organized to validate the performance of coupled ocean–wave–atmosphere systems developed within the RNR-C programme (Sect. 2.1.2) the main achievement of which has been the organization of a regional field campaign that took place in various places of the SWIO from January 21 to April 8, 2019. During this field experiment, various sensors were deployed in and around Reunion Island, and in Madagascar, Mozambique, and Mayotte, to sample atmospheric and oceanic environmental conditions during the 2018–2019 TC season. A regional radiosonde network (RS) was deployed in Mayotte (France), Toamasina (Madagascar), and Maputo (Mozambique), enabling 700 soundings to be collected over this 2 ½-month period. Two ocean gliders were launched from Reunion Island to sample the thermodynamic properties of the tropical Indian Ocean up to 500 km from the island. An unmanned airborne system (UAS <https://www.borea-l-uas.com/>), equipped with high-frequency aerosol, wind, and temperature sensors, was deployed for several weeks to measure ocean–atmosphere fluxes and aerosol concentrations in the immediate environment of TCs up to several hundred km from Reunion Island.

The third, an exploratory approach, is based on the deployment and evaluation of new and original methods of investigation to collect oceanic observations in the SWIO from biologging and seismic observations. A particularly original approach, based on biologging technology, has been explored to collect oceanic data from sea turtles equipped with autonomous environmental tags. A first experiment was carried out from January 2019 to September 2020 in the western part of the tropical Indian Ocean, with

the aim of assessing the relevance of low-cost sea turtle borne observations for ocean monitoring and modelling (Bousquet et al. 2020c). Another original approach, based on previous work by Davy et al. (2014, 2016) and Barruol et al. (2016), was also further investigated to evaluate and quantify extreme swell events from microseismic noise measurements recorded by ground-based and underwater seismometers. The analysis of data collected in RNR-C (Rindraharisaona et al. 2020) has demonstrated that terrestrial seismic stations could also be a great alternative for sampling Austral swell events by behaving as ground-based wave gauges.

2.1.2 Mesoscale modelling: improvement of mesoscale numerical models for TC forecasting

An important objective of RNR-C is to design, develop, and evaluate a high-resolution (0.5 km– 2 km) integrated modelling system based on the coupling of state-of-the-art atmosphere, ocean, and wave models. This tool, intended to prefigure fine-scale operational NWP systems to be used by WMO/RSMC Reunion (<http://severeweather.wmo.int>) in the medium term, will, in particular, investigate the internal physical processes responsible for TC intensification and produce realistic TC simulations over the most densely populated regions of the SWIO basin.

Based on the conceptual model of a tropical cyclone as a Carnot heat engine, the theory formulated by Emanuel (1986, 1988) predicts that the maximum potential intensity depends on the sea surface temperature and the outflow layer air temperature (Bister and Emanuel, 2002). In this context, an ocean–wave–atmosphere (OWA) coupled system has been developed for high-resolution modelling of tropical cyclones in the SWIO (Fig. 3). The coupling between the atmospheric model Meso-NH (<http://mesonh.aero.obs-mip.fr/>, Lac et al. 2018), the surface model SurfEX (<https://www.umr-cnrm.fr/surfex/>, Masson

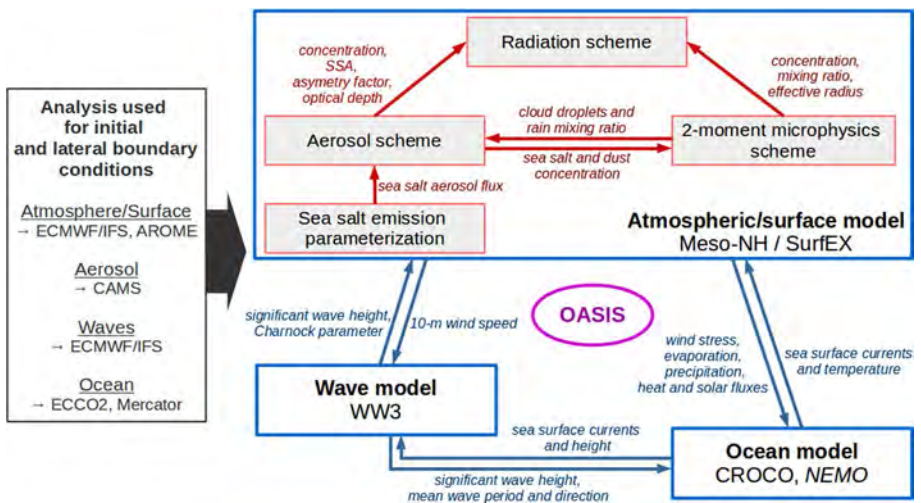


Fig. 3 Schematic diagram of the coupling systems in cyclone numerical modelling. The OWA coupling is shown in blue while the coupling inside the atmosphere/surface model is shown in red. Fields exchanged among the atmospheric, wave, and oceanic models are shown in blue italics; they are exchanged at intervals defined by the user (typically ~ 10 min). Fields exchanged among the atmospheric schemes are shown in red italics; they are exchanged at each time step

et al. 2013), the wave model WaveWatch III (<http://polar.ncep.noaa.gov/waves/wavewatch/>) and the ocean model CROCO (<http://www.croco-ocean.orgref>) was realized through the OASIS coupler (<https://portal.enes.org/oasis>, Craig et al. 2017) as described by Voldoire et al. (2017) and Pianezze et al. (2018). This coupled system is particularly innovative since it enables the user to represent (i) the air–sea interactions, which have long been recognized as a key issue in improving the accuracy of tropical cyclone intensity (e.g. Rotunno and Emanuel, 1987), (ii) the swell generated by the strong winds, and (iii) the sea salt aerosol emissions induced by the combined effects of strong winds and waves (Andreas et al. 1995). In non-polluted environments, these sea salt aerosols are the main source of condensation nuclei for cloud formation. A parameterization of such aerosol emission as a function of atmospheric, oceanic, and wave parameters (Ovadnevaite et al. 2014) has been introduced in the atmospheric/surface model. Once emitted, these aerosols are integrated in the ORILAM aerosol scheme (Tulet et al. 2005): they are transported by advection and turbulence and can be lost by sedimentation, and dry or wet deposition. The aerosol scheme was then coupled with the two-moment bulk microphysics scheme LIMA (Vié et al. 2016) as described in Hoarau et al. (2018a). Since cloud–radiation interactions are suspected to influence the track (Fovell et al. 2016), the structure (Bu et al. 2014) and the intensity (Trabing et al. 2019) of a tropical cyclone, specific developments on the secondary formation, and habits of ice crystals (Hoarau et al. 2018b) in the LIMA microphysics scheme are in progress. This will enable a better description of the ice water content, the ice crystal effective radius and the ice crystal shape, which are used as input for the radiation scheme. Attention has also been paid to initial and lateral boundary conditions for each component (atmosphere, surface, aerosol, wave and ocean) of the coupled system (see the box on the left in Fig. 3). This coupled system can be viewed as a prototype for the French operational model AROME. It has been run on several tropical cyclones (Bejisa, 2014; Fantala, 2016; Berguitta, 2018; Idai, 2019) to produce high-resolution precipitation, wind and wave fields all over the SWIO, and deliver some of these fields to the other sub-programmes.

2.1.3 Climate modelling

While it is generally accepted that global warming will have a significant impact on ocean surface temperatures, which is a factor favouring the development of TCs, no one really knows how the other ingredients involved in the formation of tropical low-pressure systems will evolve in the future. While disaster scenarios suggest an increase in intense events, some scenarios also suggest a "benevolent nature" that could counteract this pessimistic trend. In this respect, a key objective of RNR-C is to assess the consequences of climate change on the properties and potential impacts of tropical cyclones in the SWIO basin. The experimental strategy is based on two complementary approaches: (i) the use of high-resolution global and regional climate simulations to estimate the evolution of cyclonic activity at basin scale (changes in TC trajectory, intensity and structure; impact on water resources) and (ii) the use of high-resolution mesoscale coupled simulations to assess the potential impact of climate change on the structure and the impacts of TC in specific target areas such as Reunion Island.

To address this issue, high-resolution (~ 20 km–25 km) global climate simulations found with the French climate model ARPEGE-Climat (<https://www.umr-cnrm.fr/spip.php?article124&lang=en>) have been run to assess the impact of climate change on the frequency, distribution and, to a lesser extent, intensity of future tropical cyclones (Cattiaux et al. 2020). Higher-resolution simulations have also been carried out using the limited-area

climate model ALADIN-Climat and the integrated OWA model developed in the programme (Fig. 3) to analyse the response of TC to climate change in terms of structural development and determine whether changes in storm activity and/or structure will pose an additional threat to coastal areas and islands of the SWIO basin in the future (Thompson et al. submitted). The first results obtained from the analysis of the various simulations carried out in the programme are presented in Sect. 3.5.

2.2 ReNovRisk-erosion (RNR-E)

Among the impacts of cyclones landing on Reunion Island, hydrological floods, sediment fluxes and erosional processes are causes of major concern to population and infrastructures. The hydrological regime of the island's rivers stands out for the coexistence of several major parameters that predispose it to extreme vulnerability. Holding almost all the world records for rainfall between 12 h (1170 mm) and 15 days (6083 mm), the island presents a very marked relief with a peak at 3,069 m, exceptional escarpments up to 1500 m in height and having an average slope of over 70°, and very steep natural valleys and cirques. As a result, all the processes that can lead to erosion and ground movements are particularly active in Reunion Island.

The objective of the sub-programme RNR-E falls within this major issue regarding forecasting of and protection against torrential floods. Liébault et al. (2010) point out that the characterization of erosion and sediment transport in Reunion Island rivers requires better knowledge of the hydrological-hydraulic and geomorphological processes that control the production and transfer of liquid and solid flows.

To meet this target, RNR-E involves the monitoring and data acquisition at various scales of two representative hydrological catchment areas on Reunion Island: Salazie cirque and Rivière des pluies (Fig. 2b). New instrumentation has been set up in the aim of analysing and quantifying the interactions between upstream and downstream in the following processes:

- Formation of the sedimentary stock: this is linked to erosion phenomena in the upstream parts of the catchment areas and to gravity destabilization (in particular rampart collapses and landslides). GNSS, a network of geodetic markers, LiDAR and seismic surveys are being implemented on the six major large-scale landslides in the Salazie cirque and in the Rivière des Pluies watershed. We are also carrying out hydrological, hydrogeological and geochemical monitoring of groundwater and surface water at the level of these landslides. In addition, the structure from motion technique has been applied using historical aerial images, image correlation techniques and SAR interferometry to characterize landslide dynamics.
- Flow processes: completing the hydrological monitoring equipment of the experimental catchment “La Rivière des Pluies”, which is part of the French OZCAR network (<https://www.ozcar-ri.org/observatories/the-network/>), RNR-E proposes to detail the variability of the contribution of tributaries to the flash flood processes. Specific photogrammetric discharge monitoring stations are used in order to document an accurate rainfall–runoff model (Stumpf et al. 2016).
- Bedload transport: as direct measurements of the bedload transport are extremely difficult to make during a tropical cyclone, RNE-E uses the high-frequency seismic noise generated by the rivers as a proxy for the sediment transport. Eleven broadband seismometers have been deployed along two rivers, both located in the northern side of the

island (Rivière des Pluies and Rivière du Mât, Fig. 2b), in the framework of the “Rivière des Pluies” temporary seismic network (Fontaine et al. 2015). This has allowed us to analyse the spatial and temporal variations of the seismic noise along these rivers with respect to the rainfall and hydrological data, and to characterize the bedload variations during tropical storms and cyclones (Gonzalez et al. 2017; Gonzalez 2019; Gonzalez et al. submitted). A very good correlation was obtained between the seismic noise amplitude and the water level during the river flood related to TC Dumazile in March 2018 (Gonzalez 2019; Gonzalez et al. submitted). Preliminary results show that the amplitude of the high-frequency seismic signal (> 1 Hz) recorded at the seismometers may be used as a proxy for the water level during a cyclone. Spectral and polarization analyses of seismic data were also used in order to decipher the seismic signature of water flow and bedload transport.

Firstly, it was shown that the behaviour of landslides can be modelled by inverse models with a bimodal transfer function using a Gaussian-exponential impulse response, linked to the rain and piezometric level (Belle et al. 2014). Then, the recharge of the large Grand Ilet landslide (350 Mm^3) in the humid tropical season was characterized through a robust, multidisciplinary hydrological approach, notably comprising a precise water budget of the landslide. It appears that surface processes play a major role in the landslide recharge regime (Belle et al. 2018).

Then, landslide displacement mapping based on ALOS-2/PALSAR-2 data using image correlation techniques and SAR interferometry was applied to the Hell-Bourg landslide (Raucoules et al. 2018). The capability of space-borne high-resolution L-band synthetic aperture radar (SAR) images (ALOS-2/PALSAR2 data in StripMap SM1 mode) for deriving and mapping two components of the deformation of slow landslides has been investigated. The deformation was characterized on the basis of sub-pixel correlation offset tracking techniques and differential SAR interferometry. On the Hell-Bourg landslide (Fig. 2b, with displacements up to about 1 m year^{-1}), the deformation maps produced performed significantly better than the C-band or lower-resolution SAR data used in previous studies. A comparison was carried out with GNSS data acquired on the test site. Even with a reduced image set (seven acquisitions), detailed deformation maps and information on deformation evolution during 2014–2016 could be generated.

Finally, RNR-E has implemented a new methodology based on structure-from-motion processing of archive aerial photographs to quantify geomorphological changes in Reunion Island since 1978 (Rault et al. 2020). Photographic archives indeed hold a decades-long 3D history and, for the first time, our measurements reveal the cumulated signature of landslides on the Cirque de Salazie from 13 cyclones over the 37 years investigated. Such an approach demonstrates that the structure-from-motion technique is a game changer for landslide risk mitigation planning.

Most of the acquisition of the data presented above is still ongoing (as of September 2020) and is ready for the next cyclonic event in Reunion Island.

2.3 ReNovRisk-transfer (RNR-T)

RNR-T focuses specifically on the study of cyclonic hazard transfer in natural environments. It focuses on the natural risks associated with cyclones landing on Reunion Island and more specifically on the western micro-region, taking its workshop area as the Maïdo massif, the coastal strip between Saint-Paul and Saint-Leu, the back reef lagoon and the

open ocean, depending on the position along the coast (green area in Fig. 2b). The general objective is to analyse how cyclonic hazards are transferred between the natural environments of the atmosphere, the hydrosphere, the littoral zone and the open ocean. With regard to the transfer from the atmosphere to the hydrosphere and the coastline, the atmospheric hazards are the wind gusts and precipitation associated with cyclonic events. These hazards depend on many factors intrinsic to the cyclone and other factors in relation with the landfall area. Cyclonic winds are, by nature, the most intense in the upper reaches of Reunion Island, an area where the most intense cyclonic precipitation is generally also found. The scientific questions associated with these themes arise at the interfaces of the natural environments.

Between the atmosphere and the hydrosphere, the challenge concerns the quality of the precipitation data that are delivered to hydrologists to initialize hydrological models. Whether the issue is the rainfall observations or the forecasts by numerical models, the difficulties lie in the validation of the quality of the data. The spatial representativeness of rainfall and wind observations is a key factor for studying natural hazards, especially in the complex topographical context of Reunion Island. These scientific questions are being attacked by meteorological observations at the OPAR observatory (<https://opar.univ-reunion.fr/>) using new data fusion and numerical modelling methodologies to produce high-resolution rain and wind data of landfalling TCs over Reunion Island, with a focus on the Maïdo massif.

For this purpose, a numerical modelling method to produce low-cost high-resolution wind fields of landfalling TCs has been developed. To produce wind fields consistent with both the position and intensity of the system, the large-scale environment and the topography of the targeted region, the Meso-NH atmospheric model was implemented with Holland's parametric approach (Holland 1980) coupled with the use of meteorological analysis from the IFS (Integrated Forecasting System) model of ECMWF (European Centre for Medium-Range Weather Forecasts). The parameters used in the Holland formulation are deduced from the RSMC Reunion Island best-track. This so-called bogus method was set up within the framework of the SPICy programme (Système de Prévision des Inondations en contexte Cyclonique, <http://spicy.brgm.fr/fr>) and tested on 5 historical cyclones that affected Reunion Island (Bejisa, Dumile, Felleng, Gamède and Dina). The structure reproduced was shown to be realistic as long as the information on the radius of the maximum winds injected into the bogus was relevant. The wind fields reconstructed by the bogus method showed good agreement with in situ observations as soon as the orography of the island was well reproduced. This method was deployed in the framework of the ReNovRisk programme (Vérèmes 2020, Technical Report). To date, high-resolution wind fields of 6 tropical cyclones at landfall on Madagascar and Reunion Island have been produced. 10 m wind gusts were provided at a horizontal resolution of 500 m on Reunion Island for Dina (2002), Berguitta (2018) and Bejisa (2014), and on Madagascar for Enawo (2017). A horizontal resolution of 2 km was used on Madagascar for Gafilo (2004) and Ava (2018). This approach enables us to produce high-resolution wind fields at low numerical cost. It should be noted that this tool does not permit the precipitation fields to be produced since the rainbands are not reproduced by the bogus method.

Additionally, the operational product ANTILOPE (ANalyse par spaTiaLisation hOraire des PrÉcipitations) archived by the French meteorological office (Météo-France) has been implemented over Reunion Island. ANTILOPE estimates the quantity of rainfall at the scale of a 1 km²-grid from radar data corrected by rainfall data (Laurantin 2008). The archived product is calculated for a 1-h time step. It is a hybrid product of the PANTHERE quantitative precipitation estimate (QPE) (Parent du Châtelet et al. 2005) and a kriging

interpolation of the rain gauges available at the time of QPE (Pauthier et al. 2016). The variation of the radar reflectivity over the hour is analysed for each pixel of 1 km² and in steps of 5 min. This variation automatically associates a fraction of the current hour with a convective rainfall (between 0 and 60 min) and its complementary fraction to a stratiform rainfall. The stratiform part is obtained by kriging the large-scale rainfall values, whereas the convective part is obtained by detecting cells on the radar images and is corrected using the convective accumulations of the rain gauges located under these cells. The ANTILOPE data were not produced and archived by Météo-France until 2016. However, for Reunion Island, the PANTHERE rain data have been available since the end of 2013, so a reprocessing of the ANTILOPE data over the 2014–2019 period for Reunion Island is possible. ANTILOPE almost fully corrects the underestimation of the precipitation obtained from PANTHERE (Fig. 4). Within the framework of RNR-T, an external service was therefore entrusted to Météo-France to reprocess the entire database for the Reunion Island area. The 15-min time-step ANTILOPE dataset has been generated for the 2014–2019 period with a horizontal resolution of 1 km². It provides a view not only of cyclonic rains but of all rainfall on Reunion Island and will thus make it possible to assess the exceptional nature of past or future events. The ANTILOPE database is also expected to provide input data for econometric models developed by RNR-I.

Along the western slopes of the Maïdo massif, the challenge in the hydrosphere stems from a lack of knowledge of the behaviour of temporary ravines of the Maïdo massif, in particular their disconnection from the underground reservoirs and their very large infiltration capacities at the beginning of the rainy season. Time series of stream flows in these ravines are very sparse and most often uncorrelated with the simultaneous availability of good rainfall series. RNR-T will attack these obstacles, firstly by setting up hydrological instrumentation along two ravines in almost ungauged catchments and, secondly, by using a semi-distributed rainfall–runoff model (Rojas-Serna et al. 2016; De Lavenne et al. 2019). This model has fine spatial resolution (square kilometre) and hourly time steps, suited to the nonlinear behaviour of this type of ravines, and is sequentially calibrated considering

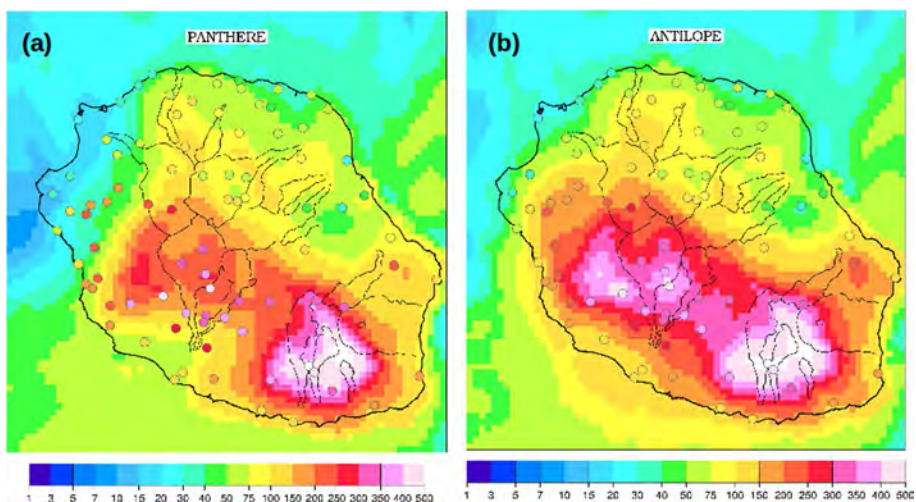


Fig. 4 Cumulative rainfall (mm.day⁻¹) observed on January 1, 2018 during TC Beguitta with PANTHERE **a** and ANTILOPE **b**. Rain gauge data are superimposed (coloured circles)

the observations available at the outlet of the catchment and at different gauging points inside the catchment (De Lavenne et al. 2019).

The Maïdo watershed is characterized on the sea side by the largest fringing reef of Reunion Island (400 m wide). Although the contributions of the watershed are weak on a yearly scale, allowing the development of the reef life, in a cyclonic context the forcing of the watershed, is not negligible. The inputs of fresh water loaded with suspension and nutrients modify the reef environment and can alter the calcification and therefore the growth of the coral. Oceanic forcings (swell) on the reef barrier remove pieces of coral, which can feed the beaches with coral debris. Water masses that submerge the reef barrier and pass through the reef system are the vector of a strong littoral drift. The instrumented site of “La Passe de l’Hermitage” (coral reef area on Fig. 2b) has been set up to quantify the processes and impacts of cyclonic events. The interdisciplinary scientific team in charge of this site is developing tools and indicators to observe, monitor and model the impacts of climate change in the coastal reef zone, and the possible synergy with local anthropogenic pressures. The measurement activity includes (1) monitoring global and local anthropogenic pressures (ocean acidification, freshwater groundwater flow, beach frequentation), and (2) monitoring indicators of beach morphological dynamics and loss of resistance and/or resilience (reproduction and recruitment of scleractinian corals and millepores, carbonate balance), and mapping the trajectories of benthic communities in response to disturbances. These activities are partially approved at the national or international level (SNO Dynalit; <https://www.dynalit.fr/>).

2.4 ReNovRisk-impacts (RNR-I)

The main goal of RNR-I is to assess both the economic vulnerability and the potential economic impacts of cyclones. Such evaluations are intended to serve as decision support tools in policy- and decision-making.

Among the impacts of natural hazards (see, for example Hallegate (2014)), RNR-I will pay special attention to two distinct effects. On the one hand, immediate direct effects, namely the direct monetary costs of destruction/reconstruction due to the damage caused by a TC event, will be considered. On the other hand, indirect long-term effects (belated observable effects caused by the consequences of a TC over the territory) will be studied focusing on i) the macroeconomic repercussions of the aforementioned damage throughout the territory (cross-sectoral effects) and ii) the consequences on socio-economic determinants (e.g. fertility or education).

For direct effects, RNR-I seeks to develop a general protocol largely based on spatialized analysis, which can include bottom-up (Reunion Island) as well as top-down (Madagascar) cases. At the core of this protocol is the idea that impacts are a combination of hazard, exposure and vulnerability. Regarding hazard, a TC presents particularities that should be taken into account, as characteristic rainfall and high-speed winds of TCs (multi hazard-inputs) can induce storm surges, flooding events and landslides (cascading hazard outputs), which are also likely to significantly amplify the vulnerability of the territory. Intersecting hazard maps with land-cover information, RNR-I produces exposure maps (of entities likely to be impacted by the hazards-output). Building from these maps, we will focus on the physical and economic dimensions of vulnerability evaluated by means of damage functions. The physical vulnerability approaches the variable degrees of individual damage that, e.g. buildings, infrastructures or crops, suffer depending on the intensity of the hazard

(confirmed by remote sensing). The economic valuation of the level of destruction, linked to the value of the land use, determines the economic vulnerability.

For the characterization of cascading output hazard, monitoring the spatial footprint of the TC impacts by remote sensing offers great potential for assessing the extent of impacted areas. For this purpose, RNR-I has developed two automated processing flows, based on high spatial resolution optical and radar satellite data (10 m), that detect changes between a reference image before the cyclone and post-event images. These two analyses are complementary. Changes detected with Sentinel-1 data, based on the normalized difference ratio, allows the extent of flooded areas to be monitored as close as possible to the cyclone event (Alexandre et al. 2020). Changes detected with Sentinel-2 data, based on the use of change vector analysis (CVA) (Mouquet et al. 2020), which has shown its potential for monitoring changes in surface states (Hussain et al. 2013), allow a better characterization of land-cover change over longer time periods. Various events in the SWIO have been processed, and the results have been made available to the public.

For indirect effects, the negative impacts are not as obvious, especially because propagation mechanisms within socio-economic dimensions remain mostly undisclosed. RNR-I tackles this issue through two complementary approaches. We first rely on modern econometric techniques (Dell et al. 2014 or Camargo and Hsiang, 2016) together with the opportunity of merging geolocated data on the magnitude of TCs, and also on both economic and social features. The econometric strategy enables us to focus on how households reorganize their lives in the aftermath of TCs. One innovation of RNR-I is to focus on the causal effect of TCs on birthrate. The second approach undertakes the construction of theoretical models (CGE), accounting for the interdependence among economic agents, to explain the transmission channels through which the indirect effects take place (Narayan (2003) or Botzen et al. (2019)).

The data of RNR-C and RNR-T will be used by RNR-I for direct comparisons with the outputs of the system detecting changes in satellite images following the passage of a tropical cyclone. Furthermore, the simulated wind fields will also be used by RNR-I as output-hazard data for the development of either simulation models—computational laboratories devoted to the ex-ante evaluation of shocks—or econometric models—statistical models based on ex-post data in the aim of uncovering relations between relevant variables—to evaluate the potential socio-economic impact of cyclones (see Sects. 3.1 and 3.4). In the particular case of TC Enawo, the cross-analysis of the modelled wind field with the results of the change detection algorithms on Sentinel 2 satellite images shows good correlations between the maximum winds and the decrease in vegetation cover over a hundred kilometres around the landfall point, despite the difference in resolution and the presence of numerous clouds at this period (not shown).

3 Presentation of cross-disciplinary results

3.1 Floods following TC Ava in the Miandrivazo region

Coming from the north-east of the island, TC Ava landed on 5 January 2018 near the city of Toamasina on the east coast of Madagascar, with sustained winds of more than 150 km h^{-1} . Overall, the cyclone severely hit and caused heavy rainfall throughout the central part of the country and particularly in the studied region of Miandrivazo (Fig. 2a). Rainfall image maps computed from RNR-C meteorological models showed that TC Ava

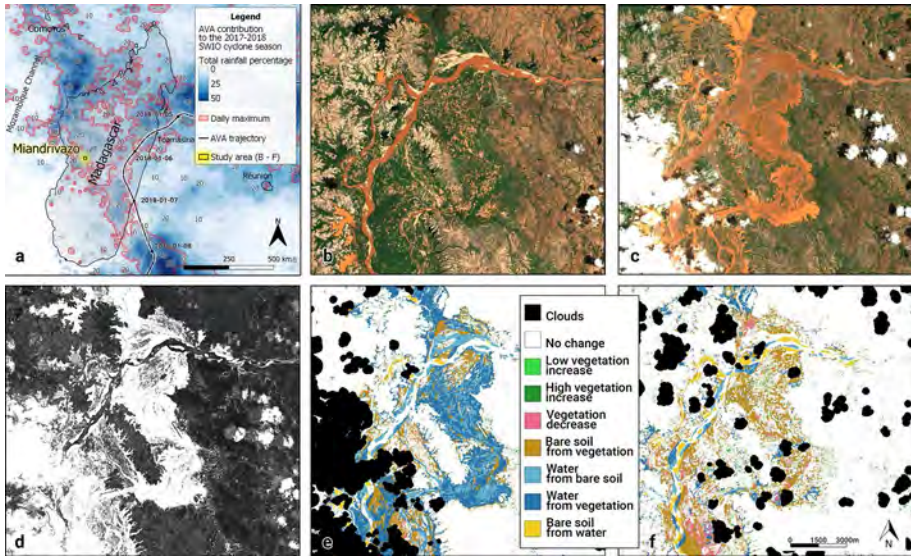


Fig. 5 Detection of changes between two remote-sensed images associated with TC Ava. **a** Location map of the Miandrivazo study site in Madagascar and meteorological conditions during TC Ava. **b** Sentinel-2 imagery of the region before the cyclone (25/12/2017) and **c** after cyclone Ava (09/01/2018). **d** Magnitude of changes between images (b) and (c) (the lighter the shade, the greater the change). **e** Classification of the main categories of changes just after the cyclone impact (09/01/2018) and **f** ten days later (19/01/2018)

brought about 20% of the total annual rains and reached the maximum daily precipitation for the whole 2017–2018 cyclone season in this area (Fig. 5a).

With the image of 25 December 2017 as a reference, we used the CVA algorithm to highlight areas of greatest change and compute classification maps of the impacts on two post-event images, 9 and 19 January 2018, respectively, 4 and 14 days after the event (Fig. 5b and c).

The results show a first rapid flooding of the entire floodplain, covering agricultural and forest plots, but sparing buildings and urban areas located on higher ground (day +4, Fig. 5d and e). Two weeks after the event, most of the flooded areas were replaced by bare wet soils, mainly affecting the agricultural parcels, which suffered strong decreases in crop cover. The main riverbed was deeply and durably modified, with the appearance of sandbanks and new water bodies (Fig. 5f).

3.2 Cyclonic heavy precipitations on landslides

A forced atmospheric high-resolution (500 m) simulation of TC Bejisa initialized and coupled at the lateral boundaries by the ocean–wave–atmosphere system (Meso-NH-OVA described previously with a 2 km resolution) has been carried out in order to obtain higher-resolution wind and rainfall maps over Reunion Island. The 24-h cumulative rainfall on 1 January 2014 during TC Bejisa shows three zones with cumulative rainfall greater than 250 mm in both the observations and the simulation (Fig. 6). The rainfall observations are a merged product of rain gauges and radar data given by the ANTILOPE QPE product. The zone of heavy rainfall in the centre of the island is relatively well reproduced by the model,

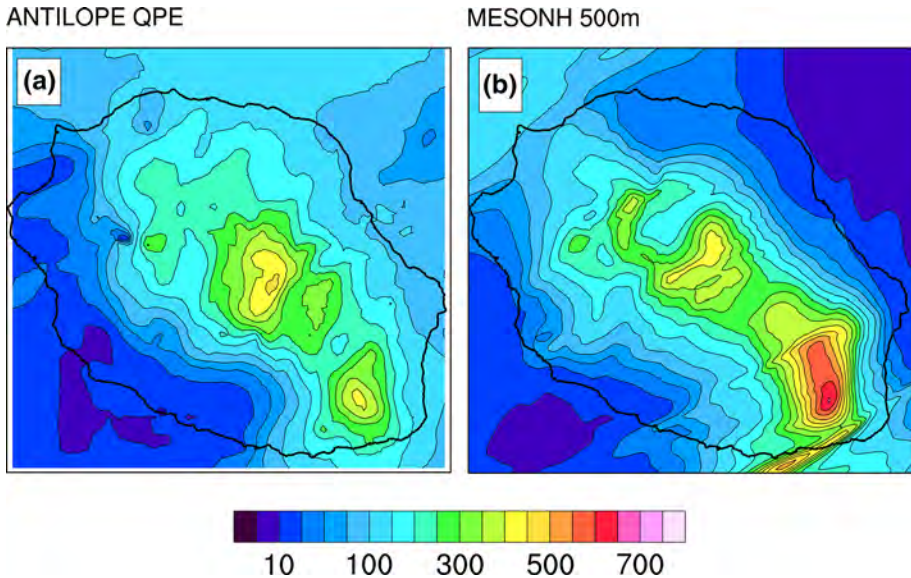


Fig. 6 Cumulative rainfall over 24 h for the day of January 1, 2014 (mm) given by ANTILOPE QPE (radar and rain gauge observations, (a)) and modelled by Meso-NH with a horizontal resolution of 500 m (b)

although the simulation tends to give slightly higher maximum values (~ 500 mm) than the merged data (~ 450 mm). In the simulation, the maximum rainfall is located on the south-eastern flank of Piton de la Fournaise (Fig. 2b) with values greater than 700 mm, whereas they barely reach 400 mm in the observations. This tendency of the models to overestimate rainfall on the south-east flank of the volcano has been found in other simulations of intense precipitation events. It should be noted, however, that the density of rain gauges is quite low and that radar acquisition in this area is partially masked by the orography. The third, northernmost, zone of maximum cumulative rainfall is overestimated by the model. While the cumulative rainfall is relatively well represented by the model on the west coast of the island, with values between 10 and 100 mm, the model tends to underestimate the cumulative rainfall over the north-east and east. This may be due to the slight shift of the modelled TC to the west compared to observations. Even though the rainfall restitution is not perfect, and taking into account the uncertainties in the production of an observed 2D rainfall field (especially in areas with low coverage in observations such as the south-eastern flank of the volcano), using a resolution of 500 m significantly improves the spatial distribution of rainfall (not shown).

During TC Bejisa (January 2014), beyond many small “normal landslides”, a significant one (1.1 million m^3) occurred in the centre of Reunion Island in the Salazie area (Fig. 2b and Fig. 7). After regular field observations, its volume was calculated by comparing two high-resolution DEM (LiDAR surveys). This landslide resulted in the accumulation of a large amount of various materials in the “Roche à Jacquot river” bed (Salazie cirque), most likely creating a temporary dam in the river. The dam vanished rapidly during Bejisa because of the strong river flow (a few tens of $m^3 s^{-1}$). Fortunately, neither the landslide nor the rupture of the dam had an impact on infrastructure or people.

In the next step, rainfall data produced by ANTILOPE will be used to estimate the slope instabilities. Groundwater is one of the multiple and various factors that significantly

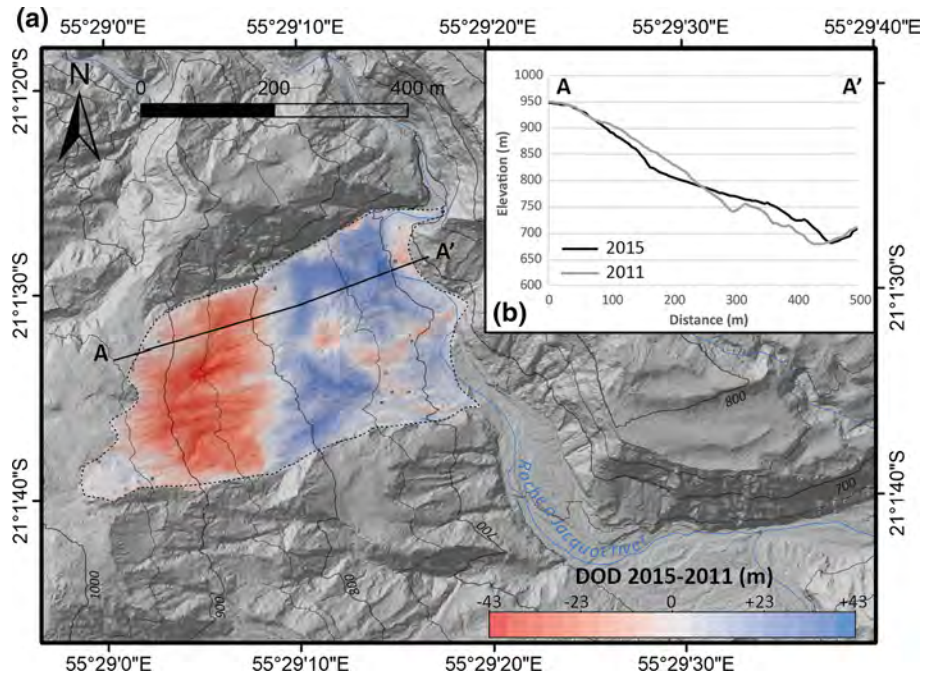


Fig. 7 1.1 Mm³ landslide triggered by the cyclone Bejisa in 2014 in Salazie. (a) DEMs of Difference (DOD) at 5 m resolution in the area affected by the landslide, surrounded by the dotted line; the red (erosion) and blue (accumulation) zones reveal major topographic changes between 2011 and 2015 (acquisition years of the DEMs). The black line A–A’ marks the ends of the 2011 and 2015 topographic profiles presented in (b) showing clear mass transfer

influence landslide displacement. A rise in water tables during aquifer recharge (e.g. after rainfalls) increases hydrostatic pressure in the media, which tends to decrease the landslide shear strength and cause the landslide to accelerate (Iverson and Major 1987; Baum and Reid 1992; Van Asch et al. 1999; Coe et al. 2003; Cappa et al. 2004; Corominas et al. 2005; Schulz et al. 2009).

The prediction of the movement pattern of landslides is assessed using physically based numerical modelling approaches (Corominas et al. 2005; Malet et al. 2005; Tacher et al. 2005; van Asch et al. 2007; Fernández-Merodo et al. 2012) or inverse numerical modelling that combines both numerical approaches and observations (Belle et al. 2014; Bernardie et al. 2015; Vallet et al. 2015). For both techniques, accurate spatial and temporal rainfall data are required.

3.3 Cyclonic swell impact on beach profile morphology

The ReNovRisk programme seeks to relate the evolution and distribution of cyclonic wave heights to the evolution of the coastline and the coastal sedimentary stock on Reunion Island. The first exploratory study was based on TC Bejisa.

The swell field was extracted from a simulation at 2 km horizontal resolution using the coupled ocean–waves–atmosphere system (CROCO, WW3 and Meso-NH) (Pianezze et al. 2018). The significant wave height and direction are shown in Fig. 8. On 1 January

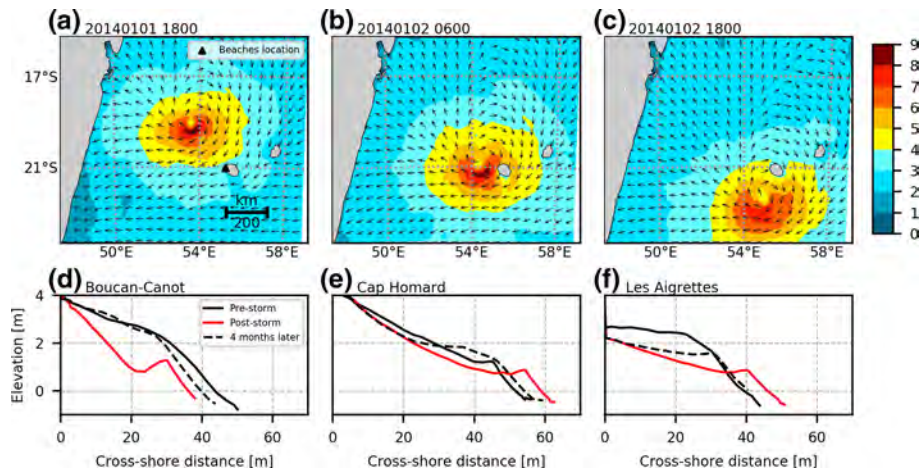


Fig. 8 Top: Significant wave height and direction simulated by Meso-NH-WW3-CrOCO during TC Bejisa. **a** 01 January 2014 at 18 UTC, **b** 02 January 2014 at 06 UTC, and **c** 02 January, 2014 at 18 UTC (Based on Pianezze et al. 2018). Bottom: Morphosedimentary evolution of beach topographic profiles caused by cyclone Bejisa at three sites: **d** Boucan Canot, **e** Cap Homard and **f** Les Aigrettes. Pre-storm topographic profiles (black lines) correspond to the date of 14 December 2013, post-storm (red lines)–17 January 2014 and the black dotted line corresponds to 4 months after Bejisa, that is, to 27 May 2014

at 18 UTC (Fig. 8a), the system was located north-west of Reunion Island and moving southwards, the maximum significant wave height, between 8 and 9 m, being concentrated under the wall of the system. When it passed closest to the island on 2 January at 06 UTC (Fig. 8b), the whole coastline was exposed to waves, and the maximum significant wave height of the cyclone was around 9 m. After Bejisa had passed close to the island’s coasts, the south and west facades were still affected by strong swell as the wave fields also propagated northwards (Fig. 8c).

At the same time, within the framework of DYNALIT, the seasonal and paroxysmal morphosedimentary dynamics of beaches were monitored (Mahabot et al. 2017a, b) along three cross-shore profiles of the carbonate sandy beaches that were impacted by the cyclonic swell of TC Béjisa: “Boucan Canot”, “Cap Homard” and “Les Aigrettes” (location on Fig. 2b).

Close to these three beaches, the temporal evolution of the cyclonic swell was characterized by a coupled simulation. The simulated significant wave height exceeded 3 m for 37 h from 1 January at 19 UTC to 3 January at 9 UTC. Since this swell was directly produced under the TC, as the TC passed along Reunion Island, the wave direction varied from south to east, affecting these beaches differently. To assess the impact of TC Bejisa on these three beaches, measurements by Differential Global Positioning System were made one month before the cyclone, two weeks after and 4 months after the cyclone. Profiles were established on a radial between the foreshore and backshore. The profile of Boucan Canot (Fig. 8d) presents the main morphological and volumetric change induced by Bejisa. The toe of beach retreat attained 7.5 m and very significant erosion can be observed along the profile, which reaches a thickness of 2 m between 20 and 25 m cross-shore distance. Along the profile, the volume change rate attained $-42.53 \pm 1.6 \text{ m}^3$. Four months after Bejisa, during fair-weather conditions, waves slowly carried material back on shore to rebuild—more or less—the original profile. However, the lower foreshore still retains the

after effects of the cyclonic swell and the head of the beach profile also shows a slight loss of sediment thickness, which can be expected to be perennial as there is no more dune recharge on this built-up coastline. After Bejisa, the Cap Homard (Fig. 8e) profile essentially shows a displacement of the beach berm by about 10 m, resulting in an advance of the beach profile of about +7.2 m. In addition, the whole profile underwent a decrease in sedimentary thickness of about 40 cm on average. In addition to this transfer between the backshore and foreshore, the cumulative sediment loss was $-6.76 \pm 2.21 \text{ m}^3$. Four months later, the beach was rebuilt with a convex berm that was larger than before Bejisa hit. Finally, the Les Aigrettes profile (Fig. 8f) shows a sediment transfer from the backshore to the foreshore and the nearshore, resulting in an advance of the beach profile by about +6.7 m. However, this advance was the result of the transfer from the backshore/foreshore to the nearshore zone. The volume change of $-23.42 \pm 1.71 \text{ m}^3$ after Bejisa is a good indicator of the lowering of the beach profile. Four months later, the profile had not recovered its initial morphology. Although beach recovery from severe storms has been shown to spread over years to decades (Dodet et al. 2018), in Reunion Island, on coral reef beaches, no long-term reconstruction of beach profiles has been demonstrated (Mahabot et al. 2017a, b).

3.4 Integration of simulated wind fields in the evaluation of direct economic impacts

Wind-induced physical damage to buildings and infrastructures can be very severe and increase their vulnerability—and the vulnerability of the assets they may contain—to TC induced hazards, such as floods. The identification of such damage, and its consequences in the socio-economic fabric, is therefore essential for the evaluation and quantification of TC impacts (Tamura 2009; Camargo and Hsiang 2015).

The simulations of high-resolution wind fields produced by ReNovRisk using the Bogus method (Sect. 3.2), given their dynamic character (output every 15 min), can be used to finely identify entities exposed to potentially damaging winds.

In the computational models for the ex-ante evaluation of economic impacts under development in RNR-I, the utilization of the high-resolution wind fields simulated enables both the entities exposed and the duration of the exposure to be identified. In turn, this thorough identification of exposed entities should allow fine estimations to be made of potential damage to buildings, infrastructures and plots. Figure 9 illustrates the potential of the simulated high-resolution wind fields in the analysis of exposure. The figure represents three snapshots of the simulation of cyclone Bejisa, over a layer of urban land use composed of buildings and infrastructures, in which the changes in wind speed can be appreciated as the cyclone moves southward (wind speeds represented have been limited to those that can cause damage, i.e. those higher than $\sim 25 \text{ m s}^{-1}$ (Tamura 2009)). As can be appreciated, the identification of entities exposed to damaging winds, together with an estimation of the duration of the exposition, is fairly straightforward with this method and highly valuable for a fine evaluation of potential direct damage.

3.5 Cyclonic impact on human reproduction in Madagascar

Estimated wind fields generated by TCs can be used within an econometric framework to investigate questions related to their impacts on social or economic characteristics (Dell et al. (2014), Hsiang and Jina (2014) or Strobl (2012)). As an example of TC social impact, RNR-I studies whether TCs may change parents' decisions

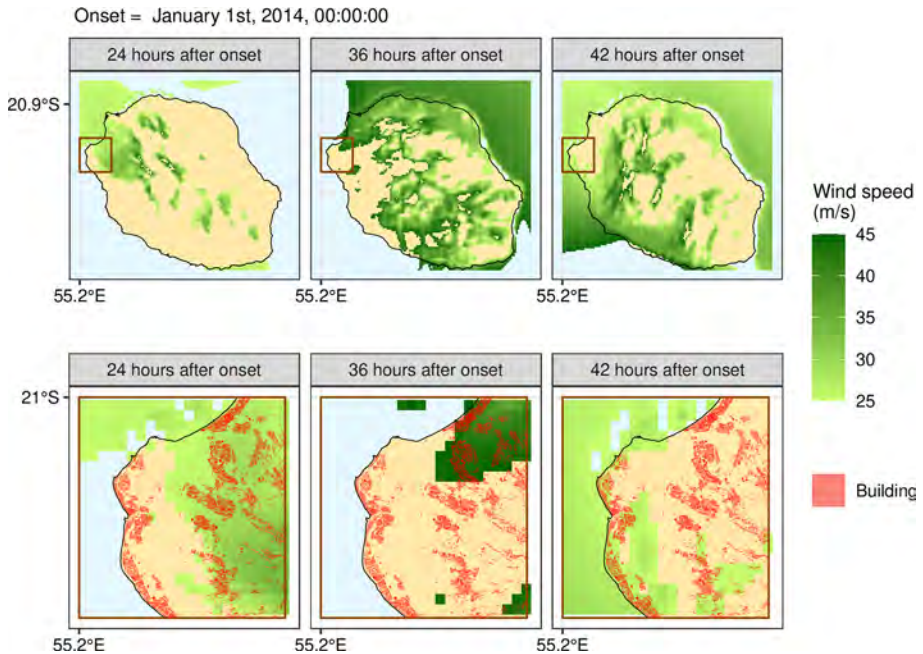


Fig. 9 Example of a GIS-based method for the evaluation of the dynamic exposure. Top from left to right: evolution of damaging wind fields (speed equal to or higher than 25 m s^{-1}) over Reunion Island taken from the simulation of TC Bejisa. Bottom from left to right: close-up maps ($15 \text{ km} \times 15 \text{ km}$) enabling the identification of buildings and infrastructures exposed (location and duration) to damaging winds

about having children in Madagascar. This is being done by using geolocated micro-data from the Malagasy Demographic and Health Survey, together with wind field data generated by tropical cyclones hitting Madagascar during the 1985–2009 period (Geiger et al. 2017). Merging geolocated data with the full fertility history of the women interviewed enables a unique dataset to be constructed, potentially emphasizing links between births and the mothers' TC experiences. RNR-I then applies panel econometric techniques, exploiting year-to-year variations in exposure to TCs, to estimate the causal effect of TCs on mothers' likelihood of giving birth. The main result of this study is that, on average and all other things being equal, exposure to wind speeds of 27.8 m s^{-1} (approximately 100 km h^{-1}) implies a total fall in the probability of giving birth of 25.6 points in the current year, together with a further decline of 5.9 and 2.0 points, respectively, one and two years after being exposed. Alternative estimations of the empirical model show that the adverse effect of TC exposure on the number of births is persistent. The estimated effect is shown to be robust to many alternative specifications of the econometric model. This new empirical evidence is consistent with economic mechanisms suggesting that TC exposure is perceived as an adverse shock—generating uncertainties in many aspects of daily life (loss of income, crops, livelihood)—that leads couples to postpone their decision to have children.

3.6 Evolution of TCs in the SWIO in the context of climate change

The evolution of tropical cyclones (frequency, intensity, trajectory, seasonality, etc.) in a warmer climate remains largely uncertain: the theory is poorly known, the series of observations are heterogeneous in time and space, and most of the multi-model climate projections available so far are too poorly resolved (100 km or more) to properly represent these phenomena. Nevertheless, two options are available: (i) to perform dedicated high-resolution simulations (50 km or less) and detect tropical cyclones using object tracking algorithms, or (ii) to exploit existing low-resolution climate projections by looking for links between cyclone activity (in monthly mean) and the large-scale environment (cyclogenesis indices).

In Cattiaux et al. (2020), we explored these two approaches, with a focus on the Southern Indian Ocean. On the one hand, we performed dedicated experiments with the CNRM-CM6-1 atmospheric model in a rotated-stretched configuration (resolution up to 12 km over the area of interest), capable of producing realistic cyclones. In a 2 K-warmer world, the model simulates a 20% decrease in the frequency of tropical cyclones in the basin, associated with a slight poleward shift in their trajectories (Fig. 10a), together with an increase in their maximum intensity and a reduction of about one month in the period of cyclonic activity (later onset, Fig. 10c). On the other hand, we calculated the cyclogenesis indices in these dedicated simulations and in the CMIP5 multi-model projections (lower resolution). The indices do not capture the decrease in frequency, but partially represent the changes in geographical (Fig. 10b) and seasonal (Fig. 10c) distribution.

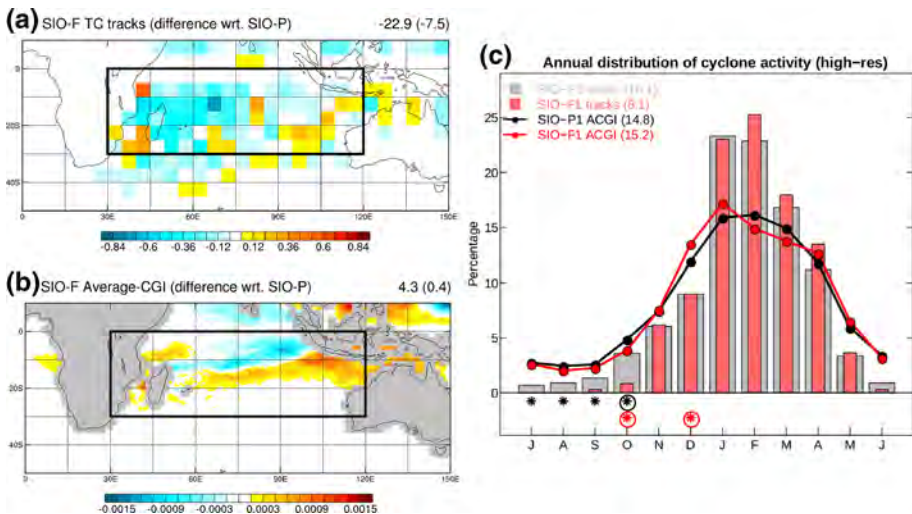


Fig. 10 Future evolution of TCs in the Indian Ocean. **a** Difference in track densities between future and present simulations. On average over the basin, we find a 20% decrease in the number of cyclone days (i.e. 7.5 days less). **b** Difference in cyclogenesis indices between present and future simulations. The indices miss the average decrease (they give +0.4 days over the basin), but suggest the southward shift observed in a). **c** Annual distribution of cyclones (bars) and cyclogenesis indices (lines) for present (grey/black) and future (red) simulations. A significant decrease at the beginning of the season (October) and a significant increase at the end of the season (February to April) are visible

These results are consistent with a similar study on the North Atlantic (Chauvin et al. 2019), and, more generally, with the scientific literature (e.g. Camargo et al. 2014). The originality here lies in the focus on the South Indian Ocean (little studied so far) and the evidence of the reduction in the length of the cyclone season (important for monitoring and vigilance systems). Ongoing studies will give a better understanding of the origins of the decrease in frequency projected by the model.

Further to the use of global climate models, another approach for evaluating future cyclonic risk is to estimate how damaging a recent historical cyclone could be if a similar one were to recur in the future (Schär 1996; Lackman 2015; Patricola 2018). In our case, we investigated Cyclone Bejisa, a climatologically typical cyclone that affected Reunion Island in early January 2014. Future environments for simulations of Bejisa-like cyclones were constructed using CMIP5 models to calculate changes in atmospheric and oceanic conditions, such as humidity and SST, between the recent climate and that of the end of the twenty-first century.

These changes were then added to ECMWF atmospheric and Mercator ocean analyses to create modified analyses of a future environment, thus permitting present versus future simulations. We conducted such simulations using the non-hydrostatic model Meso-NH with 3-km grid spacing, coupled to the ocean model CROCO for six different future environments derived from six different CMIP5 models.

Our findings suggest that future Bejisa-like cyclones will be 7% more intense, as measured by their maximum surface wind speed (Fig. 11a). Furthermore, the latitude at which future cyclones attain their lifetime maximum intensity will be displaced 2° further poleward, in line with an expansion of the tropics. In terms of trajectory, no substantial change was detected, as the present-day wind pattern was left unperturbed in order to maintain a north–south track that impacted Reunion Island. However, future cyclones were found to produce more intense rainfall, with the rainfall rates increasing by 29% on average (Fig. 11b). Additionally, future cyclones are predicted to be 9% smaller, as measured by the radius of their 17.5 m s⁻¹ winds. However, further high-resolution studies are still needed to constrain this characteristic change, as large variability persists in the literature (Knutson

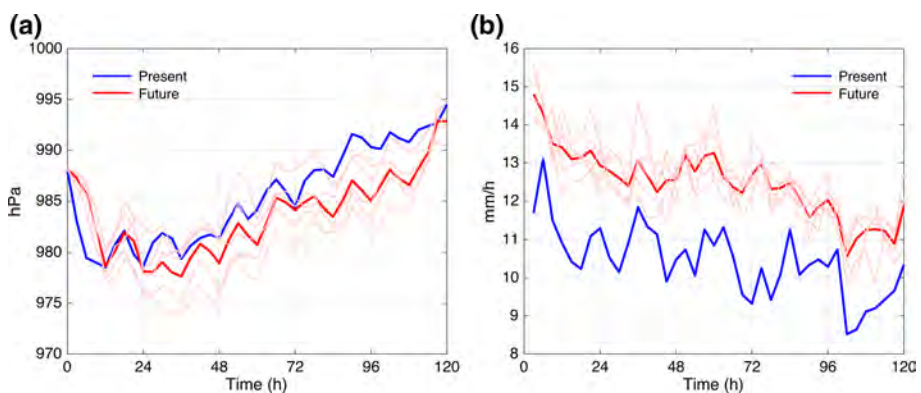


Fig. 11 Mean sea level pressure (a) and average rainfall rate within 100 km (b) of Bejisa-like cyclones simulated in Meso-NH coupled to the ocean model CROCO. A resimulation of Cyclone Bejisa in its historical environment (blue) is compared to Bejisa-like cyclones simulated in future environments derived from Coupled Model Intercomparison Project 5 (CMIP5) models (thin red lines) and their ensemble mean (red line). Projections indicate that such a typical cyclone could be characterized by significantly lower pressures and significantly heavier rainfalls in the future

2020). In addition to these atmospheric-related characteristics, we project a 0.2 m average increase in the significant ocean wave height, calculated by running the wave model WAVEWATCH III using hourly surface wind output. To the best of our knowledge, this is the first time that future changes in ocean waves have been projected for this basin. Although the change found here is modest, larger changes are anticipated for simulations based on stronger historical cyclones, with Cyclone Bejisa representing only a moderate-strength cyclone.

4 ReNovRisk database

The Sentinel remote sensing images produced during the RNR-I project have been processed and are stored on the servers and storage spaces of the SEAS-OI station, on which the project team relies (<http://www.seas-oi.fr/en/web/guest/accueil>). The SEAS-OI station is part of the French SEAS network of direct reception antennas for satellite data.

The SAR Sentinel-1 database is made up of data in the raw state or after different levels of pre-processing (spatial cropping and tiling, time filters) and processing (NDR, binary images, temporal summaries, etc.). Sentinel-2 optical data consist of raw L1C images, reflectance L2A images, cloud masks, multiple indices, and the results of change detection algorithms (classifications, temporal summaries, etc.). For each tile, covering an area of 100 km by 100 km, the entire time series (2015–2020) represents approximately 2 TB and more than 10,000 images. These numbers must be multiplied according to the geographical area and the number of S2 tiles monitored in the frame of the ReNovRisk programme.

These data from change detection chains therefore occupy very large volumes, which should be well organized to ensure a good perennial management. Work is underway to secure their storage and archiving, which currently rely mainly on the SEAS-OI infrastructure with a capacity of a few hundred TB. In addition, the metadata for each processing level is being produced to allow the harvesting of this image database. Finally, reflection is in progress to facilitate the availability of this data and, in particular, the final products (indices, change detection products), through a mapping web platform.

OSU-R (Observatoire des Sciences de l'Univers de la Reunion, CNRS, Météo-France and Université de la Reunion) organizes and supports transdisciplinary environmental research and operates a service unit (operation and maintenance of the stock of instruments, data analysis and processing). One goal of the services is the management of long-term observational data performed by its stations (that are part of European research infrastructures) and of measurement campaign datasets like the one produced in the framework of ReNovRisk. This data management is organized around 4 themes: data storage, metadata management, data processing, and data accessibility. The data storage provides long-term support and a backup guarantee, with an access by FTP for scientists and URL for data in open access. Metadata management is performed by means of OSU-R software, which allows information describing instrumentation and processing to be stored. The data processing is done through a data flow management service based on the Apache Airflow software (<https://airflow.apache.org/>), which pushes data to processing servers and data processing libraries, and classifies the data thus created. Finally, accessibility is achieved through the "GeOsur" tool (<https://geosur.univ-reunion.fr>), a web interface that aims to ensure the visibility of all the data produced. It is based on the open source software GeoNetwork (<https://geonetwork-opensource.org>) and allows the user to navigate easily through the database, using a search engine to visualize the different information on

the datasets, as well as the download links. This tool is based on standard data exchange protocols (ISO19139, OGC <https://www.ogc.org>), which allows it to be harvested to other institutional portals.

The ReNovRisk programme participates in an open science approach by making the data produced on cyclone risk available to the public. All this data management allows us to reference all the project data within the same catalogue. It will group together the data stored locally, and also data found in other databases. Finally, thanks to its interoperability, GeOsur will facilitate the transversal use of this data, both in the research field and for a wider audience. A demonstration of this interoperability is the harvesting of ReNovRisk data by another portal: PEIGO (<http://peigeo.re>), which is managed by AGORAH (<http://www.agorah.com>), the urban planning agency of Reunion Island, which aims to restore observational data in the form of cross-analyses to inform public policies.

5 Conclusions and perspectives

ReNovRisk is the first transdisciplinary programme dedicated to the study of cyclonic hazards in the Western Indian Ocean. It is composed of 4 different sub-programmes.

The first component, RNR-C, has enabled the development of new observation networks in the basin and numerical models for tropical cyclone modelling on the SWIO. The deployment of a GNSS network is intended to improve the state of the atmosphere in numerical weather prediction models through data assimilation. An intensive observation campaign was deployed in 2019 in the SWIO. New observation tools, in particular installed on marine and aerial drones, were tested in the environment of tropical cyclone Joaninha. Important numerical developments focused on the ocean–wave–atmosphere interactions, and on the representation of clouds and precipitation. The first studies have demonstrated the robustness of the modelling system, and a significant improvement in the track and intensity of the modelled tropical cyclones. ReNovRisk has also enabled high-resolution regional climate simulations for the SWIO, which have provided first answers to questions concerning the occurrence and geographical distribution of tropical cyclones in the coming decades. Moreover, high-resolution simulations of tropical cyclone Bejisa in a future climate have shown that its maximum intensity would be attained 2° further poleward, its intensity would increase by ~7%, and the precipitation rate would be strongly increased (~30%).

While RNR-C is planned to end in June 2021, the three other ReNovRisk sub-programmes are still in progress. Although they have not yet presented their final results, several scientific advances can be highlighted.

RNR-T is a first attempt to describe the integrated chain of tropical cyclone risks along a transect extending across the western volcanic plateau of Reunion Island (2000 m asl) and sloping down through ravines to the coastline. Infrastructures and preserved natural sites along the western coastal line of Reunion Island are particularly prone to overlapping cyclonic hazards (wind gusts, high precipitation, floods by ravines, transport of sediment, sea swell and submersion). A novel approach will involve cross-expertise in different domains (atmospheric physics, hydrology, sedimentology, geomorphology, coral reef growth, and ocean sciences). Complementary datasets will be required for calibrating model tools. Rainfall based on radar data corrected with rain gauge data will be estimated for catchments for which only a small number of point flow measurements are available.

RNR-E is a programme that focuses on the consequences of cyclones with the study, from upstream to downstream, of the sedimentary stock linked to ground movements and to flood-induced solid transport. The dynamics studied are characterized by different complementary methodologies. Thus, high-precision topographic surveys (GNSS network, geodetic marker, photogrammetry, and LiDAR) and seismological and electromagnetic measurement campaigns are being carried out on several landslides and rivers. Hydrological and geochemical monitoring of groundwater and surface water has also been implemented, and a broadband seismic network is monitoring the continuous transport of erosion products in rivers through the associated seismic noise. These data have made it possible to quantify, in particular with numerical modelling, precipitation and groundwater contributions to the acceleration of landslides during cyclonic events (Belle et al. 2014, 2018).

The remote sensing part of the RNR-I project has focused on the development of change detection algorithms to highlight the direct impacts of cyclones from satellite data. In order to promote their use by the largest possible number of interested parties, the processing chains developed are based on freely accessible Sentinel satellite data and are themselves published and open source. The data used come from the ESA Sentinel 1 and 2 satellites, acquired at high spatial (10 m) and temporal (5–10 day) resolutions with global coverage. Sen1Chain is the first processing chain developed that is based on SAR Sentinel 1 satellite data. It allows rapid detection of flooded areas by computing the normalized difference ratio (NDR) between two images, pre- and post-event. Based on radar data, Sen1Chain has the advantage of being insensitive to clouds, often numerous in a cyclonic context. The second processing chain developed, Sen2Chain, uses Sentinel 2 optical data to detect changes in land cover with a change vector analysis (CVA) method. As with Sen1Chain, Sen2Chain makes it possible to highlight floods linked to rainfall, but also modifications in plant cover under the action of the wind, or the appearance of bare ground. The greater sensitivity of this method to clouds is partly compensated by the high temporal acquisition frequency (5 days) increasing the probability of obtaining better quality images. Since 2015, the availability and historical depth of the Sentinel image database have allowed both processing chains to operate large time series of hundreds of images to place events in a seasonal context and highlight their exceptional nature. Several recent cyclonic events have been analysed in Madagascar (Enawo-2017 / Ava-2018), as have other events and geographical areas (Idai in Mozambique-2019, Dorian in the Bahamas—2019), on which the processing chains have demonstrated their effectiveness (Alexandre et al. 2020).

Beyond these thematic results, a significant contribution of ReNovRisk has been the networking of many scientists from different domains around collaborative programmes. ReNovRisk has brought together atmospheric physicists, hydrogeologists, geomorphologists, geophysicists, geomaticians, and economists to jointly analyse cyclonic hazards and impacts on Reunion Island and on the SWIO. These transdisciplinary collaborations have led to the development of a large set of tools to characterize the cyclonic hazards (wind, precipitation, swell) and their impacts after landfall (floods, landslides, coastline, sedimentary stock).

Furthermore, an important action of ReNovRisk is training and the communication of results. Two interoperable databases (GeOsur and Seas-OI) are under construction for free open access to the programme data with a horizon of mid-2021. Specific products developed for decision-makers and land-use planning institutes in Reunion Island will support adaptation to cyclonic hazards. Training activities are being carried out on the various scientific themes and on the tools deployed during ReNovRisk for students from SWIO countries (Mozambique and Madagascar).

ReNovRisk is intended to continue as the stakes are high for countries subject to cyclonic hazards, particularly in the SWIO, where the economic and health consequences of cyclones are significant in terms of poverty and infrastructure. As far as possible, ReNovRisk will be expanded more broadly into the fields of ecology, health, and social sciences, as the adaptation of territories to cyclone risks is a key element in building resilience to climate change.

Acknowledgements ReNovRisk was funded by the European Union through the ERDF and INTER-REG5 programmes, the région Reunion, the French state through the CPER programme, the University of Reunion, the BRGM, the IRD and the CNRS. Numerical modelling was made possible thanks to the computer resources of Météo-France. The authors would like to thank all the participants of the ReNovRisk programme.

Author contributions All the authors made significant contributions to the document through their participation in the ReNovRisk programme, the exploitation of data or numerical tools and the production of results. All authors contributed to the writing of the paper.

Funding ReNovRisk was funded by the European Union through the ERDF and INTER-REG5 programmes, the Reunion region and the French state through the CPER programme, the University of Reunion, the BRGM, the IRD and the CNRS.

Data availability Data will be available on GeoSUR (<https://geosur.univ-reunion.fr/web/>) and Seas-Oi (<http://www.seas-oi.fr/web/guest/acces-aux-donnees>) web platform from mid-2021. Beforehand, the data used can be requested from the authors.

Code availability Numerical models are in open source and available on web platforms: <http://mesonh.aero.obs-mip.fr/>, <https://www.umr-cnrm.fr/surfex/>, <http://polar.ncep.noaa.gov/waves/wavewatch/>, <http://www.croco-ocean.orgref> and <https://portal.enes.org/oasis>

Compliance with ethical standards

Conflict of interest No conflict of interests.

Ethics approval All the authors assure to have respected the scientific standard ethics in accordance with the recommendations of the publisher.

Financial interests All authors certify that they have no affiliations with or involvement in any organization or entity with any financial interest or non-financial interest in the subject matter or materials discussed in this manuscript.

Open Access This article is licensed under a Creative Commons Attribution 4.0 International License, which permits use, sharing, adaptation, distribution and reproduction in any medium or format, as long as you give appropriate credit to the original author(s) and the source, provide a link to the Creative Commons licence, and indicate if changes were made. The images or other third party material in this article are included in the article's Creative Commons licence, unless indicated otherwise in a credit line to the material. If material is not included in the article's Creative Commons licence and your intended use is not permitted by statutory regulation or exceeds the permitted use, you will need to obtain permission directly from the copyright holder. To view a copy of this licence, visit <http://creativecommons.org/licenses/by/4.0/>.

References

Alexandre C, Johary R, Catry T, Mouquet P, Révillion C, Srakotondraompiana S, Pennober G (2020) A sentinel-1 based processing chain for detection of cyclonic flood impacts. *Remote Sens* 12(2):252

- Andreas EL, Edson JB, Monahan EC, Rouault MP, Smith SD (1995) The spray contribution to net evaporation from the sea: A review of recent progress. *Boundary-Layer Meteorol* 72:3–52. <https://doi.org/10.1007/BF00712389>
- Aunay B, Rey A, Le Moigne B, Somoza K, Cance A, Salomero J (2018) Impacts de la tempête tropicale BERGUITTA sur La Reunion - Synthèse des investigations dans le cadre de la procédure de reconnaissance d'état de catastrophe naturelle. Rapport BRGM/RP-67604-FR
- Baray JL, Courcoux Y, Keckhut P, Portafaix T, Tulet P, Cammas JP, Hauchecorne A, Godin Beekmann S, De Mazière M, Hermans C, Desmet F, Sellegri K, Colomb A, Ramonet M, Sciare J, Vuillemin C, Hoareau C, Dionisi D, Dufflot V, Vèrèmes H, Porteneuve J, Gabarrot F, Gaudo T, Metzger JM, Payen G, Leclair de Bellevue J, Barthe C, Posny F, Ricaud P, Abchiche A, Delmas R (2013) Maïdo observatory: a new high-altitude station facility at Reunion Island (21° S, 55° E) for long-term atmospheric remote sensing and in situ measurements. *Atmos Meas Tech* 6:2865–2877. <https://doi.org/10.5194/amt-6-2865-2013>
- Barbary D, Leroux MD, Bousquet O (2019) The orographic effect of Reunion Island on tropical cyclone track and intensity. *Atmos Sci Lett* 20:e882. <https://doi.org/10.1002/asl.882>
- Barruol G, Reymond D, Fontaine FR, Hyvernaud O, Maurer V, Maamaatuaiahutapu K (2006) Characterizing swells in the southern Pacific from seismic and infrasonic noise analyses. *Geophys J Int* 164:516–542. <https://doi.org/10.1111/j.1365-246X.2006.02871.x>
- Barruol G, Davy C, Fontaine FR, Schlindwein V, Sigloch K (2016) Monitoring austral and cyclonic swells in the “Iles Eparses” (Mozambique Channel) from microseismic noise. *Acta Oecologica* 72:120–128. <https://doi.org/10.1016/j.actao.2015.10.015>
- Baum RL, Reid ME (1992) *Geology, Hydrology and Mechanics of the Alani-Paty Landslide, Manoa Valley, Oahu, Hawaii*. USGS 92–501, 87
- Bernardie S, Desramaut N, Malet JP, Gourlay M, Grandjean G (2015) Prediction of changes in landslide rates induced by rainfall. *Landslides* 12:481–494. <https://doi.org/10.1007/s10346-014-0495-8>
- Belle P, Aunay B, Bernardie S, Grandjean G, Ladouche MR, Join JL (2014) The application of an innovative inverse model for understanding and predicting landslide movements (Salazie cirque landslides, Reunion Island). *Landslides* 11:343–355.
- Belle P, Aunay B, Lachassagne P, Ladouche B, Join JL (2018) Control of tropical landcover and soil properties on landslides' aquifer recharge. *Piezomet and Dyn Water*. <https://doi.org/10.3390/w10101491>
- Bister M, Emanuel KA (2002) Low frequency variability of tropical cyclone potential intensity I Interannual to interdecadal variability. *J Geophys Res* 107:4801. <https://doi.org/10.1029/2001JD000776>
- Bordi I, Fraedrich K, Sutera A, Zhu X (2014) Ground-based GPS measurements: time behavior from half-hour to years. *Theor and Appl Climatol* 115:615–625
- Botzen WJW, Deschenes O, Sanders M (2019) The economic impacts of natural disasters: a review of models and empirical studies. *Rev Environ Econ and Policy* 13(2):167–188.
- Bousquet O, Lees E, Durand J, Peltier A, Duret A, Mekies D, Boissier P, Donal T, Fleischer-Dogley F, Zakariasy L (2020a) Densification of the ground-based GNSS observation network in the South-West Indian Ocean: current status, perspectives and examples of applications in meteorology and geodesy. *Front Earth Sci* 8:566105. <https://doi.org/10.3389/feart.2020.566105>
- Bousquet O, Barbary D, Bielli S, Kebir S, Raynaud L, Malardel S, Faure G (2020b) An evaluation of tropical cyclone forecast in the Southwest Indian Ocean basin with AROME-Indian Ocean convection-permitting numerical weather predicting system. *Atmos Sci Lett* 21:e950. <https://doi.org/10.1002/asl2.950>
- Bousquet O, Dalleau M, Bocquet M, Gaspar P, Bielli S, Ciccione S, Remy E, Vidard A (2020c) Sea turtles for ocean research and monitoring: overview and initial results of the STORM project in the Southwest Indian Ocean. *Front Marine Sci* 7:859 (in press)
- Bu YP, Fovell RG, Corbosiero KL (2014) Influence of Cloud-Radiative Forcing on Tropical Cyclone Structure. *J Atmos Sci* 71:1644–1662.
- Cattiaux J, Chauvin F, Bousquet O, Malardel S, Tsai CL (2020) Projected changes in the Southern Indian Ocean cyclone activity assessed from high-resolution experiments and CMIP5 models. *J Clim* 33(12):4975–4991. <https://doi.org/10.1175/JCLI-D-19-0591.1>
- Camargo SJ, Tippet MK, Sobel AH, Vecchi GA, Zhao M (2014) Testing the performance of tropical cyclone genesis indices in future climates using the HiRAM model. *J Climate* 27:9171–9196. <https://doi.org/10.1175/JCLI-D-13-00505.1>
- Camargo SJ, Hsiang SM (2015) Tropical cyclones: From the influence of climate to their socioeconomic impacts. In: M. Chavez, M. Ghil, and J. Urrutia-Fucugauchi, editors, *Extreme Events Observations, Modeling, and Economics*. Wiley, New York, ISBN 978–1–119–15701–4.
- Caine N (1980) The rainfall intensity-duration control of shallow landslides and debris flows. *Geografiska Ann: Series A, Phys Geograph* 62(1–2):23–27

- Cappa F, Guglielmi Y, Soukatchoff VM, Mudry J, Bertrand C, Charmoille A (2004) Hydromechanical modelling of a large moving rock slope inferred from slope levelling coupled to spring long-term hydrochemical monitoring: example of the La Clapière landslide (Southern Alps, France). *J Hydrol* 291:67–90.
- Chauvin F, Pilon R, Palany P, Bel Madani A (2019) Future changes in Atlantic hurricanes with the rotated-stretched ARPEGE-Climat at very high resolution. *Climate Dyn* 54:947–972.
- Coe JA, Ellis WL, Godt JW, Savage WZ, Savage JE, Michael JA, Kibler JD, Powers PS, Lidke DJ, Debray S (2003) Seasonal movement of the Slumgullion landslide determined from Global Positioning System surveys and filled instrumentation, July 1998–March 2002. *Eng Geol* 68:67–101.
- Colomb A, Kriat T, Leroux MD (2018) The rapid weakening of very severe tropical cyclone hellen (2014). *Month Weather Rev* 147:2717–2737.
- Corominas J, Moya J, Ledesma A, Lloret A, Gili JA (2005) Prediction of ground displacements and velocities from groundwater level changes at the Vallcebre landslide (Eastern Pyrenees, Spain). *Landslides* 2:83–96.
- Craig A, Valcke S, Coquart L (2017) Development and performance of a new version of the OASIS coupler, OASIS3-MCT_3.0. *Geoscientific Model Development* 10:3297–3308.
- Davy C, Barruol G, Fontaine FR, Stutzmann E, Sigloch K (2014) Tracking major storms from microseismic and hydroacoustic observations on the seafloor. *Geophys Res Lett.* <https://doi.org/10.1002/2014GL062319>
- Davy C, Stutzmann E, Barruol G, Fontaine FR, Schimmel M (2015) Sources of secondary microseisms in the Indian Ocean. *Geophys J Int* 202:1180–1189.
- Davy C, Barruol G, Fontaine FR, Cordier E (2016) Analyses of extreme swell events on La Reunion Island from microseismic noise. *Geophys J Int* 207:1767–1782.
- De Lavenne A, Andréassian V, Thirel G, Ramos MH, Perrin C (2019) A regularization approach to improve the sequential calibration of a semidistributed hydrological model. *Water Resour Res* 55:8821–8839.
- De Maria M, Sampson CR, Knaff JA, Musgrave KD (2014) Is tropical cyclone intensity guidance improving? *Bull Amer Meteor Soc* 95:387–398.
- Dell M, Jones BF, Olken BA (2014) What do we learn from the weather? The new climate-economy literature. *J Econ Lit* 52(3):740–798
- Dodet G, Castelle B, Masselink G, Scott T, Davidson M, Floc'h F, Jackson D, Suanes S (2018) Beach recovery from extreme storm activity during the 2013/14 winter along the Atlantic coast of Europe. *Earth Surf Process Landforms.* <https://doi.org/10.1002/esp.4500>
- Dow JM, Neilan RE, Rizos C (2009) The International GNSS Service in a changing landscape of Global Navigation Satellite Systems. *J Geodesy* 83:191–198
- Emanuel KA (1986) An air–sea interaction theory for tropical cyclones. part I: steady-state maintenance. *J Atmos Sci* 43:585–604. [https://doi.org/10.1175/1520-0469\(1986\)043<0585:AASITF.2.0.CO;2](https://doi.org/10.1175/1520-0469(1986)043<0585:AASITF.2.0.CO;2)
- Emanuel KA (1988) The maximum intensity of hurricanes. *J Atmos Sci* 45:1143–1155. [https://doi.org/10.1175/1520-0469\(1988\)045<1143:TMIOH.2.0.CO;2](https://doi.org/10.1175/1520-0469(1988)045<1143:TMIOH.2.0.CO;2)
- Eyring V, Bony S, Meehl GA, Senior CA, Stevens B, Stouffer RJ, Taylor KE (2016) Overview of the design and experimental organization of the Coupled Model Intercomparison Project Phase 6 (CMIP6). *Geosci Model Dev* 9:1937–1958
- Fernández-Merodo JA, García-Davalillo JC, Herrera G, Mira P, Pastor M (2012) 2D viscoplastic finite element modelling of slow landslides: the Portalet case study (Spain). *Landslides.* <https://doi.org/10.1007/s10346-012-0370-4>
- Fontaine FR, Barruol G, Gonzalez A (2015) Rivière des Pluies Project, La Reunion Island, 2015–2018; RESIF - Réseau Sismologique et géodésique Français. <http://dx.doi.org/https://doi.org/10.15778/RESIF.ZF2015>
- Fovell RG, Bu YP, Corbosiero KL, Tung W, Cao Y, Kuo H, Hsu L, Su H (2016) Influence of cloud microphysics and radiation on tropical cyclone structure and motion. *Meteorol Monograph* 56:11.1–11.27. <https://doi.org/10.1175/AMSMONOGRAPHS-D-15-0006.1>
- Geiger T, Frieler K, Bresch DN (2017) A global data set of tropical cyclone exposure (TCE-DAT). GFZ Data Services. <https://doi.org/10.5880/pik.2017.005>
- Gonzalez A, Fontaine FR, Barruol G, Recking A, Burtin A, Join JL, Delcher E, Michon L (2020) Seismic signature of a river flooding in La Reunion Island during the tropical cyclone Dumazile (March 2018), submitted to *Geophysical Journal International*
- Gonzalez A (2019) Suivi sismologique de l'impact des cyclones sur la charge de fond de la Rivière des Pluies et de la Rivière du Mât à La Reunion, Ph. D. thesis, Université de La Reunion, 171 p.

- Gonzalez A, Fontaine FR, Burtin A, Barruol G, Recking A, Join JL, Delcher E (2017) Seismic monitoring of the bedload transport in La Reunion Island rivers during tropical cyclones. EGU2017–5937, In, 19:14462. <http://adsabs.harvard.edu/abs/2017EGUGA.1914462>
- Hoarau T, Barthe C, Tulet P, Claeys M, Pinty JP, Bousquet O, Delanoë J, Vié B (2018a) Impact of the generation and activation of sea salt aerosols on the evolution of Tropical Cyclone Dumile. *J Geophys Res Atmos* 123:8813–8831. <https://doi.org/10.1029/2017JD028125>
- Hoarau T, Pinty JP, Barthe C (2018b) A representation of the collisional ice break-up process in the two-moment microphysics scheme LIMA v1.0 of Meso-NH. *Geosci Model Dev* 11:4269–4289. <https://doi.org/10.5194/gmd-11-4269-2018>
- IPCC (2013) Climate Change 2013. The physical science basis. Contribution of Working Group I to the Fifth Assessment Report of the Intergovernmental Panel on Climate Change. In T. Stocker et al. (Eds.), (p. pp. 1535). Cambridge University Press. doi: <https://doi.org/10.1017/CBO9781107415324>
- Iverson RM, Major JJ (1987) Rainfall, ground-water flow, and seasonal movement at Minor Creek landslide, northwestern California: physical interpretation of empirical relations. *Bull Geol Soc Am* 99:579–594. [https://doi.org/10.1130/0016-7606\(1987\)99%3c579:RGFASM%3e2.0.CO;2](https://doi.org/10.1130/0016-7606(1987)99%3c579:RGFASM%3e2.0.CO;2)
- Iverson RM (2000) Landslide triggering by rain infiltration. *Water Resour Res* 36(7):1897–1910
- Hallegatte S (2014) Natural Disasters and Climate Change, Springer International Publishing, XXII, 194 pp, doi:https://doi.org/10.1007/978-3-319-08933-1_2
- Holland GJ (1980) An analytic model of the wind and pressure profiles in hurricanes. *Month Wea Rev* 108:1212–1218
- Holland G (1993) WMO/TC-No. 560, Report No. TCP-31, World Meteorological Organization. Accessed: 17–03–2020. <https://wmo.asu.edu/content/world-greatest-twenty-four-hour-1-day-rainfall>.
- Kossin J, Emanuel K, Vecchi G (2014) The poleward migration of the location of tropical cyclone maximum intensity. *Nature* 509:349–352. <https://doi.org/10.1038/nature13278>
- Kossin J, Knapp KR, Olander TL, Velden CS (2020) Global increase in major tropical cyclone exceedance probability over the past four decades. Proceedings of the National Academy of Sciences May 2020, 201920849; DOI: <https://doi.org/10.1073/pnas.1920849117>
- Hsiang SM, Jina AS (2014) The Causal Effect of Environmental Catastrophe on Long-Run Economic Growth: Evidence from 6,700 Cyclones. Working Paper 20352, National Bureau of Economic Research. <https://www.nber.org/papers/w20352>
- Hussain M, Chen D, Cheng A, Wei H, Stanley D (2013) Change detection from remotely sensed images: from pixel-based to object-based approaches. *ISPRS J Photogramm and Remote Sens* 80:91–106
- Knutson T, Camargo SJ, Chan JCL, Emanuel K, Ho CH, Kossin J, Mohapatra M, Satoh M, Sugi M, Walsh K, Wu L (2020) Tropical cyclones and climate change assessment: part ii: projected response to anthropogenic warming. *Bull Am Meteorol Soc*. <https://doi.org/10.1175/BAMS-D-18-0194.1>
- Lac C, Chaboureaud JP, Masson V, Pinty JP, Tulet P, Escobar J, Leriche M, Barthe C, Aouizerats B, Augros C, Aumont P, Auguste F, Bechtold P, Berthet S, Bielli S, Bosseur F, Caumont O, Cohard JM, Colin J, Couvreur F, Cuxart J, Delautier G, Dauhut T, Ducrocq V, Filippi JB, Gazen D, Geoffroy O, Gheusi F, Honnert R, Lafore JP, Lebeaupin Brossier C, Libois Q, Lunet T, Mari C, Maric T, Mascart P, Mogé M, Molinié G, Nuissier O, Pantillon F, Peyrillé P, Pergaud J, Perraud E, Pianezze J, Redelsperger JL, Ricard D, Richard E, Riette S, Rodier Q, Schoetter R, Seyfried L, Stein J, Suhre K, Taoufour M, Thouron O, Turner S, Verrelle A, Vié B, Visentin F, Vionnet V, Wautelet P (2018) Overview of the Meso-NH model version 5.4 and its applications. *Geosci Model Dev* 11:1929–1969. <https://doi.org/10.5194/gmd-11-1929-2018>
- Lackmann GM (2015) (2015), Hurricane Sandy before 1900 and after 2100. *Bull Amer Meteor Soc* 96(4):547–560. <https://doi.org/10.1175/BAMS-D-14-00123.1>
- Lafore JP, Stein J, Asencio N, Bougeault P, Ducrocq V, Duron J, Fischer C, Hérel P, Mascart P, Masson V, Pinty JP, Redelsperger JL, Richard E, Vilà-Guerau de Arellano J (1998) The Meso-NH atmospheric simulation system. part I: adiabatic formulation and control simulations. *Ann Geophys* 16:90–109. <https://doi.org/10.1007/s00585-997-0090-6>
- Laurantin O (2008) Antilope: Hourly rainfall analysis merging radar and rain gauge data. Proc. Int. Symp. on Weather Radar and Hydrology Conf. 2008, Grenoble, France, Laboratoire d'étude des Transferts en Hydrologie et Environnement (LTHE), 2–8
- Lecacheux S, Bonnardot F, Rousseau M, Paris F, Pedreros R, Lerma NA, Quetelard H, Barbary D (2018) Probabilistic forecast of coastal waves for flood warning applications at Reunion Island (Indian Ocean). *J Coastal Res* 85:776–780. <https://doi.org/10.2112/SI85-156.1>
- Lees E, Bousquet O, Roy D, Leclair J (2020) Analysis of diurnal to seasonal variability of integrated water vapour in the South Indian Ocean Basin using ground-based GNSS and 5th generation ECMWF Reanalysis (ERA5) data. *Q. J. R. Meteorol. Soc* (**In press**)

- Leroux M, Meister J, Mekies D, Dorla A, Caroff P (2018) A climatology of Southwest Indian ocean tropical systems: their number, tracks, impacts, sizes, empirical maximum potential intensity, and intensity changes. *J Appl Meteor Climatol* 57:1021–1041. <https://doi.org/10.1175/JAMC-D-17-0094.1>
- Liébault F, Peteuil C, Remaître A (2010) Approches géomorphologiques de la production sédimentaire des torrents. *Sciences Eaux & Territoires*, n°2: 128–35. <https://doi.org/https://doi.org/10.14758/SET-REVUE.2010.2.15>
- Lu J, Deser C, Reichler T (2009) Cause of the widening of the tropical belt since 1958. *Geophys Res Lett* 36(3):L03803
- Mahabot MM, Pennober G, Suanez S, Troadec R, Delacourt C (2017a) Effect of tropical cyclones on short-term evolution of carbonate sandy beaches on Reunion Island. *Indian Ocean J Coast Res* 33(4):839–853
- Mahabot MM, Jaud M, Pennober G, Le Dantec N, Troadec R, Suanez S, Delacourt C (2017b) The basics for a permanent observatory of shoreline evolution in tropical environments; lessons from back-reef beaches in La Reunion Island, *Comptes Rendus Geoscience*, 349(6–7). ISSN. <https://doi.org/10.1016/j.crte.2017.09.010>
- Malet JP, Van Asch ThWG, Van Beek R, Maquaire O (2005) Forecasting the behaviour of complex landslides with a spatially distributed hydrological model. *Nat Hazards and Earth Syst Sci* 5:71–85. <https://doi.org/10.5194/nhess-5-71-2005>
- Masson V, Le Moigne P, Martin E, Faroux S, Alias A, Alkama R, Belamari S, Barbu A, Boone A, Bouysse F, Brousseau P, Brun E, Calvet JC, Carrer D, Decharme B, Delire C, Donier S, Essaouini K, Gibelin AL, Giordani H, Habets F, Jidane M, Kerdraon G, Kourzeneva E, Lafaysse M, Lafont S, Lebeaupin Brossier C, Lemonsu A, Mahfouf JF, Marguinaud P, Mokhtari M, Morin S, Pigeon G, Salgado R, Seity Y, Taillefer F, Tanguy G, Tulet P, Vincendon B, Vionnet V, Voldoire A (2013) The SURFEXv7.2 land and ocean surface platform for coupled or offline simulation of earth surface variables and fluxes. *Geosci Model Dev* 6:929–960. <https://doi.org/10.5194/gmd-6-929-2013>
- Mavume AF, Rydberg L, Lutjeharms JRE (2008) Climatology of tropical cyclones in the South-West Indian Ocean; landfall in Mozambique and Madagascar. *West Indian Ocean J Mar Sci* 8:15–36
- Meyer V, Becker N, Markantonis V, Schwarze R, Van den Bergh JCM, Bouwer LM, Bubeck P, Ciavola P, Genovese E, Green C, Hallegatte S, Kreibich H, Lequeux Q, Logar I, Papyrakis E, Pfurtscheller C, Poussin J, Przyluski V, Thieken AH, Viavattene C (2013) Review article: assessing the costs of natural hazards - state of the art and knowledge gaps. *Nat Hazards and Earth Syst Sci* 13(5):1351–1373
- Mile M, Benáček P, Rózsa S (2019) The use of GNSS zenith total delays in operational arome/hungary 3d-var over a central European domain. *Atmosph Measure Techniq* 12(3):1569–1579
- Mittal R, Tewari M, Radhakrishnan C, Ray P, Singh T, Nickerson AK (2019) Response of tropical cyclone Phailin (2013) in the Bay of Bengal to climate perturbations. *Clim Dyn* 53:2013–2030. <https://doi.org/10.1007/s00382-019-04761-w>
- Mouquet P, Alexandre C, Rasolomamonjy J, Rosa J, Cattray T, Révillion C, Rakotondraompiana S, Pennober G (2020) SENTINEL-1 AND SENTINEL-2 time series processing chains for cyclone impact monitoring in South WestIndian Ocean. *Int Arch Photogramm Remote Sens Spatial Inf Sci*. <https://doi.org/10.5194/isprs-archives-XLIII-B3-2020-1593-2020>
- Narayan PK (2003) Macroeconomic impact of natural disasters on a small island economy: evidence from a CGE model. *Appl Econ Lett* 10(11):721–723. <https://doi.org/10.1080/1350485032000133372>
- Neumann CJ (1993) Global guide to tropical cyclone forecasting. Chap 1: Global overview. TD 560 - TCP 31, WMO, Genève, Suisse, 1.1–1.37
- Ovadnevaite J, Manders A, de Leeuw G, Ceburnis D, Monahan C, Partanen AI, Korhonen H, O'Dowd CD (2014) A sea spray aerosol flux parameterization encapsulating wave state. *Atmos Chem Phys* 14(4):1837–1852. <https://doi.org/10.5194/acp-14-1837-2014>
- Parent du Châtelet J, Tabary P, Guimera M (2005) The PANTHERE Project and the Evolution of the French Operational Radar Network and Products : Rain-estimation, Doppler winds, and Dual-Polarisation (Le projet PANTHERE), 32nd American Meteorological Society Radar Conference, Albuquerque, NM, <http://ams.confex.com/ams/pdfpapers/96217.pdf>
- Parker CL, Bruyère CL, Mooney PA, Lynch AH (2018) The response of land-falling tropical cyclone characteristics to projected climate change in northeast Australia. *Clim Dyn* 51:3467–3485. <https://doi.org/10.1007/s00382-018-4091-9>
- Patricola CM, Wehner MF (2018) Anthropogenic influences on major tropical cyclone events. *Nature* 563:339–346. <https://doi.org/10.1038/s41586-018-0673-2>
- Pauthier B, Bois B, Castel T, Thévenin D, Smith CC, Richard Y (2016) Mesoscale and local scale evaluations of quantitative precipitation estimates by weather radar products during a heavy rainfall event, *Advances in Meteorology*, vol. 2016, Article ID 6089319, 9 pages

- Pianezze J, Barthe C, Bielli S, Tulet P, Jullien S, Cambon G, Bousquet O, Claeys M, Cordier E (2018) A new coupled ocean-waves-atmosphere model designed for tropical storm studies: example of tropical cyclone Bejisa (2013–2014) in the south-west Indian ocean. *J Adv Model Earth Syst*. <https://doi.org/10.1002/2017MS001177>
- Quetelard H, Bessemoulin P, Peterson TC, Burton A, Boodhoo Y, Cerveny RS (2007) WMO CCI Rapporteur for climate extremes decision, World Meteorological Organization. Accessed: 17–03–2020. <https://wmo.asu.edu/content/>
- Raucoules D, de Michele M, Aunay B (2018) Landslide displacement mapping based on ALOS-2/PAL-SAR-2 data using image correlation techniques and SAR interferometry: application to the Hell-Bourg landslide (Salazie Circle, La Reunion Island). *Geocarto Int*. <https://doi.org/10.1080/10106049.2018.1508311>
- Rault C, Dewez TJB, Aunay B (2020) Structure-from-motion processing of aerial archive photographs: sensitivity analyses pave the way for quantifying geomorphological changes since 1978 in La Reunion Island. *ISPRS Ann. Photogramm Remote Sens Spatial Inf Sci* 2:773–780. <https://doi.org/10.5194/isprs-annals-V-2-2020-773-2020>
- Rotunno R, Emanuel KA (1987) An air-sea interaction theory for tropical cyclones. part II: evolutionary study using a nonhydrostatic axisymmetric numerical model. *J Atmos Sci* 44:542–561. [https://doi.org/10.1175/1520-0469\(1987\)044%3c0542:AAITFT%3e2.0.CO;2](https://doi.org/10.1175/1520-0469(1987)044%3c0542:AAITFT%3e2.0.CO;2)
- Rindrahisaona EJ, Cordier E, Barruol G, Fontaine FR, Singh M (2020) Assessing swells in La Reunion Island from terrestrial seismic observations, oceanographic records and offshore wave models. *Geophys J Int* 221:1883–1895. <https://doi.org/10.1093/gji/ggaa117>
- Rojas-Serna C, Lebecherel L, Perrin C, Andreassian V, Oudin L (2016) How should a rainfall-runoff model be parameterized in an almost ungauged catchment? a methodology tested on 609 catchments. *Water Resour. Res* 52:4765–4784. <https://doi.org/10.1002/2015WR018549>
- Schär C, Frei C, Lüthi D, Davies HC (1996) Surrogate climate-change scenarios for regional climate models. *Geophys Res Lett*. <https://doi.org/10.1029/96GL00265>
- Schulz WH, McKenna JP, Kibler JD, Biavati G (2009) Relations between hydrology and velocity of a continuously moving landslide -evidence of pore-pressure feedback regulating landslide motion? *Landslides* 6:181–190. <https://doi.org/10.1007/s10346-009-0157-4>
- Seity Y BP, Malardel S, Hello G, Bénard P, Bouttier F, Lac C, Masson V (2011) The AROME-France convective-scale operational model. *Mon Wea Rev* 139:976–991. <https://doi.org/10.1175/2010MWR3425.1>
- Staten PW, Lu J, Grise KM, Davis SM (2018) Birner T (2018) Re-examining tropical expansion. *Nat Clim Change* 8:768–775. <https://doi.org/10.1038/s41558-018-0246-2>
- Staten PW, Grise KM, Davis SM, Karnauskas KB, Waugh DW, Maycock A, Fu Q, Cook K, Adam O, Simpson IR, Allen RJ, Rosenlof K, Chen G, Ummenhofer CC, Quan X, Kossin JP, Davis NA, Son S (2020) Tropical widening: From global variations to regional impacts. *Bull Amer Meteor Soc* 101(6):E897–E904. <https://doi.org/10.1175/BAMS-D-19-0047.1>
- Strobl E (2012) The economic growth impact of natural disasters in developing countries: evidence from hurricane strikes in the Central American and Caribbean regions. *J Dev Econ* 97(1):130–141
- Stumpf A, Augereau E, Delacourt C, Bonnier J (2016) Photogrammetric discharge monitoring of small tropical mountain rivers: a case study at Rivière Des Pluies, Reunion Island". *Water Resour Res* 52(6):4550–4570. <https://doi.org/10.1002/2015WR018292>
- Tacher L, Bonnard C, Laloui L, Parriaux A (2005) Modelling the behaviour of a large landslide with respect to hydrogeological and geomechanical parameter heterogeneity. *Landslides* 2:3–14. <https://doi.org/10.1007/s10346-004-0038-9>
- Tamura Y (2009) Wind-induced damage to buildings and disaster risk reduction. The Seventh Asia-Pacific Conference on Wind Engineering, November 8–12, 2009, Taipei, Taiwan
- Terry J, Kim I-H, Jolivet S (2013) Sinuosity of tropical cyclone tracks in the South West Indian Ocean: spatio temporal patterns and relationships with fundamental storm attributes. *Appl Geogr* 45:29–40. <https://doi.org/10.1016/j.apgeog.2013.08.006>
- Thompson C, Barthe C, Bielli S, Tulet P, Pianezze J Projecting Characteristic Changes of a Typical Tropical Cyclone under Climate Change in the South West Indian Ocean. Submitted to *J. Geophys. Res.*
- Trabing BC, Bell MM, Brown BR (2019) Impacts of radiation and upper-tropospheric temperatures on tropical cyclone structure and intensity. *J Atmos Sci* 76:135–153. <https://doi.org/10.1175/JAS-D-18-0165.1>
- Tulet P, Crassier V, Cousin F, Suhre K, Rosset R (2005) ORILAM, a three-moment lognormal aerosol scheme for mesoscale atmospheric model: online coupling into the Meso-NH-C model and validation on the Escompte campaign. *J Geophys Res* 110:D18201. <https://doi.org/10.1029/2004JD005716>

- Vallet A, Charlier JB, Fabbri O, Bertrand C, Carry N, Mudry J (2016) Functioning and precipitation-displacement modelling of rainfall-induced deep-seated landslides subject to creep deformation. *Landslides* 13:653–670.
- Van Asch TWJ, Buma J, Van Beek LPH (1999) A view on some hydrological triggering systems in landslides. *Geomorphology* 30:25–32.
- Vérèmes H (2020) Application de la méthode dite « de bogus » dans le programme ReNovRisk-TRANS-FERTS, Technical report, Université de La Reunion; Région Reunion. 2020. <https://doi.org/10.26171/Veron>
- Veron F (2015) Ocean sprays. *Annu Rev Fluid Mech* 47(1):507–538.
- Vié B, Pinty JP, Berthet S, Leriche M (2016) LIMA (v10): a quasi two-moment microphysical scheme driven by a multimodal population of cloud condensation and ice freezing nuclei. *Geosci Model Develop* 9(2):567–586. <https://doi.org/10.5194/gmd-9-567-2016>
- Vitart F, Ardilouze C, Bonet A, Brookshaw A, Chen M, Codorean C, Déqué M, Ferranti L, Fucile E, Fuentes M, Hendon H, Hodgson J, Kang HS, Kumar A, Lin H, Liu G, Liu X, Malguzzi P, Mallas I, Manoussakis M, Mastrangelo D, MacLachlan C, McLean P, Minami A, Mladek R, Nakazawa T, Najm S, Nie Y, Rixen M, Robertson AW, Ruti P, Sun C, Takaya Y, Tolstykh M, Venuti F, Waliser D, Woolnough S, Wu T, Won DJ, Xiao H, Zaripov R, Zhang L (2017) The seasonal to sub-seasonal forecast project database. *Bull Am Meteor Soc* 98:163–173. <https://doi.org/10.1175/BAMS-D-16-0017.1>
- Voldoire A, Decharme B, Pianezze J, Lebeaupin Brossier C, Sevault F, Seyfried L, Garnier V, Bielli S, Valcke S, Alias A, Accensi M, Arduin F, Bouin MN, Ducrocq V, Faroux S, Giordani H, Léger F, Marsaleix P, Rainaud R, Redelsperger JL, Richard E, Riette S (2017) SURFEX v8.0 interface with OASIS3-MCT to couple atmosphere with hydrology, ocean, waves and sea-ice models, from coastal to global scales. *Geosci Model Dev* 10:4207–4227. <https://doi.org/10.5194/gmd-10-4207-2017>
- WMO (2016) Tropical Cyclone Programme, Regional Association I – Tropical Cyclone Operational Plan for the South-West Indian Ocean. Report No. TCP-12, Report No. TCP-12, WMO-No. 1178, https://library.wmo.int/doc_num.php?explnum_id=4031

Publisher's Note Springer Nature remains neutral with regard to jurisdictional claims in published maps and institutional affiliations.

Authors and Affiliations

Pierre Tulet¹  · Bertrand Aunay²  · Guilhem Barruol^{3,4}  · Christelle Barthe¹  · Remi Belon² · Soline Bielli¹  · François Bonnardot⁵  · Olivier Bousquet¹  · Jean-Pierre Cammas^{1,6}  · Julien Cattiaux⁷  · Fabrice Chauvin⁷ · Idriss Fontaine⁸ · Fabrice R. Fontaine^{3,9}  · Franck Gabarrot⁶ · Sabine Garabedian⁸ · Alicia Gonzalez^{3,4} · Jean-Lambert Join³ · Florian Jouvenot¹⁰ · David Nortes-Martinez⁸  · Dominique Mékiès¹ · Pascal Mouquet¹⁰ · Guillaume Payen⁶ · Gwenaëlle Pennober¹⁰ · Joris Pianezze¹  · Claire Rault² · Christophe Revillion¹⁰ · Elisa J. Rindhararisaona^{3,4} · Kevin Samyn² · Callum Thompson¹  · Hélène Vérèmes^{1,6} 

¹ LACy, Laboratoire de l'Atmosphère et des Cyclones (UMR 8105, Université de la Reunion, CNRS, Météo-France), Saint-Denis de La Reunion, France

² BRGM, Bureau de Recherches Géologiques et Minières, Saint-Denis de La Reunion, France

³ LGSR, Laboratoire Géosciences Reunion (Université de La Reunion, IPGP), Saint-Denis de La Reunion, France

⁴ Université de Paris, Institut de physique du globe de Paris, CNRS, Paris, France

⁵ DIROI, Direction Interrégionale Océan Indien (Météo-France), Saint-Denis de la Reunion, France

⁶ OSUR, Observatoire des Sciences de l'Univers de La Reunion (UMS 3365, Université de la Reunion, CNRS, Météo-France), Saint-Denis de la Reunion, France

⁷ CNRM, Centre National de la Recherche Météorologique (UMR 3589, Météo-France, CNRS), Toulouse, France

-
- ⁸ CEMOI, Centre d'Economie et de Management de l'Océan Indien (Université de la Reunion), Saint-Denis de La Reunion, France
- ⁹ Université de Paris, Institut de physique du globe de Paris, CNRS F-75005 Paris, France. Observatoire volcanologique et sismologique de la Martinique, Institut de physique du globe de Paris, F-97250 Fonds Saint Denis, France
- ¹⁰ Espace-Dev, Espace pour le Développement (UMR 228, IRD, Université de la Guyane, Université de La Reunion, Université des Antilles, Université de Montpellier), Montpellier, France